NASA/TM–2016-219337/Volume II/Part 2

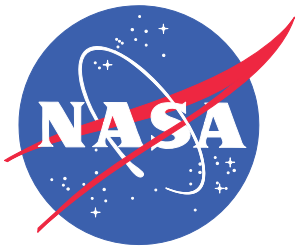

Crew Exploration Vehicle (CEV) (Orion) Occupant Protection

Appendices Part 2

Nancy J. Currie-Gregg/NESC
Langley Research Center, Hampton, Virginia

Michael L. Gernhardt
Johnson Space Center, Houston, Texas

Charles Lawrence
Glenn Research Center, Cleveland, Ohio

Jeffrey T. Somers
KBRwyle, Houston, Texas

September 2016

NASA STI Program . . . in Profile

Since its founding, NASA has been dedicated to the advancement of aeronautics and space science. The NASA scientific and technical information (STI) program plays a key part in helping NASA maintain this important role.

The NASA STI program operates under the auspices of the Agency Chief Information Officer. It collects, organizes, provides for archiving, and disseminates NASA's STI. The NASA STI program provides access to the NTRS Registered and its public interface, the NASA Technical Reports Server, thus providing one of the largest collections of aeronautical and space science STI in the world. Results are published in both non-NASA channels and by NASA in the NASA STI Report Series, which includes the following report types:

- TECHNICAL PUBLICATION. Reports of completed research or a major significant phase of research that present the results of NASA Programs and include extensive data or theoretical analysis. Includes compilations of significant scientific and technical data and information deemed to be of continuing reference value. NASA counter-part of peer-reviewed formal professional papers but has less stringent limitations on manuscript length and extent of graphic presentations.

- TECHNICAL MEMORANDUM. Scientific and technical findings that are preliminary or of specialized interest, e.g., quick release reports, working papers, and bibliographies that contain minimal annotation. Does not contain extensive analysis.

- CONTRACTOR REPORT. Scientific and technical findings by NASA-sponsored contractors and grantees.

- CONFERENCE PUBLICATION. Collected papers from scientific and technical conferences, symposia, seminars, or other meetings sponsored or co-sponsored by NASA.

- SPECIAL PUBLICATION. Scientific, technical, or historical information from NASA programs, projects, and missions, often concerned with subjects having substantial public interest.

- TECHNICAL TRANSLATION. English-language translations of foreign scientific and technical material pertinent to NASA's mission.

Specialized services also include organizing and publishing research results, distributing specialized research announcements and feeds, providing information desk and personal search support, and enabling data exchange services.

For more information about the NASA STI program, see the following:

- Access the NASA STI program home page at *http://www.sti.nasa.gov*

- E-mail your question to help@sti.nasa.gov

- Phone the NASA STI Information Desk at 757-864-9658

- Write to:
  NASA STI Information Desk
  Mail Stop 148
  NASA Langley Research Center
  Hampton, VA 23681-2199

NASA/TM–2016-219337/Volume II/Part 2

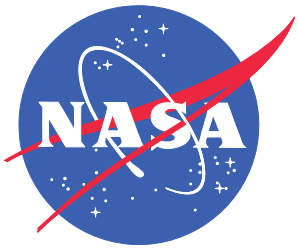

Crew Exploration Vehicle (CEV) (Orion) Occupant Protection

Appendices Part 2

Nancy J. Currie-Gregg/NESC
Langley Research Center, Hampton, Virginia

Michael L. Gernhardt
Johnson Space Center, Houston, Texas

Charles Lawrence
Glenn Research Center, Cleveland, Ohio

Jeffrey T. Somers
KBRwyle, Houston, Texas

National Aeronautics and
Space Administration

Langley Research Center
Hampton, Virginia 23681-2199

September 2016

Available from:

NASA Center for AeroSpace Information
7115 Standard Drive
Hanover, MD 21076-1320
443-757-5802

Table of Contents

Nomenclature

AFB	Air Force Base
AFRL	Air Force Research Library
AIS	Abbreviated Injury Scale
ANSI	American National Standards Institute
ASCII	American Standard Code for Information Interchange
ATD	Anthropomorphic Test Devices
ATK	Alliant Techsystems
ATLS	Advanced Trauma Life Support
BDR	Brinkley Dynamic Response
BMD	Bone Mineral Density
CAD	Computer-Aided Design
CCD	Crew Cursor Device
CCIP	Constellation Crew Injury Prediction [ATD]
CEV	Crew Exploration Vehicle
CFC	Channel Frequency Class
CM	Crew Module
CPU	Central Processing Unit
CSDM	Cumulative Strain Damage Measure
CSSS	Constellation Space Suit System
CxP	Constellation Program
D	Dimensional
DAC	Design Analysis Cycle
DoD	Department of Defense
DOF	Degree of Freedom
DRI	Dynamic Response Index
DR_x	X-axis Dynamic Response
DR_y	Y-axis Dynamic Response
DSS	Decelerator System Simulation
DU	Display Unit
DXA	Dual-energy X-ray Absorbance
EFA	Exploratory Factor Analysis
EOM	End of Mission
EuroSID	European Side-Impact Dummy
EVA	Extravehicular Activity
F/B	Fighter/Bomber
FAA	Federal Aviation Administration
FACB	Flight Activities Control Board
FE	Finite Element
FEM	Finite Element Model
FMVSS	Federal Motor Vehicle Safety Standard
FR	Front Right
FS	Flight Status
FTSS	First Technologies Safety Systems
G	Gravitational constant
GM	General Motors

GRC	Glenn Research Center
GSI	Gadd Severity Index
HANS®	Head and Neck Support®
HIA	Horizontal Impact Accelerator
HIC	Head Injury Criteria
HRP	Human Research Program
HSIR	Human-Systems Integration Requirements
IARV	Injury Assessment Reference Values
IRC	Injury Reference Criteria
IRL	Indy Racing League
IS	Injury Severity
IWE	Independent Witness® Encrypted Format File
IWI	Independent Witness® Unencrypted Binary File
JSC	Johnson Space Center
LaRC	Langley Research Center
lb	pound
LM	Lockheed Martin
LOC	Loss of Consciousness
LS-DYNA®	Finite Element Analysis Software by Livermore Software Technology Corporation
LSTC	Livermore Software Technology Corporation
MADYMO	MAthematical DYnamic Modeling
MATLAB®	MATrix LABoratory data analysis program from The Mathworks
mm	millimeter
MOB	Medical Operations Board
mph	miles per hour
msec	millisecond
MTSO	Management and Technical Support Office
N	Newton
NASA	National Aeronautics and Space Administration
NASCAR	National Association for Stock Car Auto Racing
NESC	NASA Engineering and Safety Center
NFS	Not Further Specified
NHTSA	National Highway Traffic Safety Administration
Nm	Newton meter
NRB	NESC Review Board
OOB	Out-of-Board
OPRA	Order Probit Regression Analysis
ORIS	Operationally Relevant Injury Scale
OSU	Ohio State University
PMHS	Post-Mortem Human Subject
PRA	Probabilistic Risk Assessment
S&G	Sprague-Geers
SAA	Space Act Agreement
SAE	Society of Automotive Engineering
SAR	Search and Rescue

SC	Suit Connector
SE	Self-Egress
SID	Side-Impact ATD
SIMon	Simulated Injury Monitor
SMCCB	Space Medicine Configuration Control Board
SME	Subject Matter Expert
SRD	System Requirement Document
SSP	Space Shuttle Program
STD-DEV	Standard Deviation
TASS	TNO Automotive Safety Solutions
TBI	Traumatic Brain Injury
THUMS	Total HUman Model for Safety
TMA	Transport Modified Anthropometric
US	United States
USAF	United States Air Force
USN	United States Navy
USRA	Universities Space Research Association
VDT	Vertical Drop Tower
WP	Wright Patterson
WPAFB	Wright-Patterson Air Force Base
WSTC	Wayne State Tolerance Curve

Appendix D. WPAFB Model Parameter Peak Value Comparison

D.1 Head X Translational Acceleration

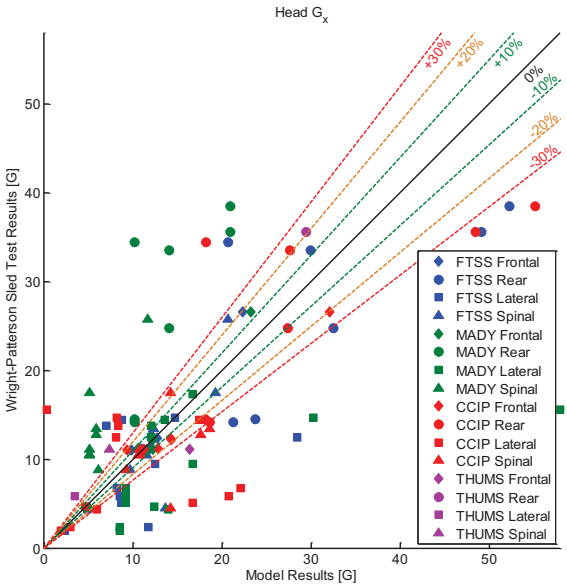

D.2 Head Y Translational Acceleration

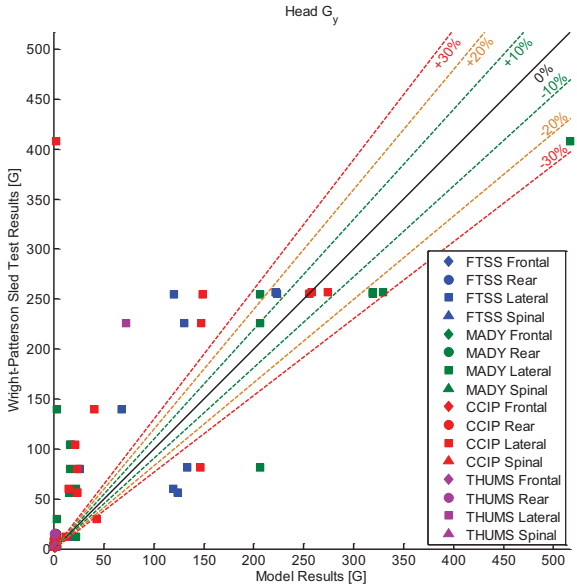

D.3 Head Z Translational Acceleration

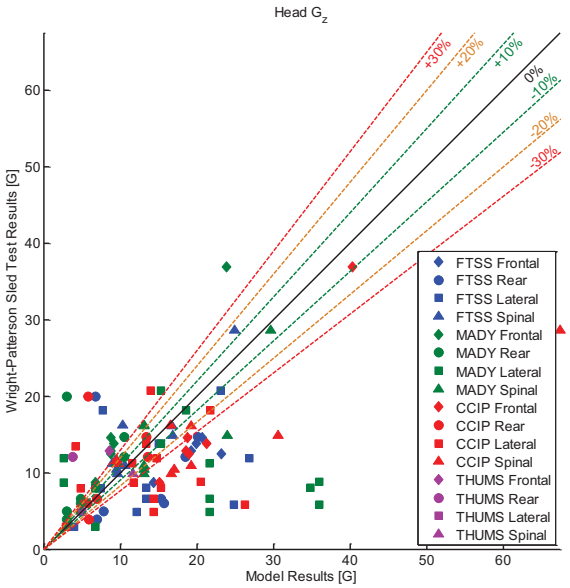

Figure D-3: Head Z Translational Acceleration

D.4 Head Resultant Translational Acceleration

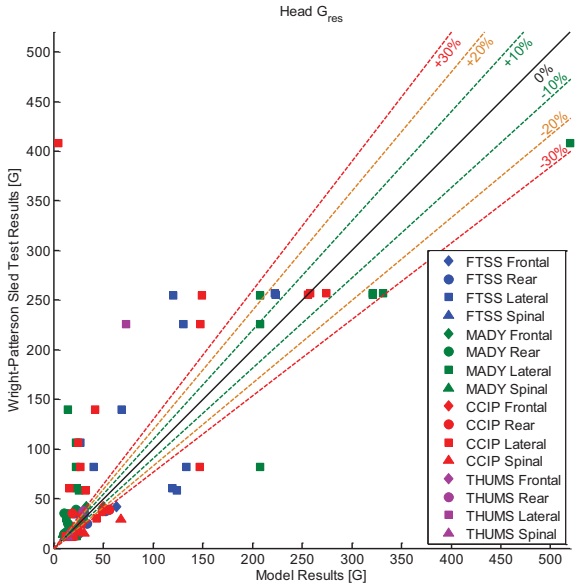

Figure D-4: Head Resultant Translational Acceleration

D.5 Head X Translational Velocity

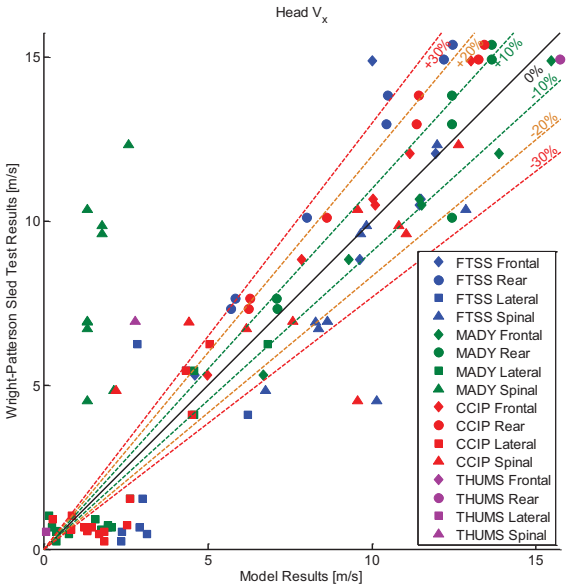

Figure D-5: Head X Translational Velocity

D.6 Head Y Translational Velocity

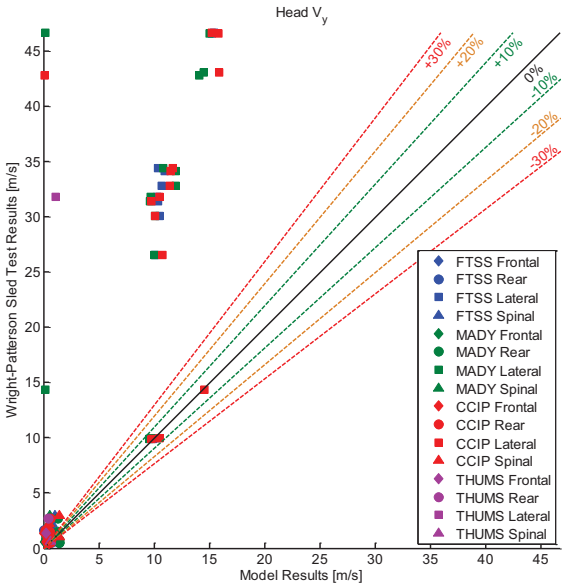

Figure D-6: Head Y Translational Velocity

D.7 Head Z Translational Velocity

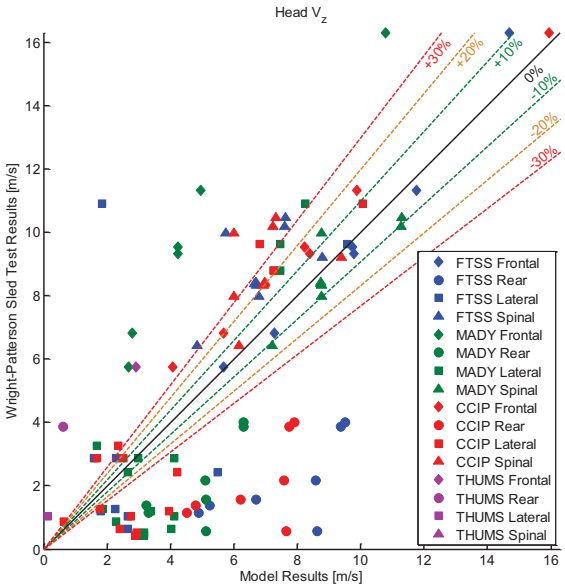

Figure D-7: Head Z Translational Velocity

D.8 Head Resultant Translational Velocity

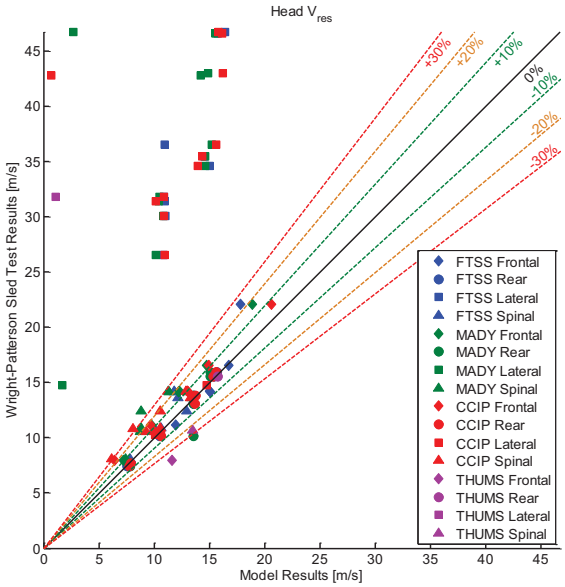

Figure D-8: Head Resultant Translational Velocity

D.9 Head Y Rotational Acceleration

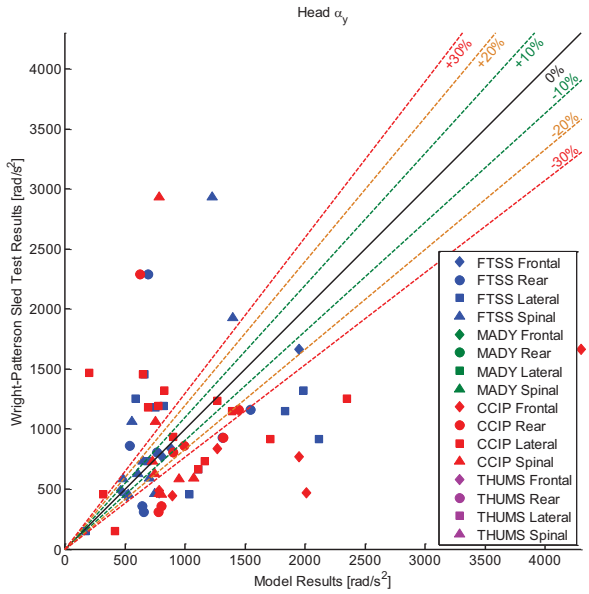

Figure D-9: Head Y Rotational Acceleration

D.10 Head Y Rotational Velocity

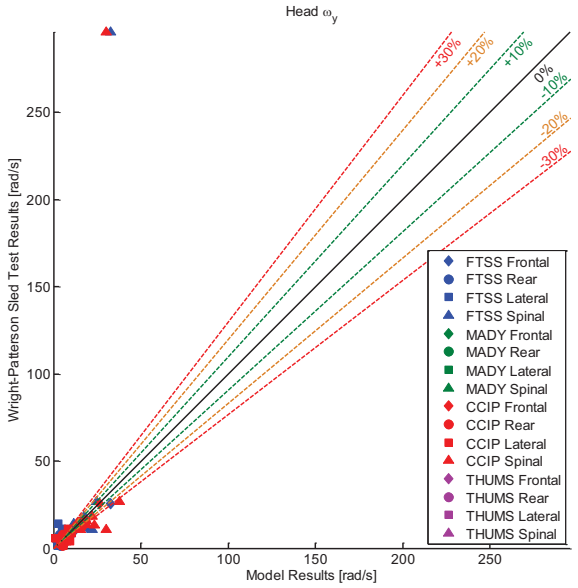

Figure D-10: Head Y Rotational Velocity

D.11 Head X+ Movement

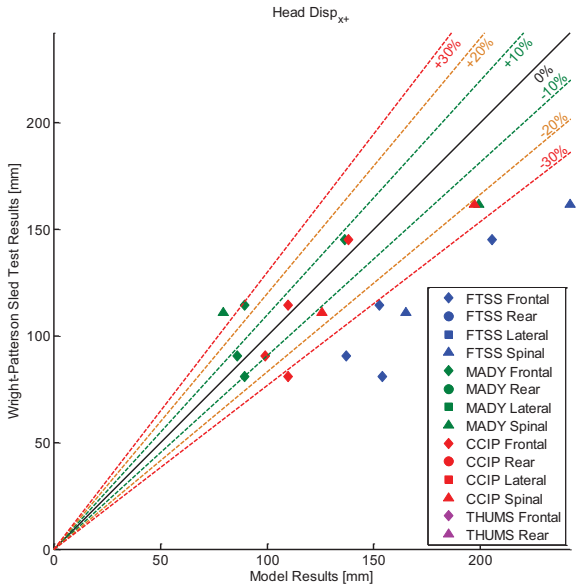

Figure D-11: Head X+ Movement

D.12 Head X- Movement

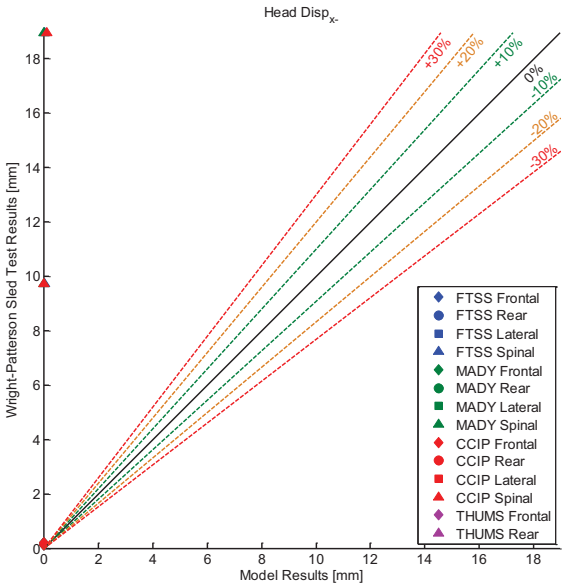

Figure D-12: Head X- Movement

D.13 Head Y Movement

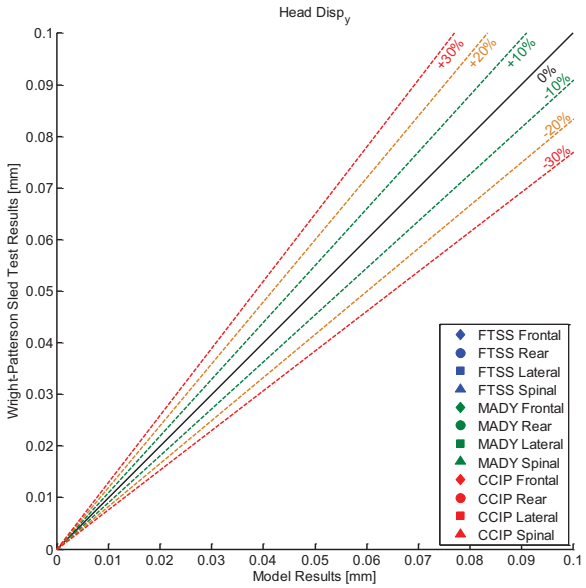

Figure D-13: Head Y Movement

D.14 Head Z+ Movement

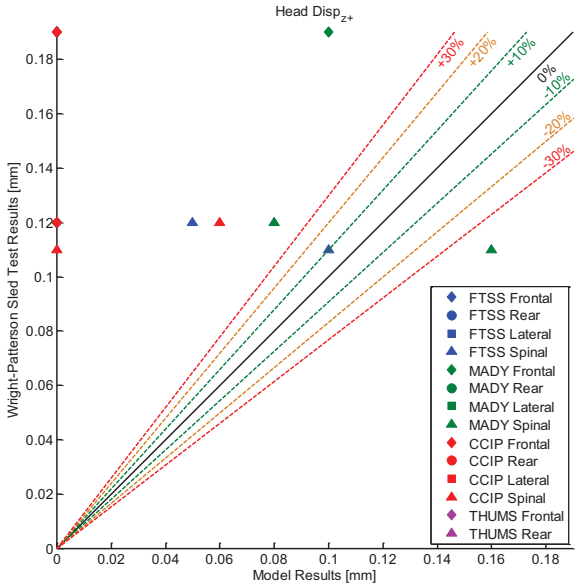

Figure D-14: Head Z+ Movement

D.15 HIC 15

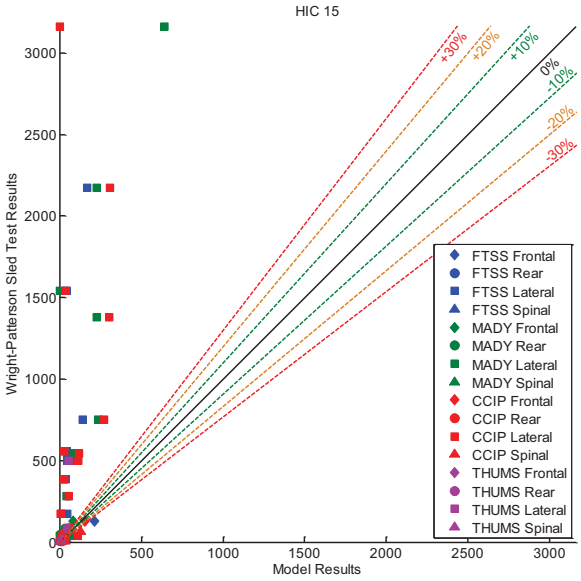

Figure D-15: HIC 15

D.16 HIC 36

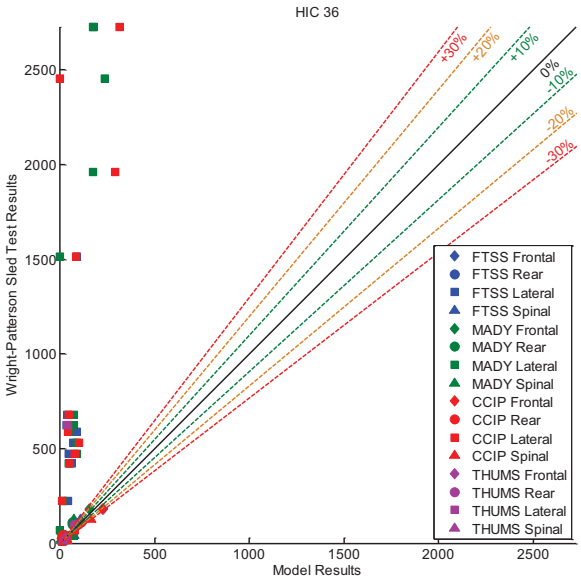

Figure D-16: HIC 36

D.17 Neck X Shear

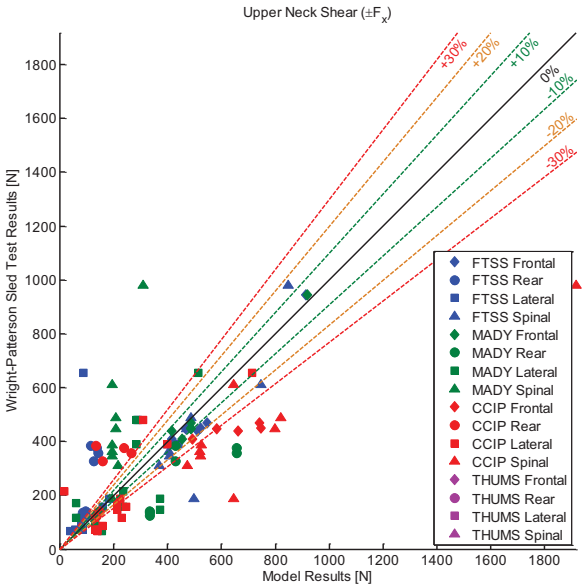

Figure D-17: Neck X Shear

D.18 Neck Y Shear

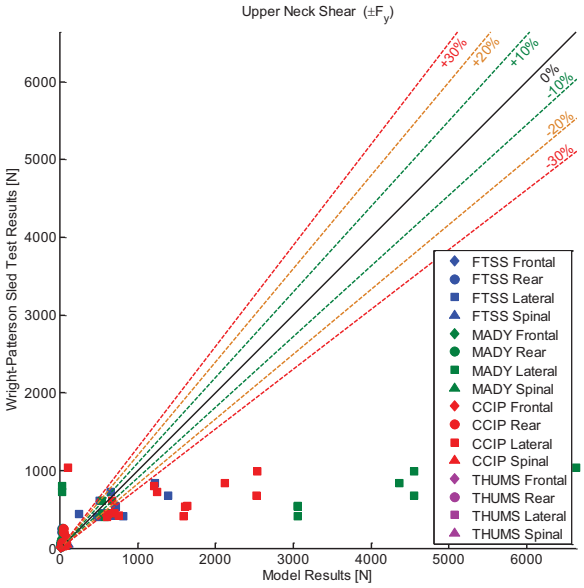

Figure D-18: Neck Y Shear

D.19 Neck Axial Tension

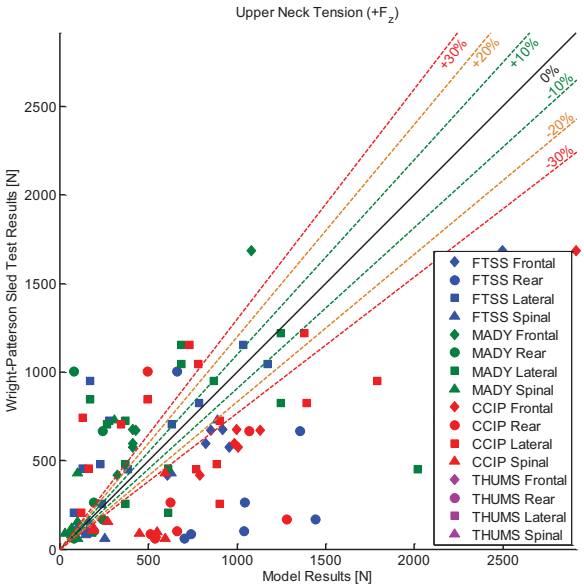

Figure D-19: Neck Axial Tension

D.20 Neck Axial Compression

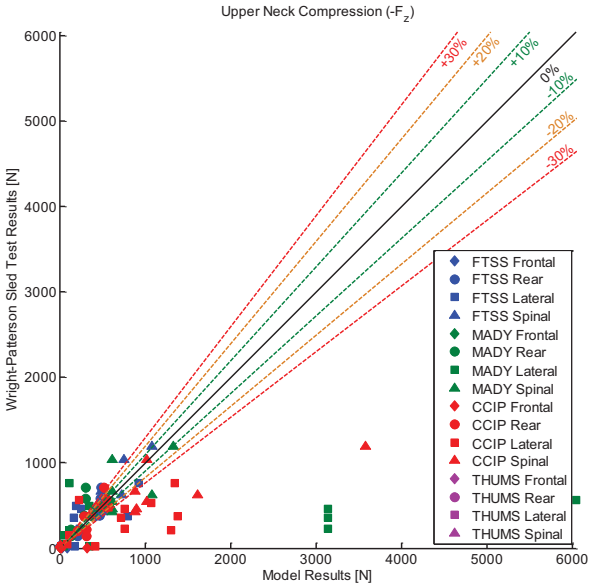

Figure D-20: Neck Axial Compression

D.21 Neck Flexion

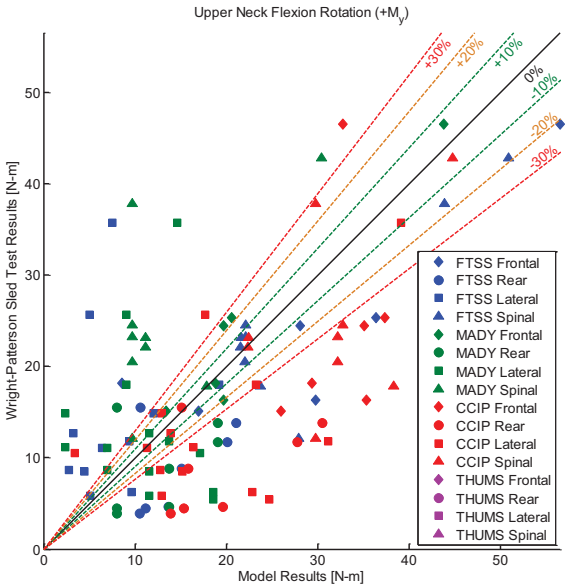

Figure D-21: Neck Flexion

D.22 Neck Extension

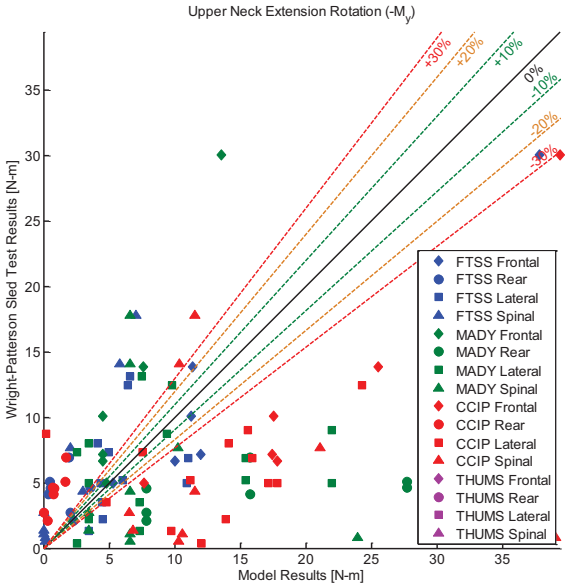

Figure D-22: Neck Extension

D.23 Neck Lateral Moment

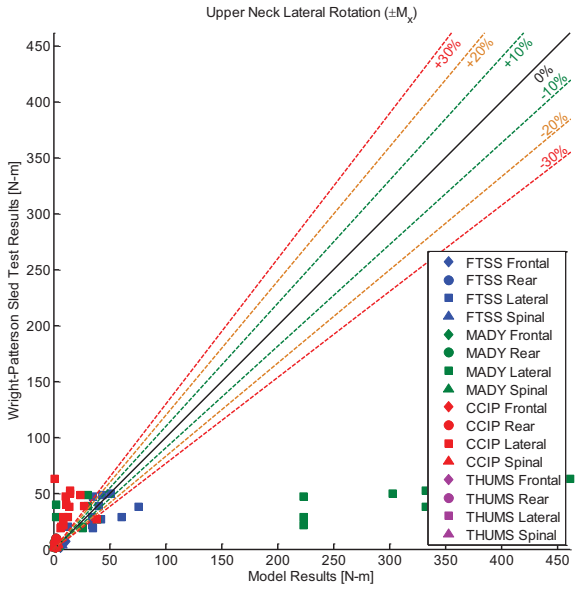

Figure D-23: Neck Lateral Moment

D.24 Neck Rotation

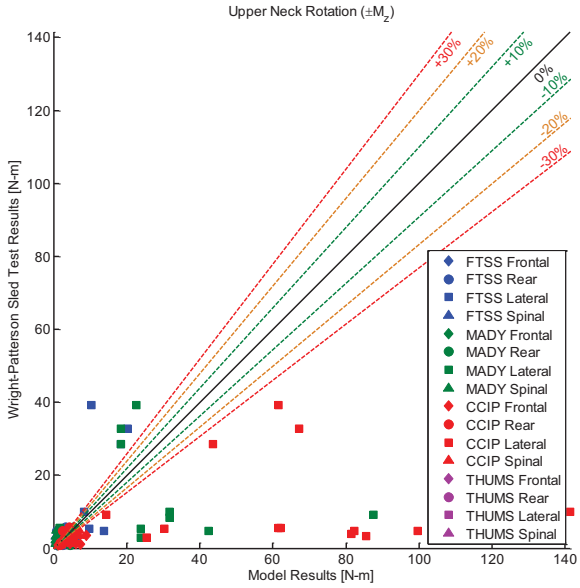

Figure D-24: Neck Rotation

D.25 Nij

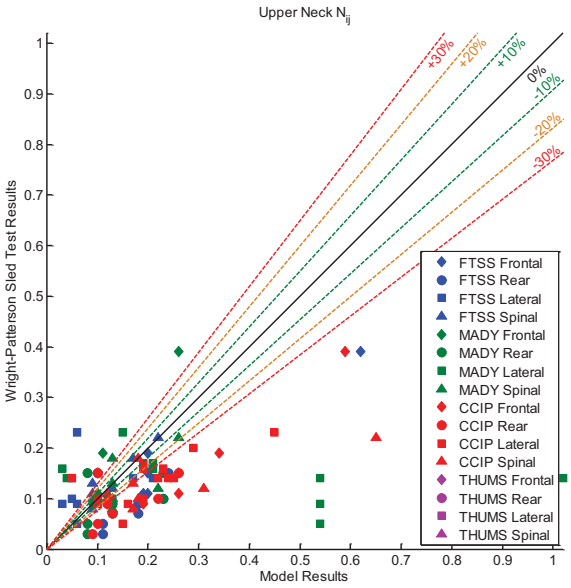

Figure D-25: Nij

D.26 Nkm

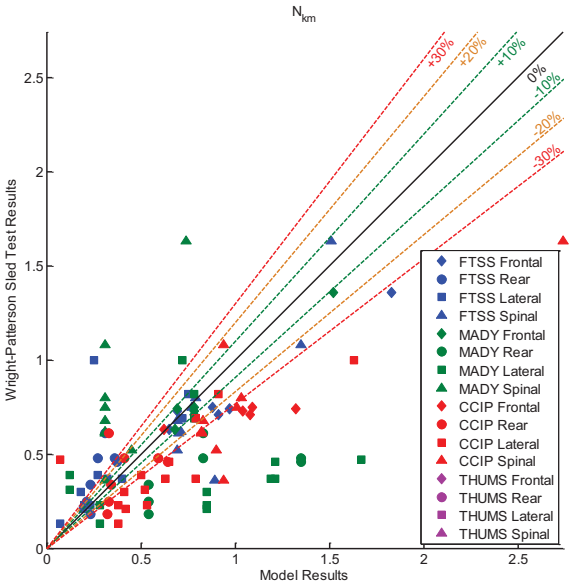

Figure D-26: Nkm

D.27 Chest X Acceleration

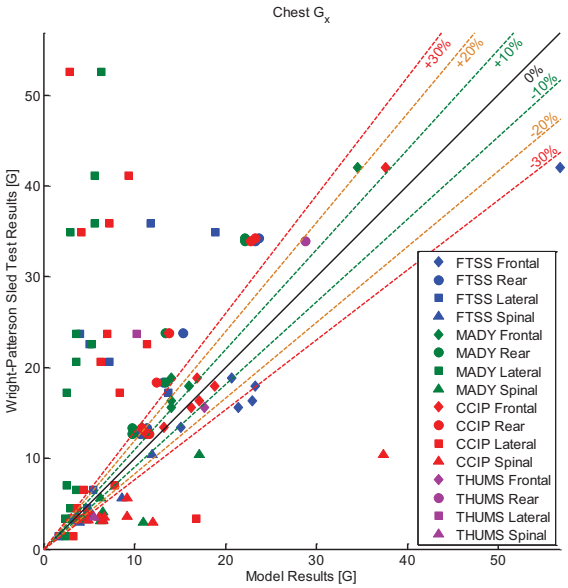

Figure D-27: Chest X Acceleration

D.28 Chest Y Acceleration

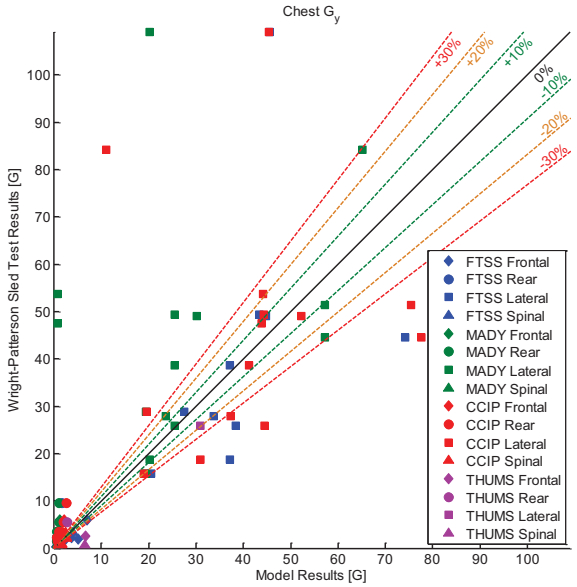

Figure D-28: Chest Y Acceleration

D.29 Chest Z Acceleration

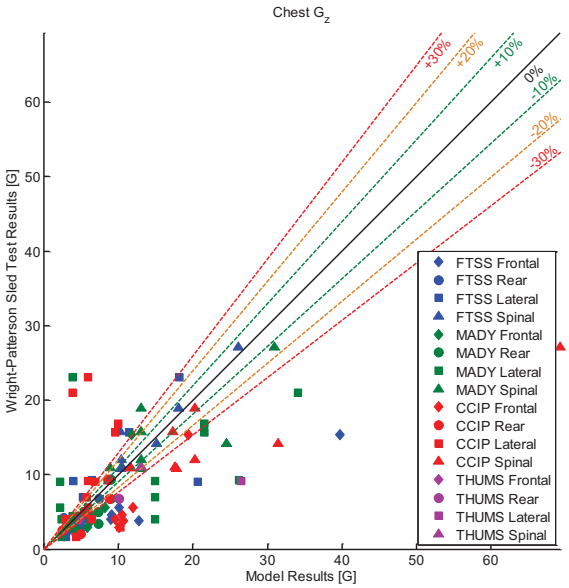

Figure D-29: Chest Z Acceleration

D.30 Chest Resultant Acceleration

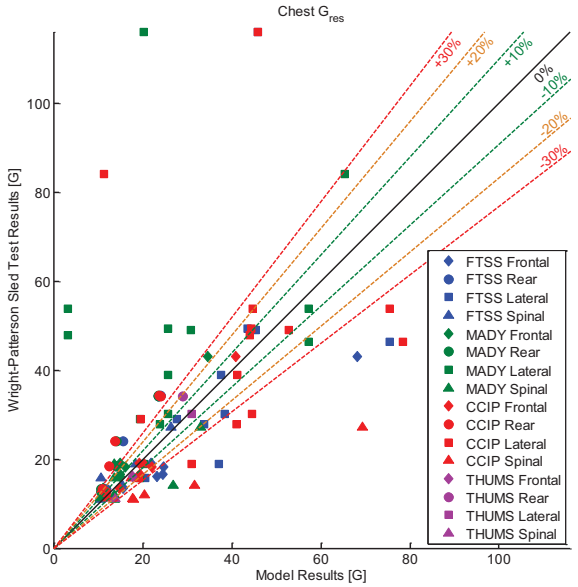

Figure D-30: Chest Resultant Acceleration

D.31 Chest X+ Movement

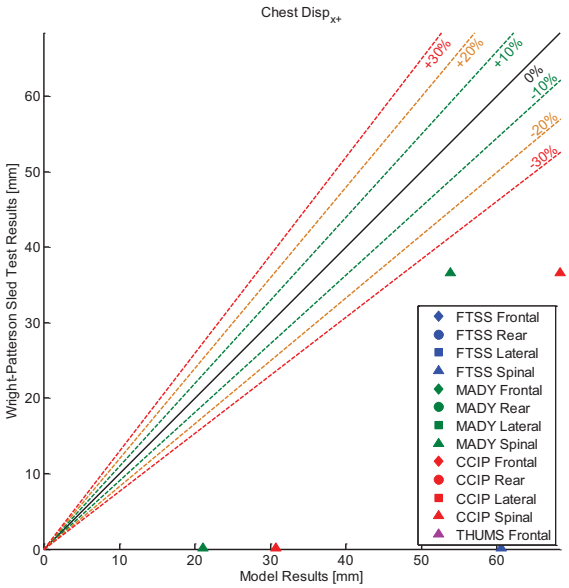

Figure D-31: Chest X+ Movement

D.32 Chest X- Movement

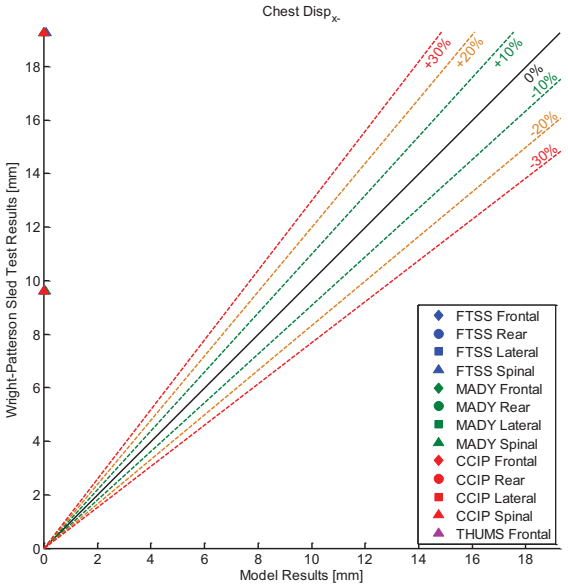

Figure D-32: Chest X- Movement

D.33 Shoulder Y Movement

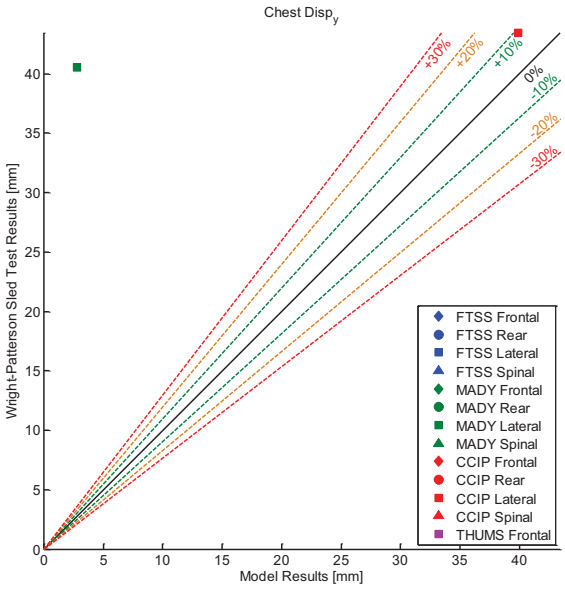

Figure D-33: Shoulder Y Movement

D.34 Chest Z+ Movement

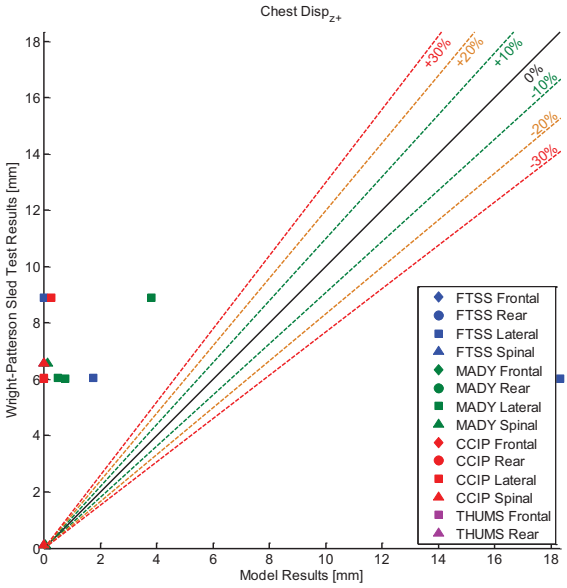

Figure D-34: Chest Z+ Movement

D.35 Lumbar X Shear

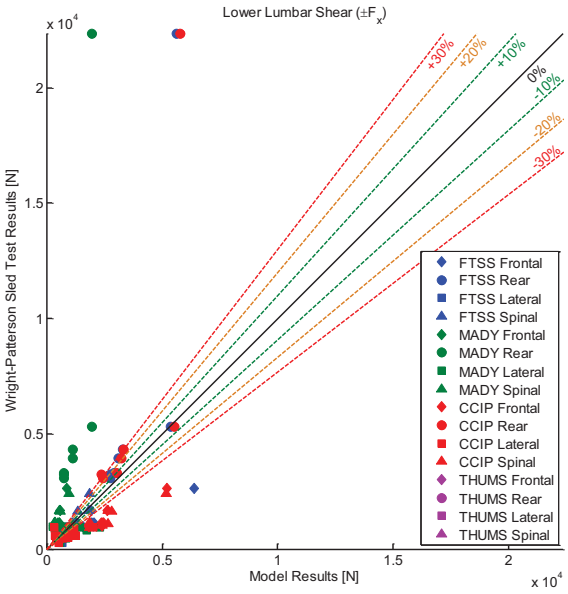

Figure D-35: Lumbar X Shear

D.36 Lumbar Axial Tension

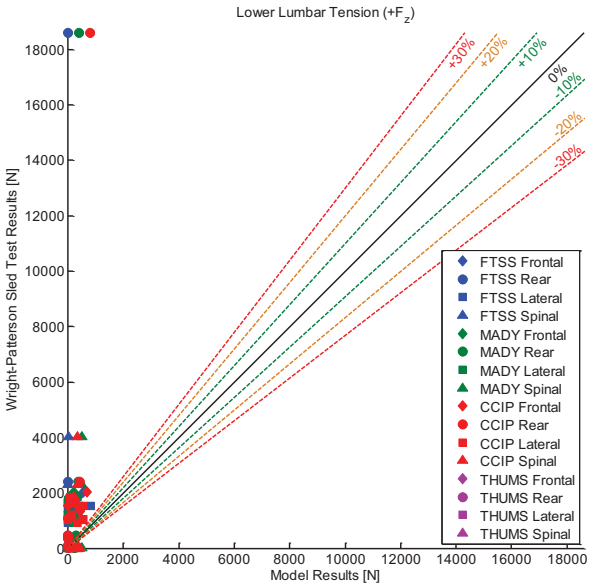

Figure D-36: Lumbar Axial Tension

D.37 Lumbar Axial Compression

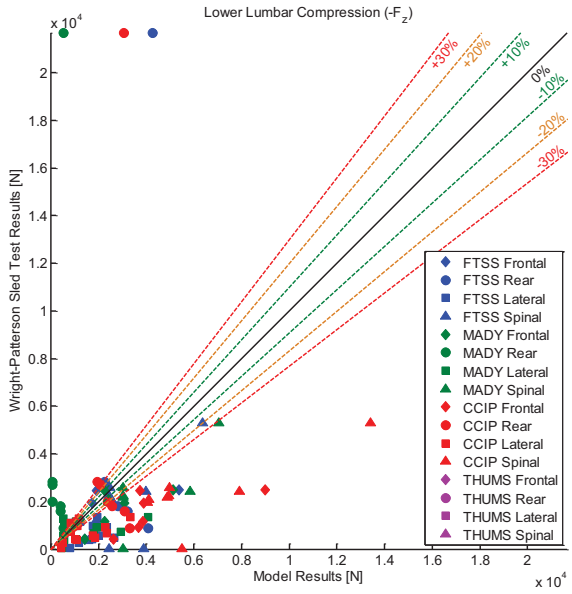

Figure D-37: Lumbar Axial Compression

D.38 Lumbar Flexion

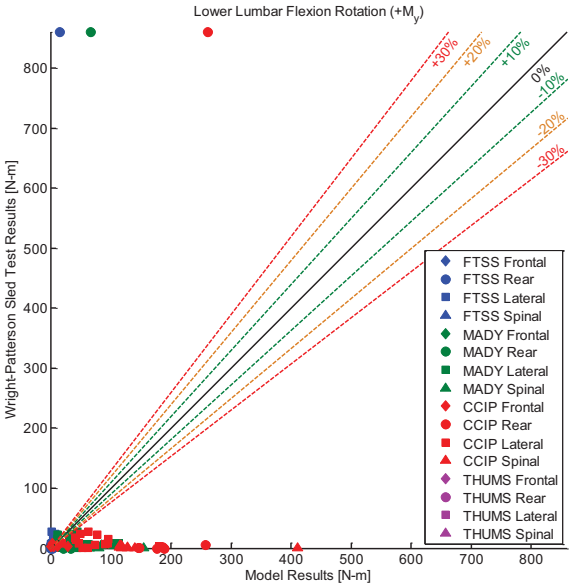

Figure D-38: Lumbar Flexion

D.39 Lumbar Extension

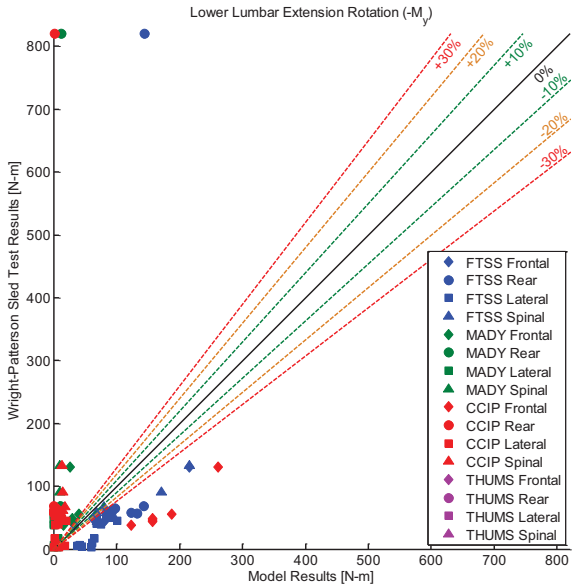

Figure D-39: Lumbar Extension

D.40 Left Lap Belt Force

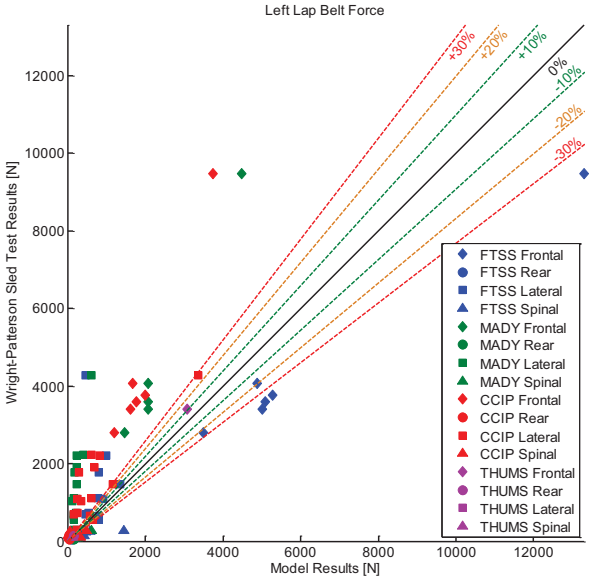

Figure D-40: Left Lap Belt Force

D.41 Right Lap Belt Force

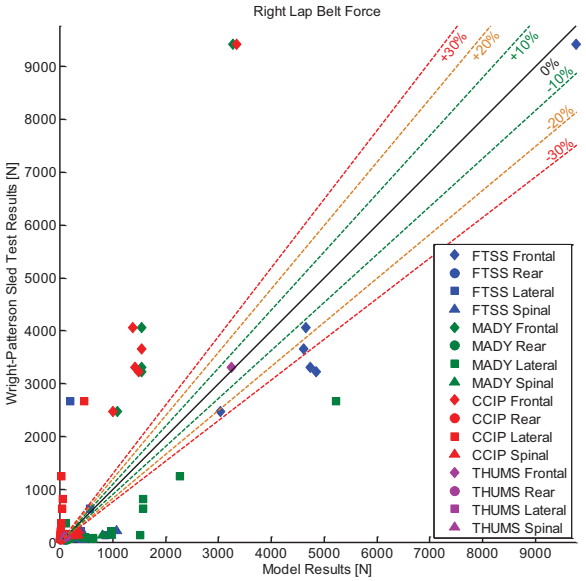

Figure D-41: Right Lap Belt Force

D.42 Left Shoulder Belt Force

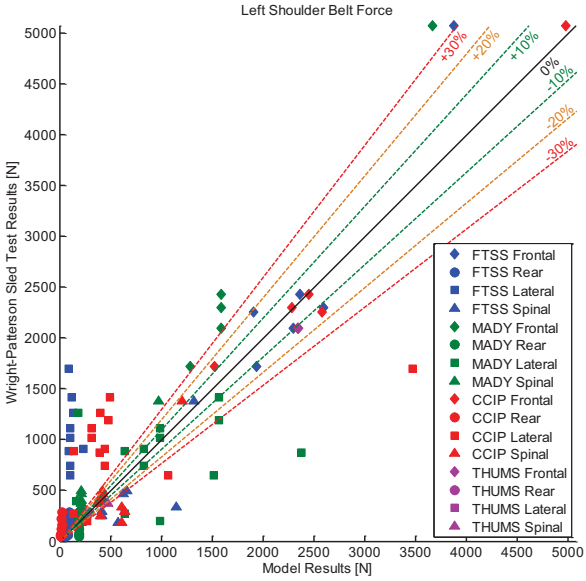

Figure D-42: Left Shoulder Belt Force

D.43 Right Shoulder Belt Force

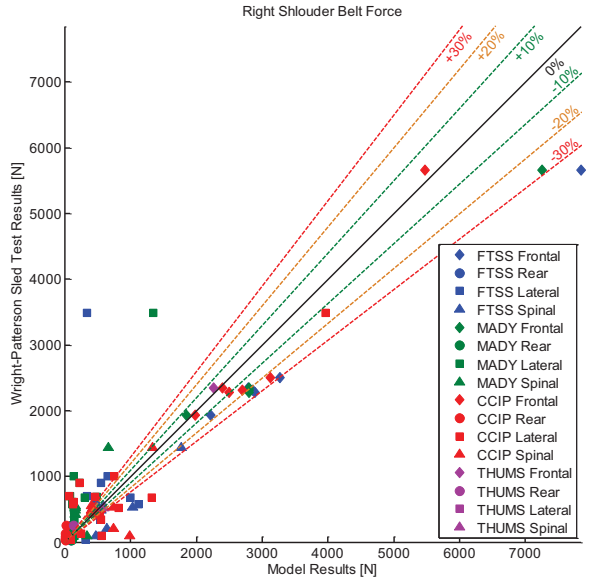

Figure D-43: Right Shoulder Belt Force

D.44 Crotch Belt Force

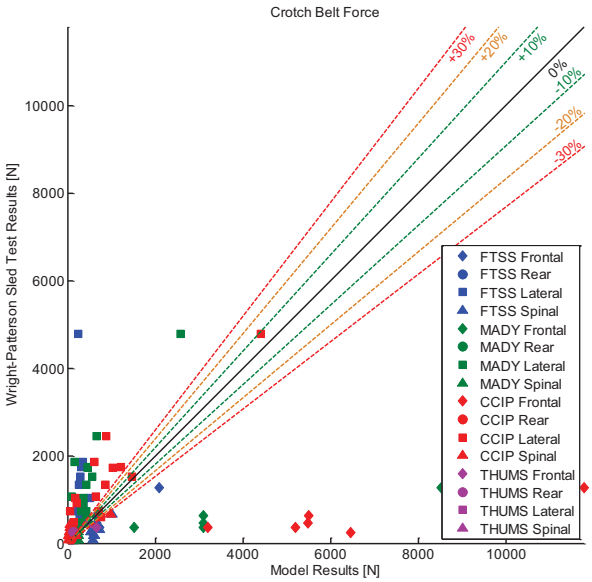

Figure D-44: Crotch Belt Force

Appendix E. THUMS Wright-Patterson Sled Test Comparison Results

CIB Report Number: WFU2009-040

Virginia Tech – Wake Forest University
Center for Injury Biomechanics

FINAL REPORT
Wright/Patterson Modeling Results

PREPARED FOR

Nancy Currie, Brad Granderson,

Jeff Somers

PREPARED BY

Joel Stitzel, Kerry Danelson

Virginia Tech – Wake Forest University

Center for Injury Biomechanics

Wake Forest University School of Medicine

Medical Center Boulevard, Winston-Salem, NC 27157

Phone: (336) 716-5597, jstitzel@wfubmc.edu

Table of Contents

List of Tables

List of Figures

Abstract

The purpose of this study was to determine the similarity between the response of the THUMS model and the Hybrid III Anthropometric Test Device (ATD) given existing Wright-Patterson (WP) sled tests. There were four tests selected for this comparison with frontal, spinal, rear, and lateral loading. The THUMS was placed in a sled configuration that replicated the WP configuration and the recorded seat acceleration for each test was applied to model seat. Once the modeling simulations were complete, they were compared to the WP results using two methods. The first was a visual inspection of the sled test videos compared to the THUMS d3plot files. This comparison resulted in an assessment of the overall kinematics of the two results. The other comparison was a comparison of the plotted data recorded for both tests. The metrics selected for comparison were seat acceleration, belt forces, head acceleration and chest acceleration. These metrics were recorded in all WP tests and were outputs of the THUMS model. Once the comparison of the THUMS to the WP tests was complete, the THUMS model output was also examined for possible injuries in these scenarios. These outputs included metrics for injury risk to the head, neck, thorax, lumbar spine and lower extremities. The metrics to evaluate head response were peak head acceleration, HIC_{15}, and HIC_{36}. For the neck, N_{ij} was calculated. The thorax response was evaluated with peak chest acceleration, the Combined Thoracic Index (CTI), sternal deflection, chest deflection, and chest acceleration- 3 ms clip. The lumbar spine response was evaluated with lumbar spine force. Finally the lower extremity response was evaluated by femur and tibia force. The results of the simulation comparisons indicate the THUMS model had a similar response to the Hybrid III dummy given the same input. The primary difference seen between the two was a more flexible response of the THUMS compared to the Hybrid III. This flexibility was most pronounced in the neck flexion, shoulder deflection and chest deflection. Due to the flexibility of the THUMS, the resulting head and chest accelerations tended to lag the Hybrid III acceleration trace and have a lower peak value. The results of the injury metric comparison identified possible injury trends between simulations. Risk of head injury was highest for the lateral simulations. The risk of chest injury was highest for the rear impact. However, neck injury risk was approximately the same for all simulations. The injury metric value for lumbar spine force was highest for the spinal impact. The leg forces were highest for the rear and lateral impacts. The results of this comparison indicate the THUMS model performs in a similar manner as the Hybrid III ATD. The differences in the responses of model and the ATD are primarily due to the flexibility of the THUMS. This flexibility of the THUMS would be a more human like response. Based on the similarity between the two models, the THUMS should be used in further testing to assess risk of injury to the occupant.

1 Introduction

1.1 Existing Models

Finite element models (FEMs) have been used extensively to simulate impacts to predict the likelihood of injury in these scenarios. There are several total body models in use today; however, for this study the Total HUman Model for Safety (THUMS) was used. This model was developed for use in automotive testing and has been extensively validated against post mortem human subject (PMHS) data [1]. In previous evaluations of the ORION crew module, THUMS was also used to evaluate possible injuries in severe x- and z-direction loading. An advantage of the THUMS model is the injury risk assessment capabilities are not limited by load cell placement. Therefore, the user can examine a body region of interest for possible injury sources.

1.2 Injury Metrics

The main focus of this study was to compare the response of the THUMS to that of a Hybrid III (H3) Anthropometric Test Device (ATD) given the same testing configurations. Several injury metrics were selected and examined to compare the results of the THUMS simulations to the data collected during the Wright-Patterson (WP) sled tests. These injury metrics were selected because they were recorded during the WP tests and could be evaluated based on the response of the THUMS. The metrics selected were seat acceleration, belt forces, chest acceleration, and head acceleration.

After the response of the two models were compared, the THUMS output was evaluated for additional injury metrics to evaluate risk of injury to the occupant. The major body regions covered were the head, neck, thorax, lumbar spine, and lower extremities. The head metrics evaluated were peak head acceleration, HIC_{15}, and HIC_{36}. Head acceleration was used to calculate the values for the Head Injury Criterion (HIC), both HIC_{15} and HIC_{36}. These two metrics were developed based on the risk of skull fracture given head acceleration into a padded or unpadded surface [2, 3]. The curve relating the HIC value to risk of injury is the same for HIC_{15} and HIC_{36}.

The next body region examined was the neck. The selected injury metric to assess risk of injury to the neck was the Nij. Nij is calculated based on loads and moments observed in the neck. The injury criteria include the four injury mechanisms of neck injury: tension-extension, tension-flexion, compression-extension, and compression-flexion [3, 4].

The metrics selected to assess thorax injury were chest deflection, sternal deflection, chest acceleration, the Combined Thoracic Index (CTI), and chest acceleration- 3 ms clip. Chest acceleration was used to calculate CTI and chest acceleration- 3 ms clip. The risk of injury calculated for CTI, chest acceleration and sternal deflection. Additionally, lumbar spine forces were evaluated for each simulation.

The final body region evaluated was the lower extremity. In all cases, the forces in the femurs and tibias were evaluated. All injury metrics are included in the body of the document or in one of the appendices for completeness.

2 Methods

The configuration of the FEM for the simulations of interest involved the integration of multiple components and models. This section describes each of the individual components of the final model and the simulations conducted with this FEM. First, the initial FEM model configuration will be examined. The next section explains the acceleration pulses modeled for each WP sled test. After this, the final model configuration is illustrated and a test matrix is included which details the simulations completed. The final section examines the data collected for injury metric comparisons across simulations.

2.1 Initial Model Configuration

The FEM of the occupant used in this analysis was a modified version of the THUMS version 1.61c. This model had been previously modified for NASA simulations to stabilize the model response in Z-loading configurations. The modifications implemented include different response curves for the pelvis flesh and lung tissue. Additionally, all element failure criteria were removed to assess loading values in all the elements for the entire simulation. All simulations were conducted on a Linux cluster computer in LSDYNA version 971 (LSTC, Livermore, California) with a time step of 6.67E-7 seconds.

The seat configuration used was the same seat configuration and material properties as the WP sled test seat. This model was provided by NASA's task group one. This seat consisted of a rigid back with a cushioned head rest and a cushioned seat bottom. A floorboard was included and the feet of the THUMS were restrained to this component. The floorboard used with the THUMS model was translated in the X-direction to accommodate the original knee bend of the THUMS model. The WP restraint system is a five point harness configuration. Figure 1 illustrates the initial THUMS model before placement in the seat and Figure 2 and Figure 3 illustrate the WP seat configurations.

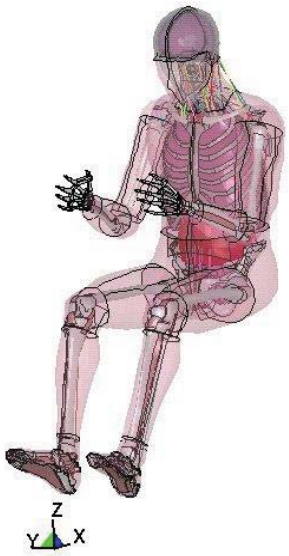

Figure 1: Isolated THUMs model prior to integration with the seat.

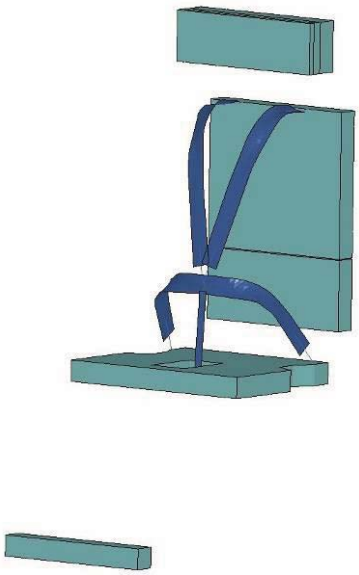

Figure 2: Seat configuration for anterior/posterior and inferior/superior loading pulses.

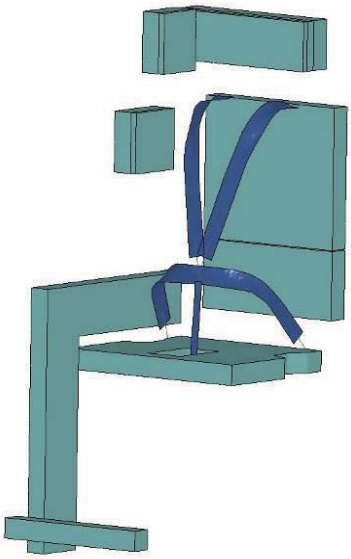

Figure 3: Seat configuration for lateral loading simulations.

2.2 **Accelerations**

There were four landing scenarios modeled in the simulations with corresponding tests conducted at Wright-Patterson Air Force Base. The four tests selected were 8202, 8208, 8212, and 8245. These tests were selected to represent loading in the frontal (8202), spinal (8208), rear (8212), and lateral (8245) directions. The input for the THUMS simulations was the acceleration of the seat. This acceleration was applied directly to the modeled seat. Before simulations were conducted, the acceleration data from the WP sled testing was slightly modified.

Prior to use in the simulation, the seat acceleration was filtered, zeroed and truncated. All filtering was conducting using CFC 600 [6]. After the data was initially filtered, the data was zeroed. To zero the data, the first 10 milliseconds of data were taken as the calibration data for the remainder of the pulse. This section of the data was averaged and the resultant value was subtracted from the remainder of the data. Starting at 10 milliseconds into the pulse, the data was traced backwards until the first time the acceleration crossed the x-axis. This time point was taken as the time zero for the simulation. Finally, the data was truncated to minimize the amount of time required to run the simulation. The end time of the simulation was taken as 20 milliseconds after the maximum velocity of the pulse. The acceleration and velocity data for the frontal simulation (8202) is shown in Figure 4. After running some initial simulations, it was determined that the truncation step missed some acceleration spikes in the resulting model outputs. Therefore, additional simulations were conducted to insure these spikes were included in the final modeling output. The modified and truncated acceleration data is included in Appendix 1. The long simulation acceleration data (modified but manually truncated) is included in Appendix 2.

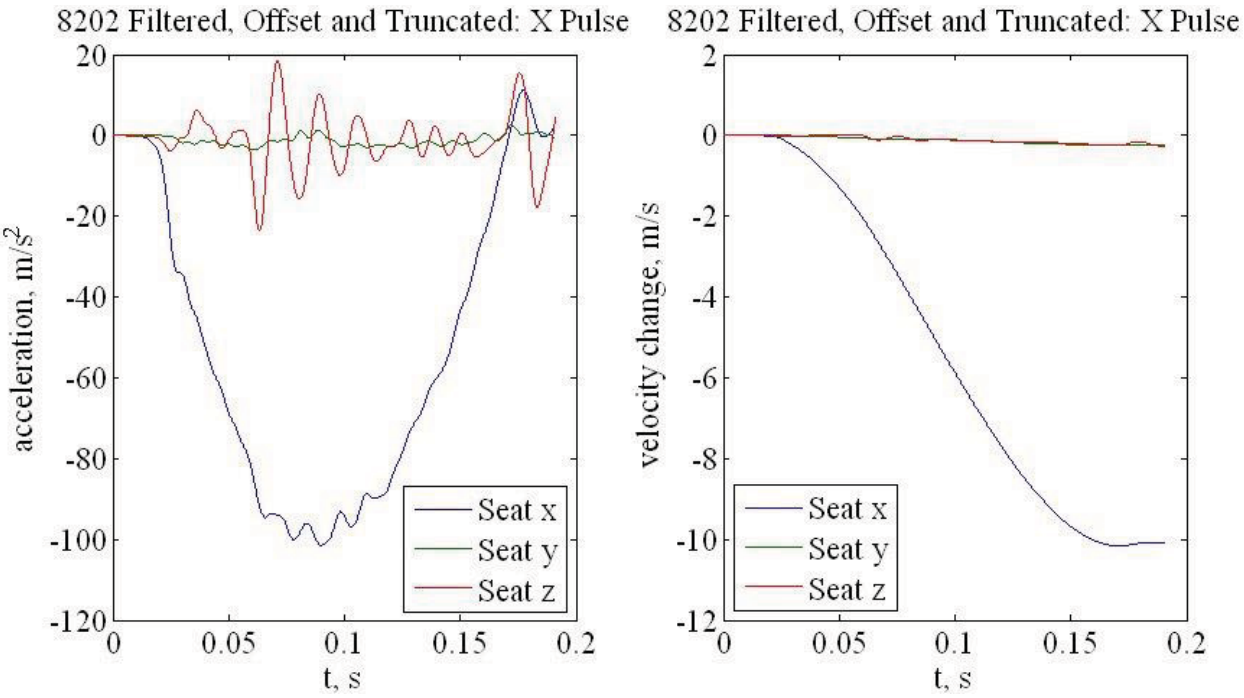

Figure 4: Acceleration and velocity data from WP Sled test 8202.

2.3 Final Model Configurations

The four WP sled tests selected for use with the THUMS model are further described in the test matrix shown in Table 1. The corresponding directions of loading for each simulation are illustrated in Figure 5.

Table 1: Test Matrix for the simulations conducted

Simulation Number	Acceleration (g's)	Delta-V (m/s)	Pulse	Simulation Time (ms)
8202	10	10	+X (frontal), short	180
			+X (frontal), long	260
8208	10	15	+Z (spinal), short, X gravity	170
			+Z (spinal), short, Z gravity	170
			+Z (spinal), long, X gravity	410
8212	20	-10	-X (rear), short	125
			-X (rear), long	210
8245	10	10	-Y (lateral), short	170
			-Y (lateral), long	260

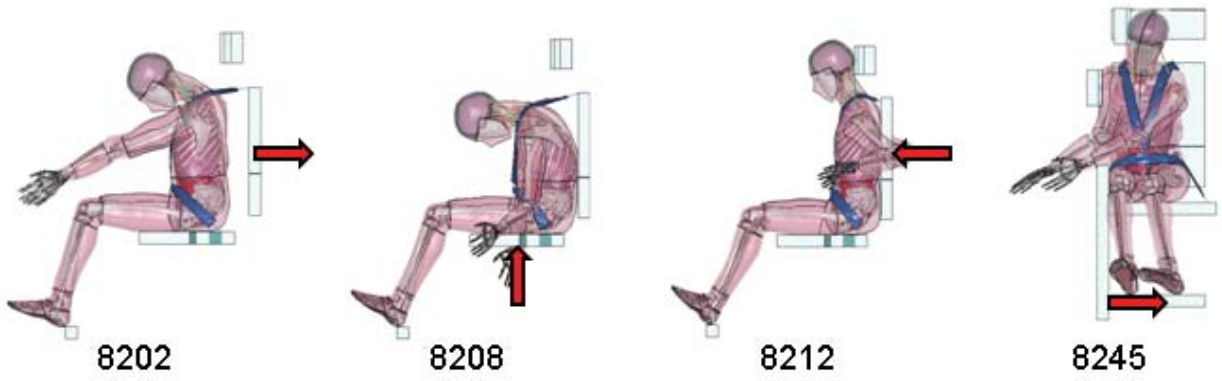

Figure 5: Illustration of seat directions for each pulse.

2.4 Injury Metric Calculations

There were several metrics selected to evaluate the body response in comparison to the H3 ATD and the potential for injury in various regions throughout the body. The regions of interest were the head, neck, thorax, lumbar spine, and lower extremity. Additionally, the tension in all belts and the acceleration of the seat were evaluated for each simulation.

2.4.1 Head Metrics

The metrics selected to evaluate the risk of injury to the head were peak head acceleration, HIC_{15} and HIC_{36}. Peak head acceleration was measured by the nodal acceleration of a single node located at the center of the head (node 8890001) as shown in Figure 6. HIC_{15} and HIC_{36} were calculated from the acceleration recorded by this node.

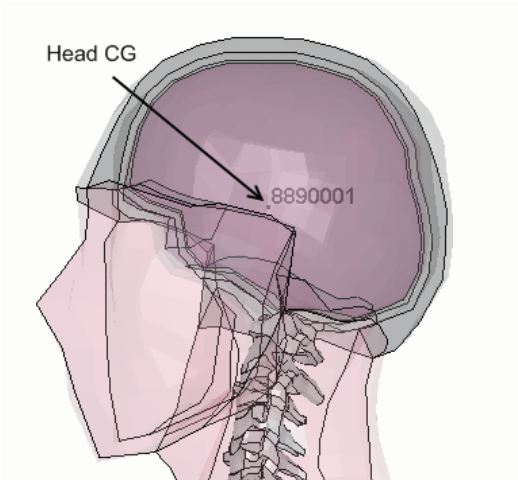

Figure 6: Location of the node used to record head acceleration in the THUMS model.

2.4.2 Neck Metrics

The metric selected to evaluate risk of injury to the neck is the N_{ij}. This metric takes into account the forces and moments in the neck during the simulation. This metric was measured

using the section plane command in LS-PrePost. Figure 7 illustrates the location of the neck section plane.

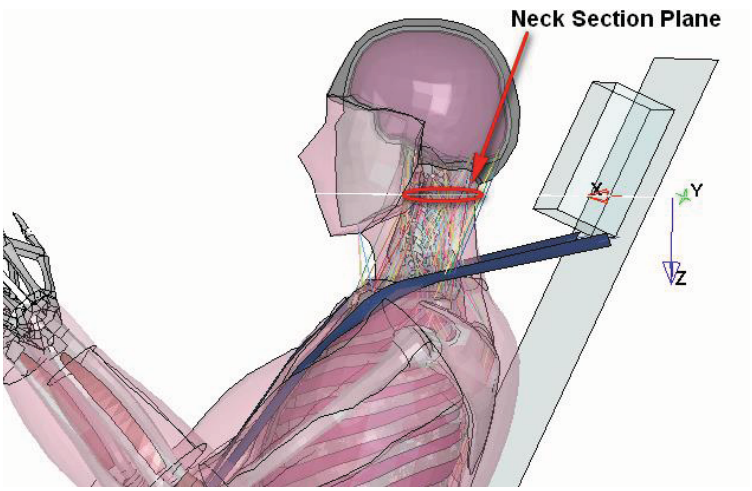

Figure 7: Neck section plane location from LS-PrePost.

2.4.3 **Chest metrics**

Several injury metrics were selected to evaluate the response of the chest. They include sternal deflection, chest deflection, and peak chest acceleration. Risk of injury to the chest was calculated using the chest acceleration 3 ms clip and CTI. The first chest metric evaluated was sternal deflection. Deflection was the change in the distance from the sternum to the ninth thoracic vertebra. This distance was measured between nodes in the THUMS model. The red line in Figure 8 illustrates the distance between the two nodes used to measure deflection. Figure 9 illustrates the same measurement of deflection at the time of maximum compression during the simulation. Given the model results, a custom Matlab code calculates the deflection of the sternum along this line as the simulation progresses. A negative value of deflection indicates a compressive load. The maximum deflection value was the value compared across simulations. This value can also be compared to the injury risk curves shown in Figure 10.

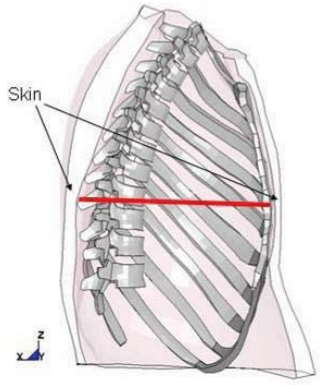

Figure 8: Deflection measurement line in the THUMS thorax.

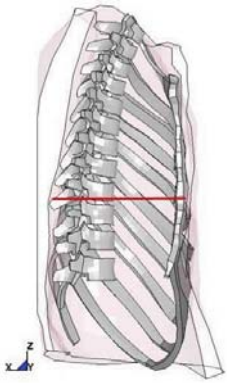

Figure 9: Deflection of the rib cage during a simulation.

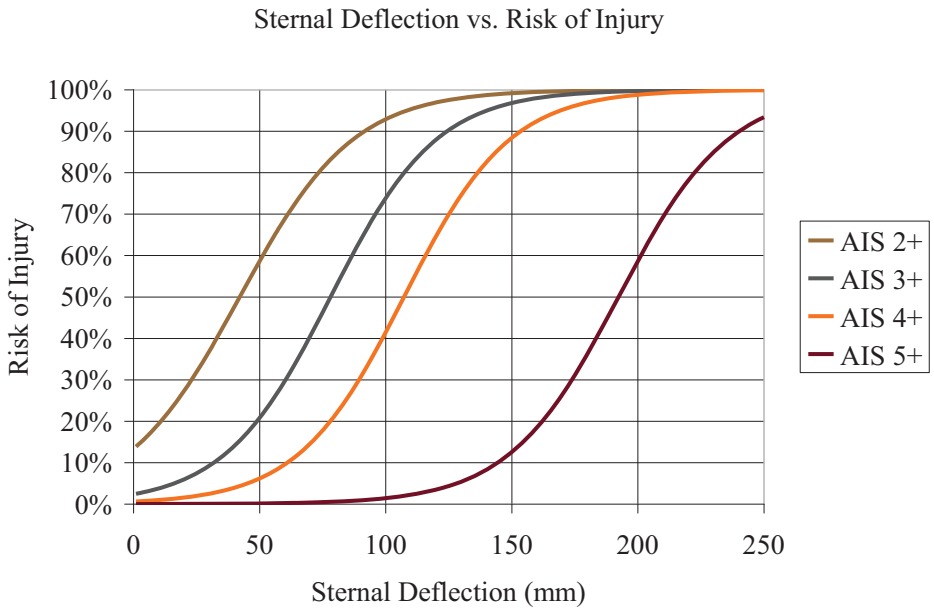

Figure 10: Plot of the injury risk given a range of sternal deflection values [3].

Another metric to describe the compression of the chest was the chest deflection metric. This metric measures the deflection of seven ribs along a line from the sternum to the spine. Each line is horizontal; therefore, the front node is not on the same rib as the rear node. These deflections were measured to assess the overall response of the thorax. Figure 11 illustrates the nodes compared and the lines measured for this metric.

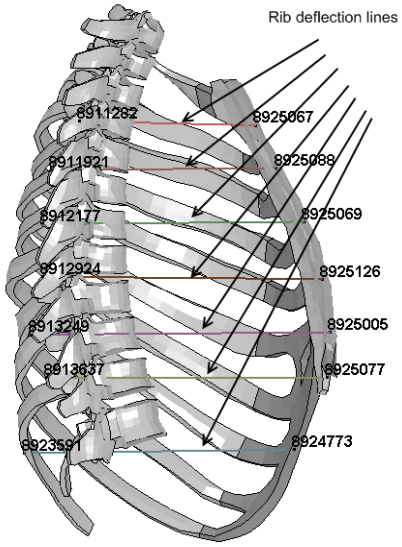

Figure 11: Rib Deflection measurement lines

2.4.4 **Lumbar Spine Metric**

Lumbar spine forces were the injury metric evaluated for the lumbar spine. This force was measured with a section plane between T12 and L1. Figure 12 illustrates the location of the section plane used to measure lumbar forces.

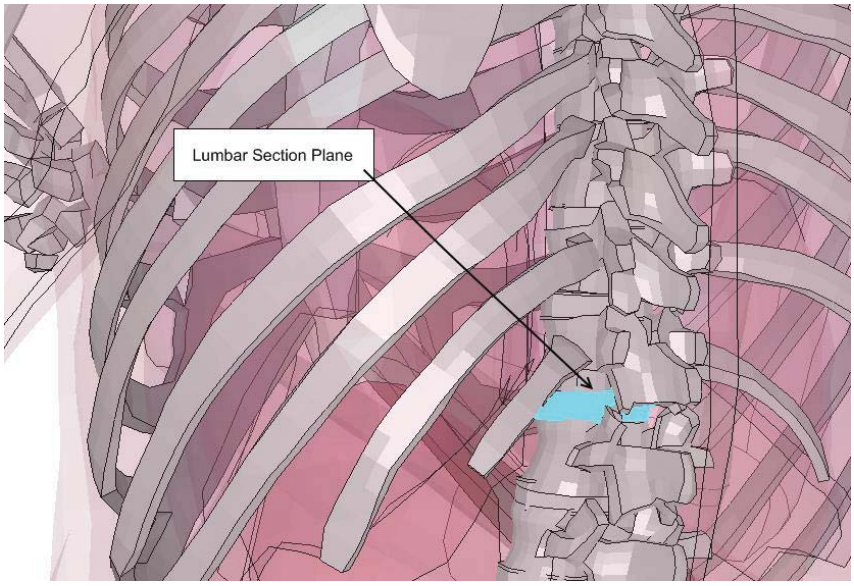

Figure 12: Location of section plane used to measure the lumbar force.

2.4.5 **Lower Extremity Metric**

The forces in both femurs and tibias were evaluated for each simulation using the section force command. The section force was defined through each bone in the locations highlighted in Figure 13.

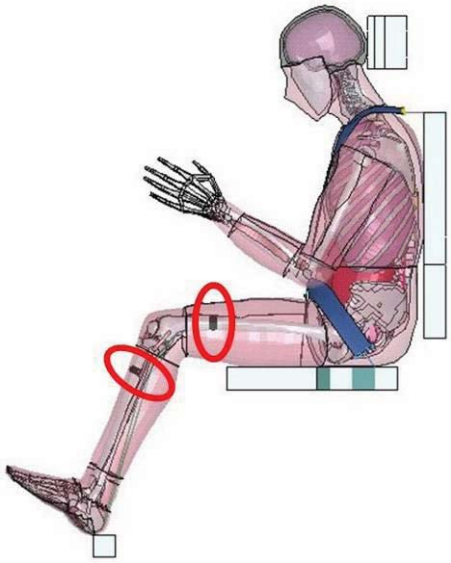

Figure 13: Location of femur and tibia section planes for leg force measurement.

3 Results

The results of this study can be divided into two sections: Comparison of the THUMS model response with the Hybrid III response, and injury metric results from the THUMS model for each loading scenario.

3.1 Comparison of the THUMS and the Hybrid III response

To compare the two results, two methods were used. The first was a qualitative visual assessment of the THUMS movement to the Hybrid III by using the test videos and comparing them to the THUMS d3plot output. The next method for comparison was plotting the head acceleration, chest acceleration, seat acceleration, and forces in the belts for both the tests and the simulations to demonstrate the similarities and differences in response.

3.1.1 Visual Comparison

A qualitative visual assessment of the THUMS response and the Hybrid III response was the first step in determining the differences in the response of these two simulations of the landing conditions. Pictures from the d3plot files of the model and the Hybrid III test videos were taken at the time of maximum engagement of the occupant with the restraint system. Maximum engagement was defined as the time where the occupant had fully loaded the belts or the seat structure and before rebound occurred. Also, screen captures of a time progression of each simulation are included in Appendix 17. The first load case, 8202 (frontal), is shown in Figure 14 and Figure 15. These figures illustrated the more flexible response of THUMS neck and back when compared to the Hybrid III.

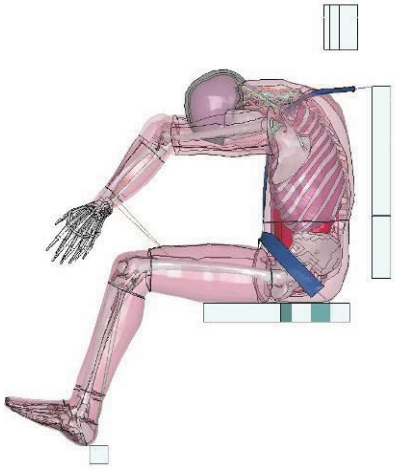

Figure 14: THUMS at maximum belt engagement for load case 8202.

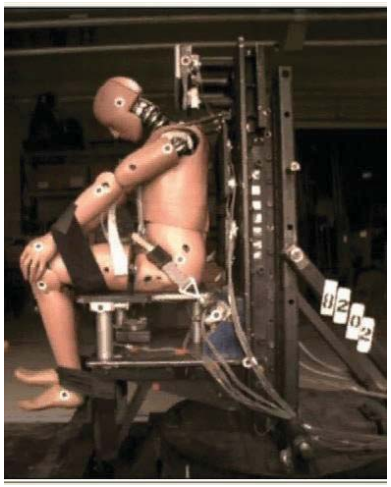

Figure 15: Hybrid III at maximum belt engagement for load case 8202.

The next loading condition was a spinal impact (8208). The THUMS experienced a large downward displacement of the head due to the lack of a head restraint and the more flexible neck and upper back. In this test, it is important to note that due to the configuration of the sled, gravity is acting along the X-axis (anterior to posterior) instead of the Z-axis (superior to inferior) in the Wright-Patterson test. For the THUMS simulations, gravity was applied in both the X and Z directions to compare the results. Figure 16 and Figure 17 illustrate maximum engagement with the belts for both the simulation and the test case.

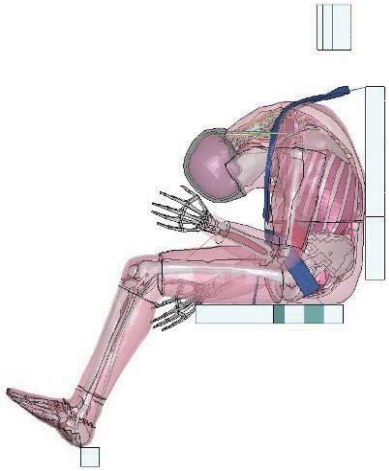

Figure 16: THUMS at maximum belt engagement for load case 8208.

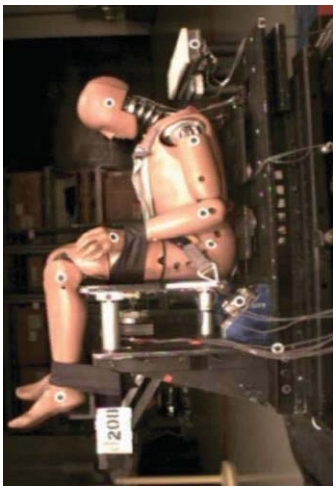

Figure 17: Hybrid III at maximum belt engagement for load case 8208.

The rear impact (8212) demonstrated less of a difference between the models because the seat engages the posterior aspect of the occupant. This rigid seat engagement does not allow as much movement by the occupant; therefore, the flexibility differences between the two occupants are not as apparent. The one difference of note was the increased chest compression

of the THUMS model due to the more flexible chest. Figure 18 and Figure 19 illustrate this difference.

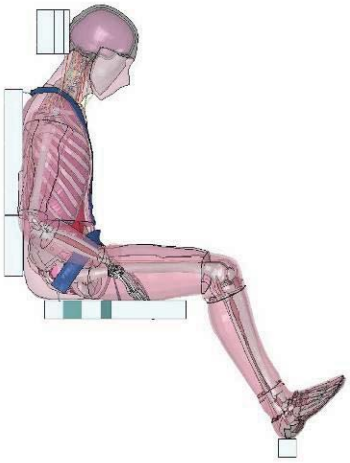

Figure 18: THUMS at maximum belt engagement for load case 8212.

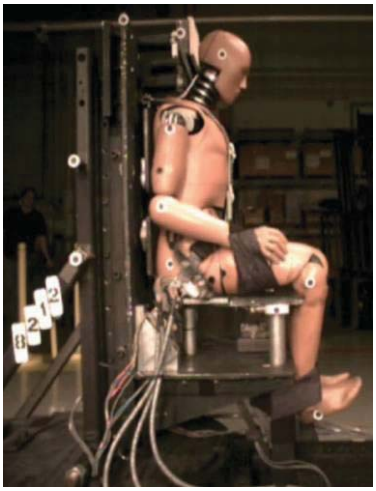

Figure 19: Hybrid III at maximum belt engagement for load case 8212.

The final case was a lateral impact (8245) of the occupant into the support structure of the seat. In this case, the flexibility of the THUMS model allowed for more head rotation about the upper head rest, more shoulder deflection at the level of the should restraint pad, and an uneven loading of the harness system due to the twisting of the occupant. These differences are illustrated in Figure 20 and Figure 21.

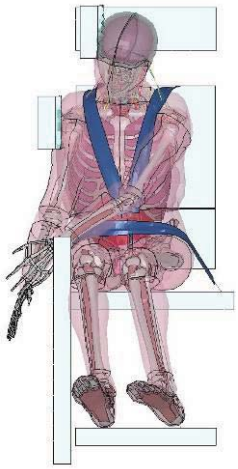

Figure 20: THUMS at maximum belt engagement for load case 8245.

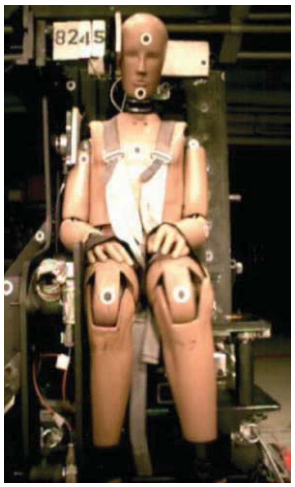

Figure 21: Hybrid III at maximum belt engagement for load case 8245.

3.1.2 Comparison of Resulting Accelerations and Forces

To further examine the differences between the response of the THUMS and the Hybrid III ATD, four measured quantities were compared between the simulations. These included head acceleration, chest acceleration, seat acceleration, and force in the belts. For the THUMS model, the seat acceleration from the Wright-Patterson tests was the input used to initiate the motion of the THUMS model. This was expected to be the same as the Wright-Patterson tests; however, it is included to demonstrate that the model seat had the same motion as the test seat. For clarity, the head, chest and seat acceleration plots will be include in the text and the belt force plots will be included as Appendix 3.

Seat Acceleration

The seat acceleration was expected to be the same as the Wright-Patterson test results since the seat acceleration was the input used for the simulations. Figure 22 to Figure 25 illustrated the seat acceleration of the seat in the primary direction of the simulation. For brevity, only the longer pulse comparisons are included.

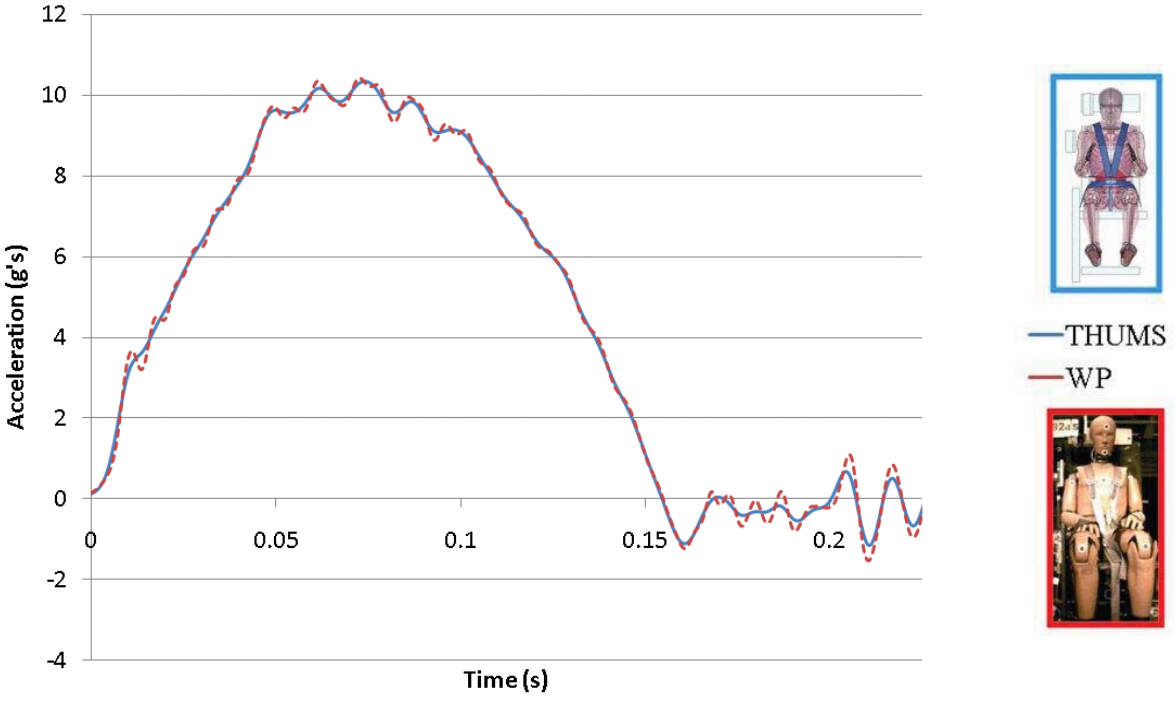

Figure 22: Test 8202 (frontal) seat acceleration, X-axis plot.

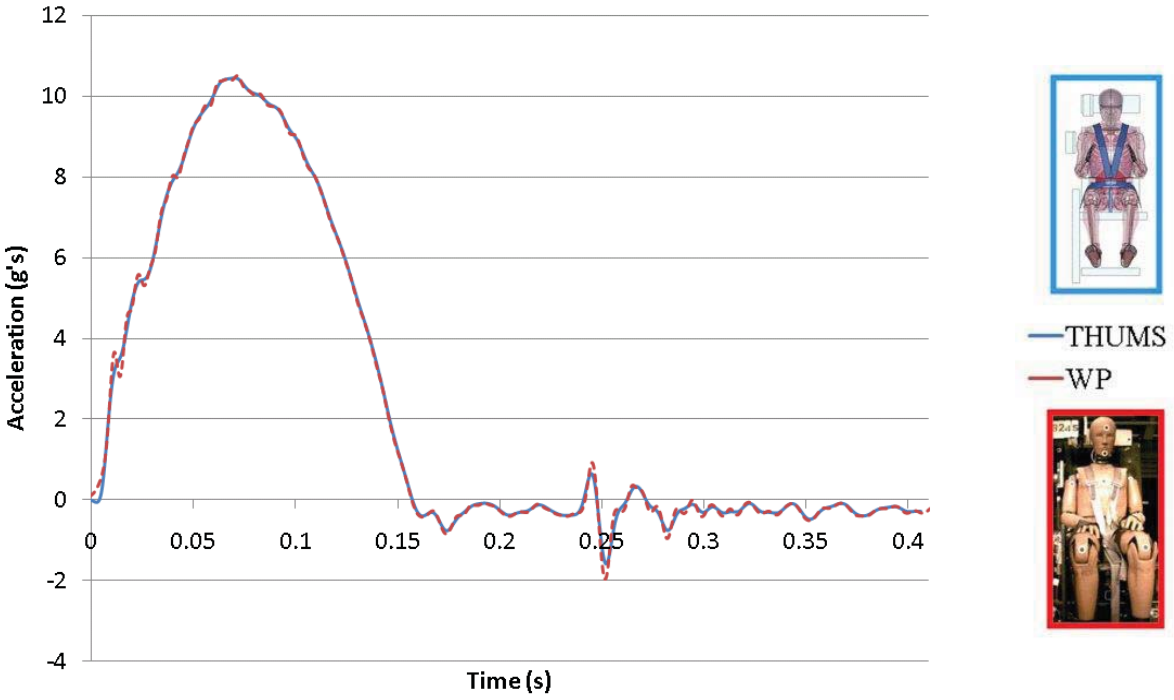

Figure 23: Test 8208 (spinal) seat acceleration, Z-axis plot.

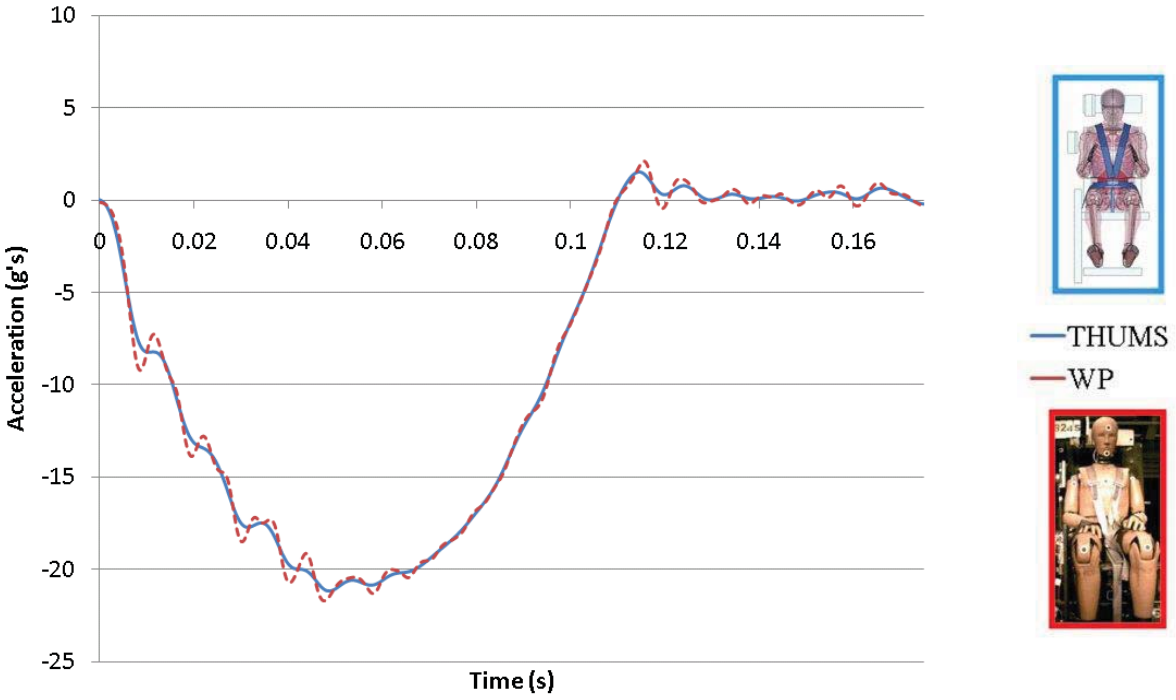

Figure 24: Test 8212 (rear) seat acceleration, X-axis plot.

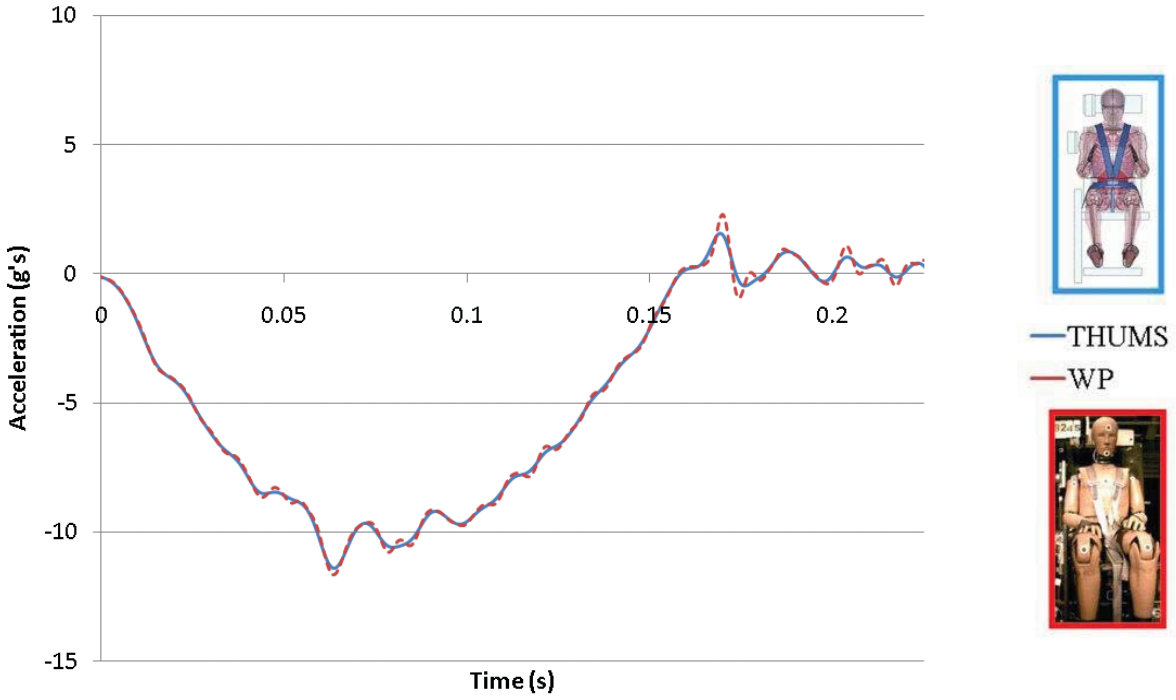

Figure 25: Test 8245 (lateral) seat acceleration, Y-axis plot.

Head Acceleration

The first body region measurement compared between the simulations and the sled tests was the head acceleration of the occupant. This acceleration was measured in the THUMS by tracking the acceleration of a node at the center of gravity of the head. In a Hybird III dummy, head acceleration is measured with a tri-axial accelerometer placed in the head. Figure 26 through Figure 29 are the plots of the head acceleration for both the simulation and the test. On each comparison plot for all comparisons, the THUMS acceleration or force is shown in blue and the matching Hybrid III measurement is shown in red. The head acceleration of the THUMS model lags the acceleration of the Hybrid III ATD head acceleration. This lag was expected due to the more compliant neck of the THUMS model.

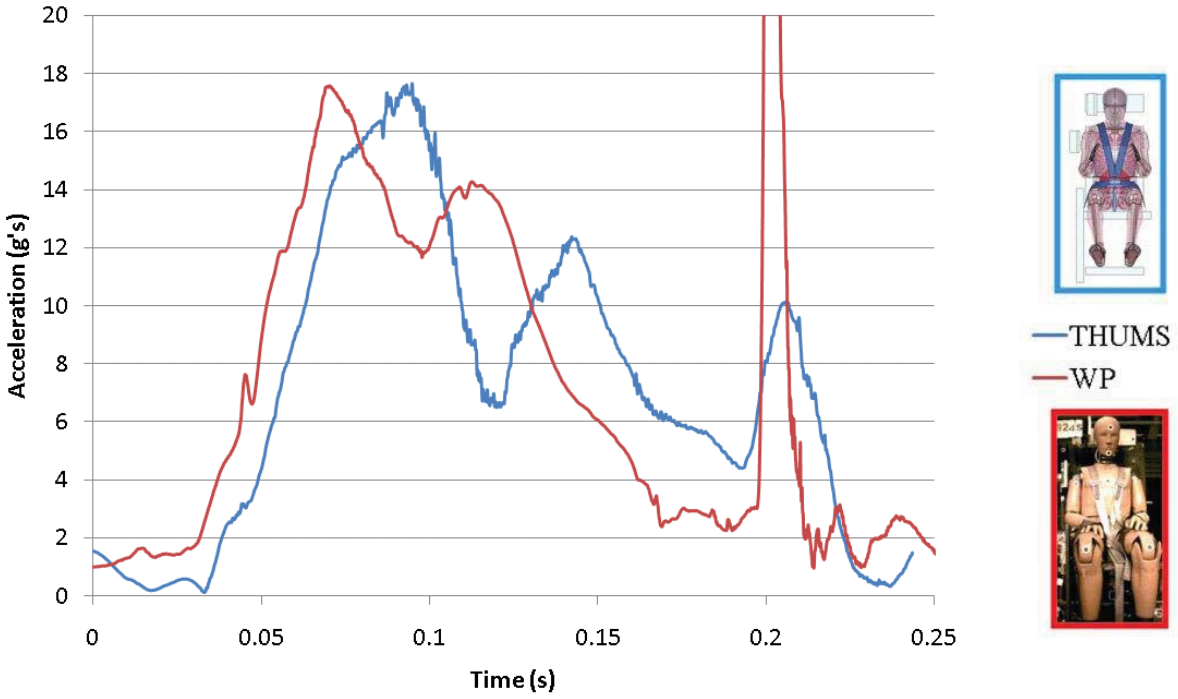

Figure 26: Test 8202 (frontal) head acceleration.

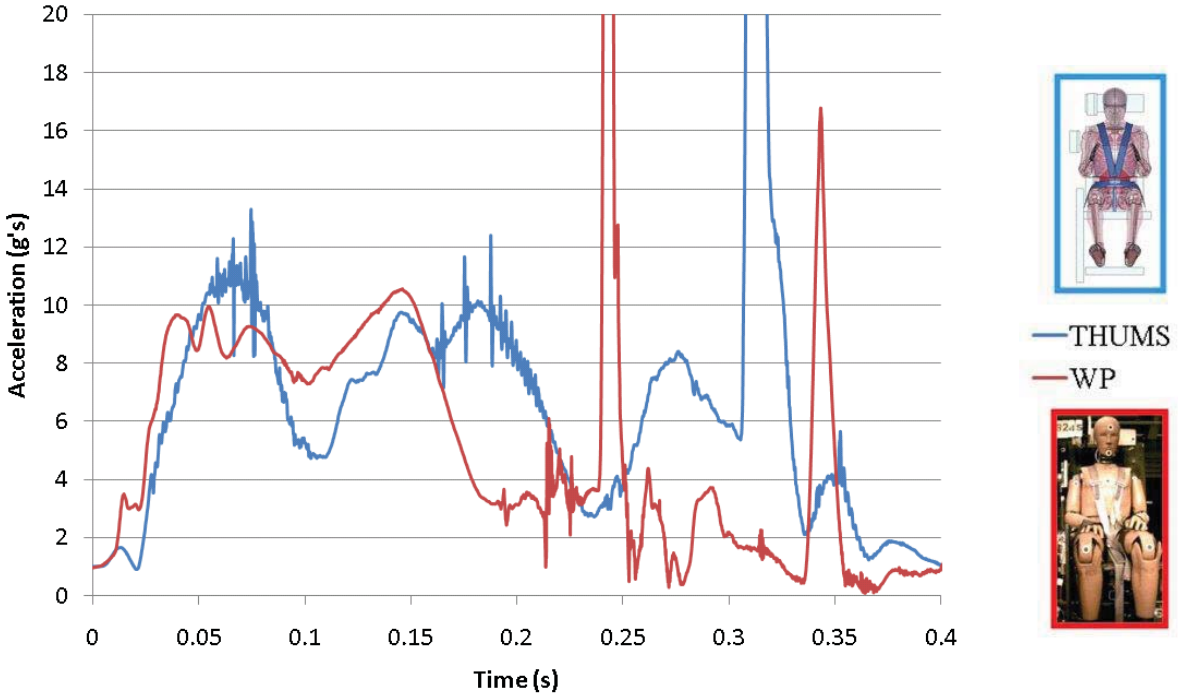

Figure 27: Test 8208 (spinal) head acceleration.

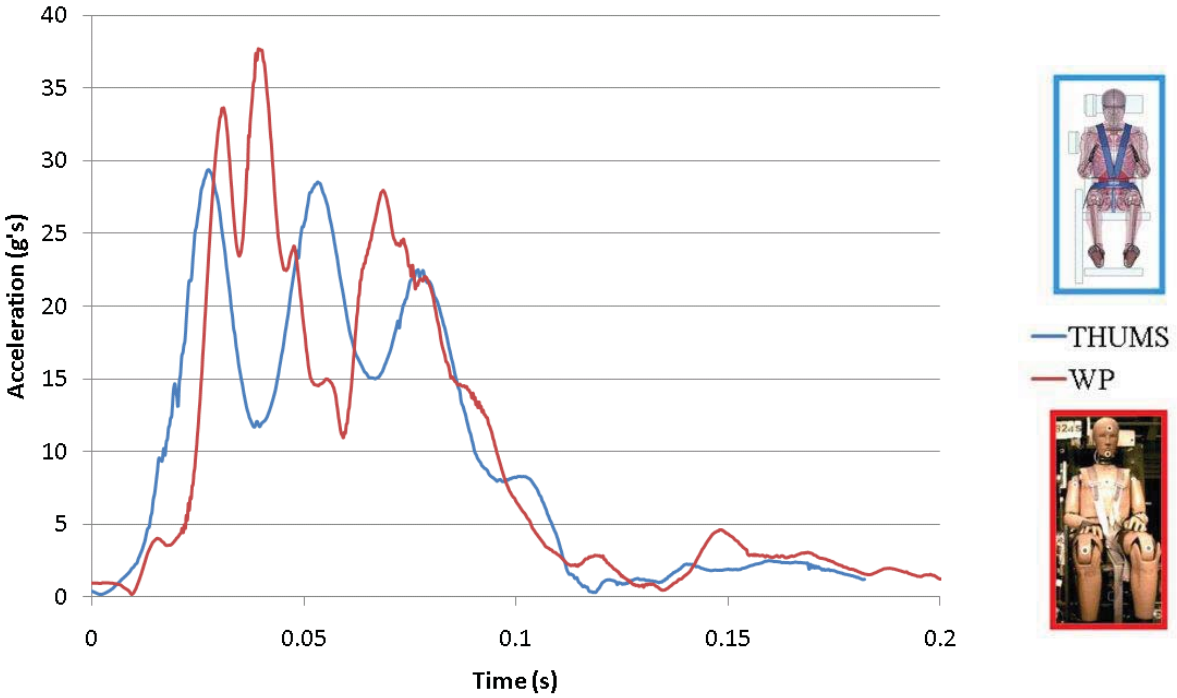

Figure 28: Test 8212 (rear) head acceleration.

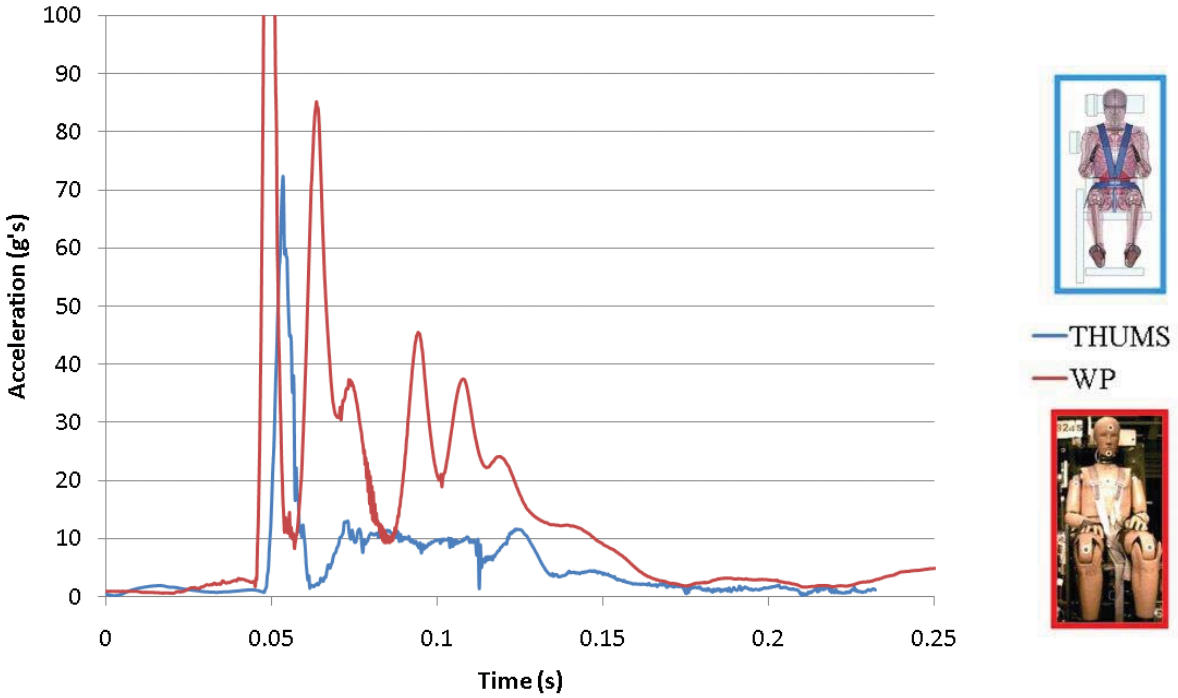

Figure 29: Test 8245 (lateral) head acceleration.

Chest Acceleration

Next, the chest acceleration of the THUMS and Hybrid III were compared. The plots in Figure 30 to Figure 33 demonstrate the similarity between the two. In general, the THUMS model had the same peaks as the Hybrid III.

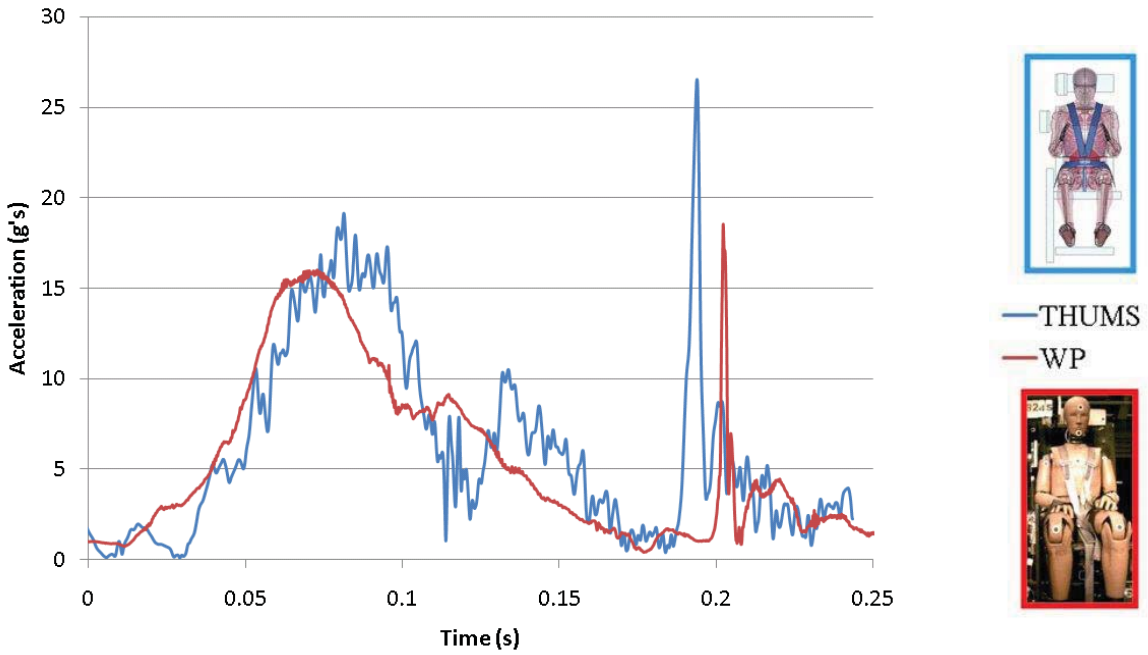

Figure 30: Test 8202 (frontal) chest acceleration.

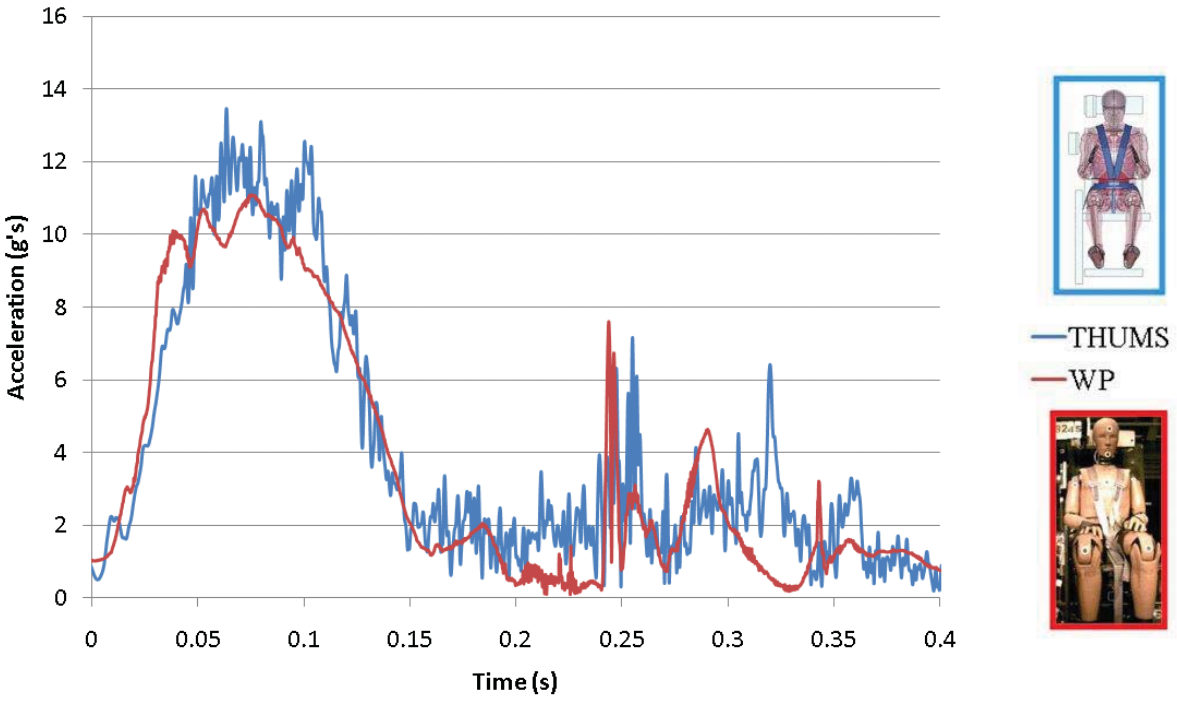

Figure 31: Test 8208 (spinal) chest acceleration.

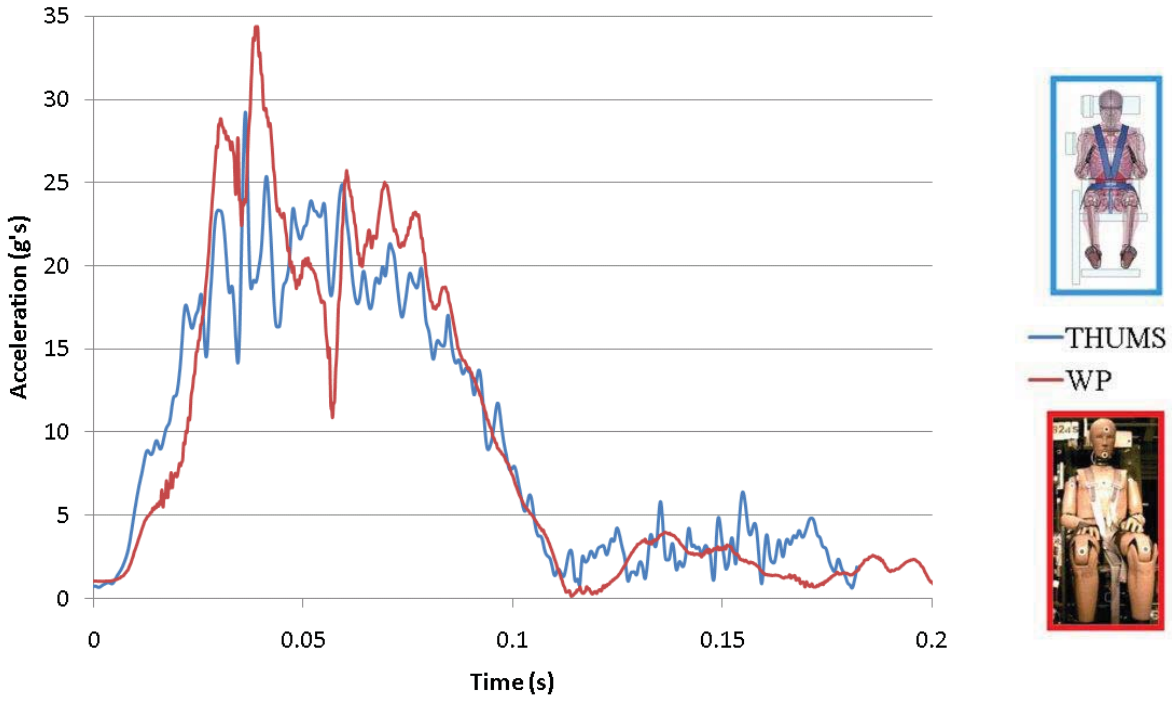

Figure 32: Test 8212 (rear) chest acceleration.

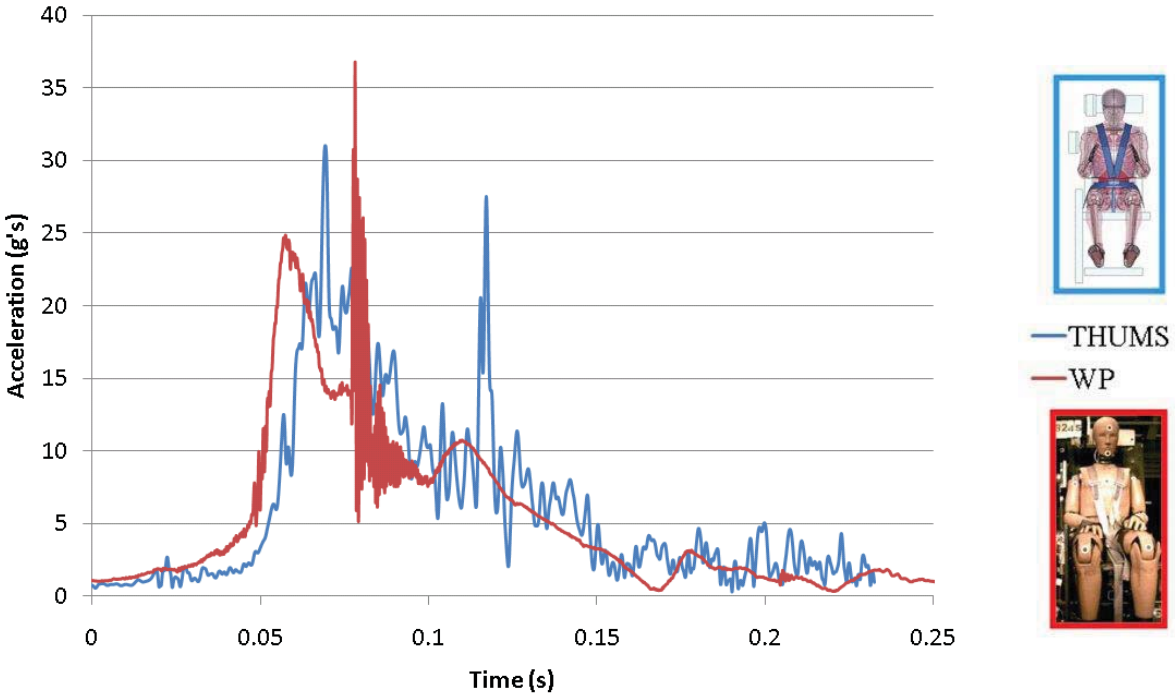

Figure 33: Test 8245 (lateral) chest acceleration.

3.2 THUMS Injury Metric Results

In addition to comparing the results of the THUMS modeling to the Wright-Patterson testing results, injury metrics for various body regions were also calculated. These results are extensive with the maximum values and plots included in Appendix 4 to 16. To summarize these results, the maximum value for each metric was plotted for each body region. From these plots, trends in the injury metric values depending on the simulation can be examined. These plots are shown in Figure 34 to Figure 40.

To compare possible injury mechanisms across simulations, a select group of injury metrics were evaluated to obtain a percent risk of injury. For the head simulations, this was HIC_{15} and HIC_{36} shown in Figure 41 and Figure 42. For the neck, the N_{ij} was calculated and shown in Figure 43. Chest injury was assessed through the CTI and chest acceleration with a 3 ms clip. The chest injury risks are shown in Figure 44 to Figure 46.

The lateral impact simulation (8245) resulted in the highest risk of head injury followed by the spinal impact (8208). Both of these simulations had a head strike to the seat resulting in higher head accelerations. For the risk of chest injury, the rear impact simulation (8212) had the highest risk of injury due to compression of the chest by the rear of the seat. All of the simulations had a similar risk of neck injury.

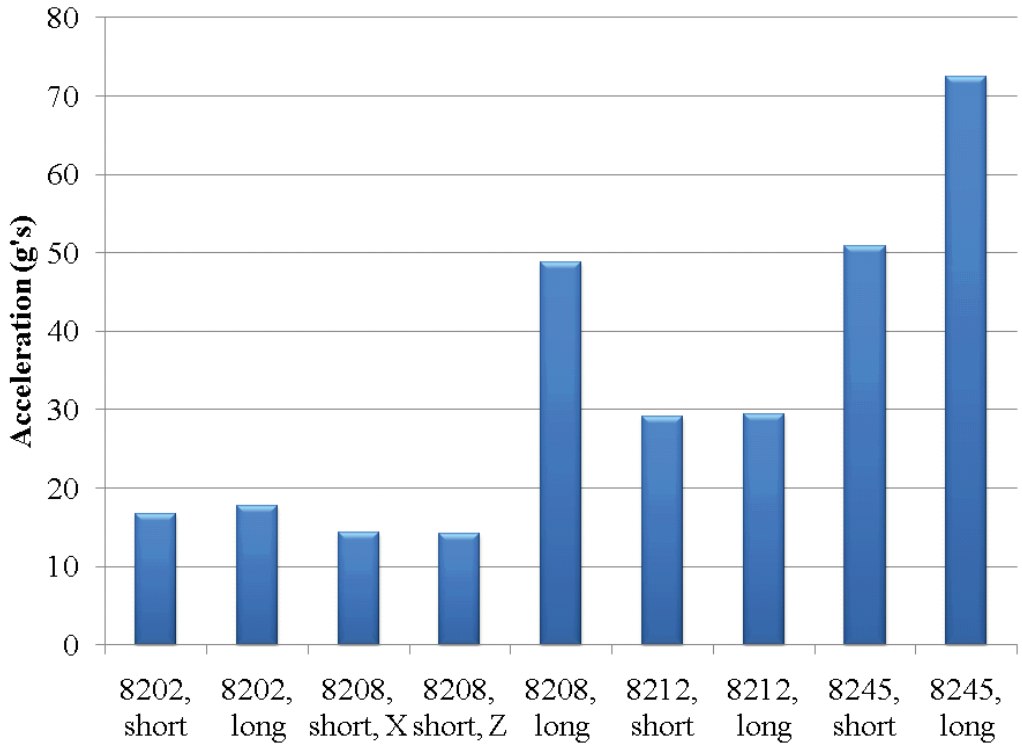

Figure 34: Head acceleration value for each simulation

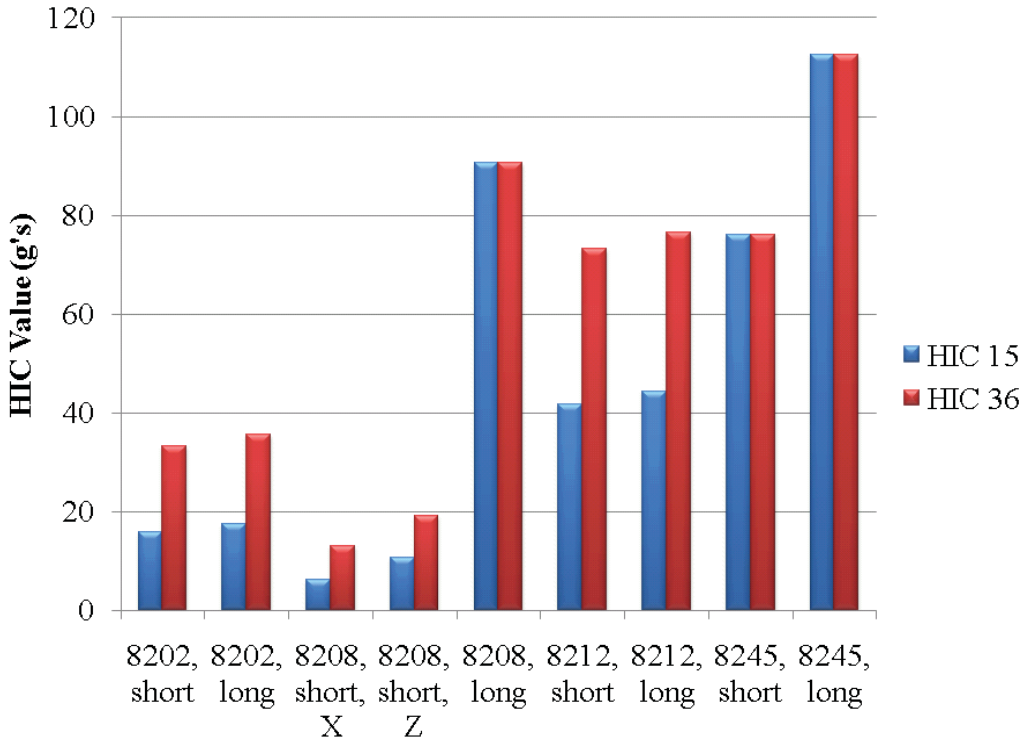

Figure 35: HIC values for each simulation

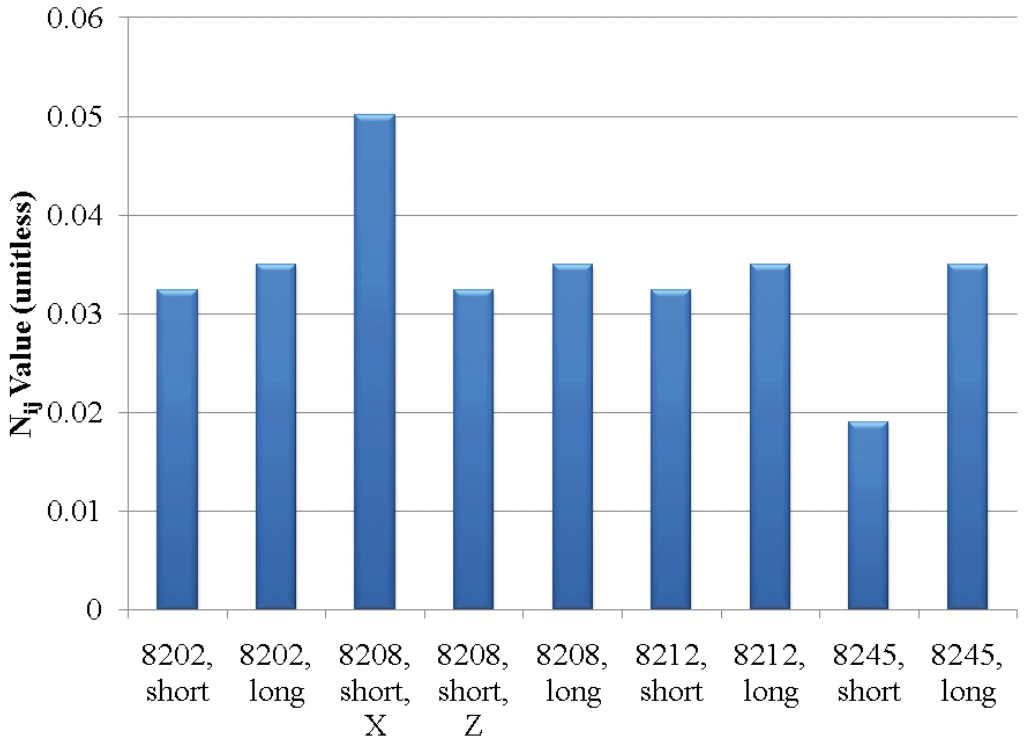

Figure 36: N_{ij} value for each simulation.

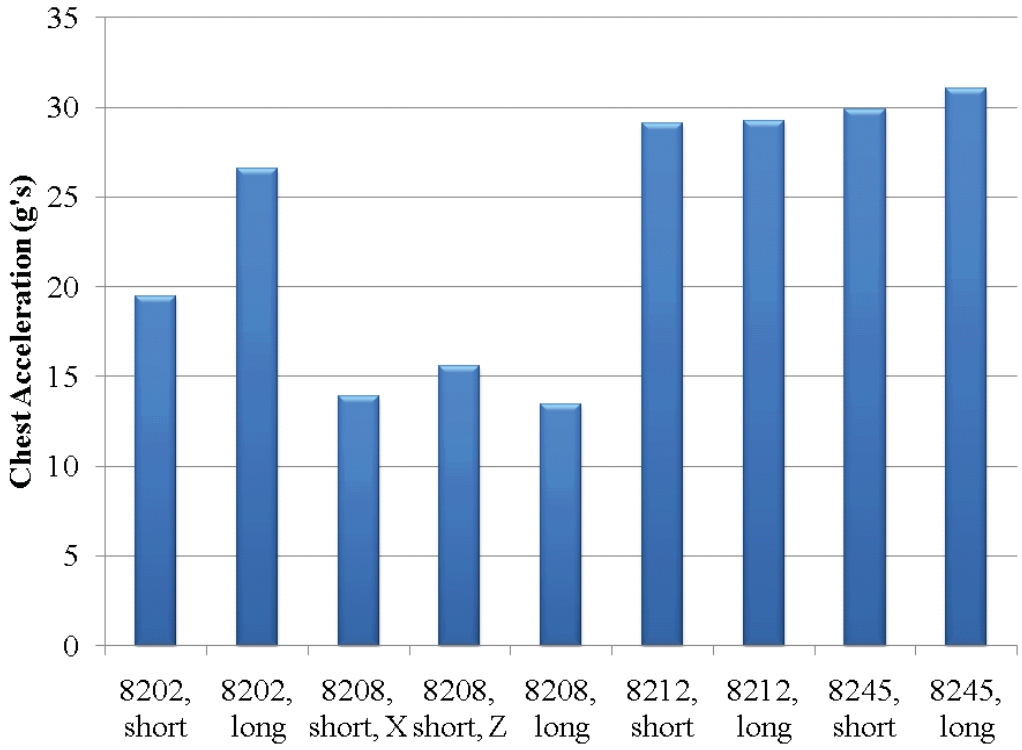

Figure 37: Chest acceleration values for each simulation

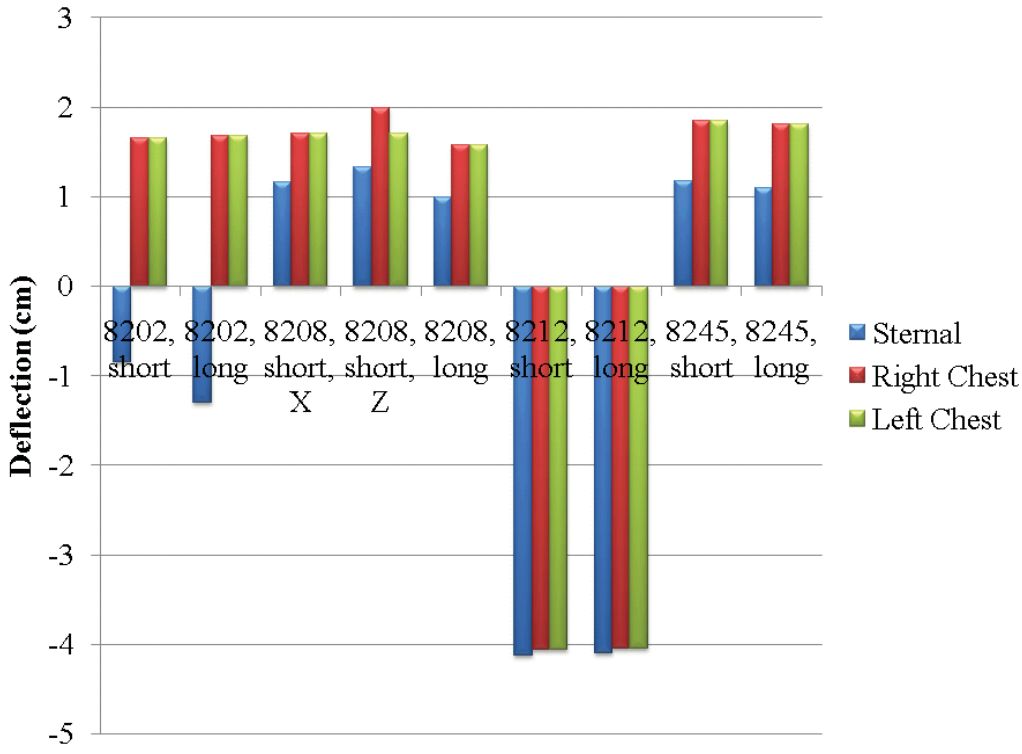

Figure 38: Chest deflection values for each simulation.

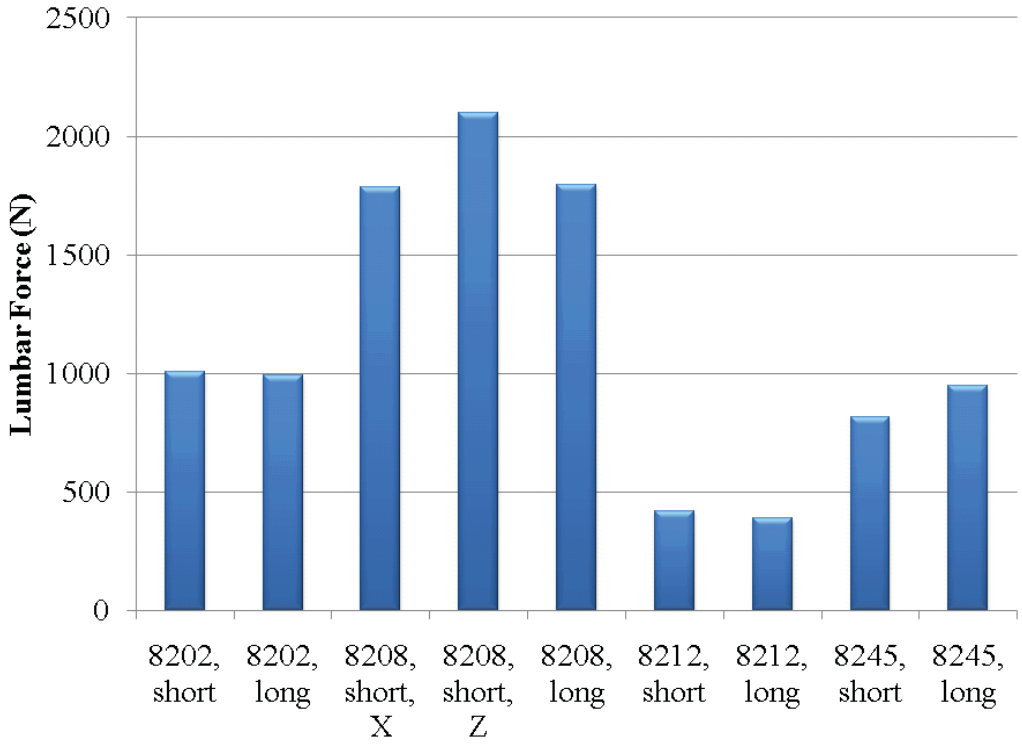

Figure 39: Lumbar force value for each simulation.

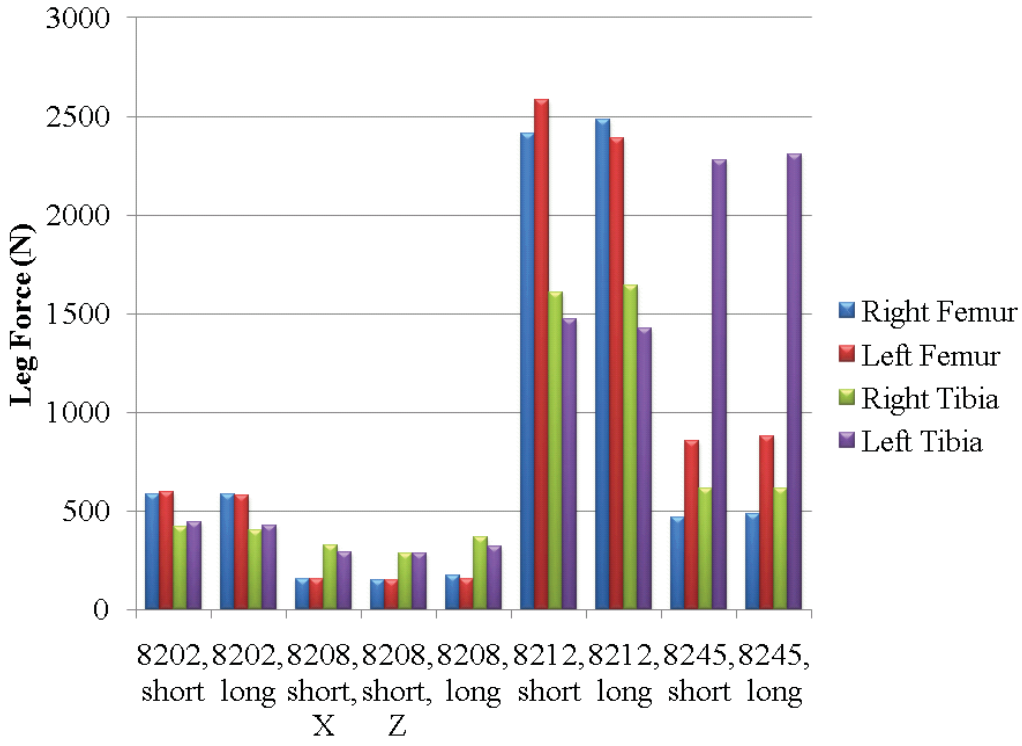

Figure 40: Leg force values for each simulation.

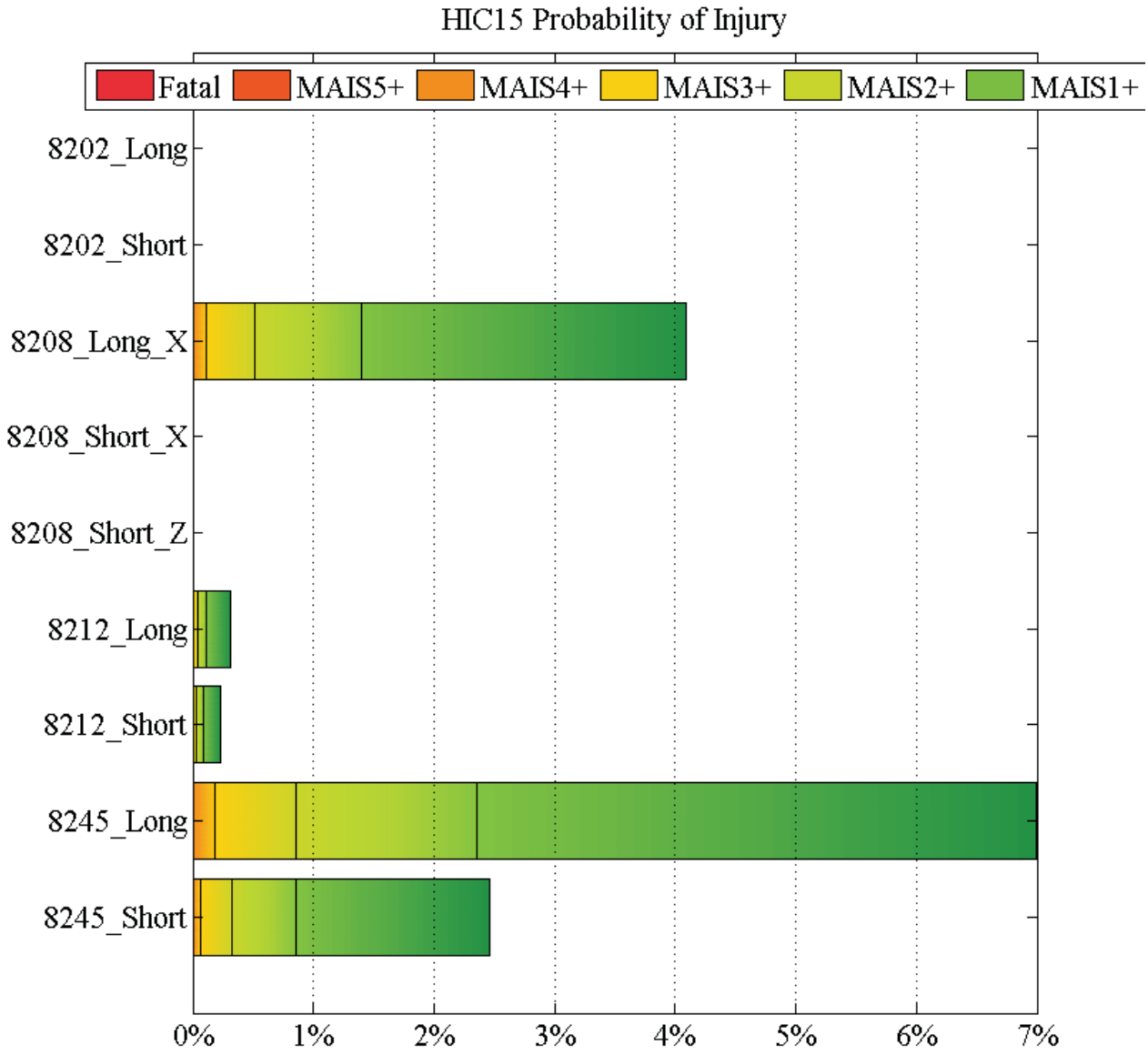

Figure 41: Risk of head injury based on HIC_{15}.

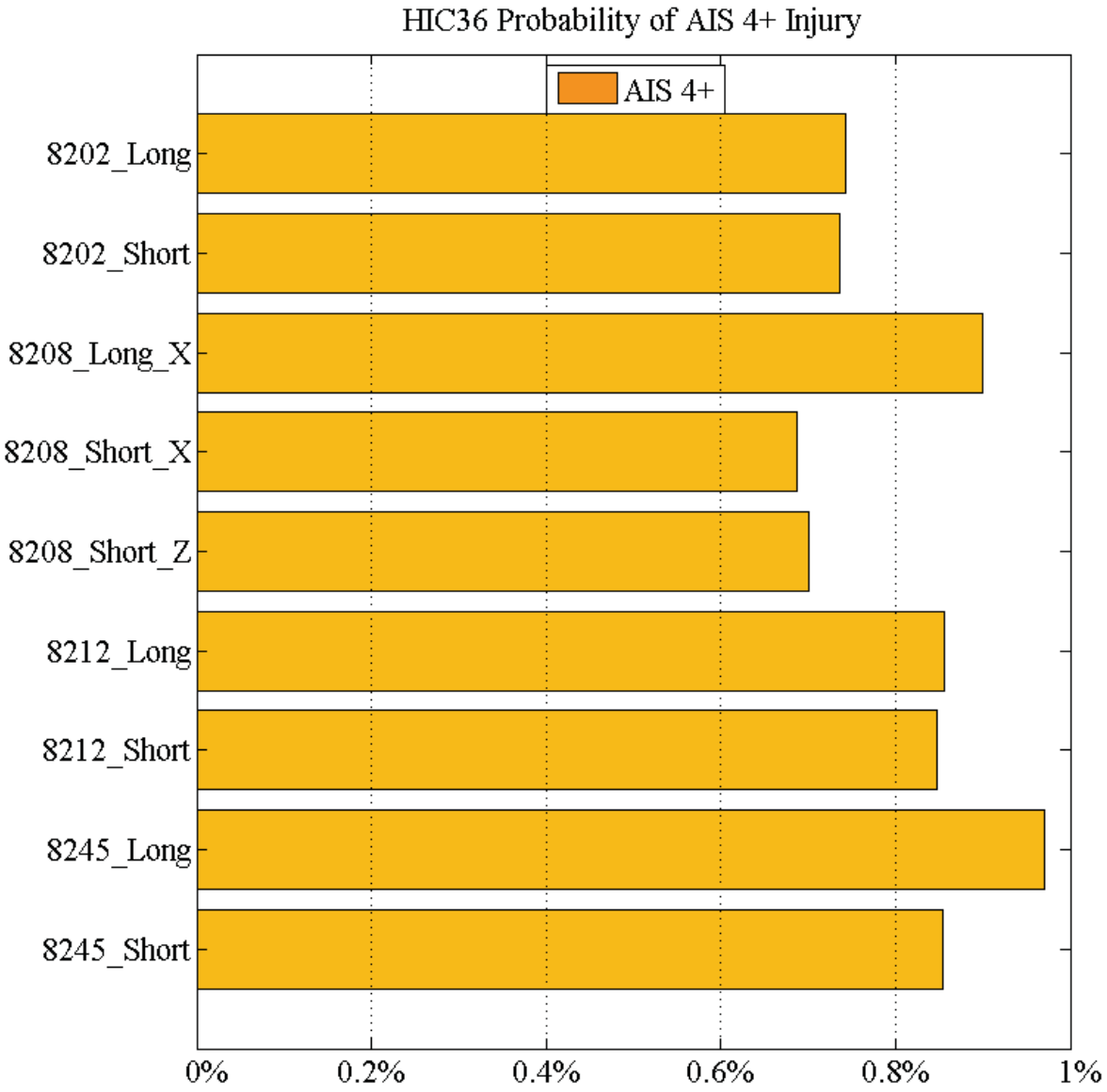

Figure 42: Risk of head injury based on HIC_{36}.

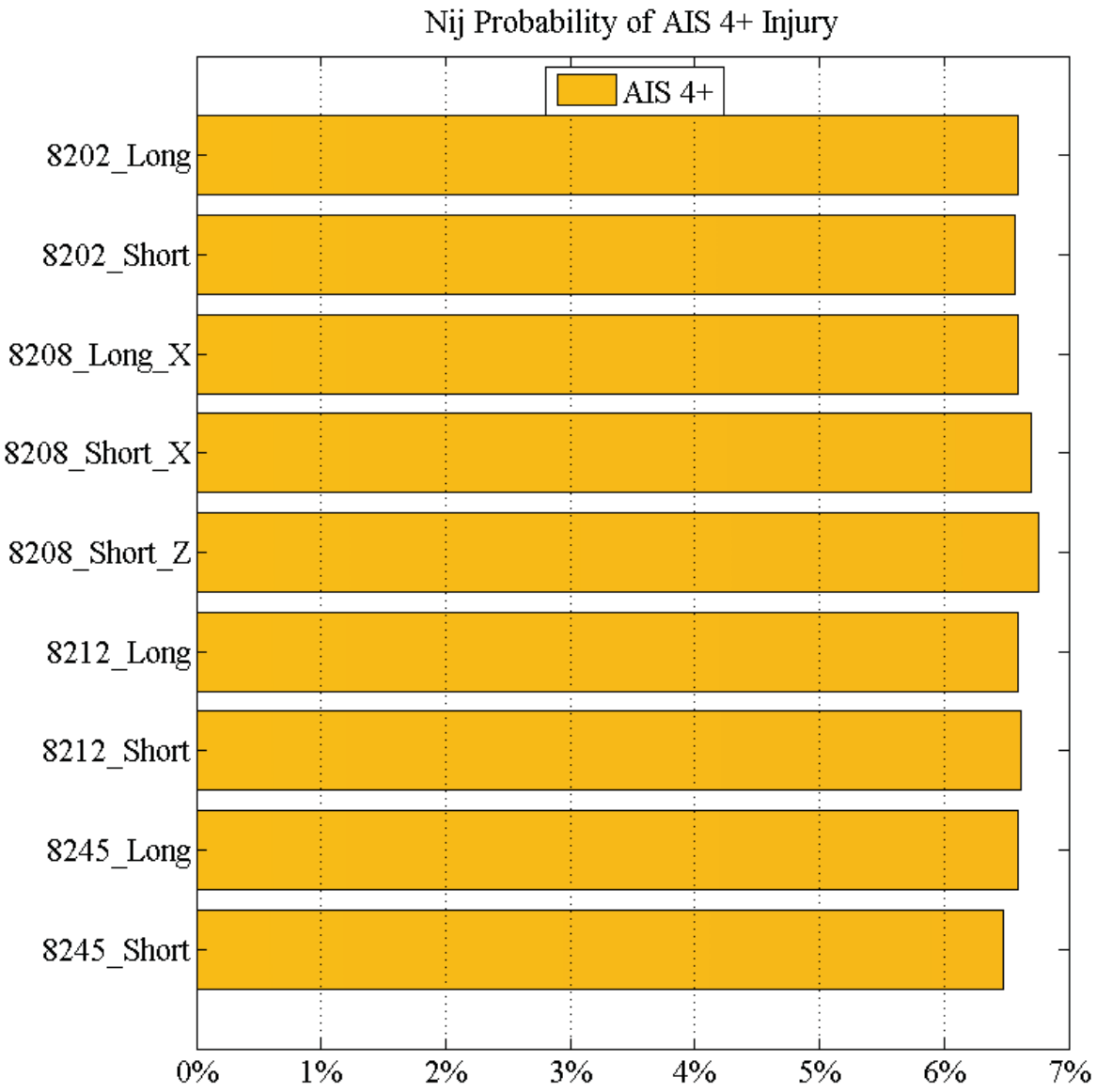

Figure 43: Risk of head injury based on N_{ij}.

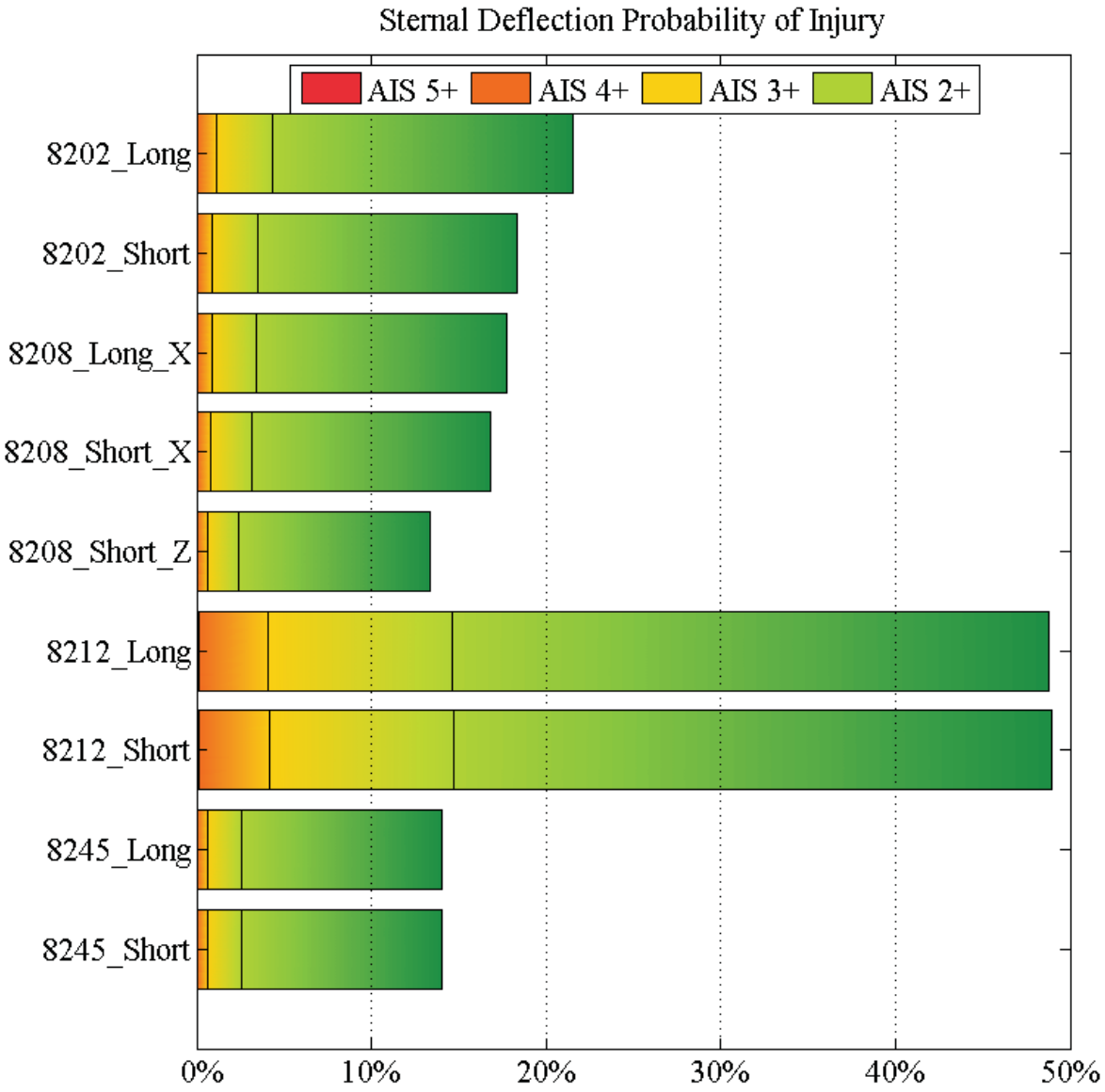

Figure 44: Risk of chest injury based on sternal deflection.

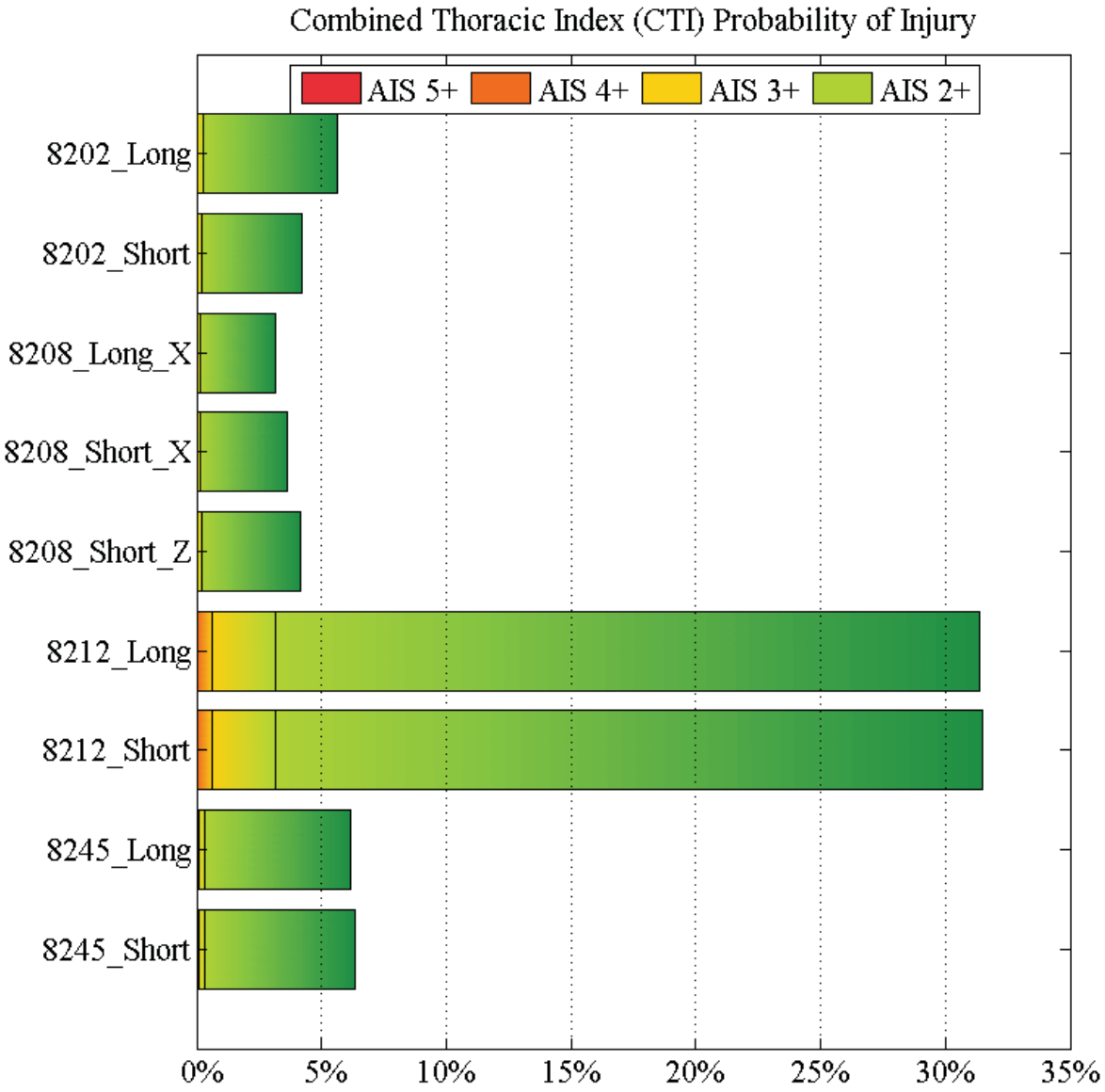

Figure 45: Risk of chest injury based on CTI.

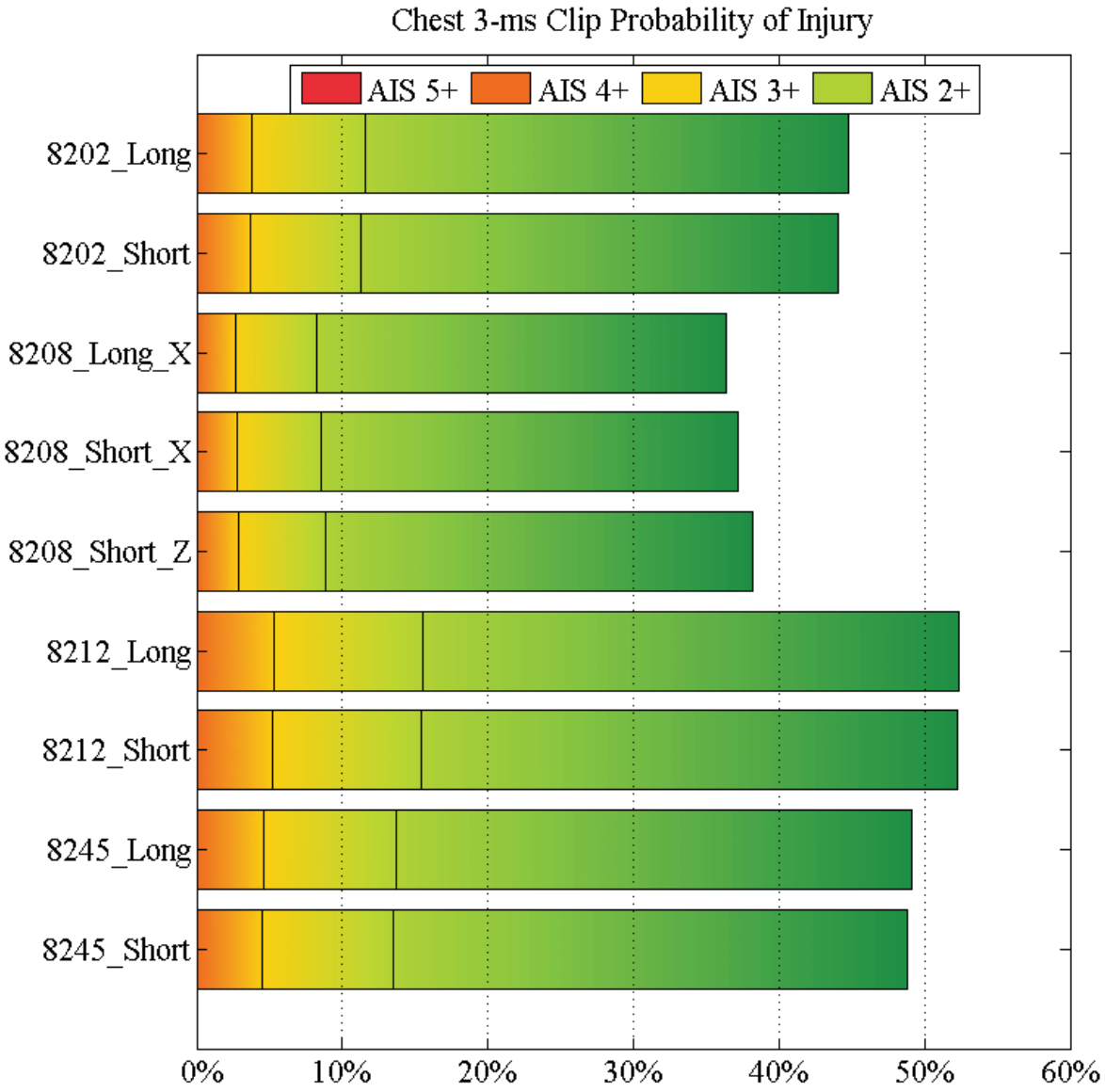

Figure 46: Risk of chest injury based on chest acceleration, 3-ms clip.

3.3 **Discussion**

There were several trends in the values of the injury metrics examined for these simulations. The head injury metrics (head acceleration, HIC_{15} and HIC_{36}) all indicated that the longer spinal pulse, the rear impact pulse, and the lateral pulse all resulted in higher head metric values. These simulations all had a head strike to a seat component which resulted in higher head acceleration values. For neck injury, only the N_{ij} values were examined. For all simulations, the N_{ij} values were similar; therefore, there is no indication any of the loading scenarios would be more likely to cause neck injury.

For the chest injury metrics, acceleration and deflection were compared. For chest acceleration, the spinal impact had lower values than all of the other simulations. The frontal, rear, and spinal tests had similar acceleration values. The other metric examined was the deflection of the chest. This was measured both at the sternum and along the ribs. For the spinal, rear and lateral impacts, the values of each of the metrics were close to each other. Additionally, only the rear impact had the largest deflection in compression for all metrics. The frontal impact simulation showed a different trend. The largest sternal deflection was in compression and the largest rib deflection was in expansion. In this simulation, the ribcage was initially compressed by the belt system, and then it expanded during rebound.

The lower body metrics compared were all force measurements including the lumbar spine, the femurs, and the tibias. As expected, the lumbar force measurements were highest during the spinal loading simulation. The leg forces varied based on the bone and the simulation. The frontal and spinal impacts had lower leg force values then the rear and lateral impacts. This was due to relatively little engagement of the leg with the seat system. In the rear and lateral impacts, the legs had higher loads. In the rear impact simulations, the femurs experienced higher loads than the tibias. In the lateral impact simulations the left tibia experience higher loads then any of the other bones. This was most likely due to the knee to knee impact during the simulation.

Due to the configuration of the WP test sled, the spinal impact scenario was performed so that gravity was acting in the X-direction instead of the Z-direction. Since the purpose of this study was to compare the THUMs response to the actual test data, gravity was also applied in the X-direction for long and short THUMS simulations. However, in an actual spinal loading event, gravity would be acting in the Z-direction. An additional short simulation was conducted with Z-axis gravity to determine possible differences in the injury metric values. For the majority of the metrics, there was little difference between these two simulations. However, the lumbar force was higher and the N_{ij} was lower in the Z-gravity simulation.

The largest chest deflection values were a compression of approximately 4 cm during the rear impact loading scenarios. Additionally, there was little variation between the three chest compression measurement techniques for this simulation. This value is significantly higher than chest deflection values seen in the H3 ATD. In a previous report on VIE loading, the response of a H3 chest during a simulated impacted was compared to that of a matched PMHS test conducted at Ohio State University (OSU). The H3 test results demonstrated a slight compression with approximately 0.83 cm of compression. The comparison PMHS test had approximately 3 cm of compression. At 4 cm of compression, the WP test results more closely match the PMHS test results.

3.4 **Limitations**

One limitation of this study is the relative lack of biomechanical data on bony failure properties of occupants exposed to long term zero-gravity. This exposure has the well documented effect of the reduction in bone mineral density [8]. The corresponding decrease in

biomechanical strength is unknown. However, much of the human tolerance data in biomechanical literature is derived from PMHS testing. Generally, the subjects used in the studies tend to be older individuals with corresponding age related bone strength reduction. In this respect, the PMHS data is more like the returning crew members then the crew members before launch.

4 Conclusions

The results of this comparison indicate the THUMS model performs in a similar manner as the Hybrid III ATD. The differences in the responses of model and the ATD are primarily due to the flexibility of the THUMS. This THUMS flexibility is more similar to the response of a human occupant. Based on the similarity between the two models, the THUMS should be used in further testing to assess risk of injury to the occupant.

5 References

[1] M. Iwamoto, Y. Kisanuki, I. Wantanabe, K. Furusu, K. Miki, and J. Hasegawa, "Development of a Finite Element Model of the Total Human Model for Safety (THUMS) and Application to Injury Reconstruction," in *IRCOBI*, Munich, Germany, 2002.

[2] P. Prasad and H. Mertz, "The Position of the United States Delegation to the ISO Working Group 6 on the Use of HIC in the Automotive Environment," in *SAE Government/Industry Meeting and Exposition, SAE Paper no. 851246*, 1985.

[3] R. Eppinger, E. Sun, F. Bandak, M. Haffner, N. Khaewpong, M. Maltese, S. Kuppa, T. Nguyen, E. Takhounts, R. Tannous, A. Zhang, and R. Saul, "Development of Improved Injury Criteria for the Assessment of Advanced Automotive Restraint Systems - II," NHTSA, Ed., 1999.

[4] P. Prasad and R. Daniel, "A Biomechanical Analysis of Head, Neck, and Torso Injuries to Child Surrogates Due to Sudden Torso Acceleration," *SAE Paper no. 841656,* 1984.

[5] AAAM, "Abbreviated Injury Scale, 1998 Revision (AIS-98)," Association for the Advancement of Automotive Medicine, Committee on Injury Scaling. , Des Plains, IL 1998.

[6] SAE, "Surface Vehicle Recommended Practice, SAE J211," JUL 2007.

[7] C. K. Kroell and D. C. Schneider, "Impact Tolerance and Response of the Human Thorax," in *15th Stapp Car Crash Conference*, 1971, pp. 84-134.

[8] A. D. LeBlanc, E. R. Spector, H. J. Evans, and J. D. Sibonga, "Skeletal responses to space flight and the bed rest analog: a review," *J Musculoskelet Neuronal Interact,* vol. 7, pp. 33-47, Jan-Mar 2007.

Appendix 1: Modified and truncated acceleration data.

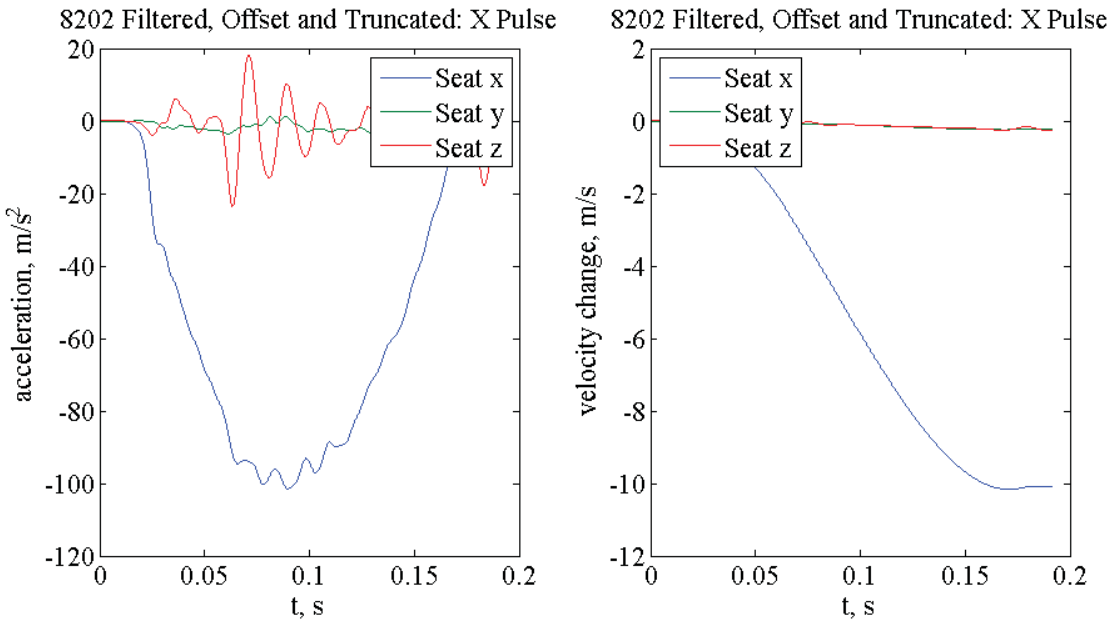

Figure 47: Pulse 8202, frontal impact.

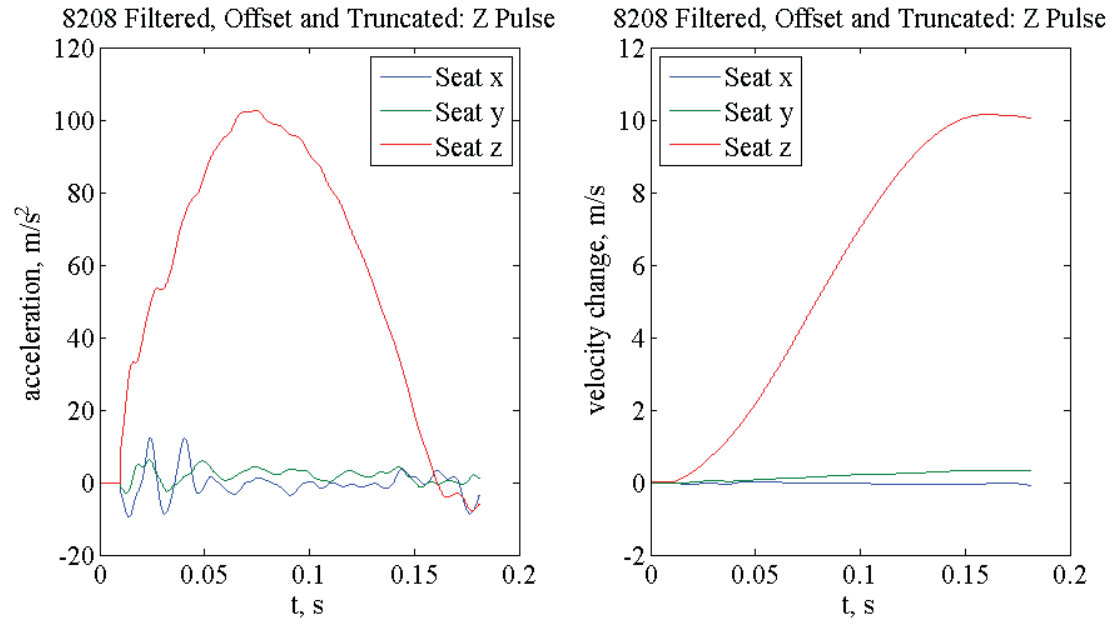

Figure 48: Pulse 8208, spinal impact.

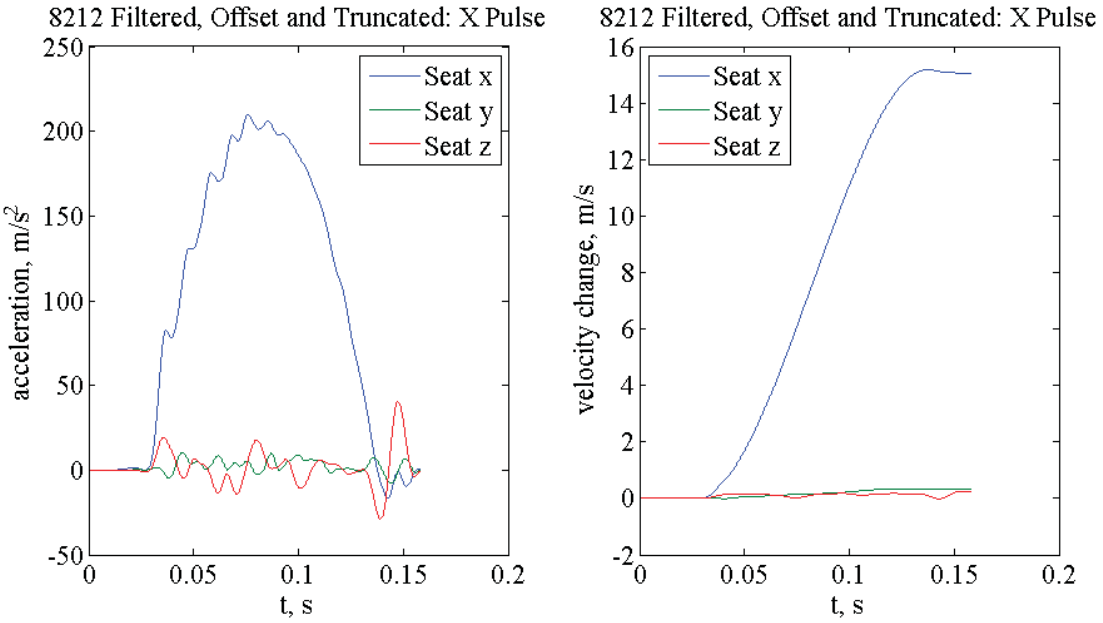

Figure 49: Pulse 8212, rear impact.

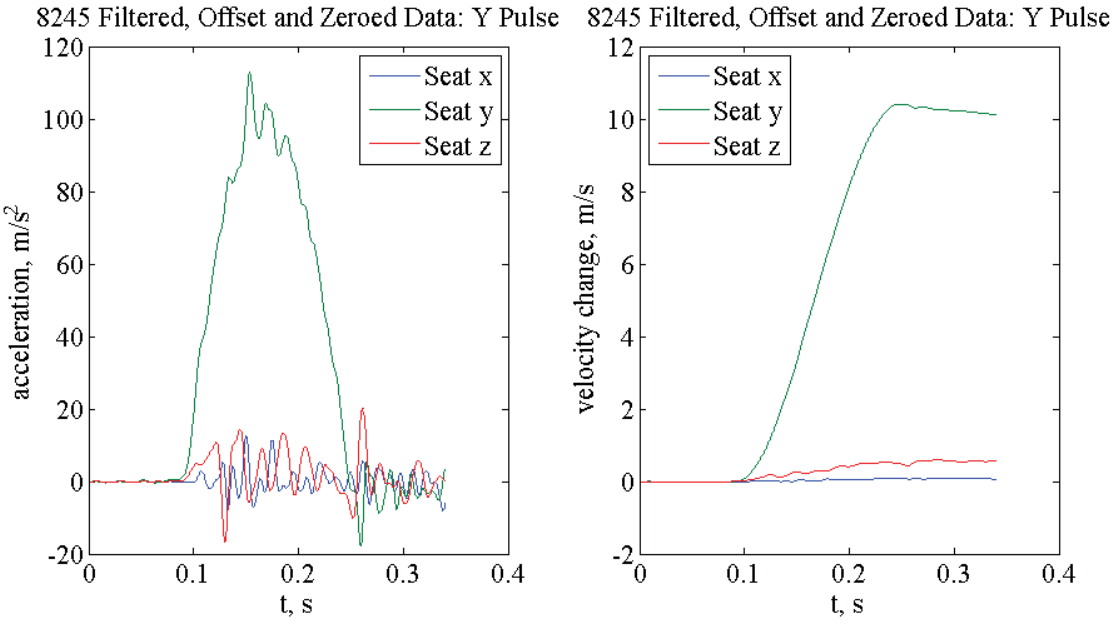

Figure 50: Pulse 8245, lateral impact.

Appendix 2: Modified and truncated acceleration data, longer pulse.

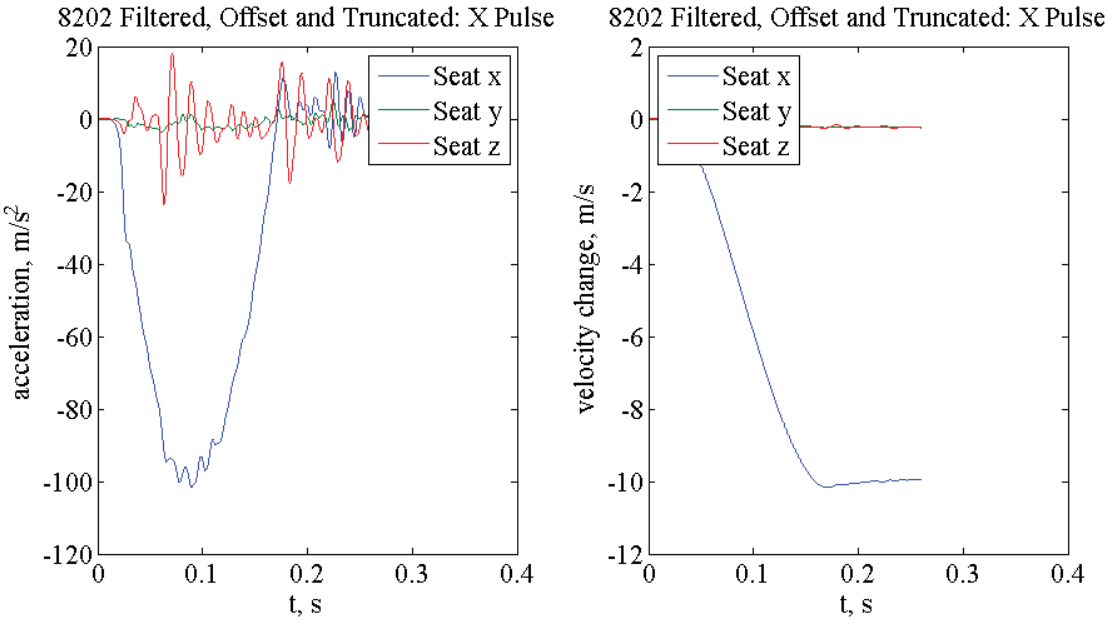

Figure 51: Pulse 8202, frontal impact.

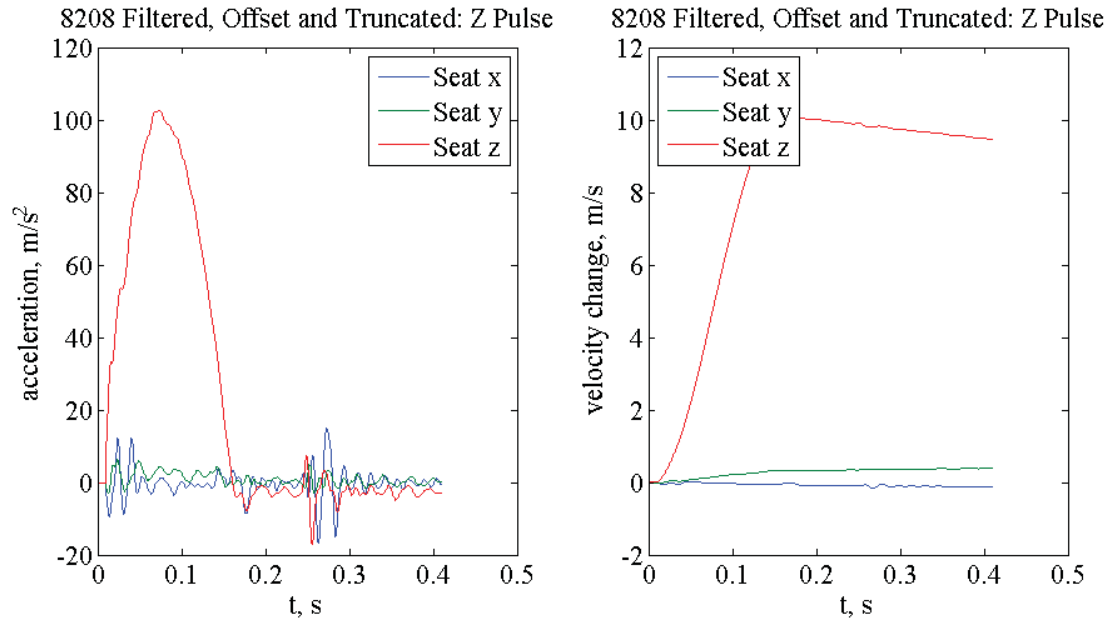

Figure 52: Pulse 8208, spinal impact.

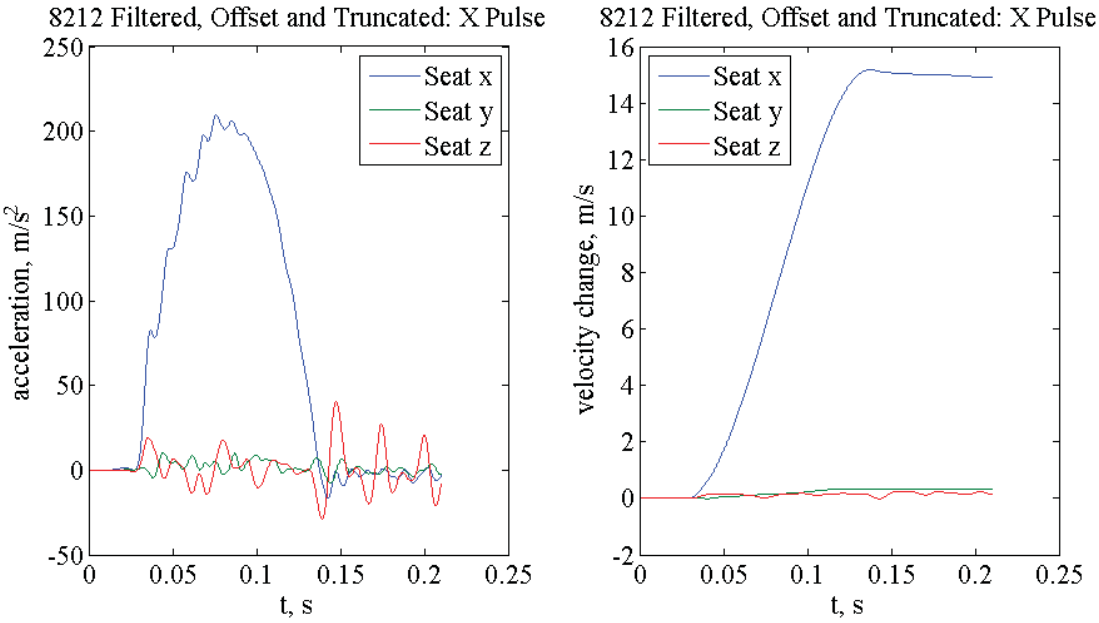

Figure 53: Pulse 8212, rear impact.

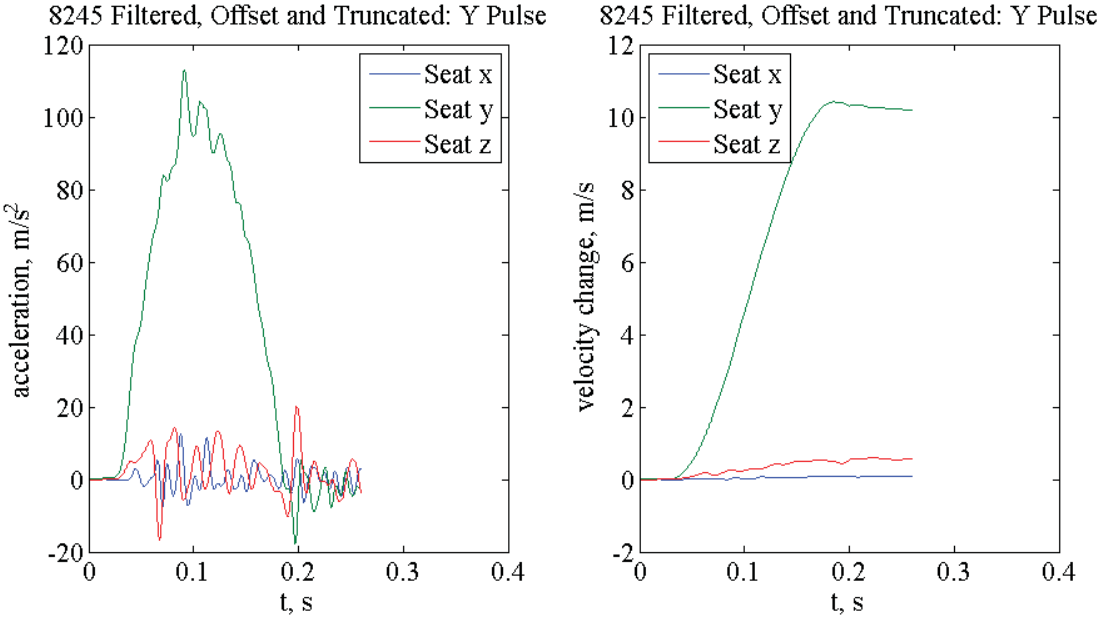

Figure 54: Pulse 8245, lateral impact.

Appendix 3: Seat belt force comparisons for all simulations.

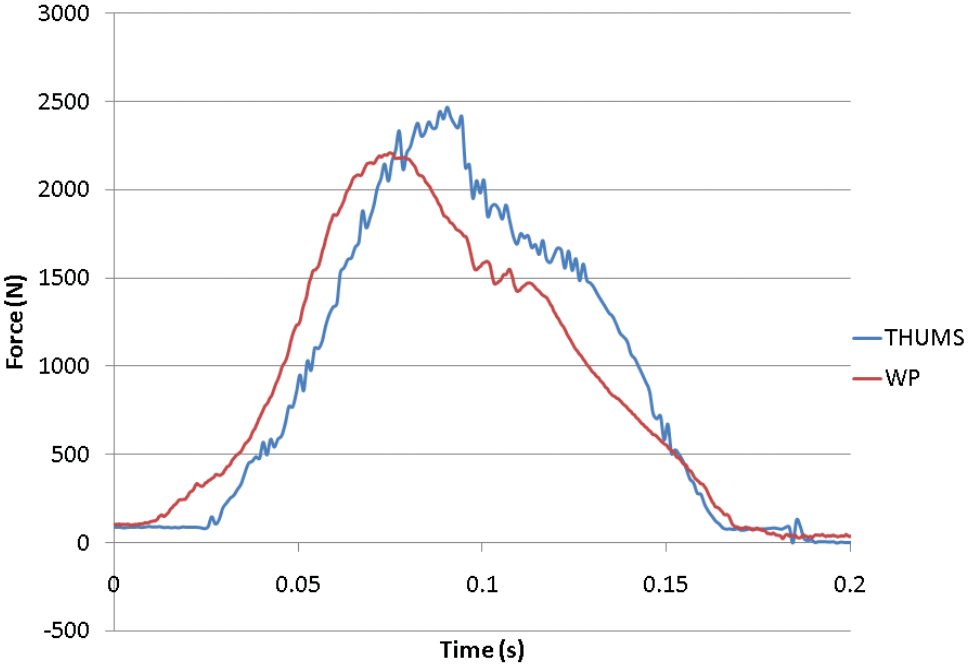

Figure 55: Pulse 8202, Left shoulder belt force.

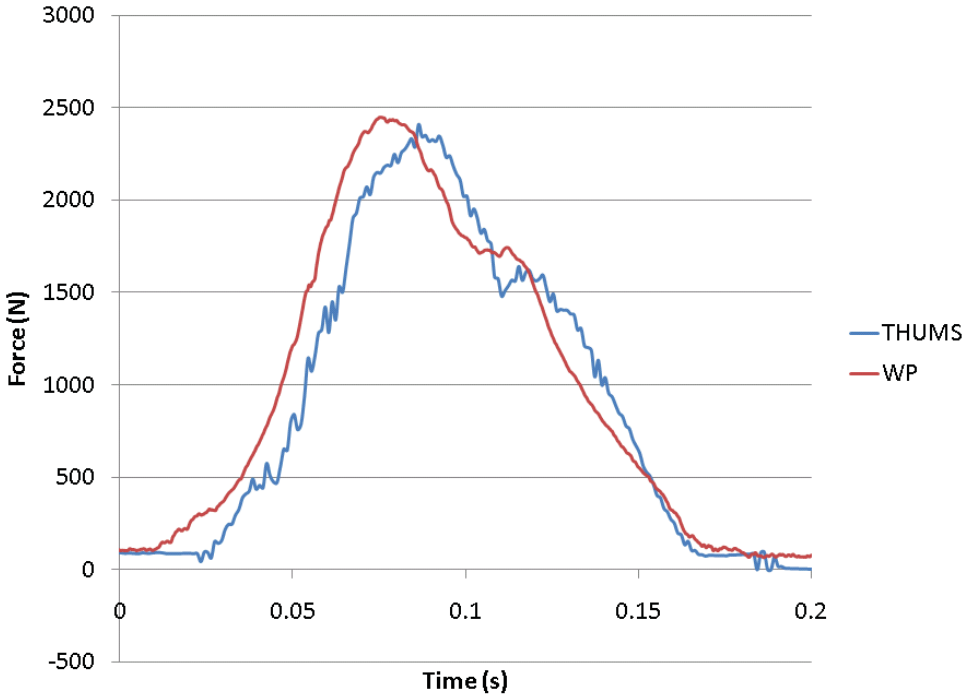

Figure 56: Pulse 8202, Right shoulder belt force.

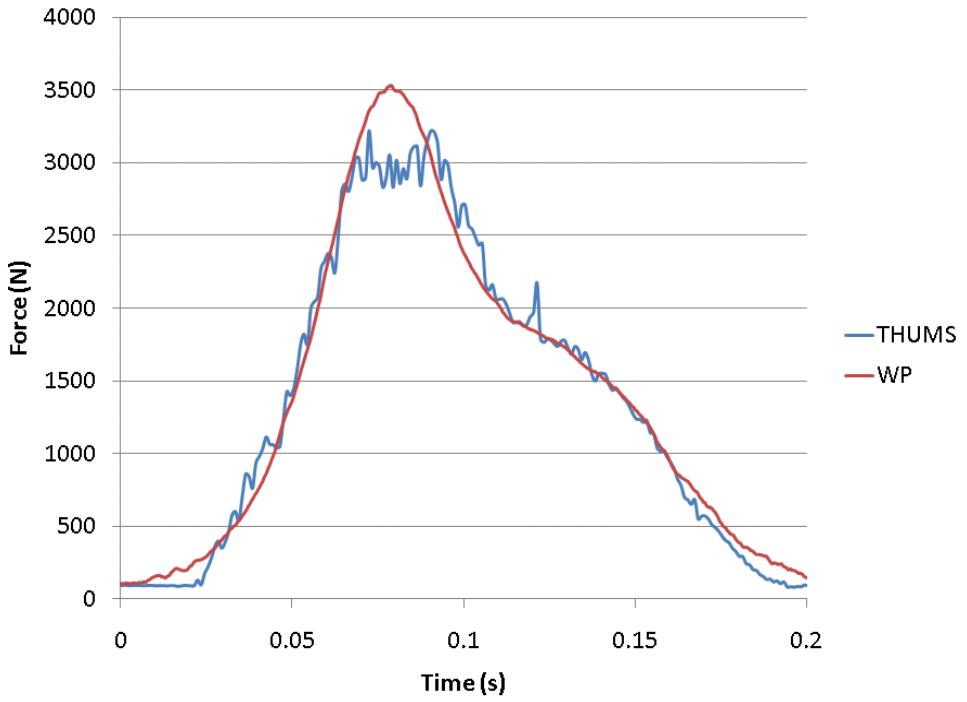

Figure 57: Pulse 8202, Left lap belt force.

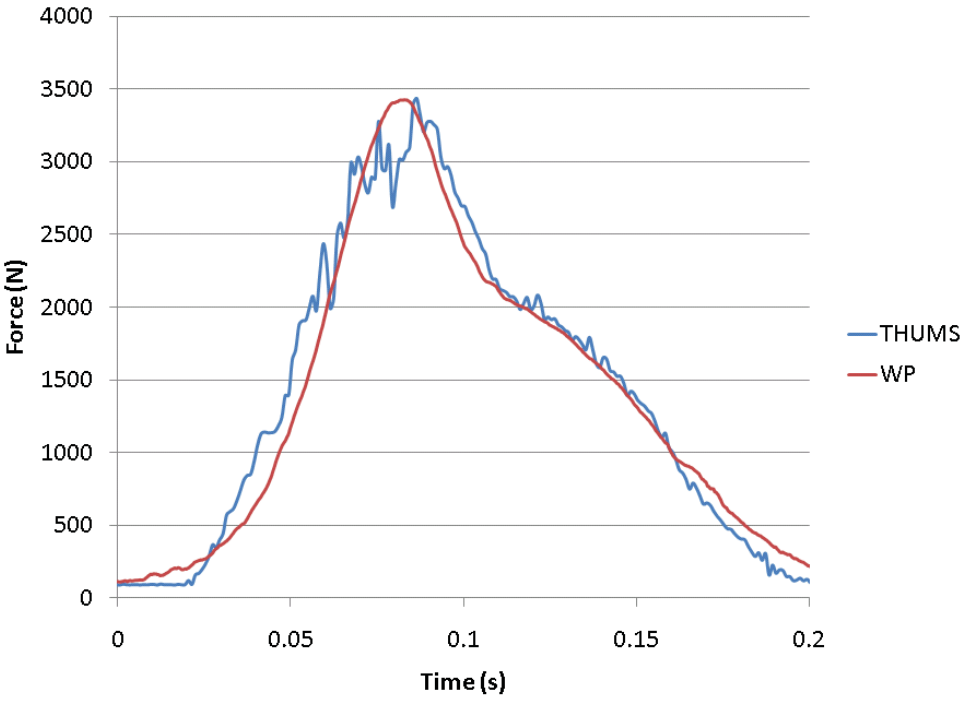

Figure 58: Pulse 8202, Right lap belt force.

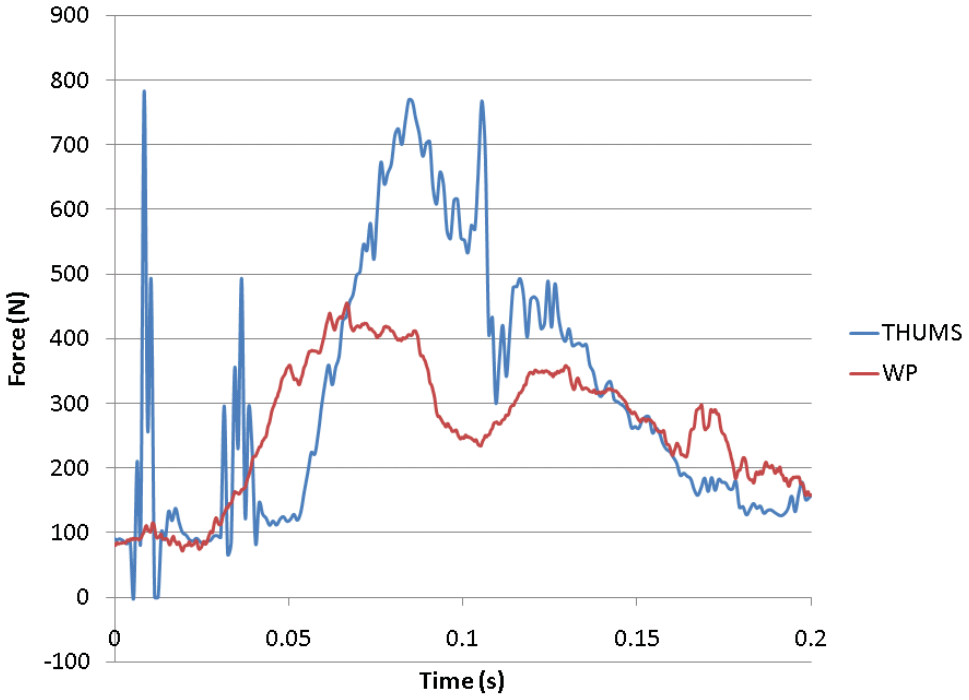

Figure 59: Pulse 8202, Crotch belt force.

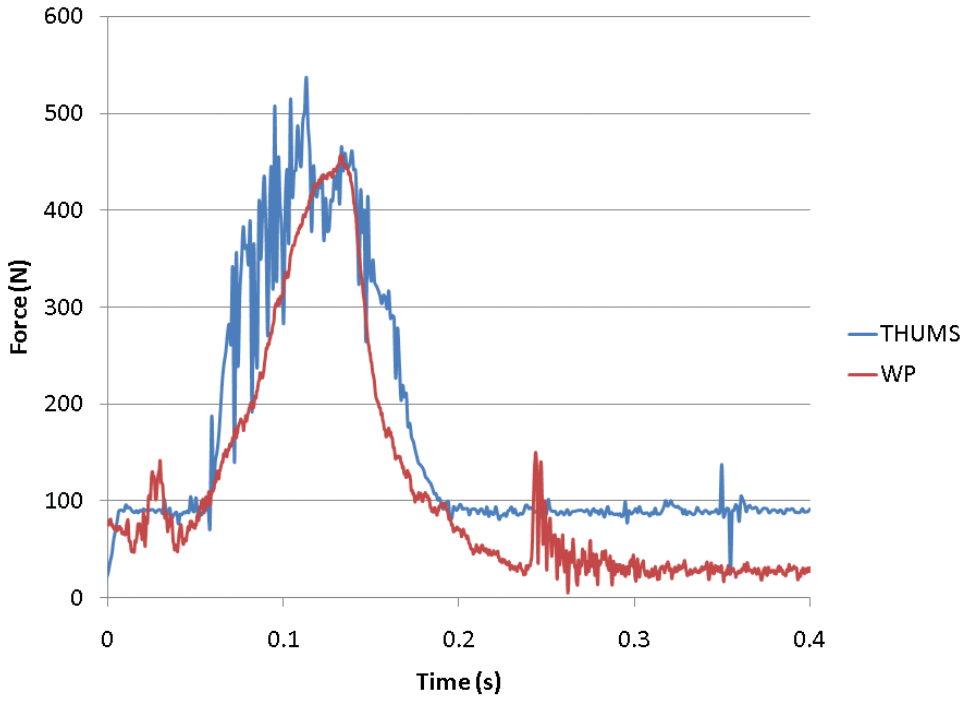

Figure 60: Pulse 8208, Left shoulder belt force.

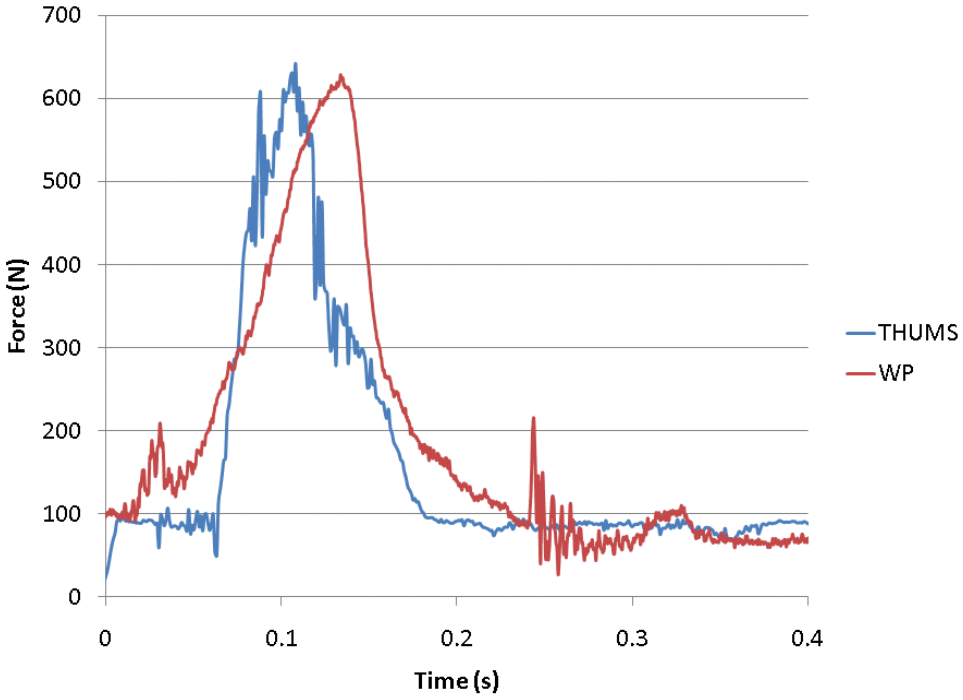

Figure 61: Pulse 8208, Right shoulder belt force.

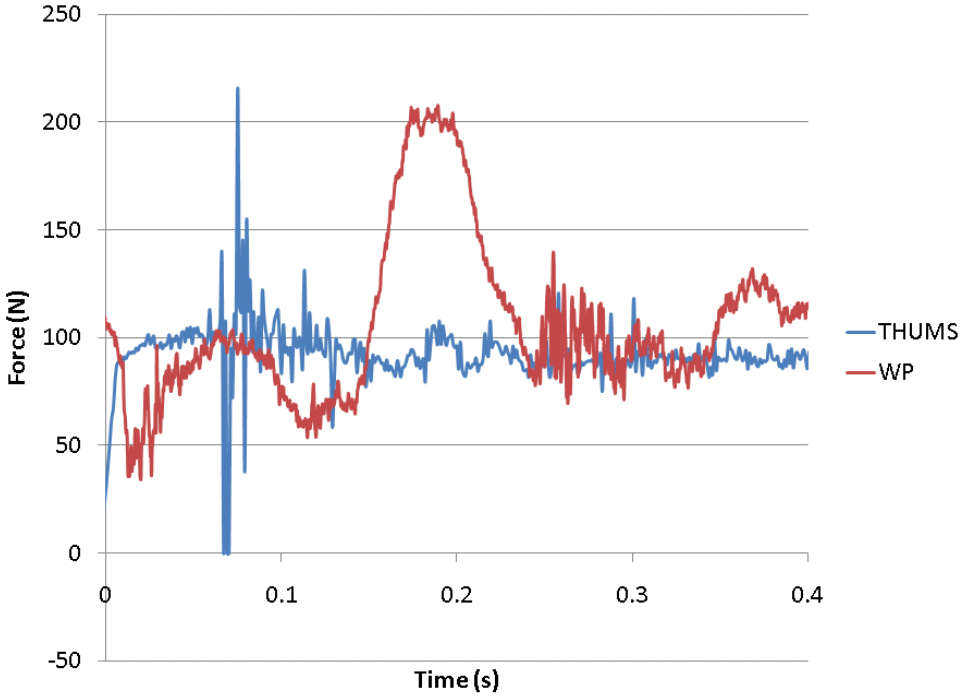

Figure 62: Pulse 8208, Left lap belt force.

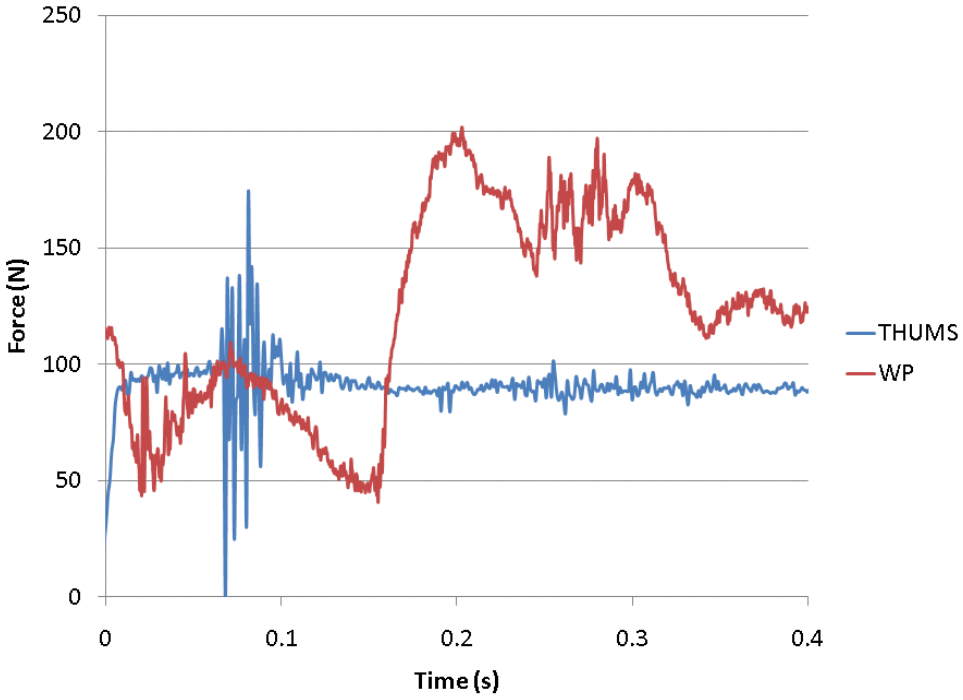

Figure 63: Pulse 8208, Right lap belt force.

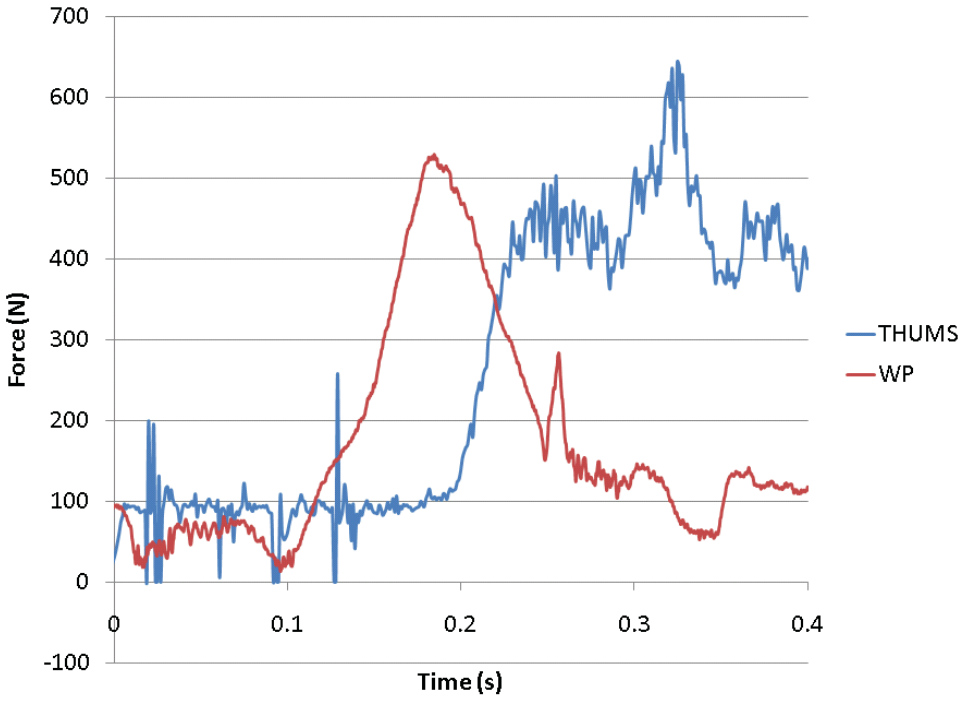

Figure 64: Pulse 8208, Crotch belt force.

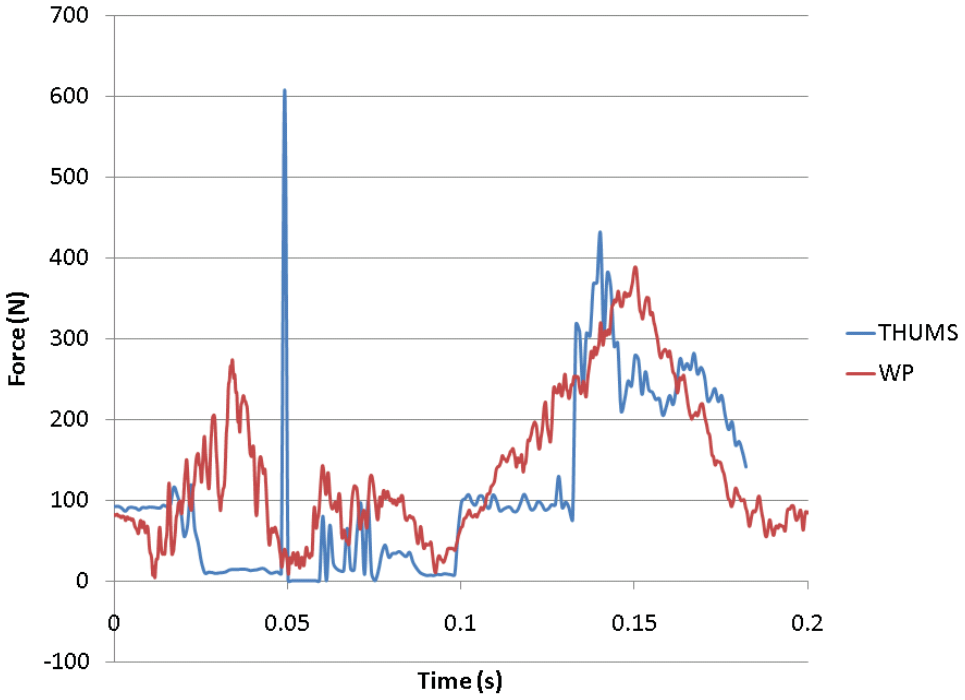

Figure 65: Pulse 8212, Left shoulder belt force.

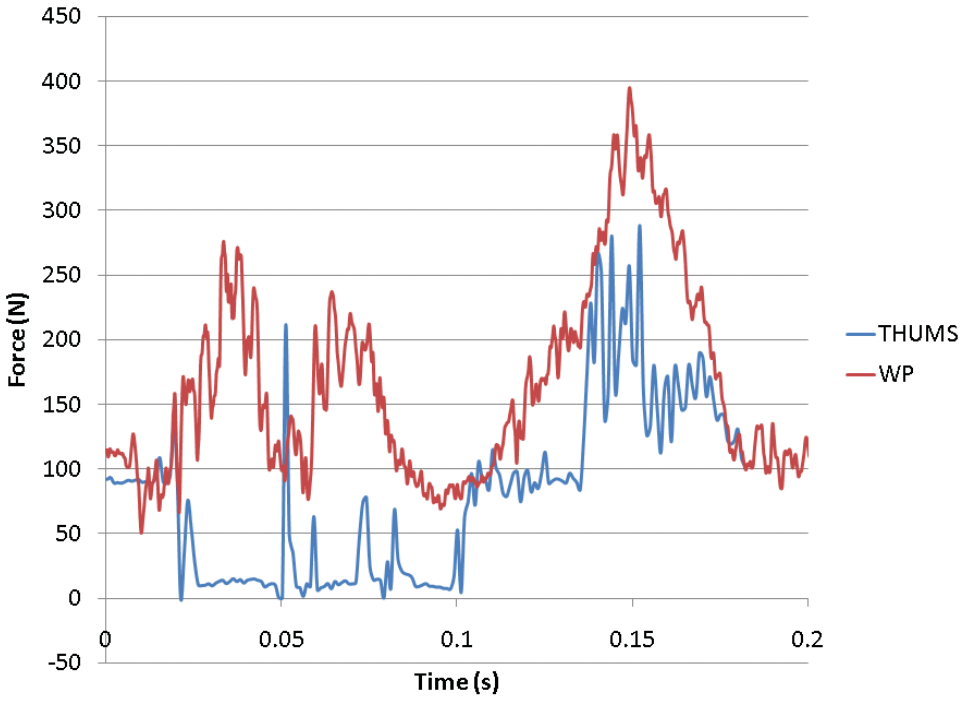

Figure 66: Pulse 8212, Right shoulder belt force.

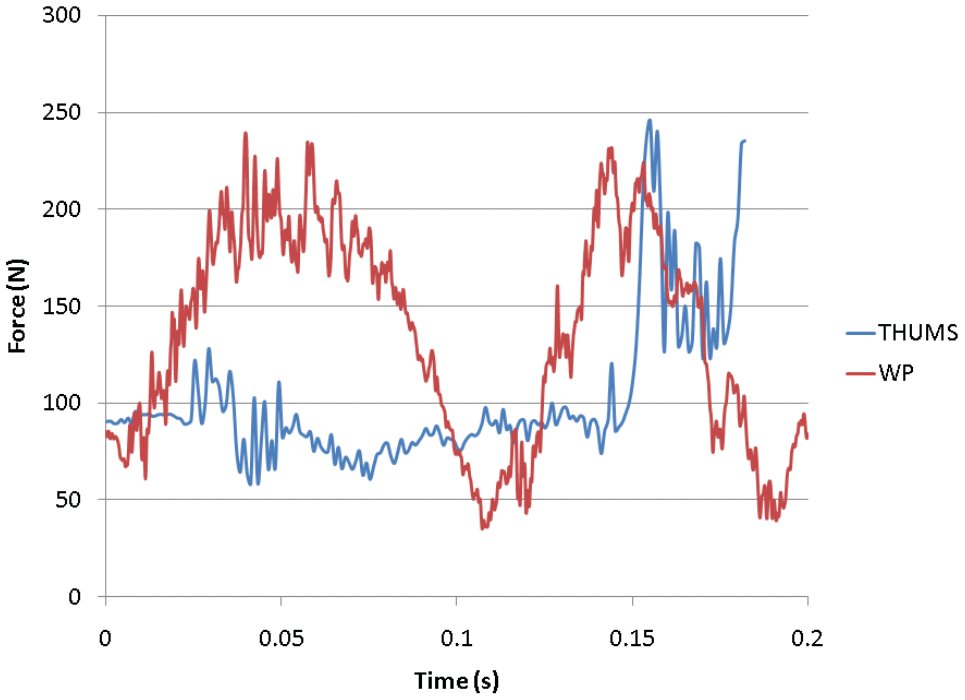

Figure 67: Pulse 8212, Left lap belt force.

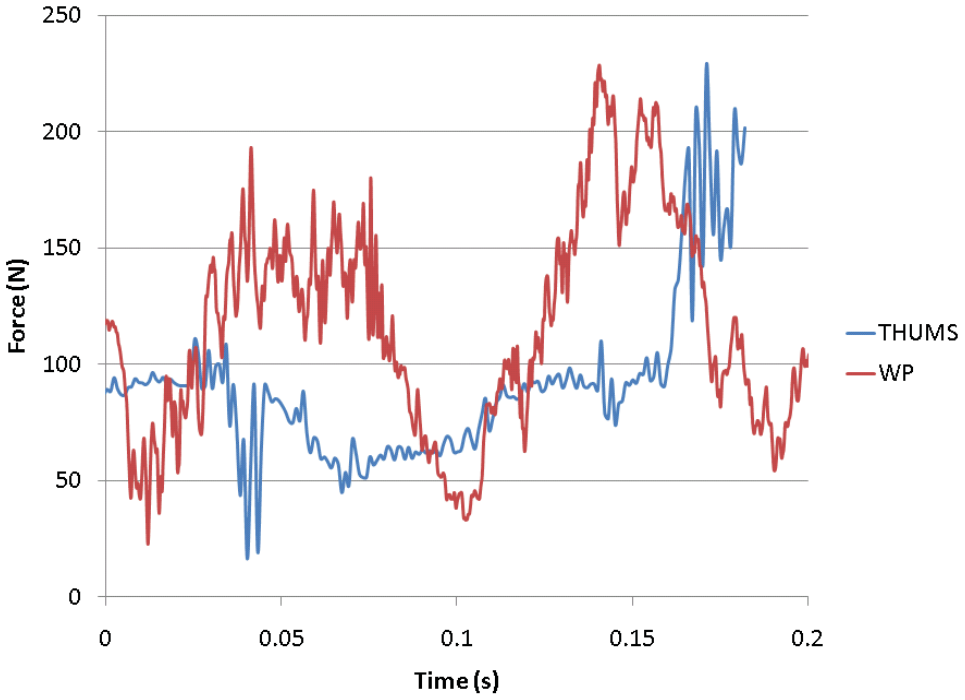

Figure 68: Pulse 8212, Right lap belt force.

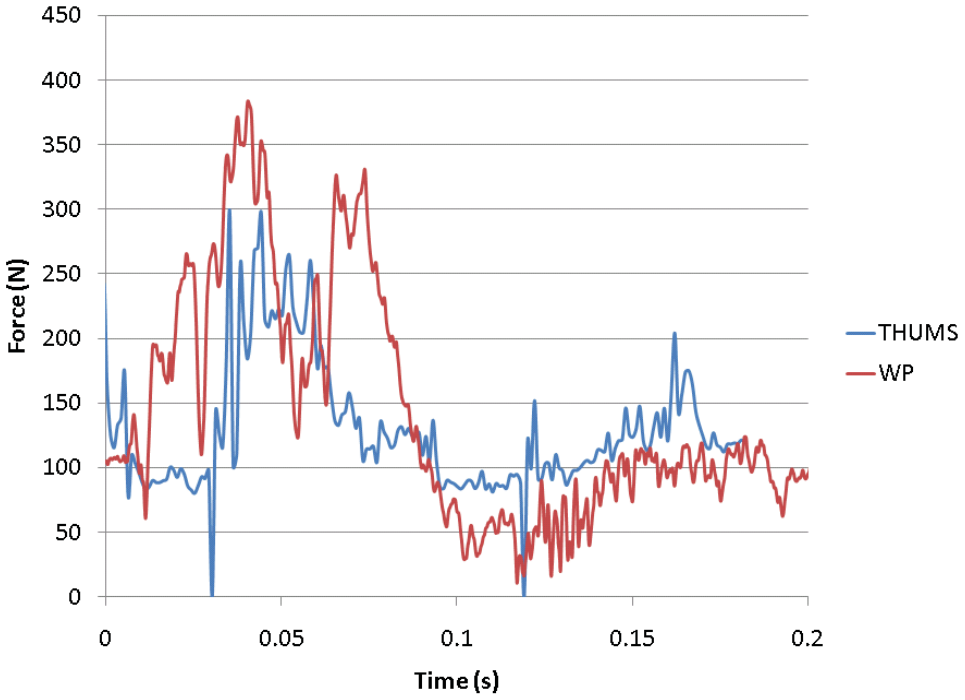

Figure 69: Pulse 8212, Crotch belt force.

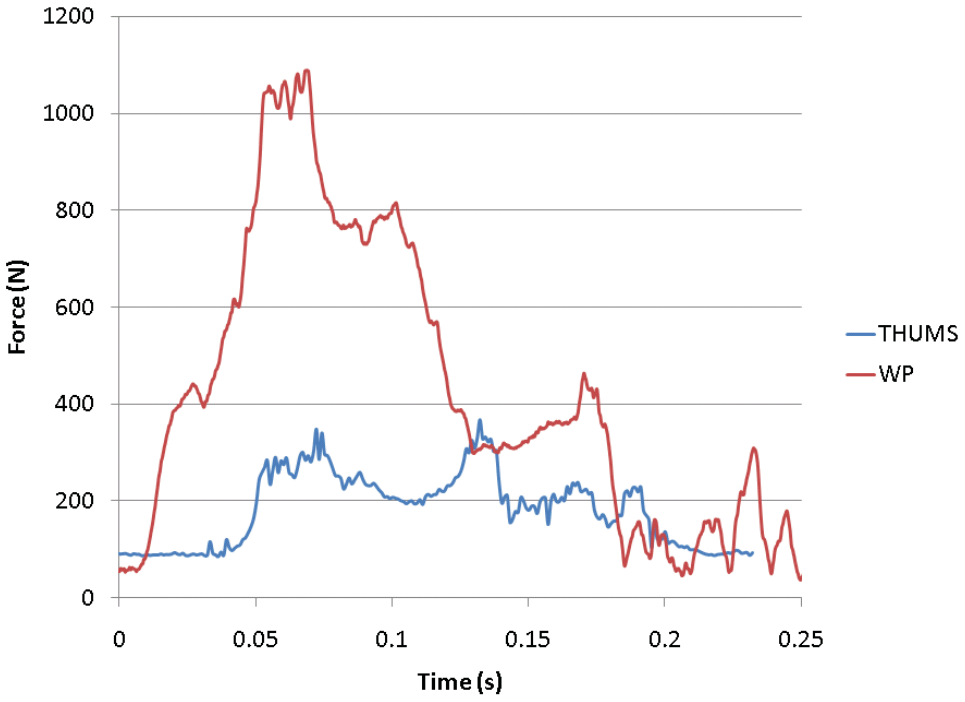

Figure 70: Pulse 8245, Left shoulder belt force.

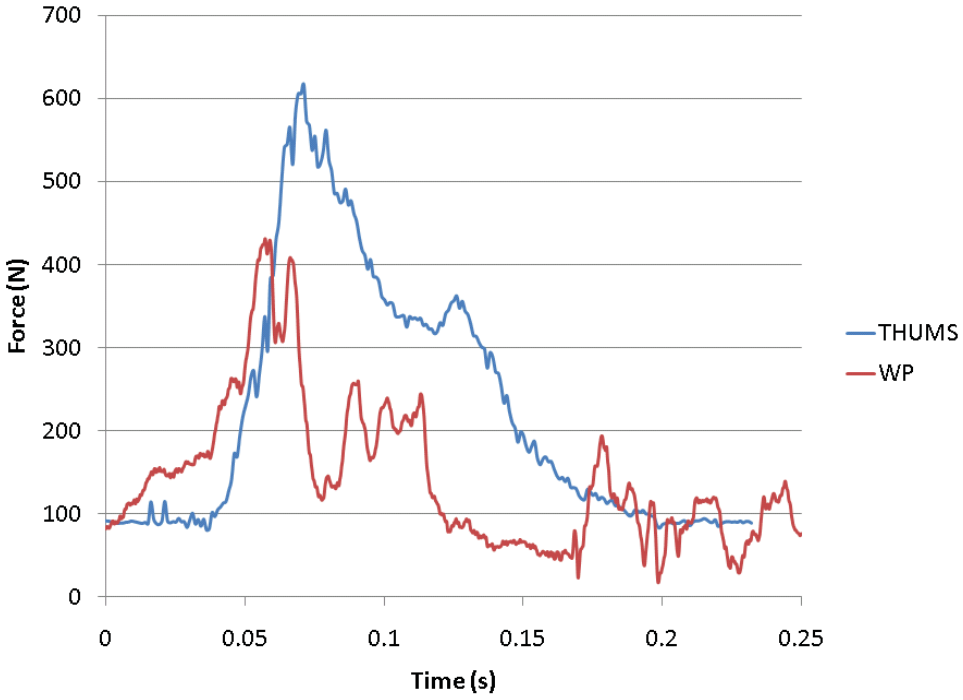

Figure 71: Pulse 8245, Right shoulder belt force.

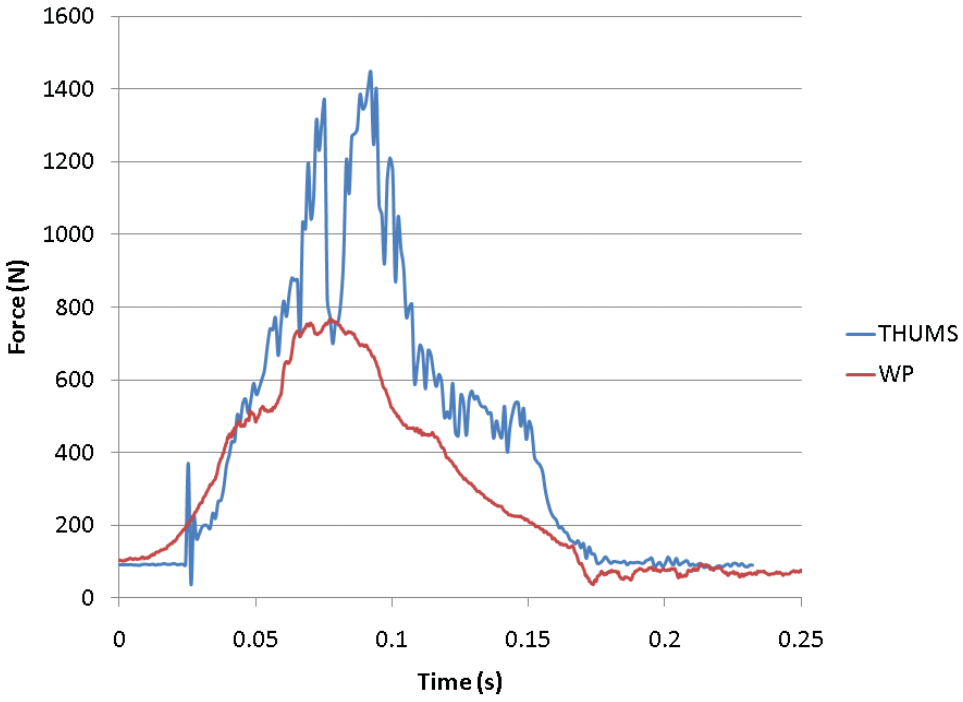

Figure 72: Pulse 8245, Left lap belt force.

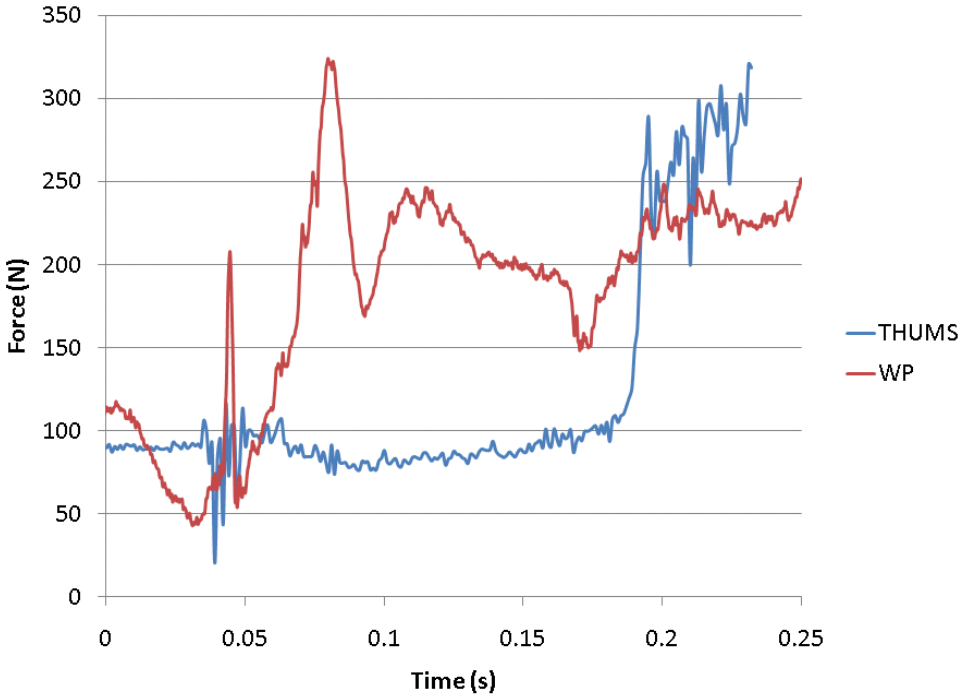

Figure 73: Pulse 8245, Right lap belt force.

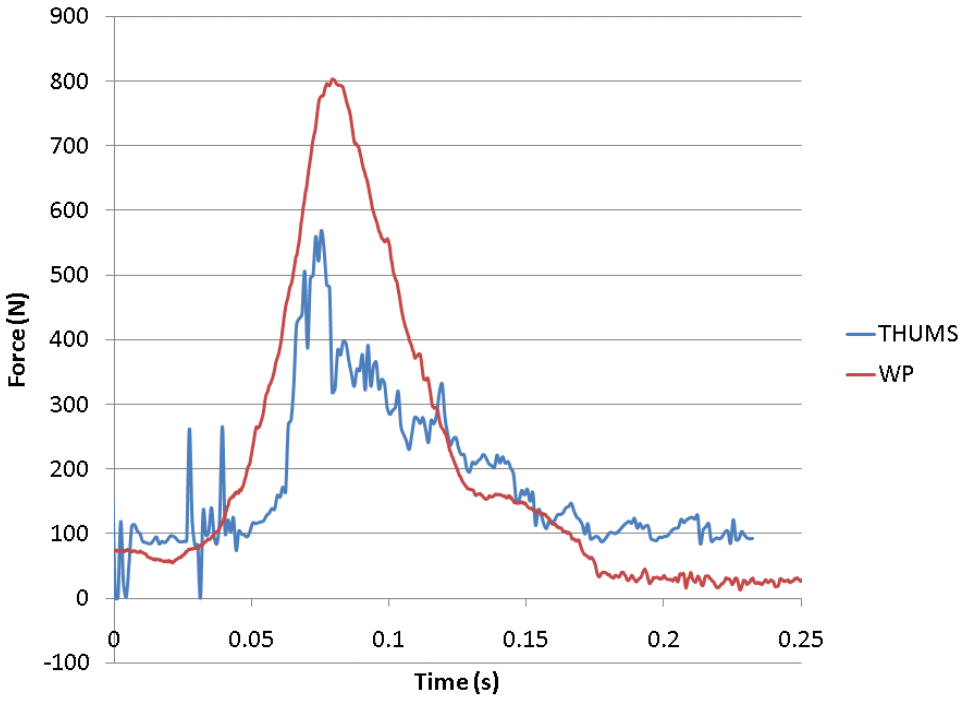

Figure 74: Pulse 8245, Crotch belt force.

Appendix 4: Head Injury, Peak Head Acceleration

Table 2: Tabulated Head Acceleration

Simulation	Head Acceleration (g's)
8202, Frontal, Short pulse	16.741
8202, Frontal, Long pulse	17.642
8208, Spinal, Short pulse, X-axis gravity	14.354
8208, Spinal, Short pulse, Z-axis gravity	14.092
8208, Spinal, Long pulse, X-axis gravity	48.717
8212, Rear, Short pulse	29.044
8212, Rear, Long pulse	29.364
8245, Lateral, Short pulse	50.870
8245, Lateral, Long pulse	72.384

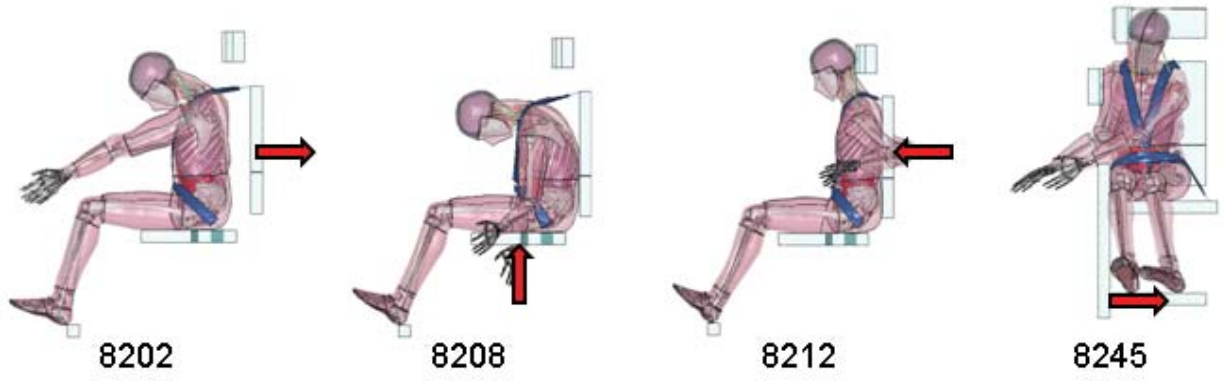

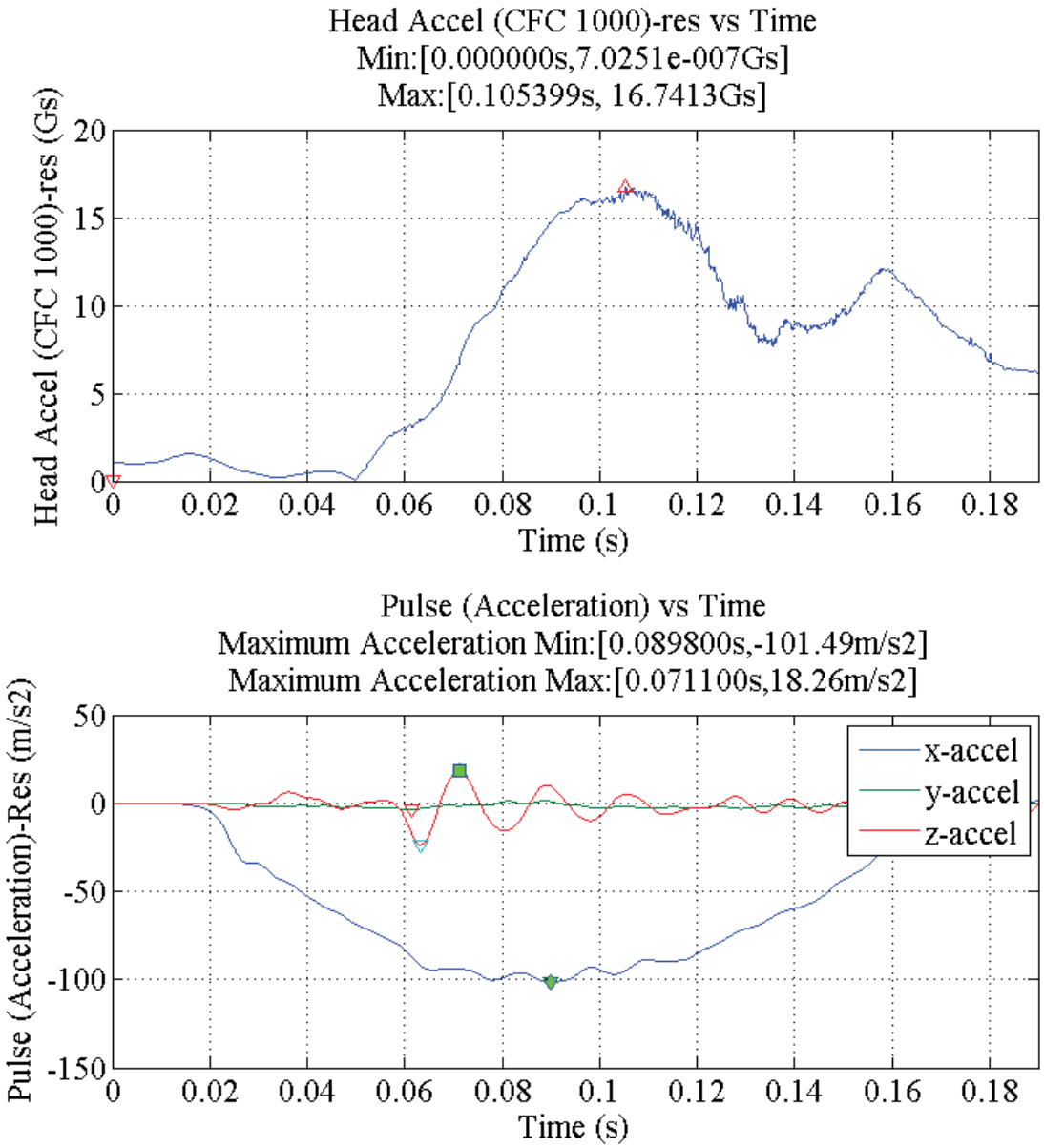

Figure 75: Head acceleration for simulation 8202 (Frontal), short pulse.

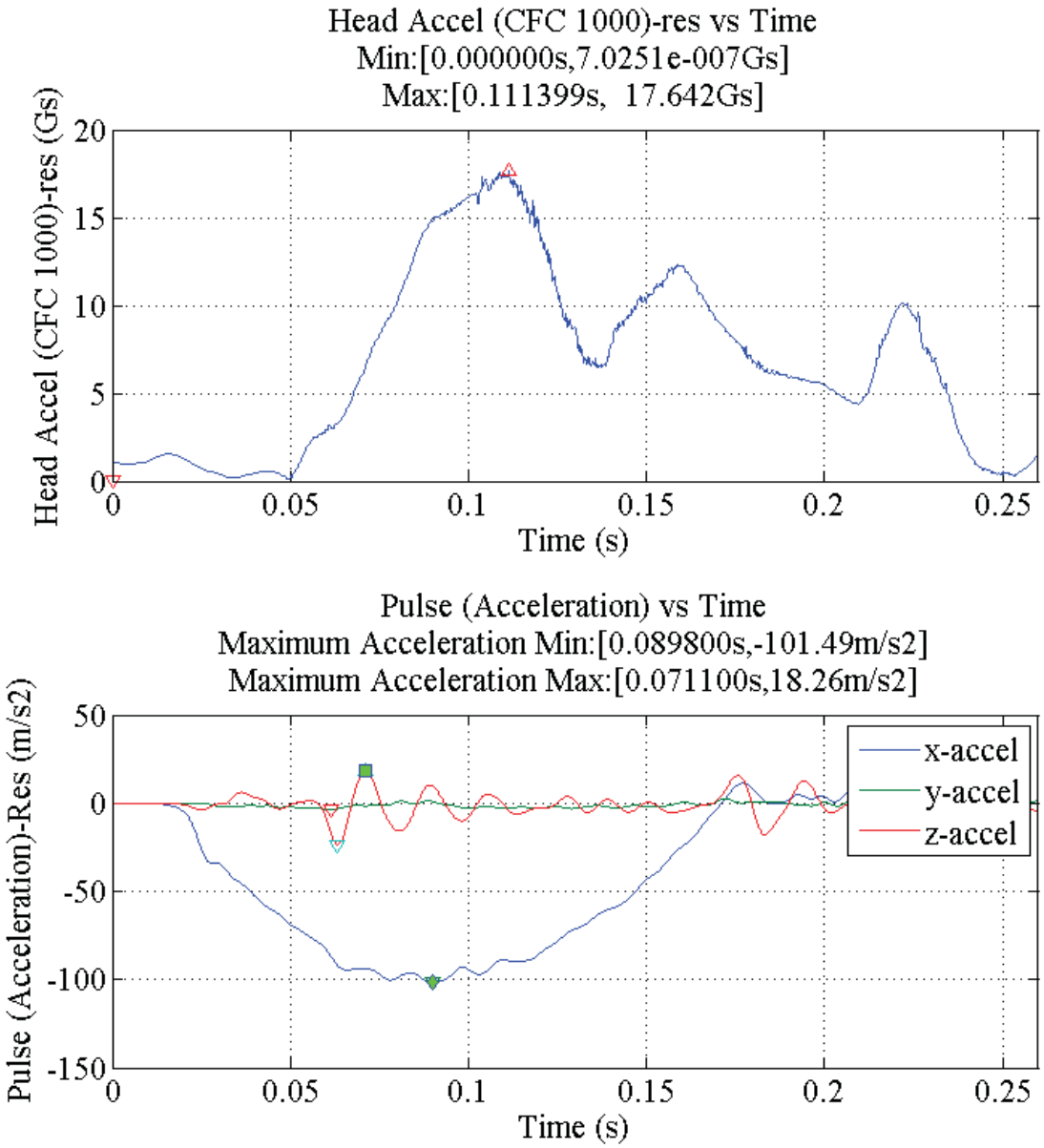

Figure 76: Head acceleration for simulation 8202 (Frontal), long pulse.

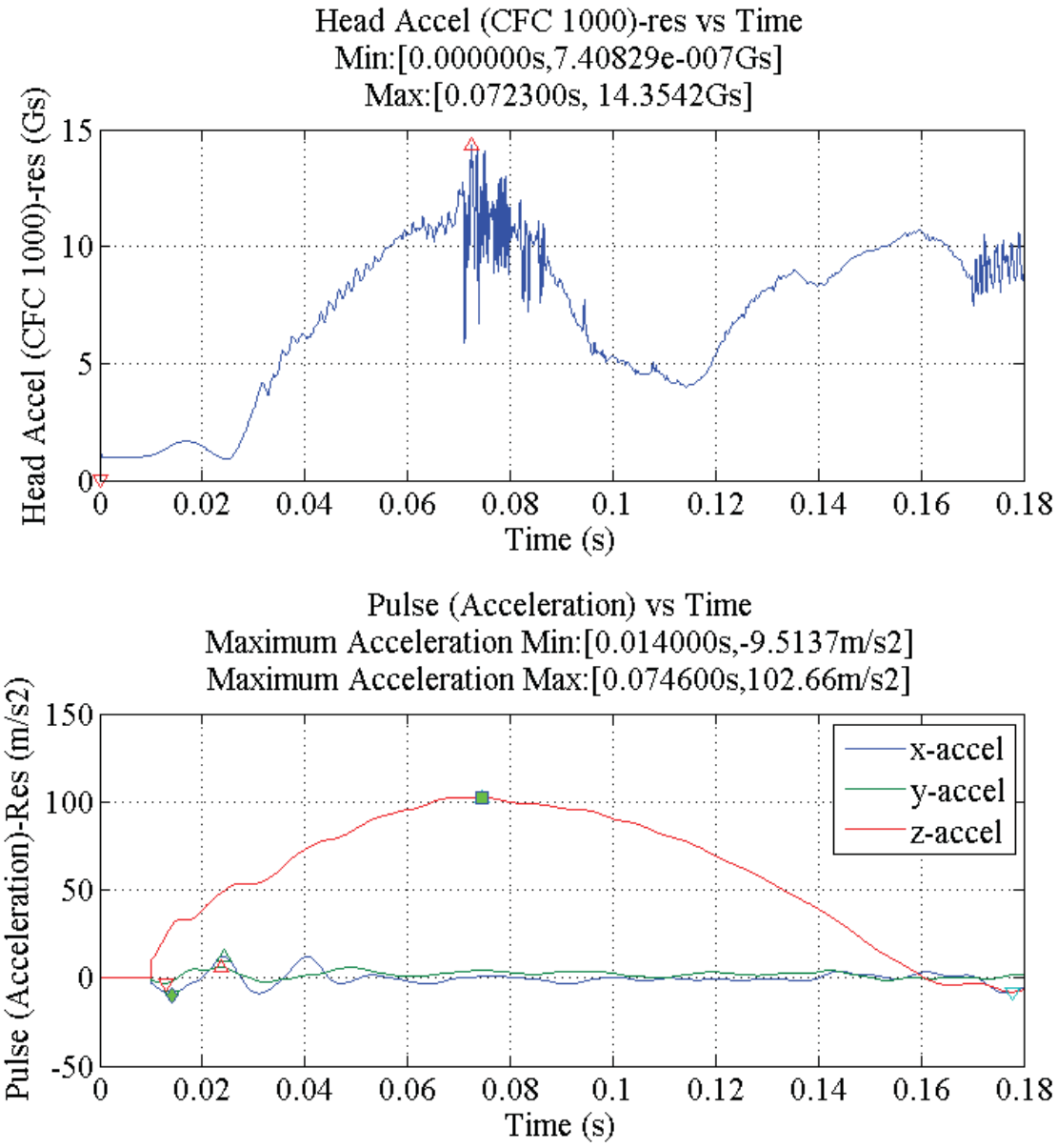

Figure 77: Head acceleration for simulation 8208 (Spinal), short pulse, X-axis gravity.

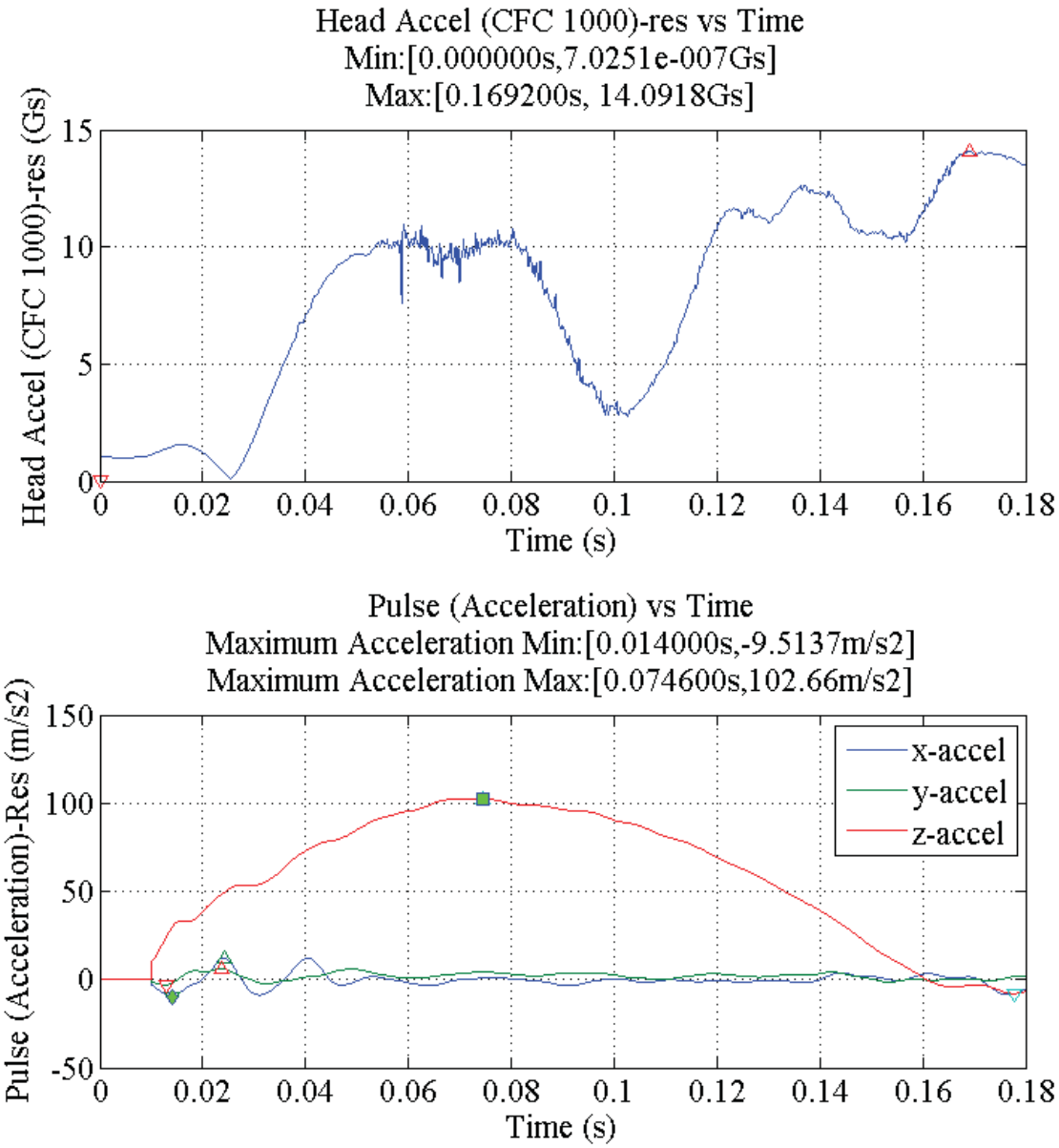

Figure 78: Head acceleration for simulation 8208 (Spinal), short pulse, Z-axis gravity.

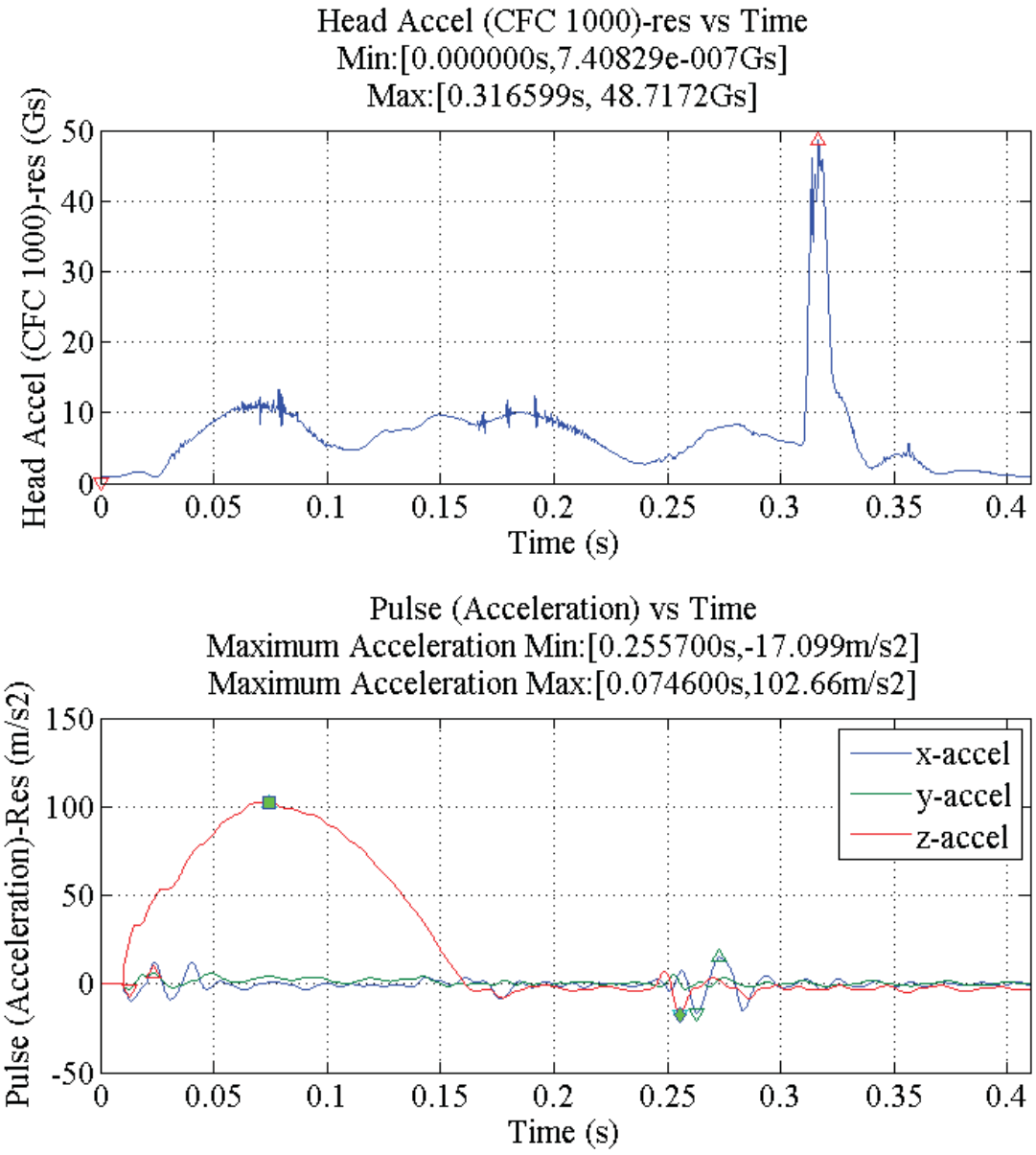

Figure 79: Head acceleration for simulation 8208 (Spinal), long pulse, X-axis gravity.

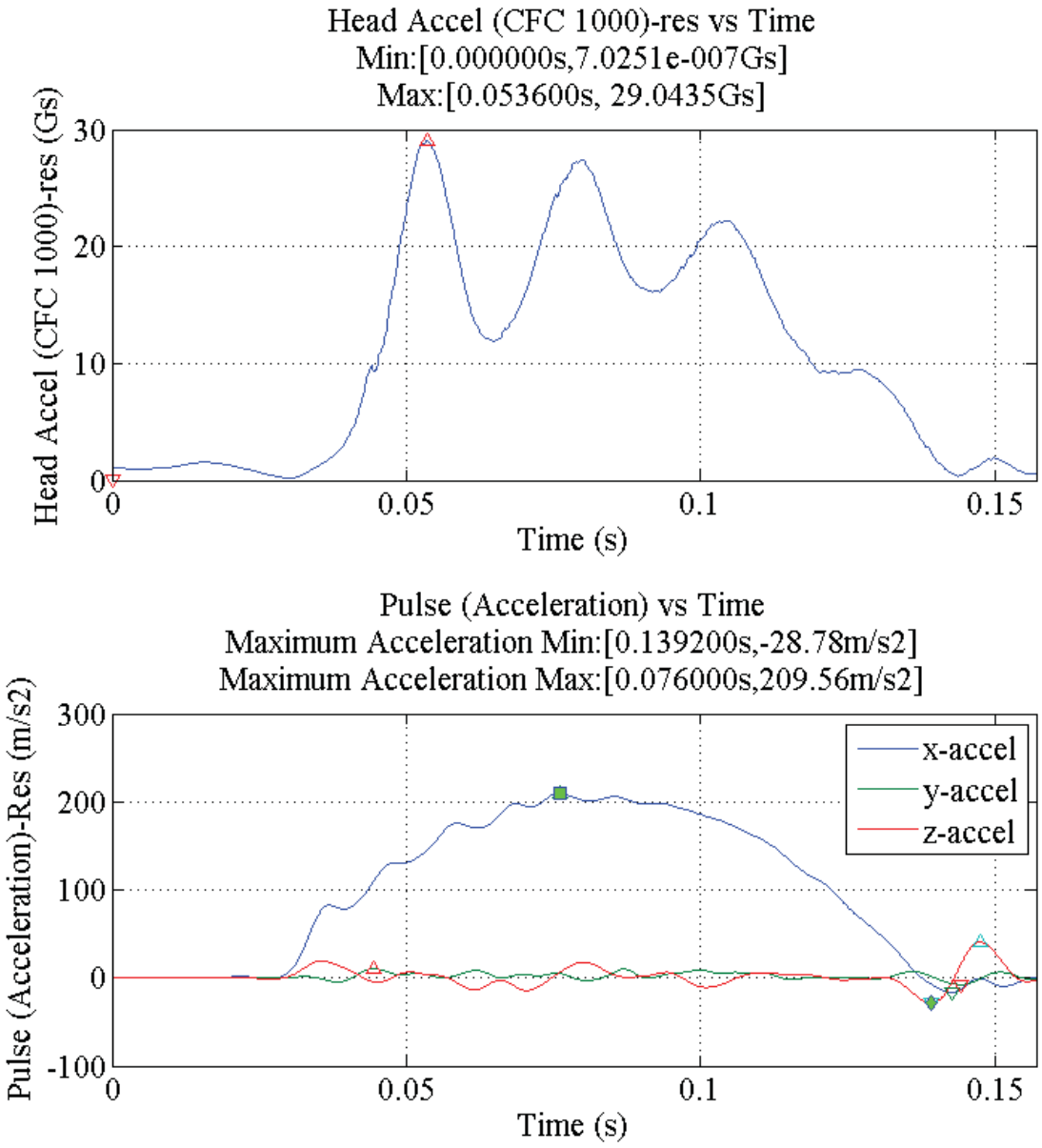

Figure 80: Head acceleration for simulation 8212 (Rear), short pulse.

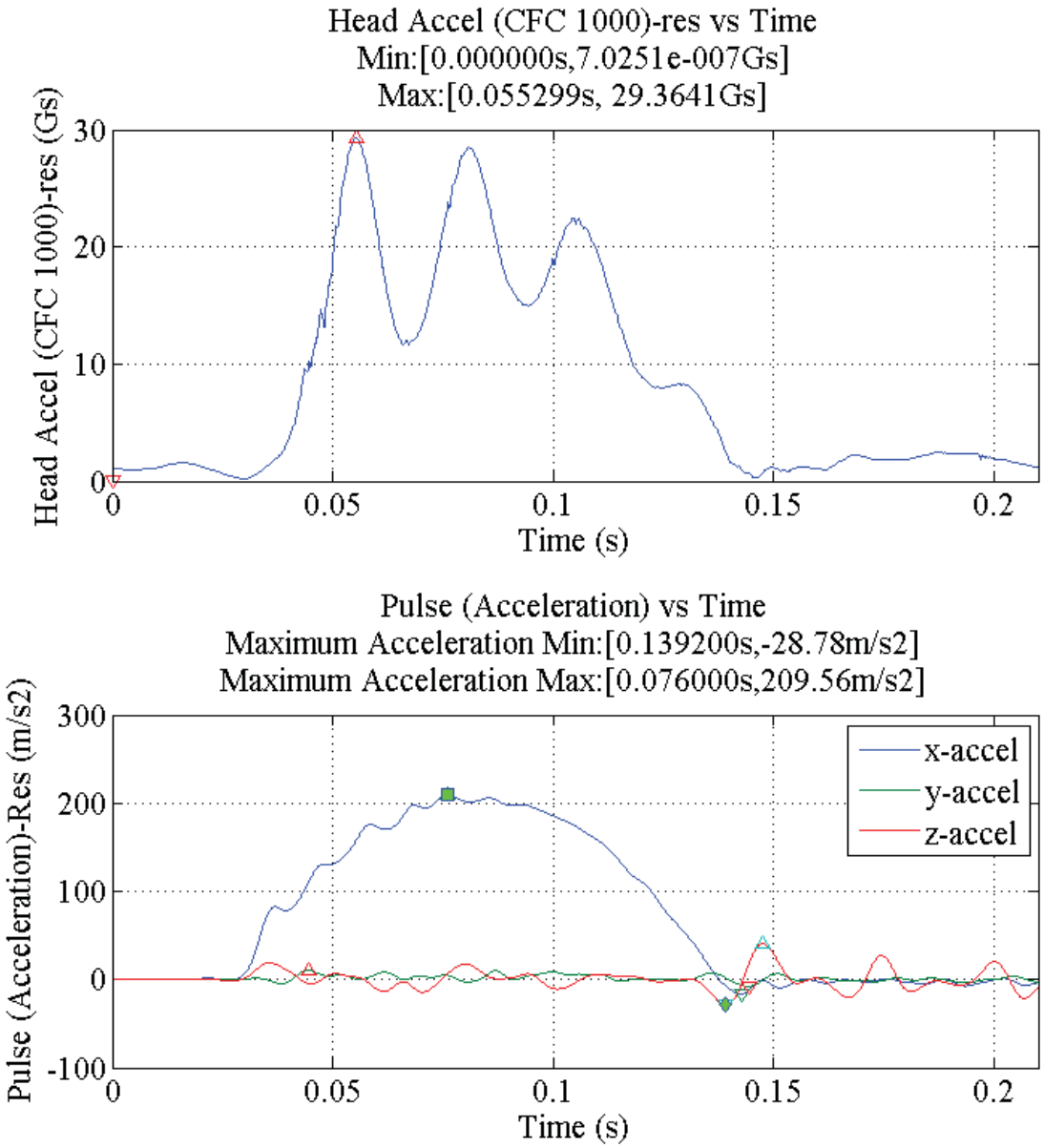

Figure 81: Head acceleration for simulation 8212 (Rear), long pulse.

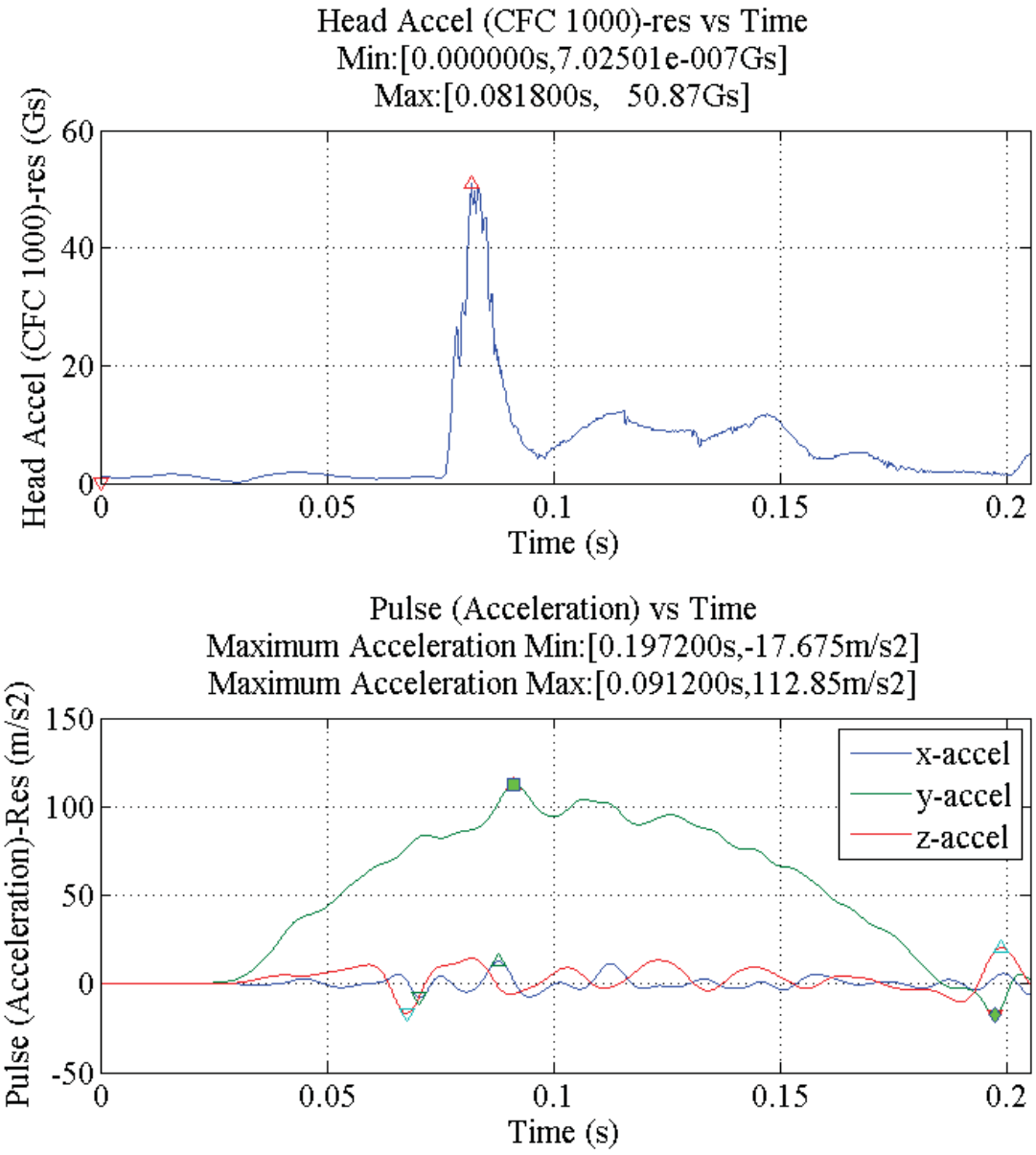

Figure 82: Head acceleration for simulation 8245 (Lateral), short pulse.

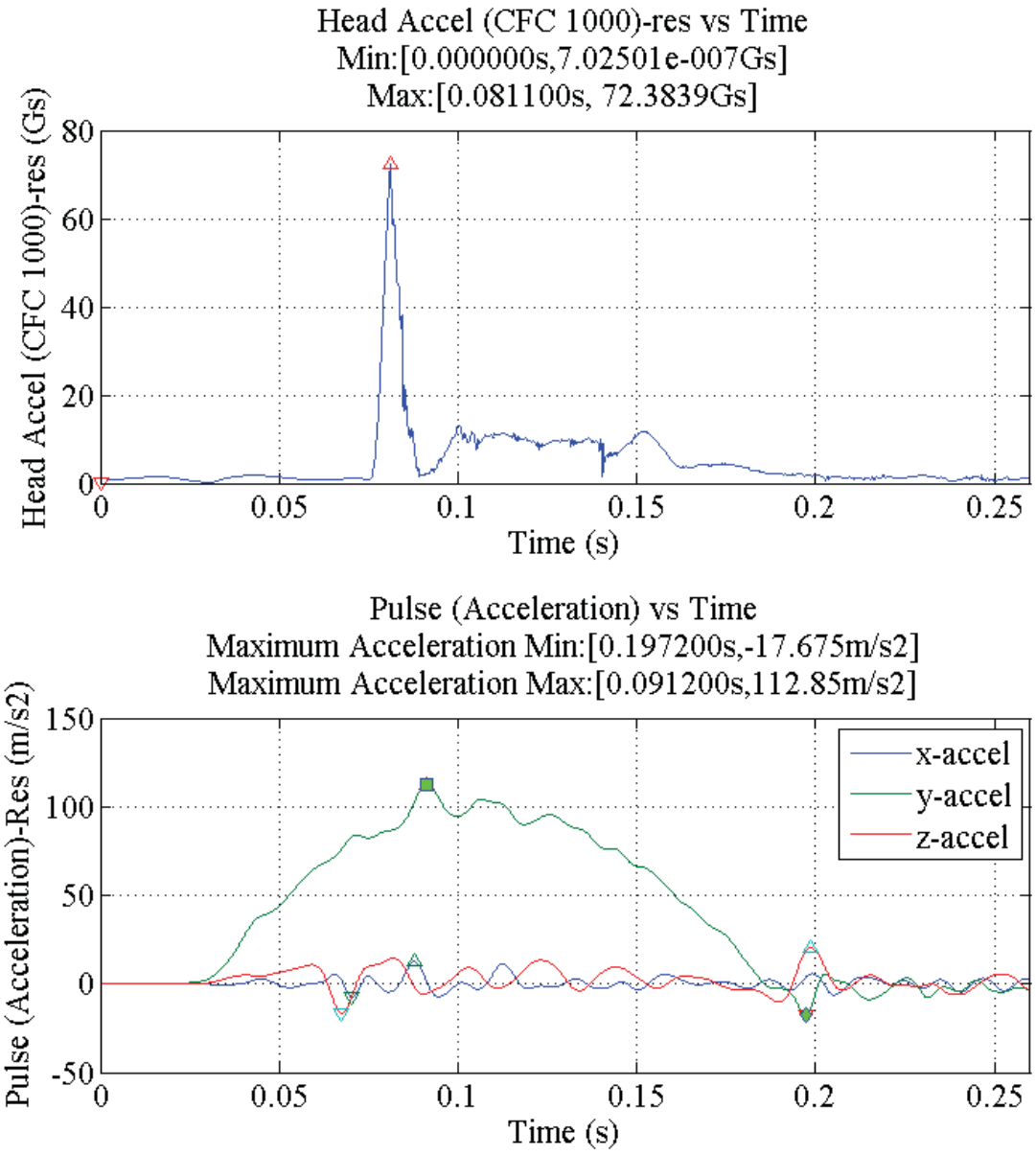

Figure 83: Head acceleration for simulation 8245 (Lateral), long pulse.

Appendix 5: Head Injury, HIC_{15}

Table 3: Tabulated HIC_{15}

Simulation	HIC_{15}
8202, Frontal, Short pulse	15.744
8202, Frontal, Long pulse	17.491
8208, Spinal, Short pulse, X-axis gravity	6.189
8208, Spinal, Short pulse, Z-axis gravity	10.710
8208, Spinal, Long pulse, X-axis gravity	90.686
8212, Rear, Short pulse	41.754
8212, Rear, Long pulse	44.311
8245, Lateral, Short pulse	75.980
8245, Lateral, Long pulse	112.474

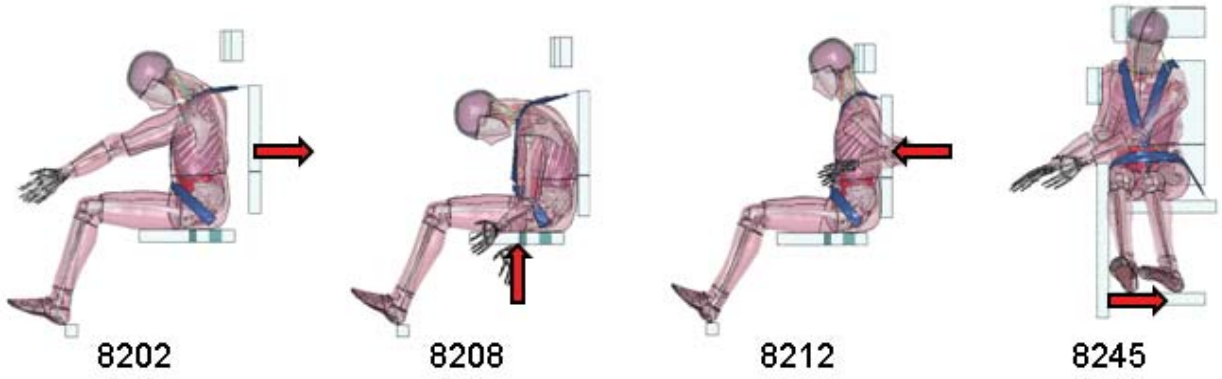

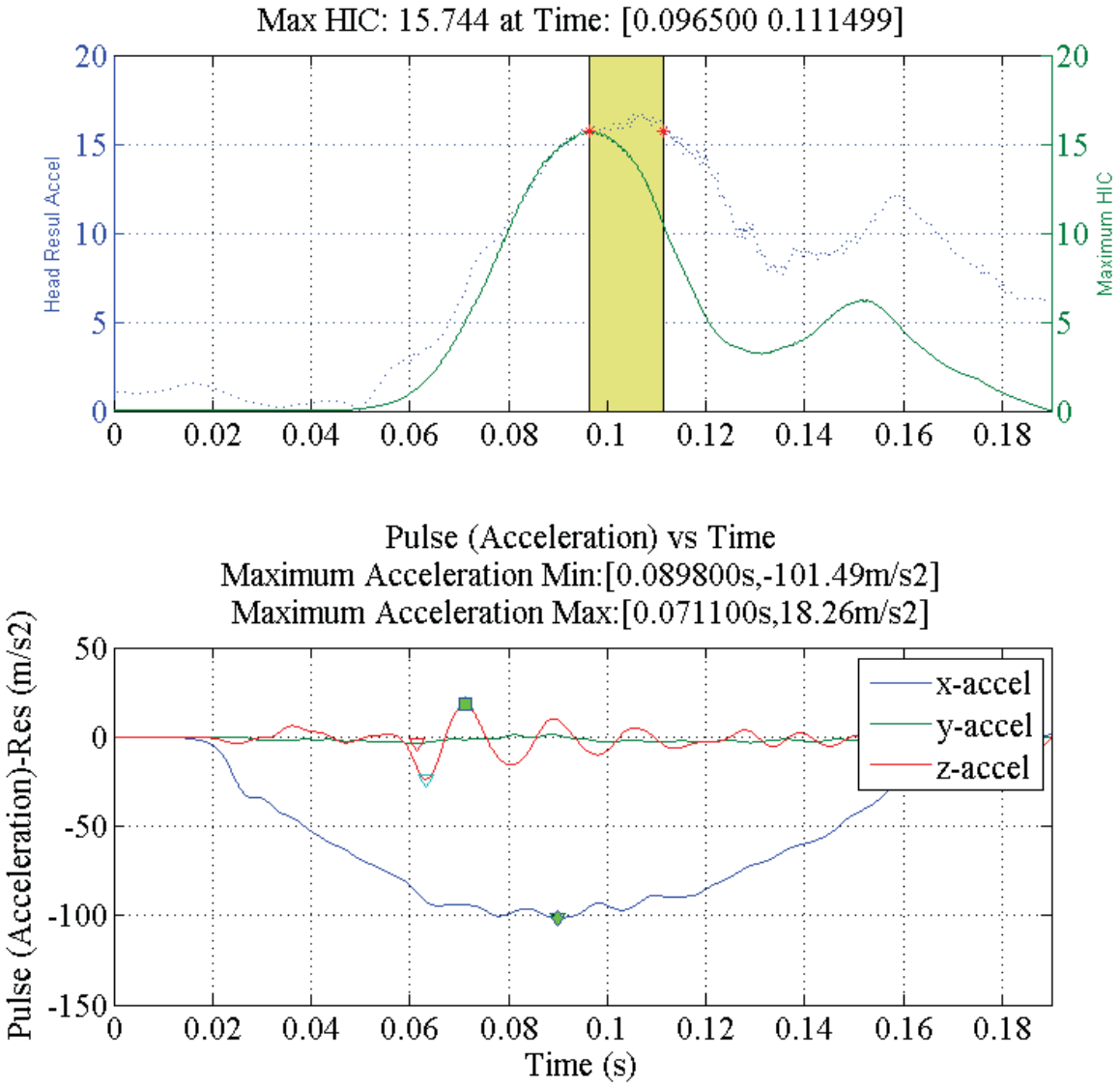

Figure 84: HIC_{15} for simulation 8202 (Frontal), short pulse.

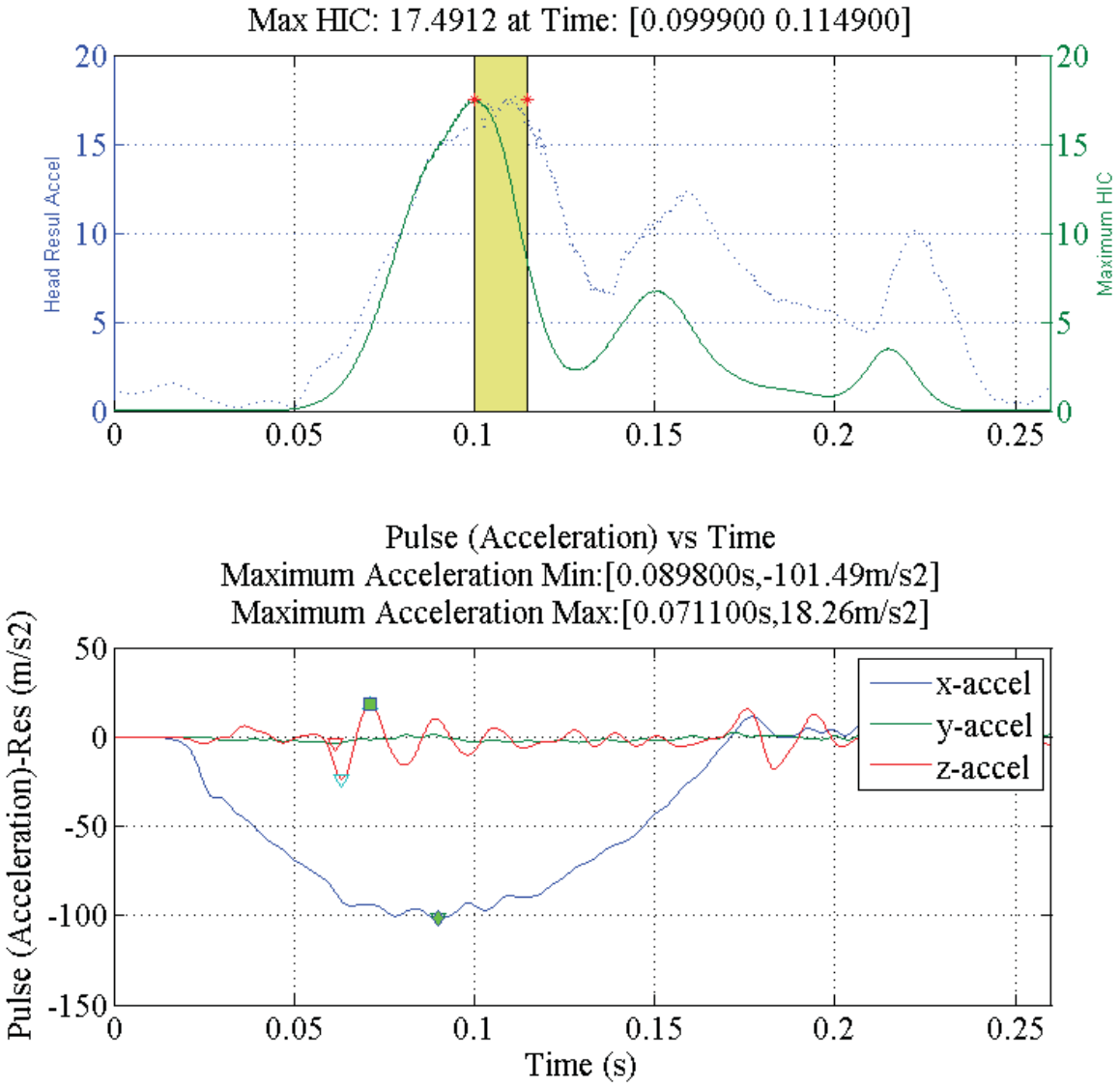

Figure 85: HIC_{15} for simulation 8202 (Frontal), long pulse.

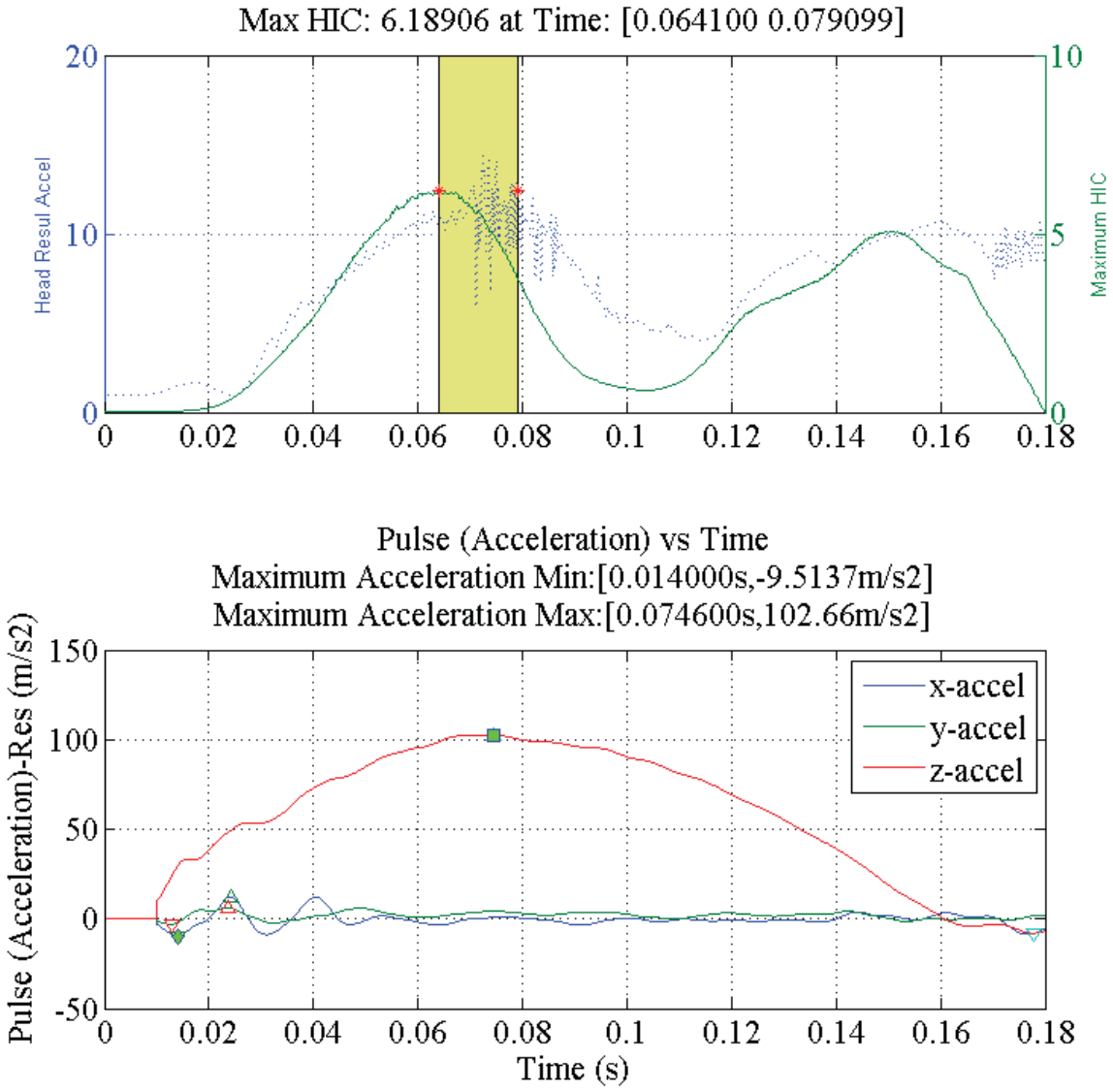

Figure 86: HIC_{15} for simulation 8208 (Spinal), short pulse, X-axis gravity.

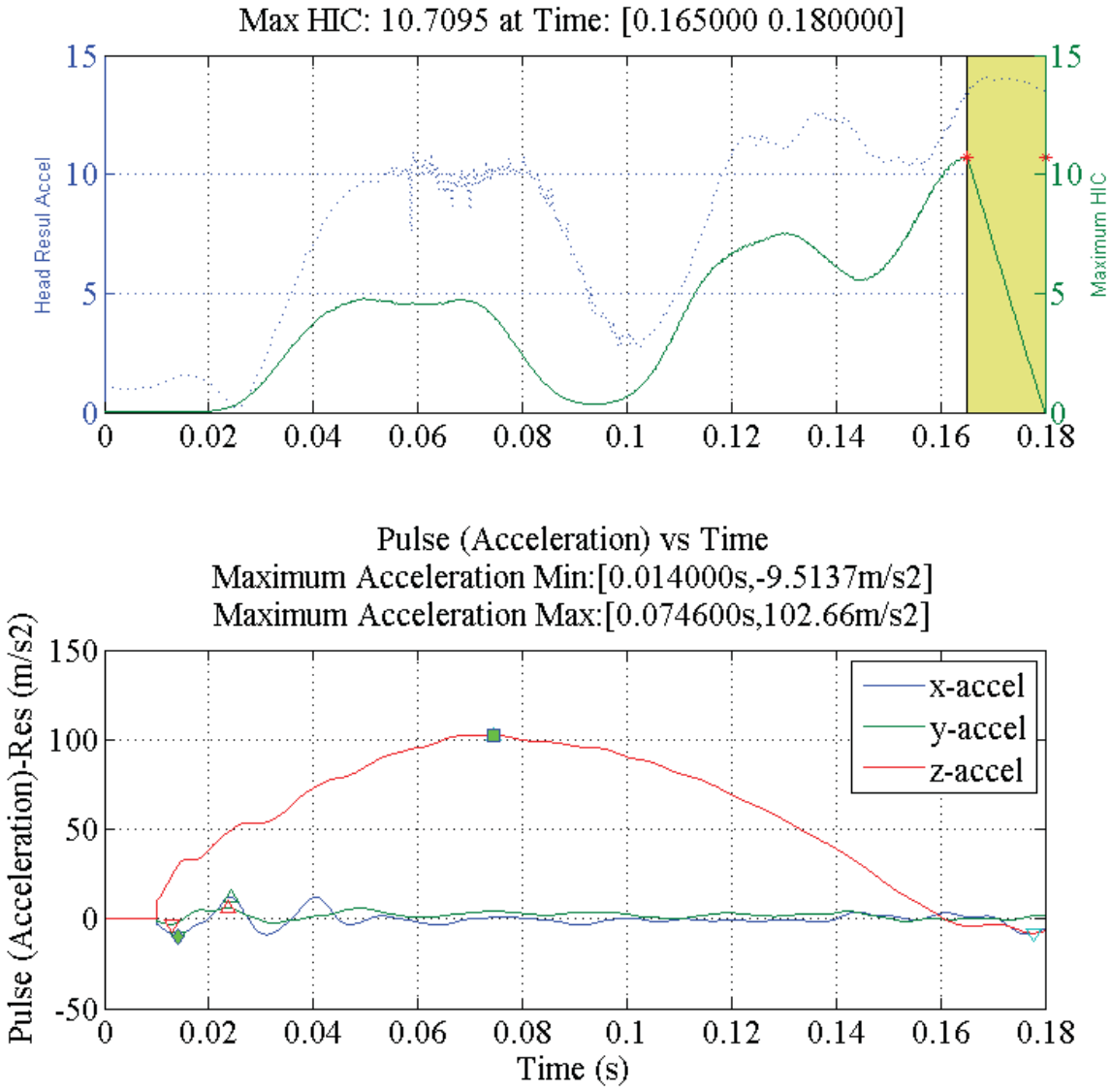

Figure 87: HIC_{15} for simulation 8208 (Spinal), short pulse, Z-axis gravity.

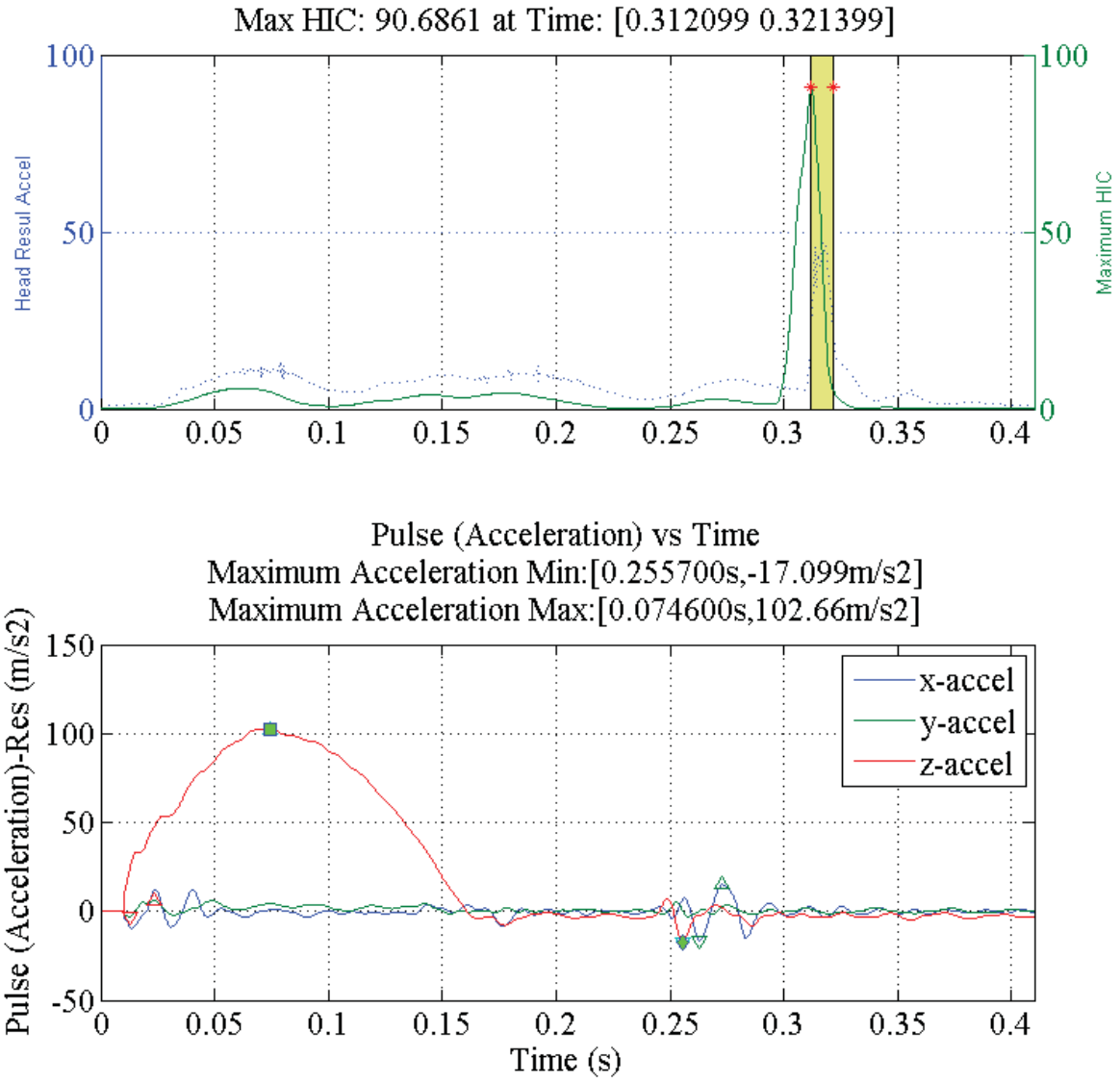

Figure 88: HIC_{15} for simulation 8208 (Spinal), long pulse, X-axis gravity

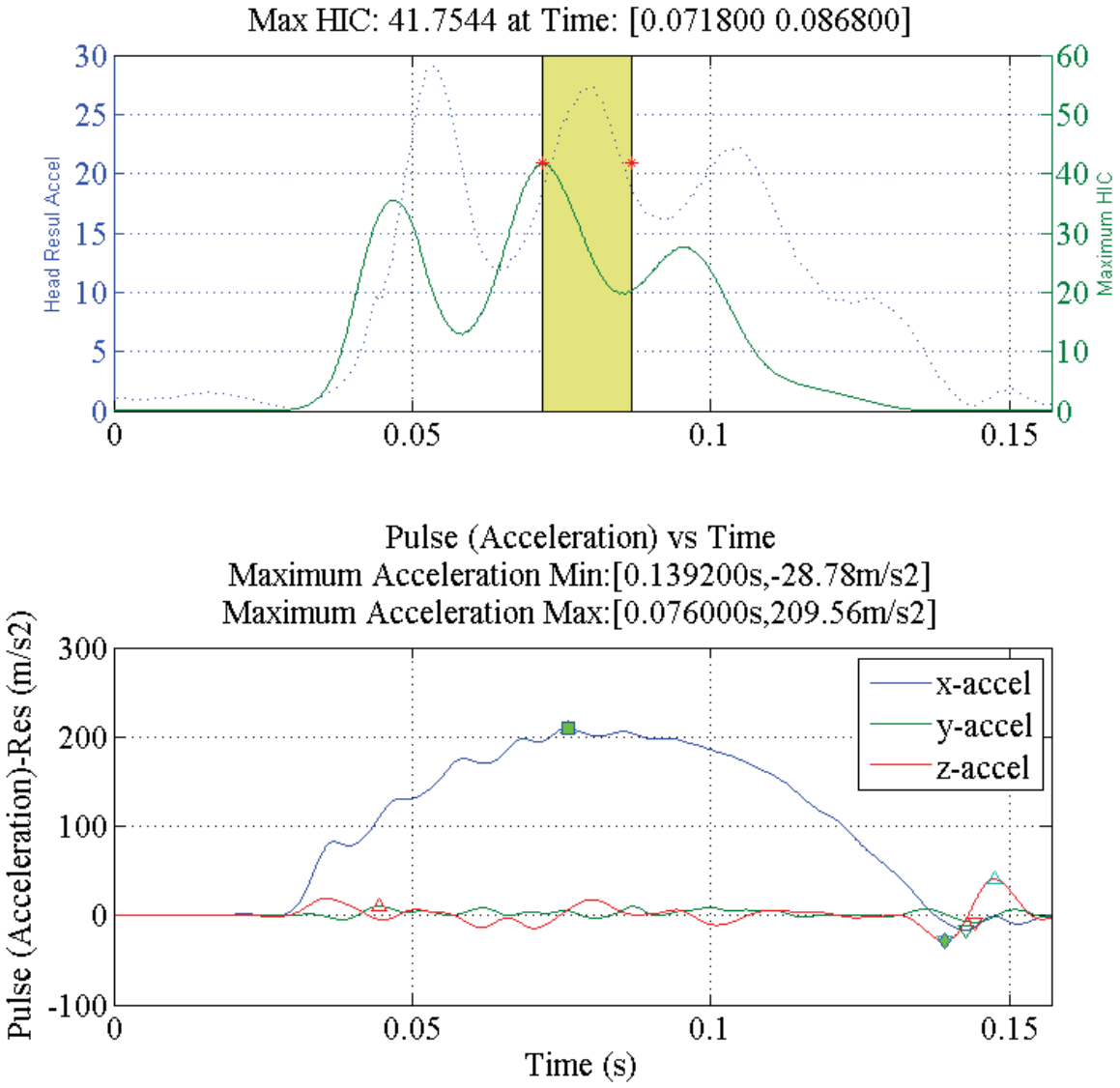

Figure 89: HIC_{15} for simulation 8212 (Rear), short pulse.

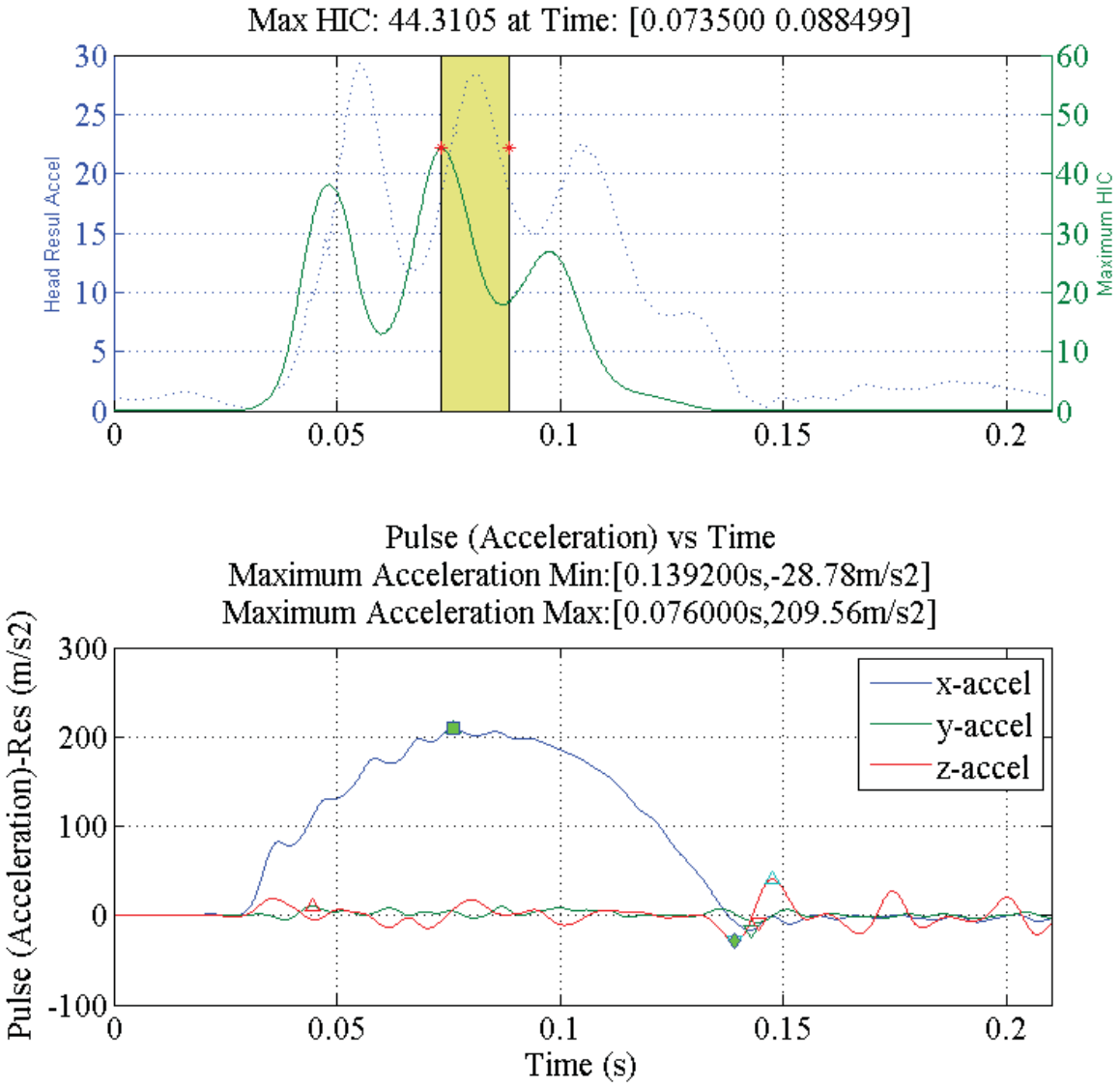

Figure 90: HIC_{15} for simulation 8212 (Rear), long pulse.

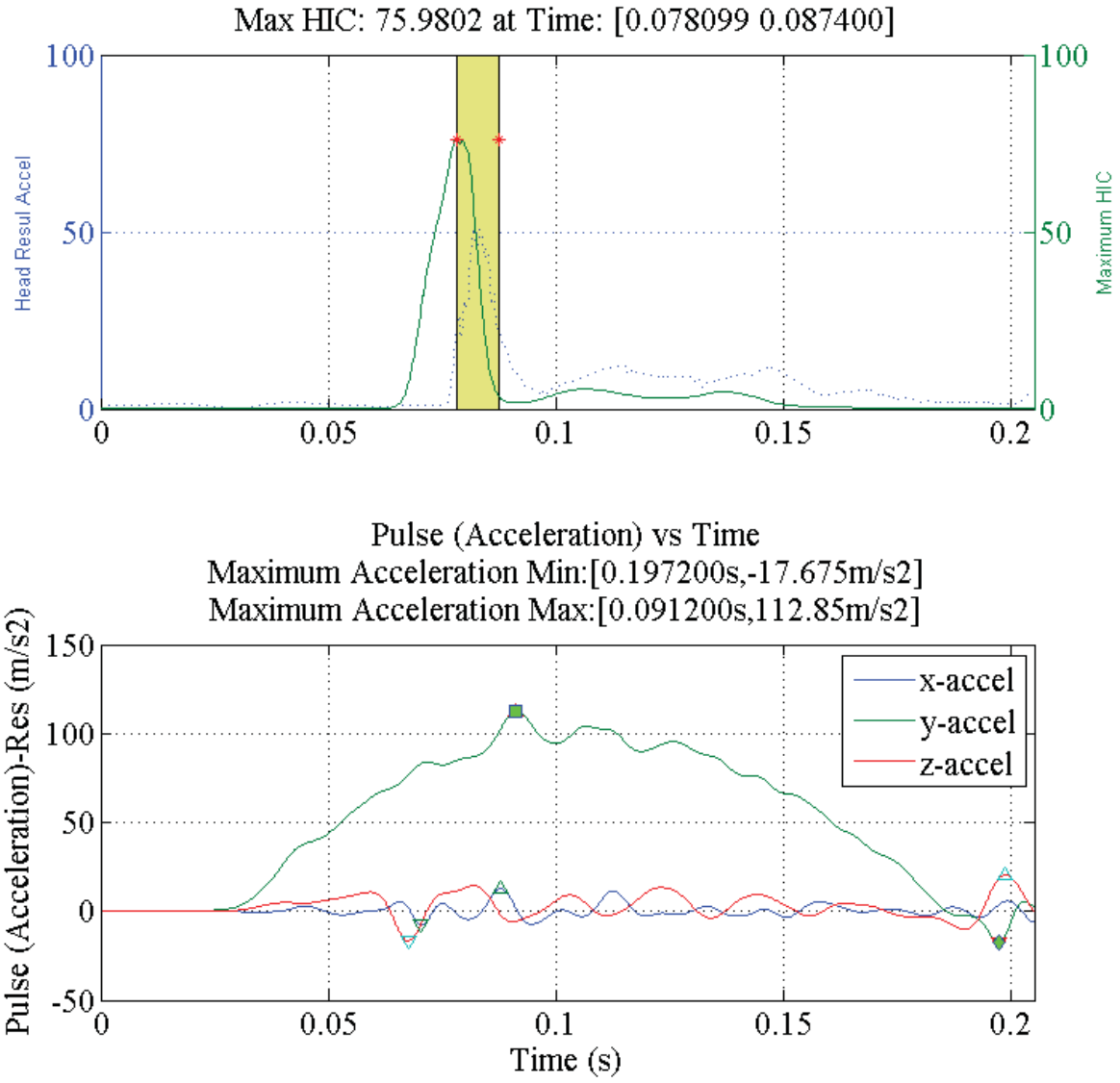

Figure 91: HIC_{15} for simulation 8245 (Lateral), short pulse.

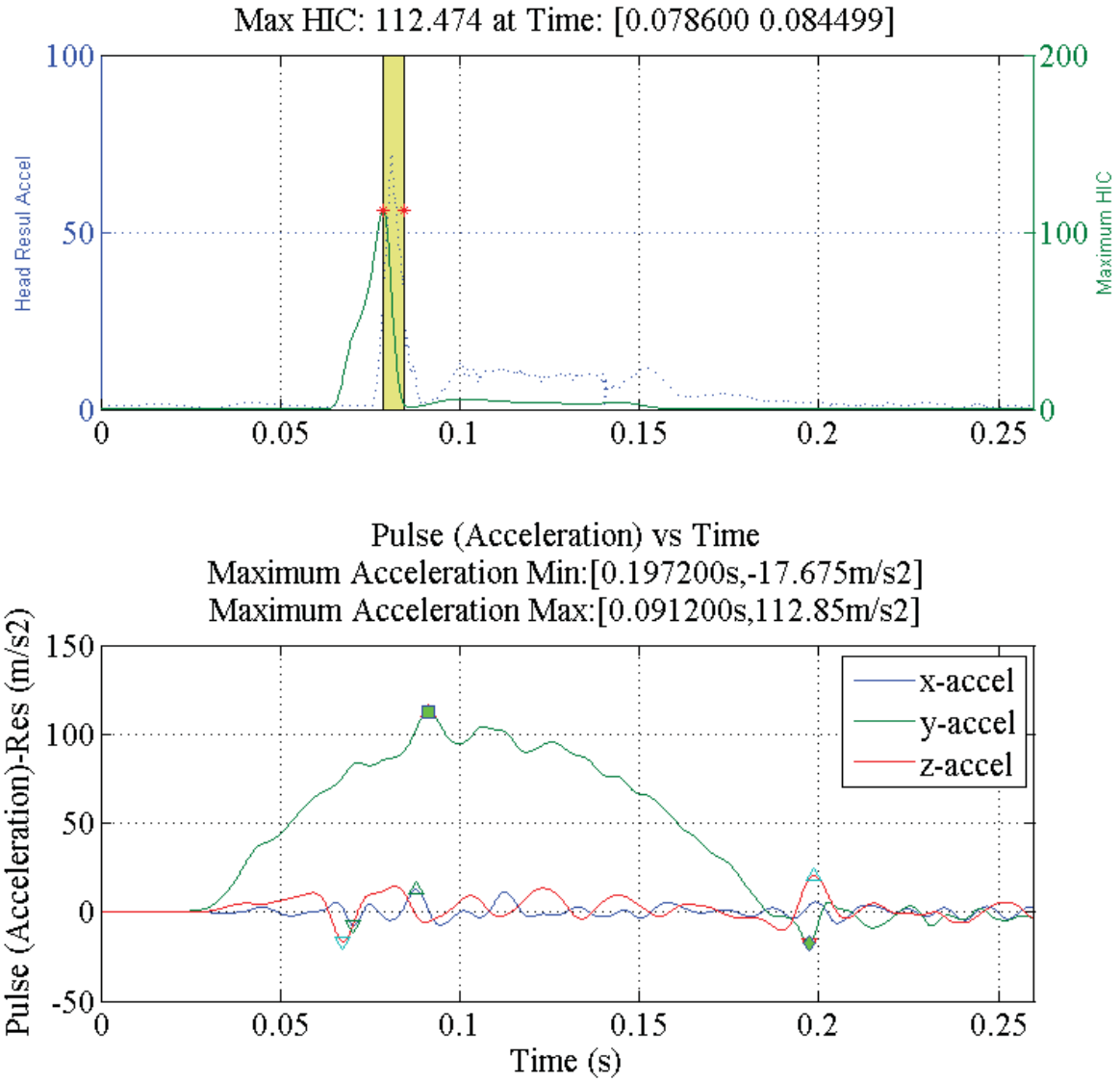

Figure 92: HIC_{15} for simulation 8245 (Lateral), long pulse.

Appendix 6: Head Injury, HIC_{36}

Table 4: Tabulated HIC_{36}

Simulation	HIC_{36}
8202, Frontal, Short pulse	33.123
8202, Frontal, Long pulse	35.641
8208, Spinal, Short pulse, X-axis gravity	12.967
8208, Spinal, Short pulse, Z-axis gravity	18.964
8208, Spinal, Long pulse, X-axis gravity	90.686
8212, Rear, Short pulse	73.255
8212, Rear, Long pulse	76.406
8245, Lateral, Short pulse	75.980
8245, Lateral, Long pulse	112.474

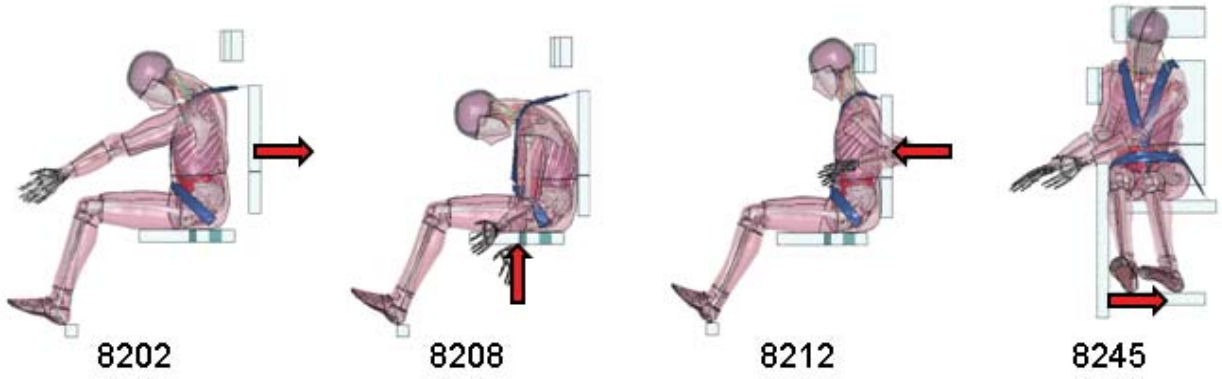

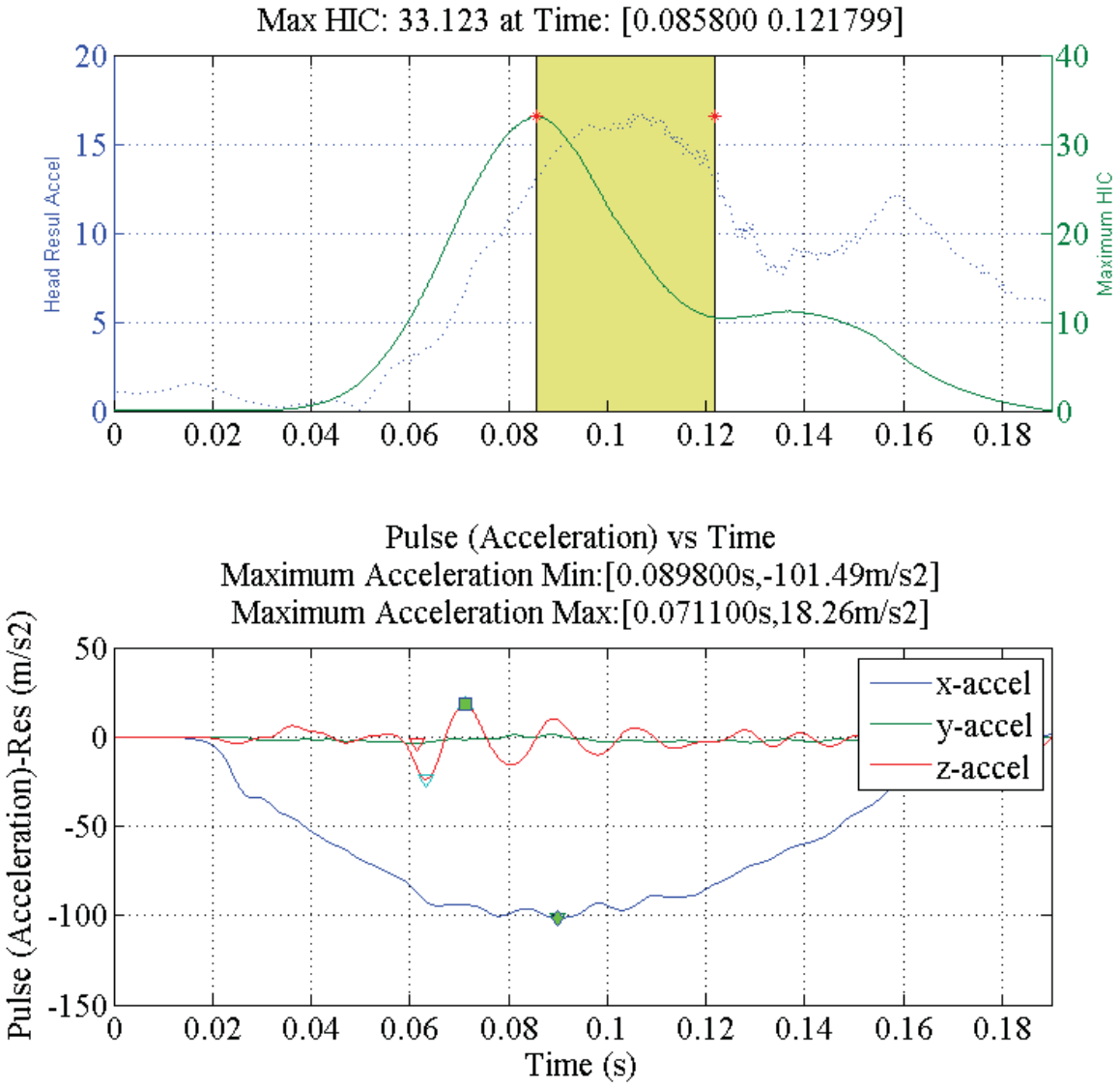

Figure 93: HIC_{36} for simulation 8202 (Frontal), short pulse.

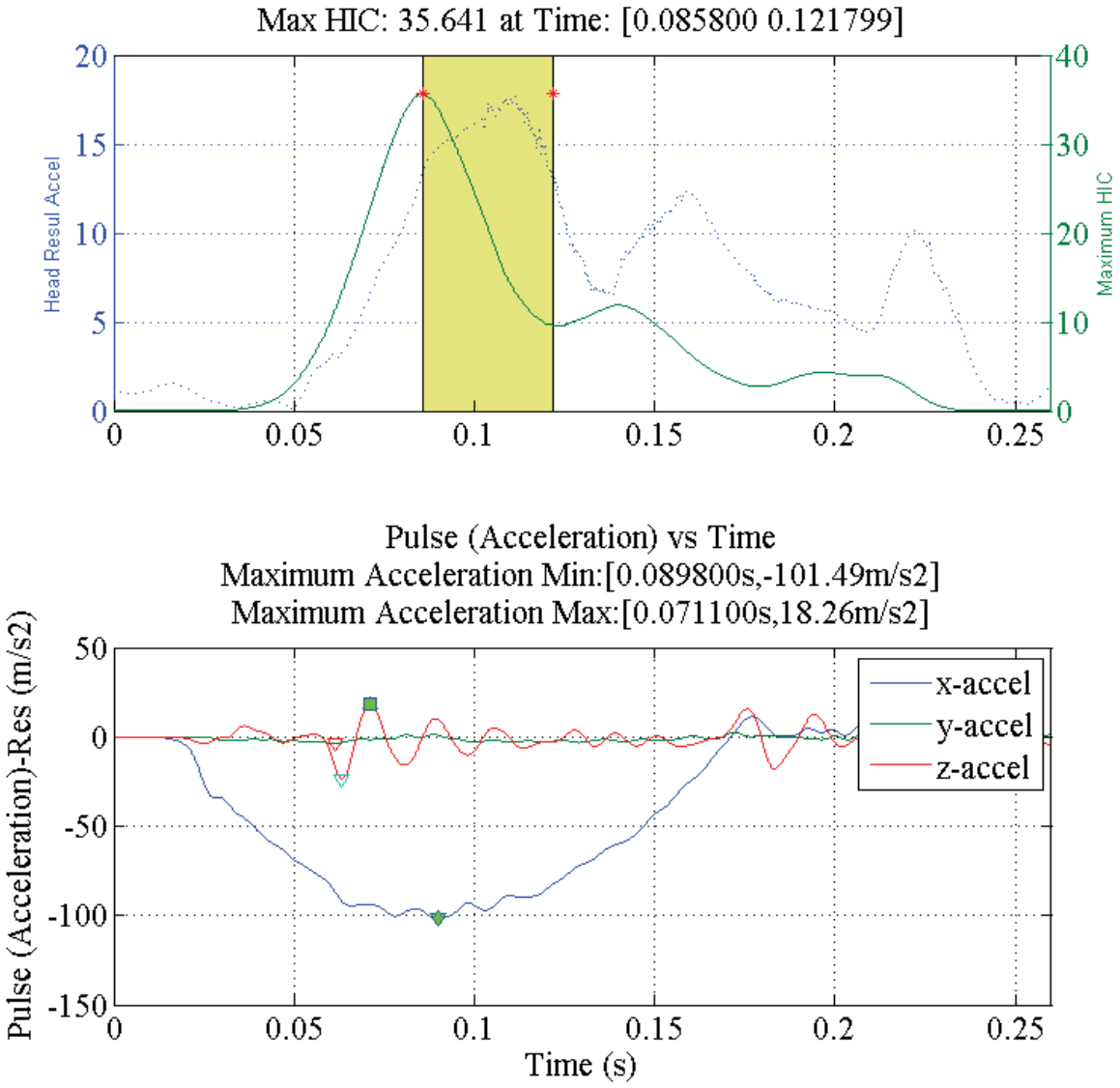

Figure 94: HIC_{36} for simulation 8202 (Frontal), long pulse.

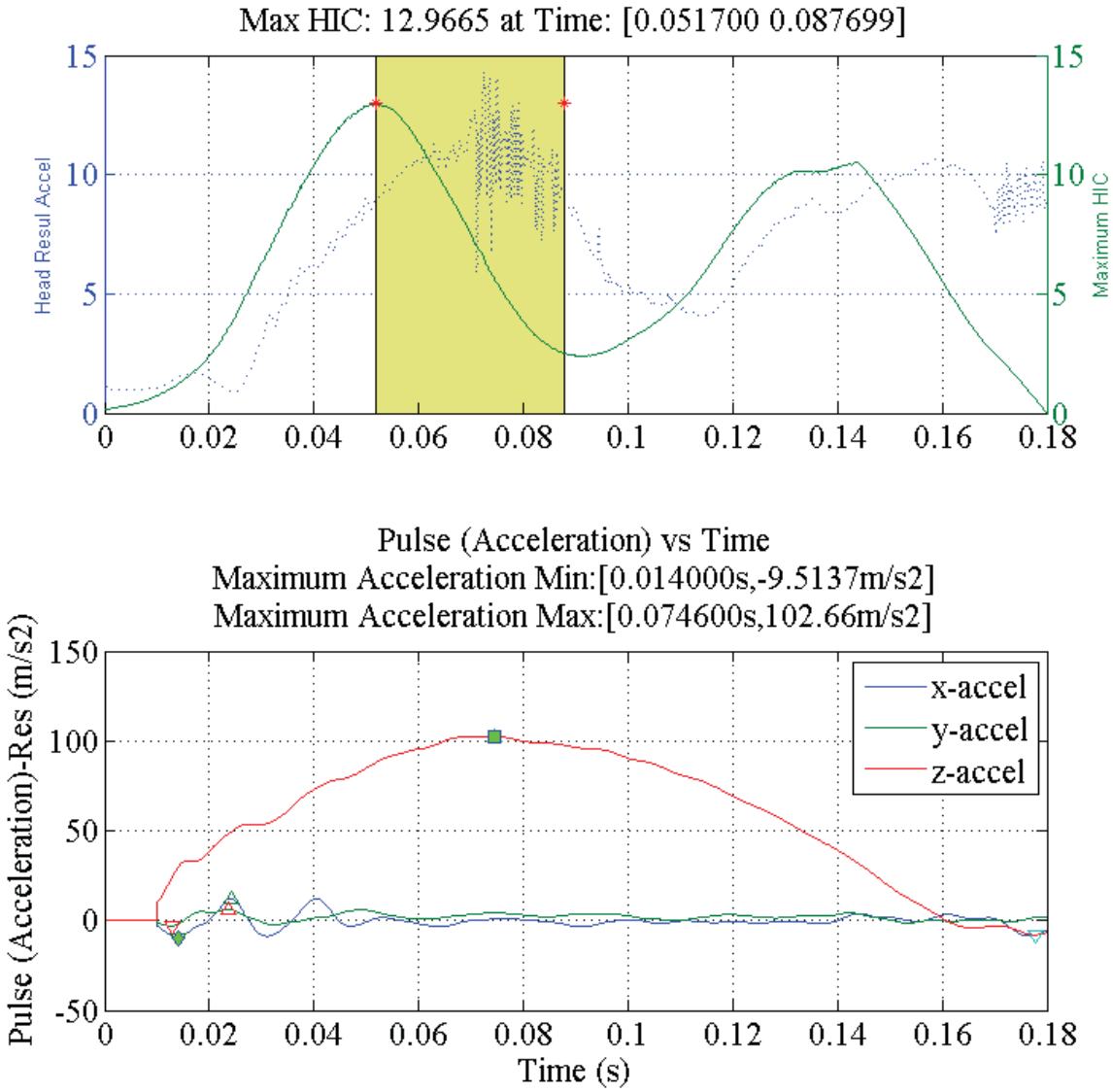

Figure 95: HIC_{36} for simulation 8208 (Spinal), short pulse, X-axis gravity.

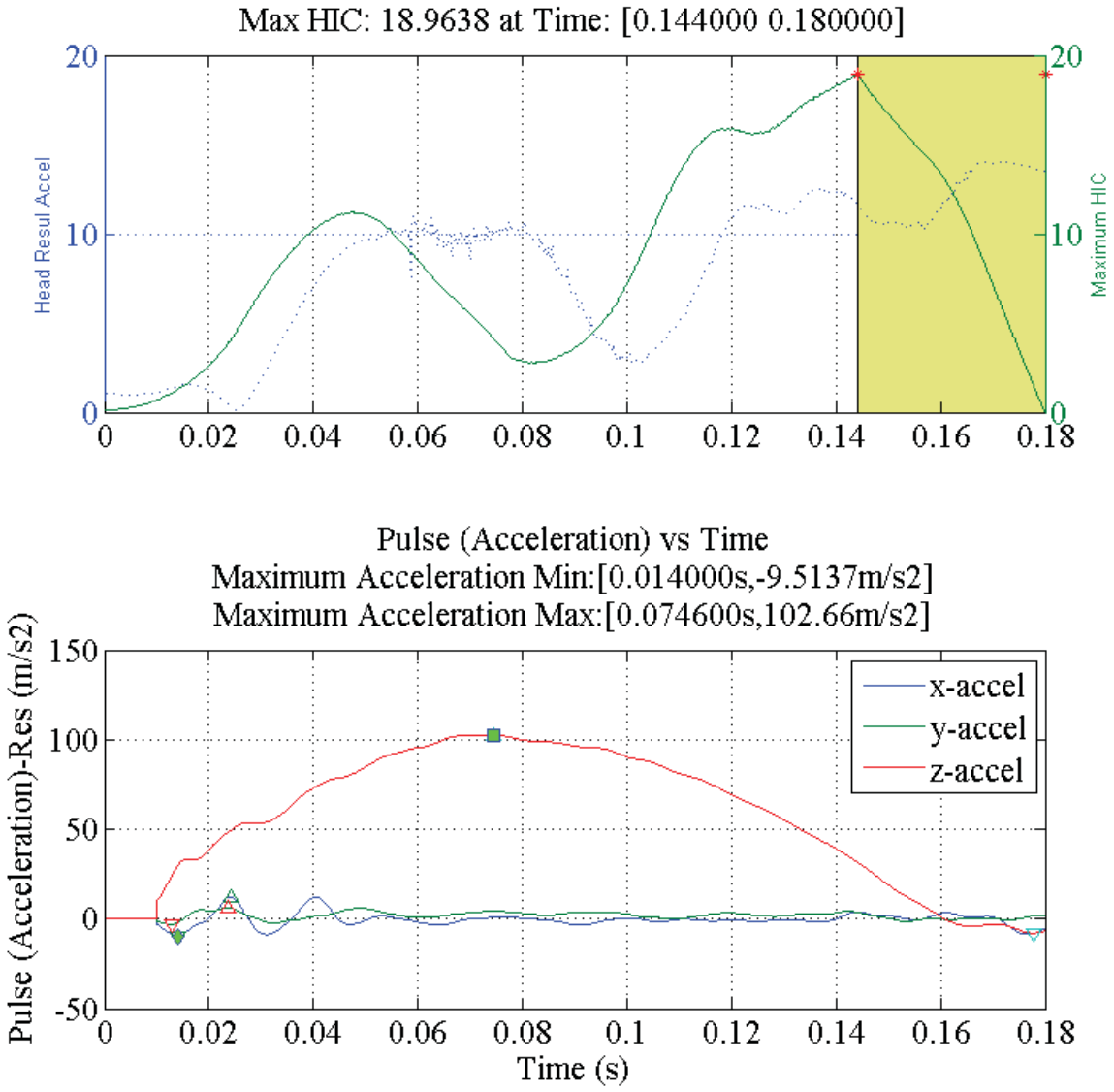

Figure 96: HIC_{36} for simulation 8208 (Spinal), short pulse, Z-axis gravity.

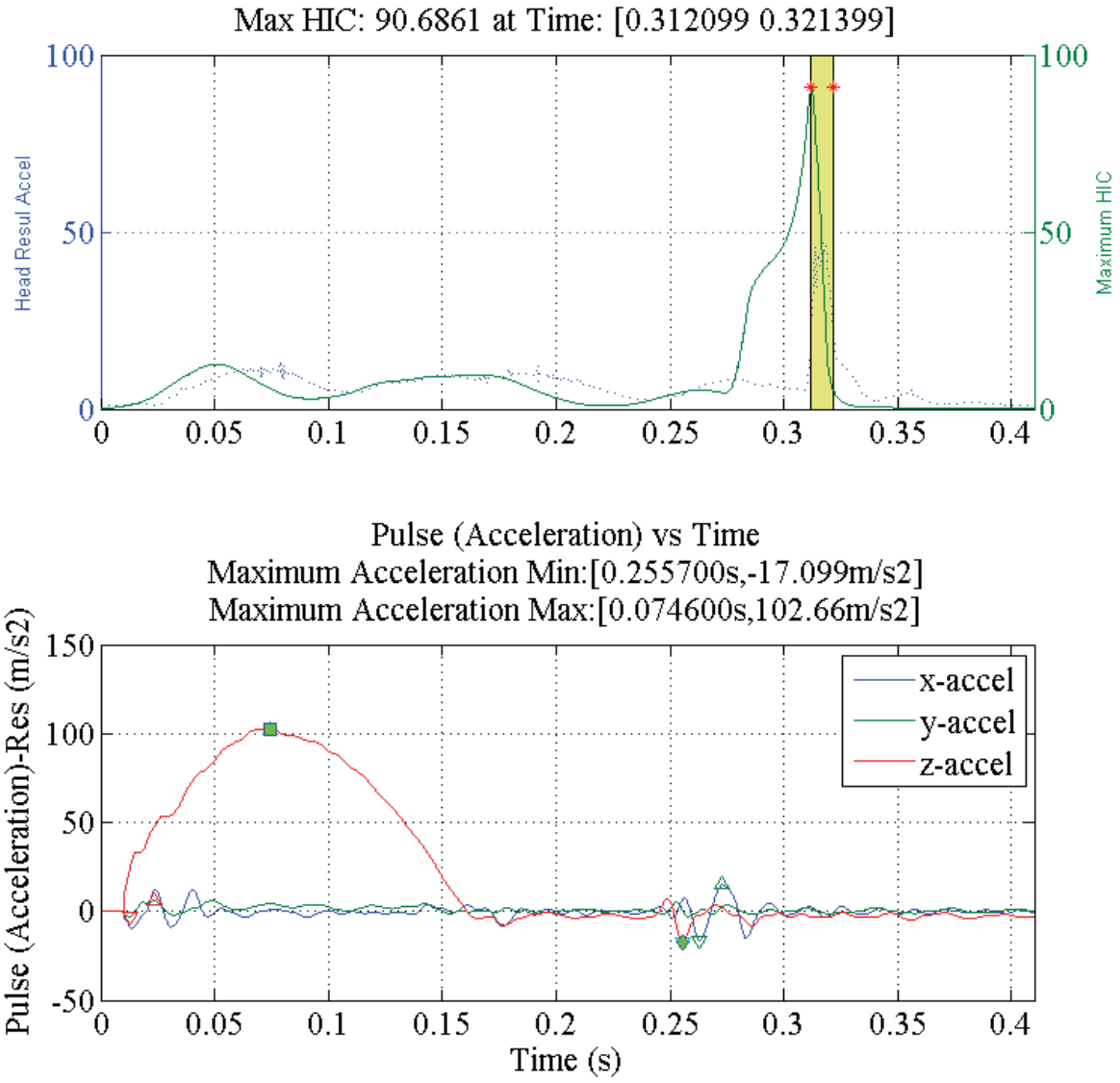

Figure 97: HIC_{36} for simulation 8208 (Spinal), long pulse, X-axis gravity.

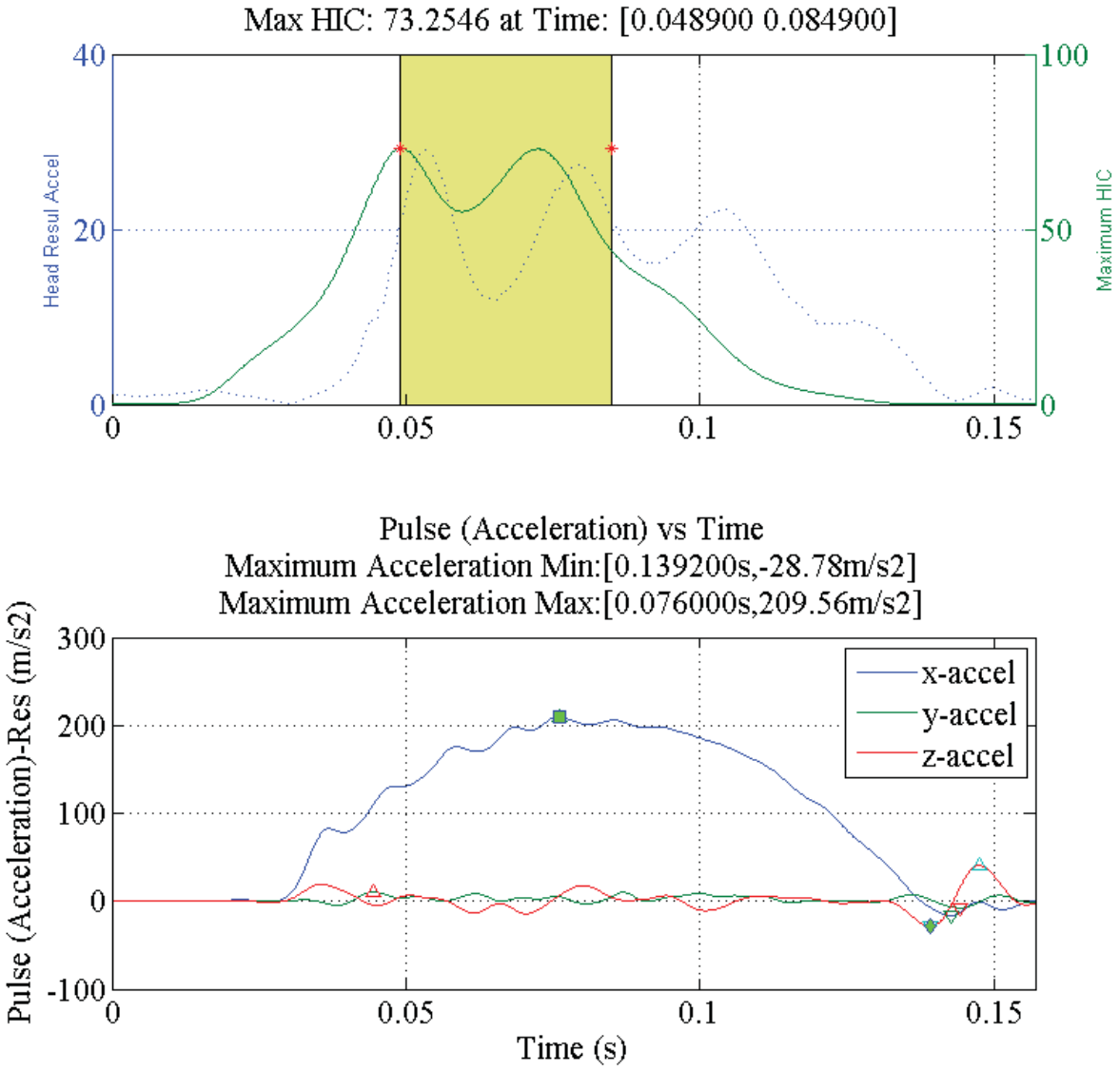

Figure 98: HIC_{36} for simulation 8212 (Rear), short pulse.

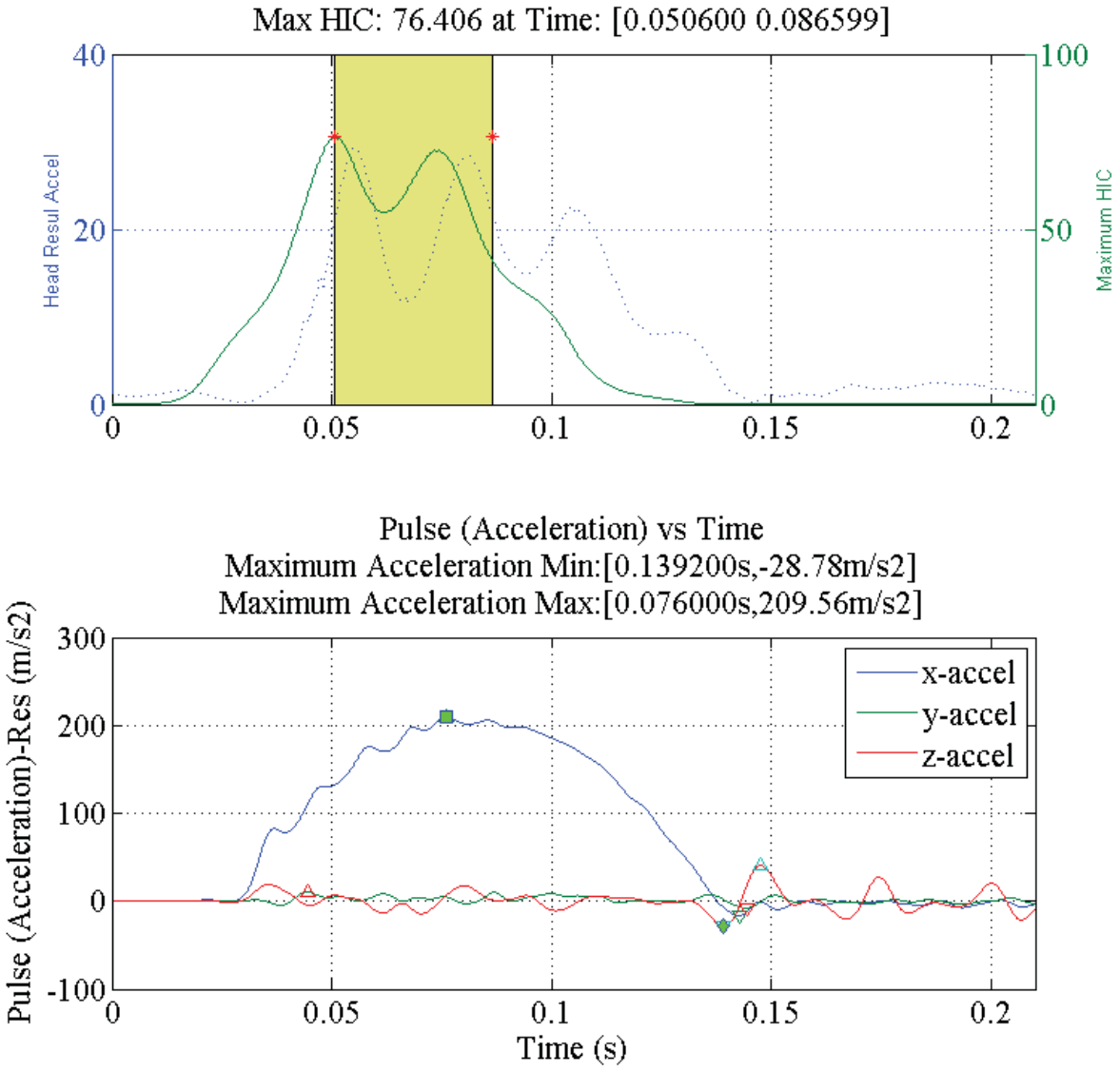

Figure 99: HIC_{36} for simulation 8212 (Rear), long pulse.

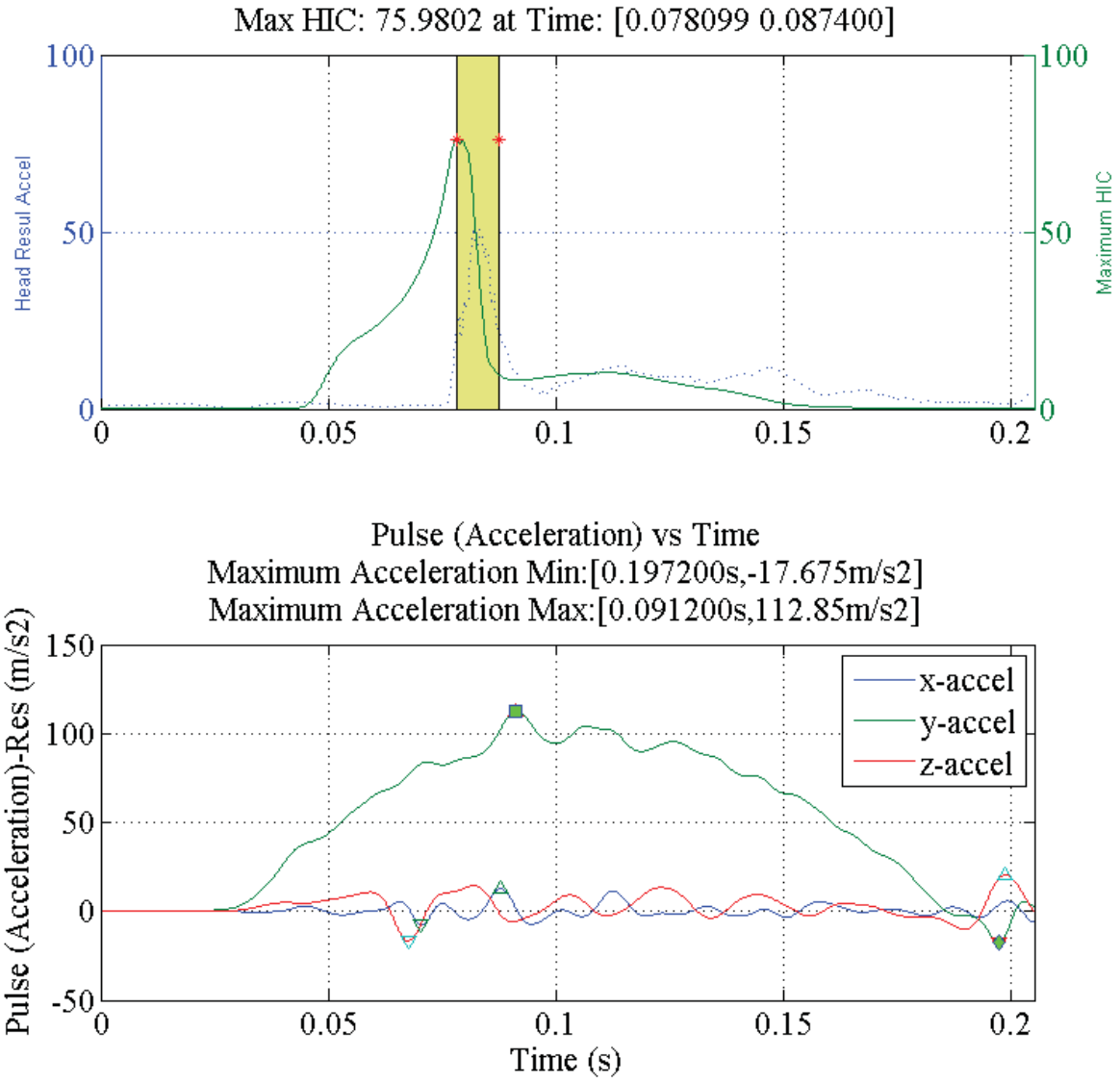

Figure 100: HIC_{36} for simulation 8245 (Lateral), short pulse.

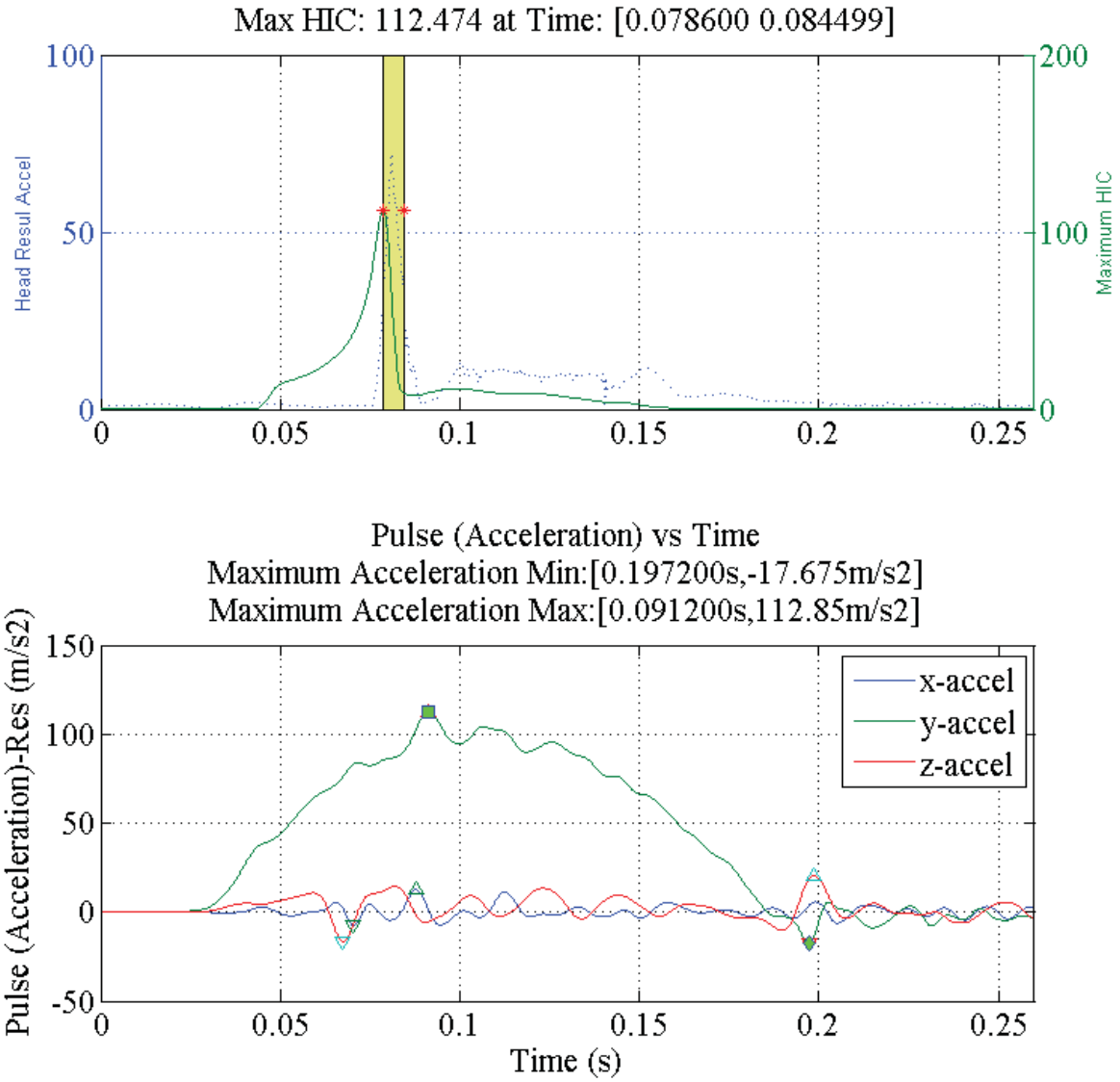

Figure 101: HIC_{36} for simulation 8245 (Lateral), long pulse.

Appendix 7: Neck Injury, N_{ij}

Table 5: Tabulated N_{ij}

Simulation	N_{ij}
8202, Frontal, Short pulse	0.0324
8202, Frontal, Long pulse	0.0349
8208, Spinal, Short pulse, X-axis gravity	0.0501
8208, Spinal, Short pulse, Z-axis gravity	0.0324
8208, Spinal, Long pulse, X-axis gravity	0.0349
8212, Rear, Short pulse	0.0324
8212, Rear, Long pulse	0.0349
8245, Lateral, Short pulse	0.0190
8245, Lateral, Long pulse	0.0349

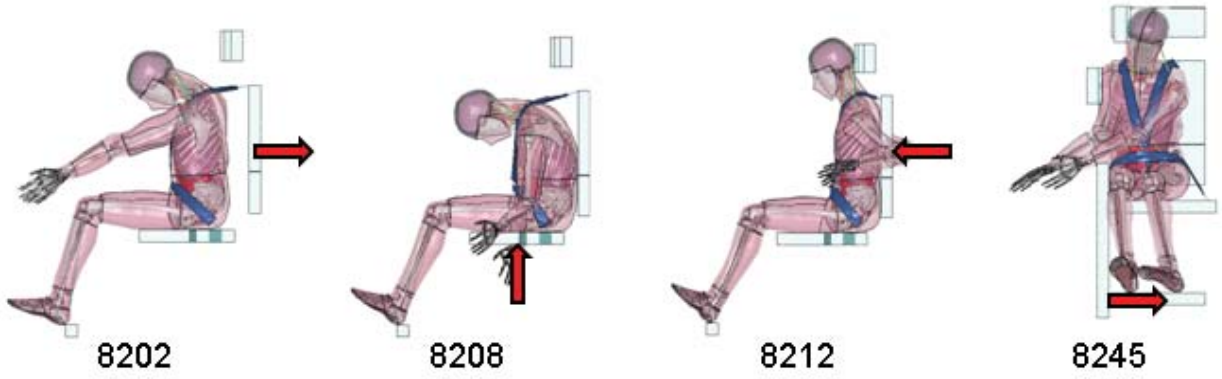

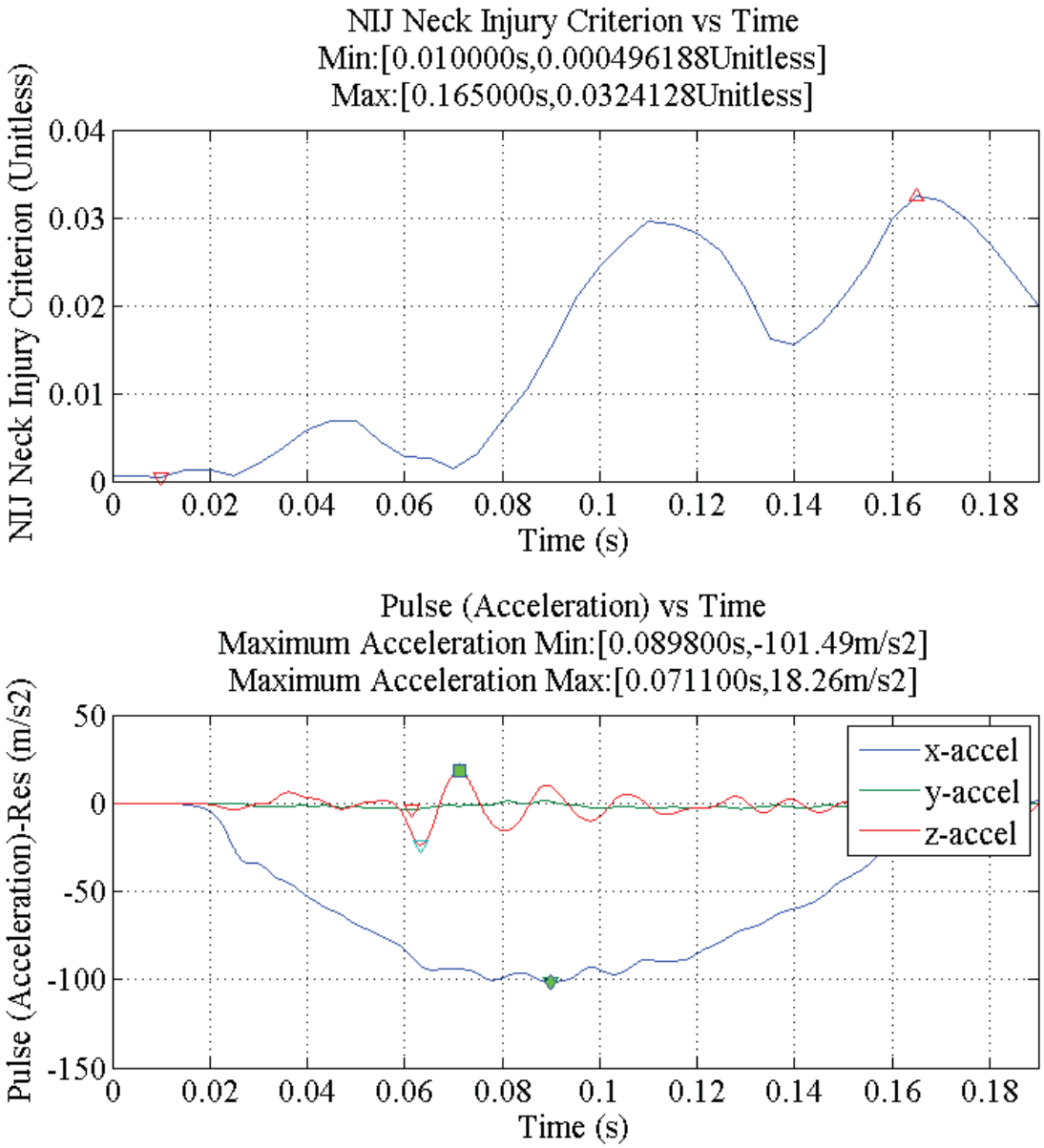

Figure 102: N_{ij} for simulation 8202 (Frontal), short pulse.

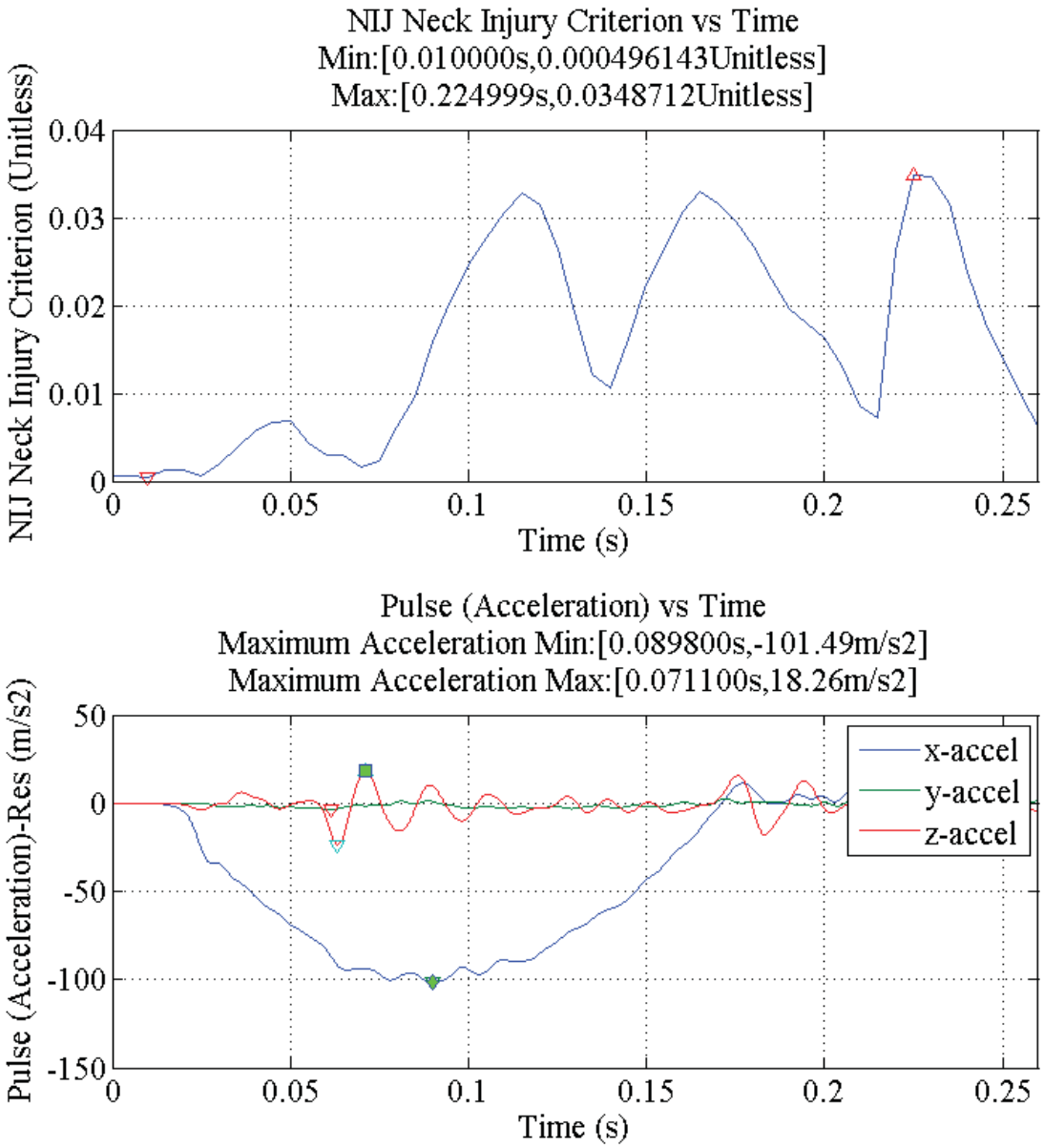

Figure 103: N_{ij} for simulation 8202 (Frontal), long pulse.

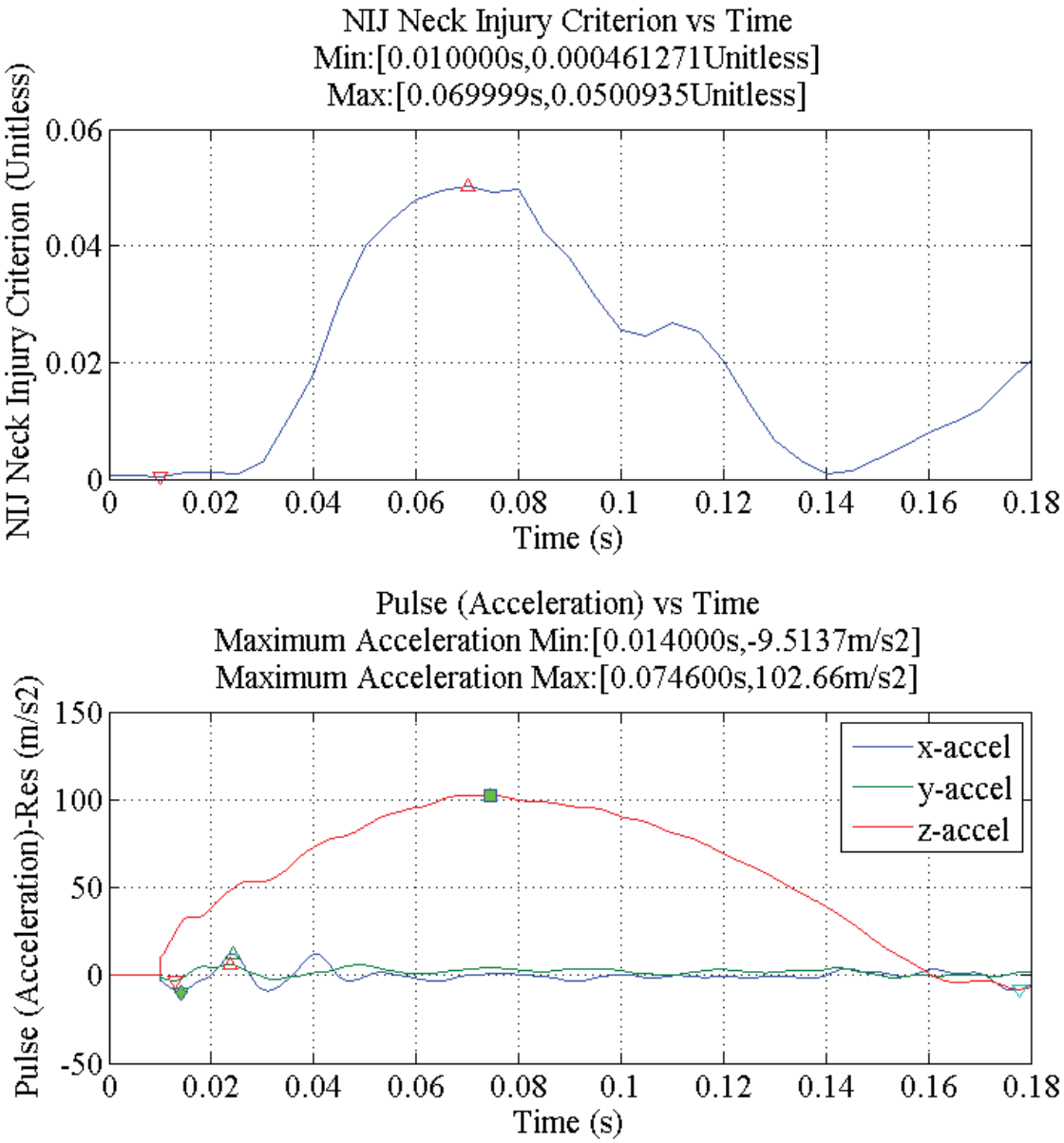

Figure 104: N_{ij} for simulation 8208 (Spinal), short pulse, X-axis gravity.

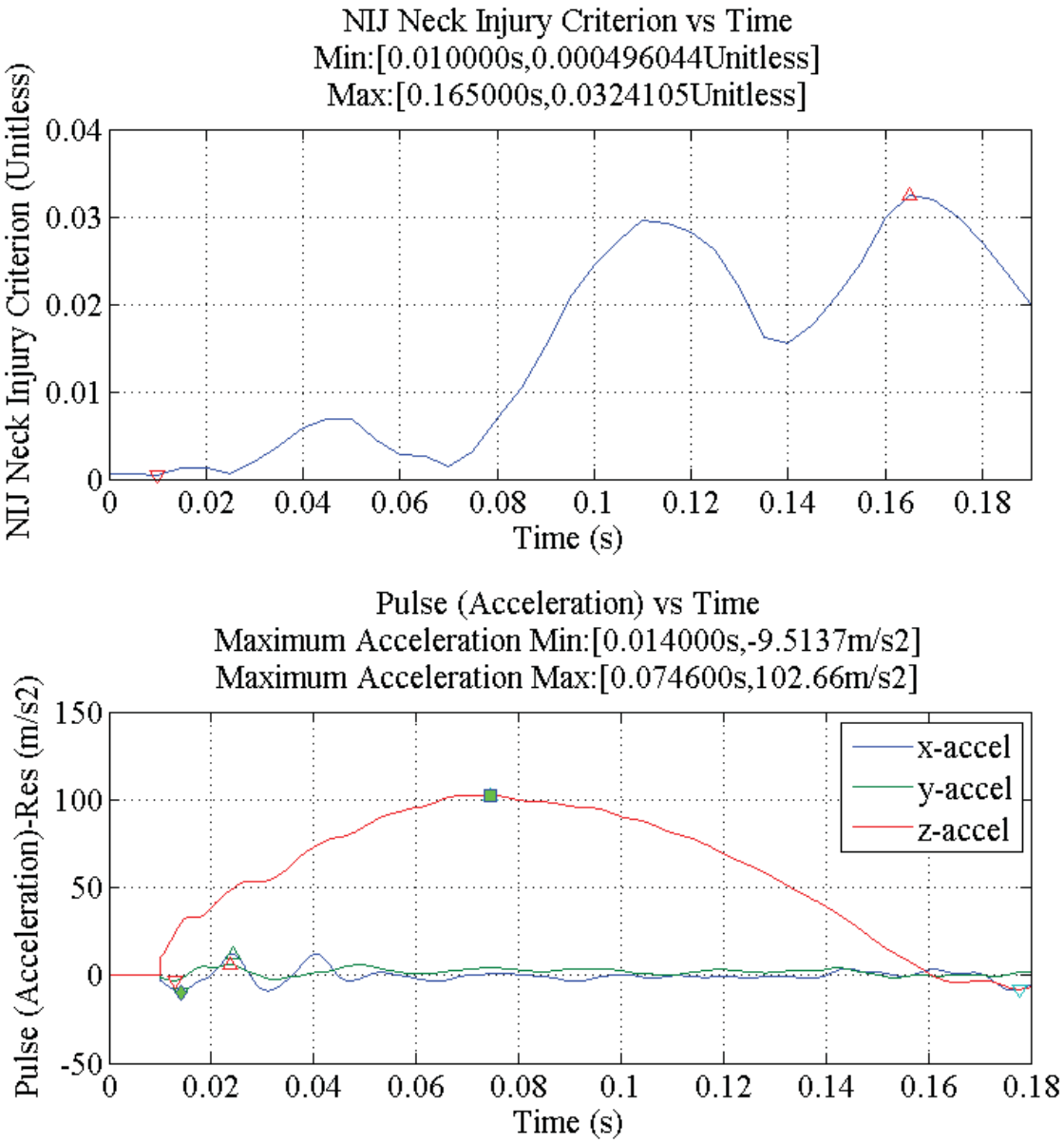

Figure 105: N_{ij} for simulation 8208 (Spinal), short pulse, Z-axis gravity.

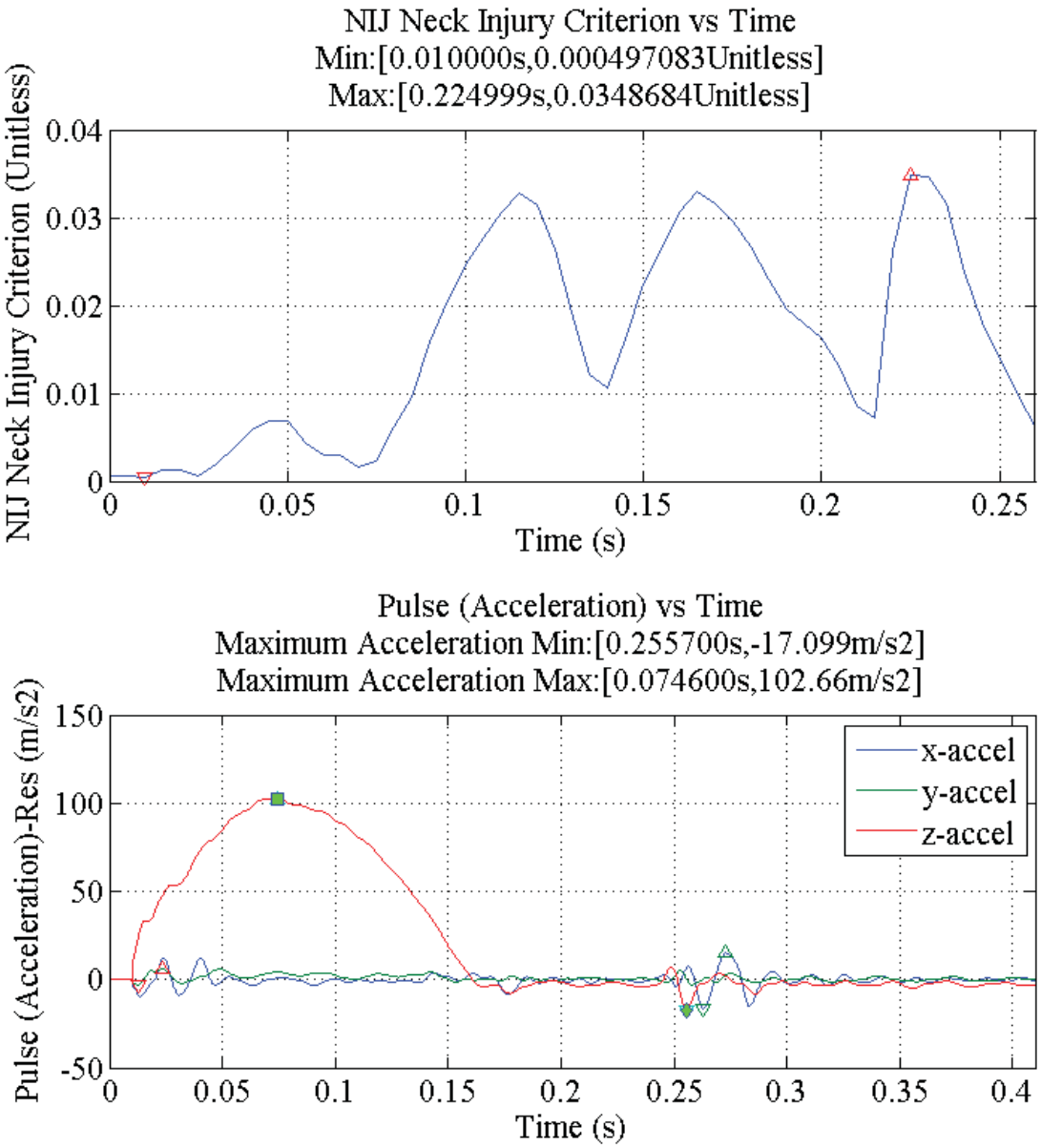

Figure 106: N_{ij} for simulation 8208 (Spinal), long pulse, X-axis gravity.

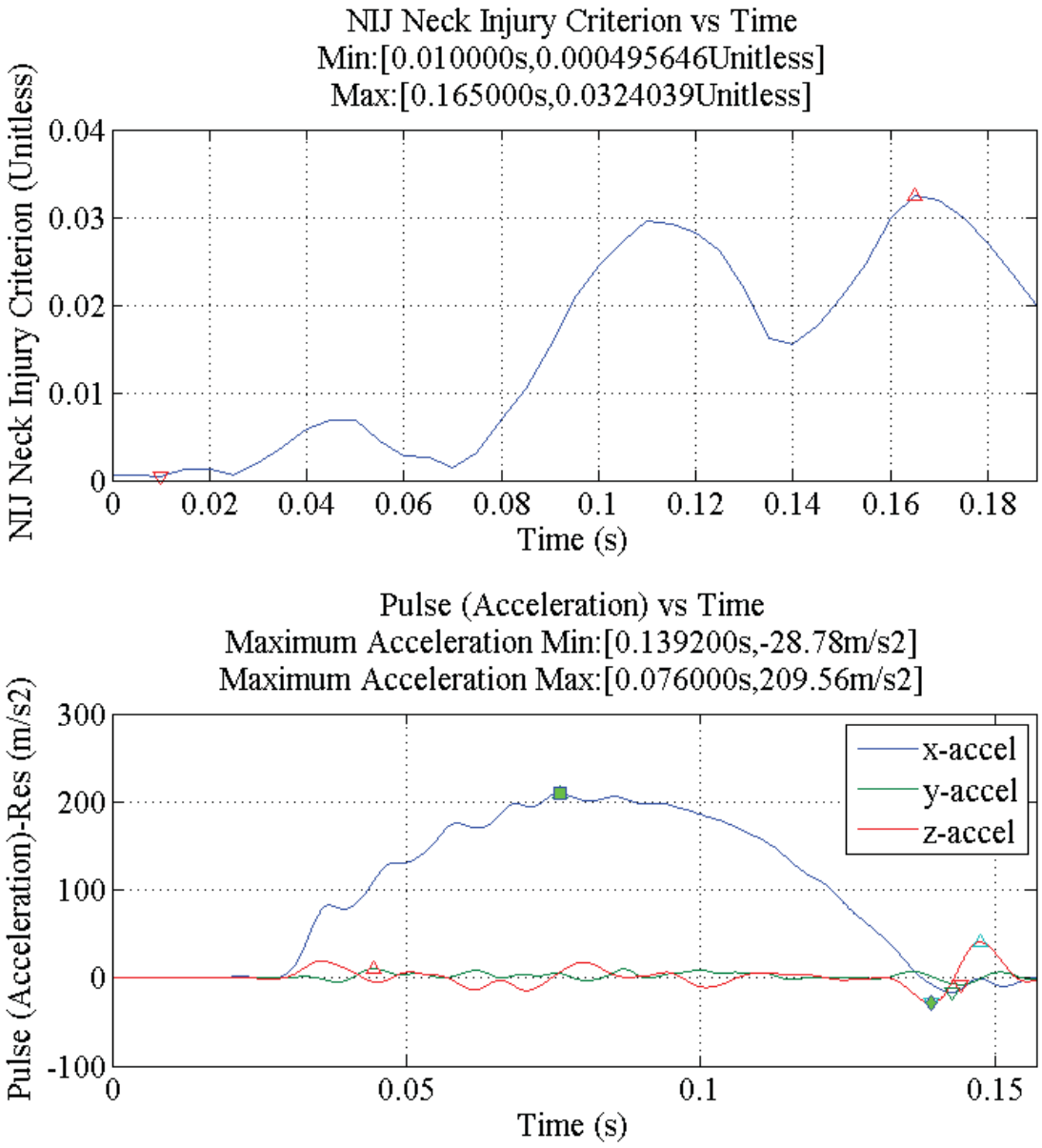

Figure 107: N_{ij} for simulation 8212 (Rear), short pulse.

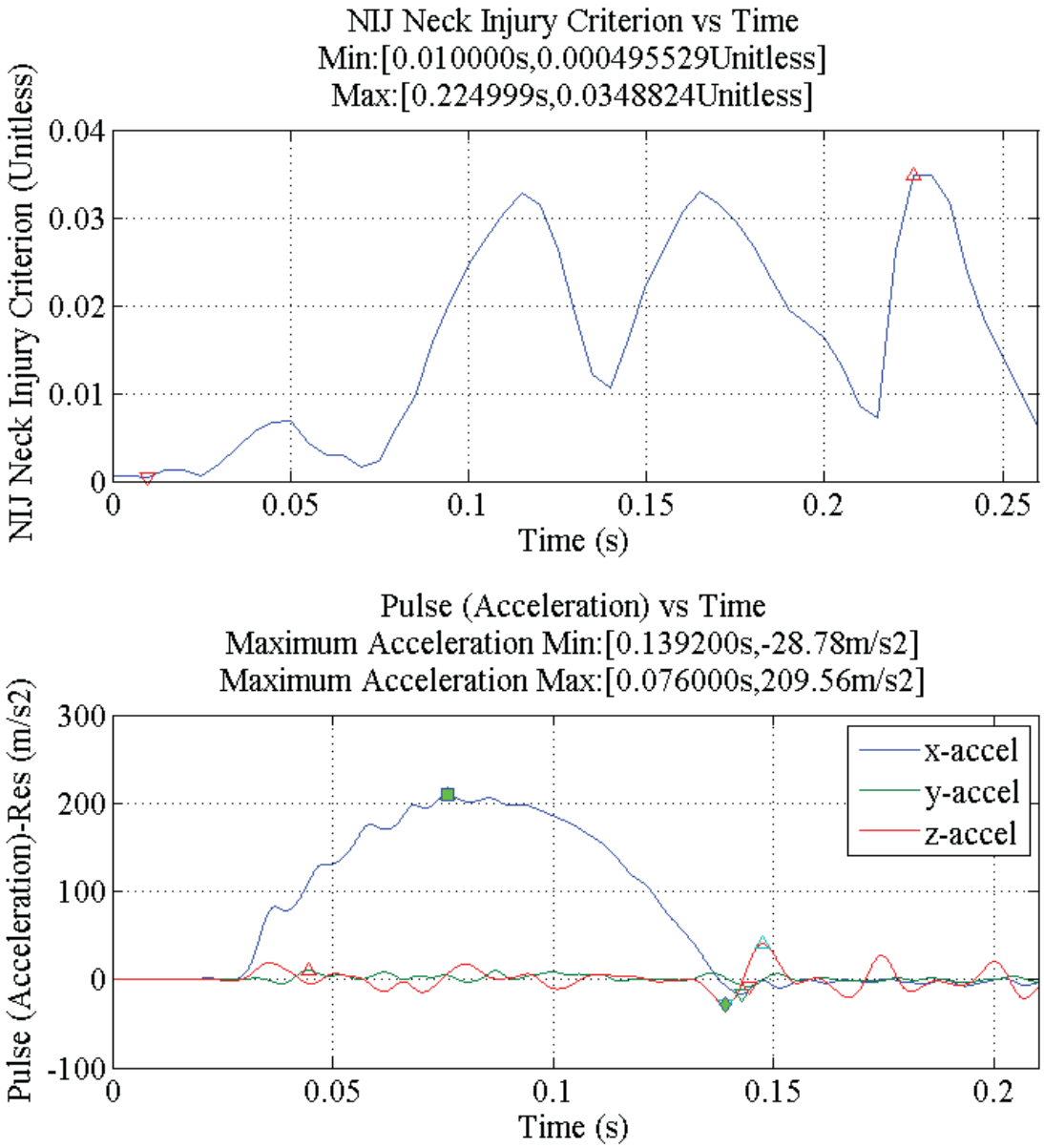

Figure 108: N_{ij} for simulation 8212 (Rear), long pulse.

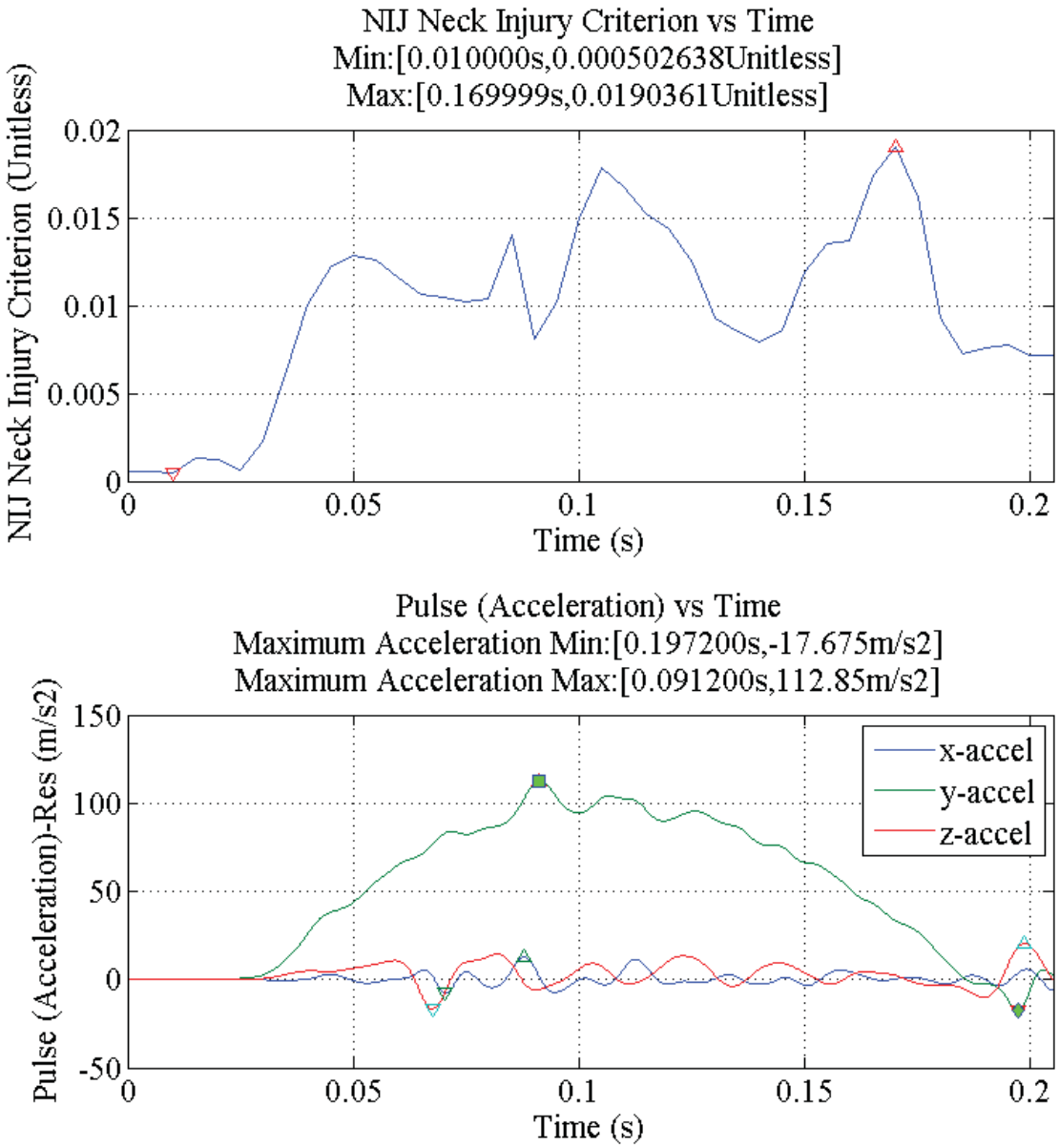

Figure 109: N_{ij} for simulation 8245 (Lateral), short pulse.

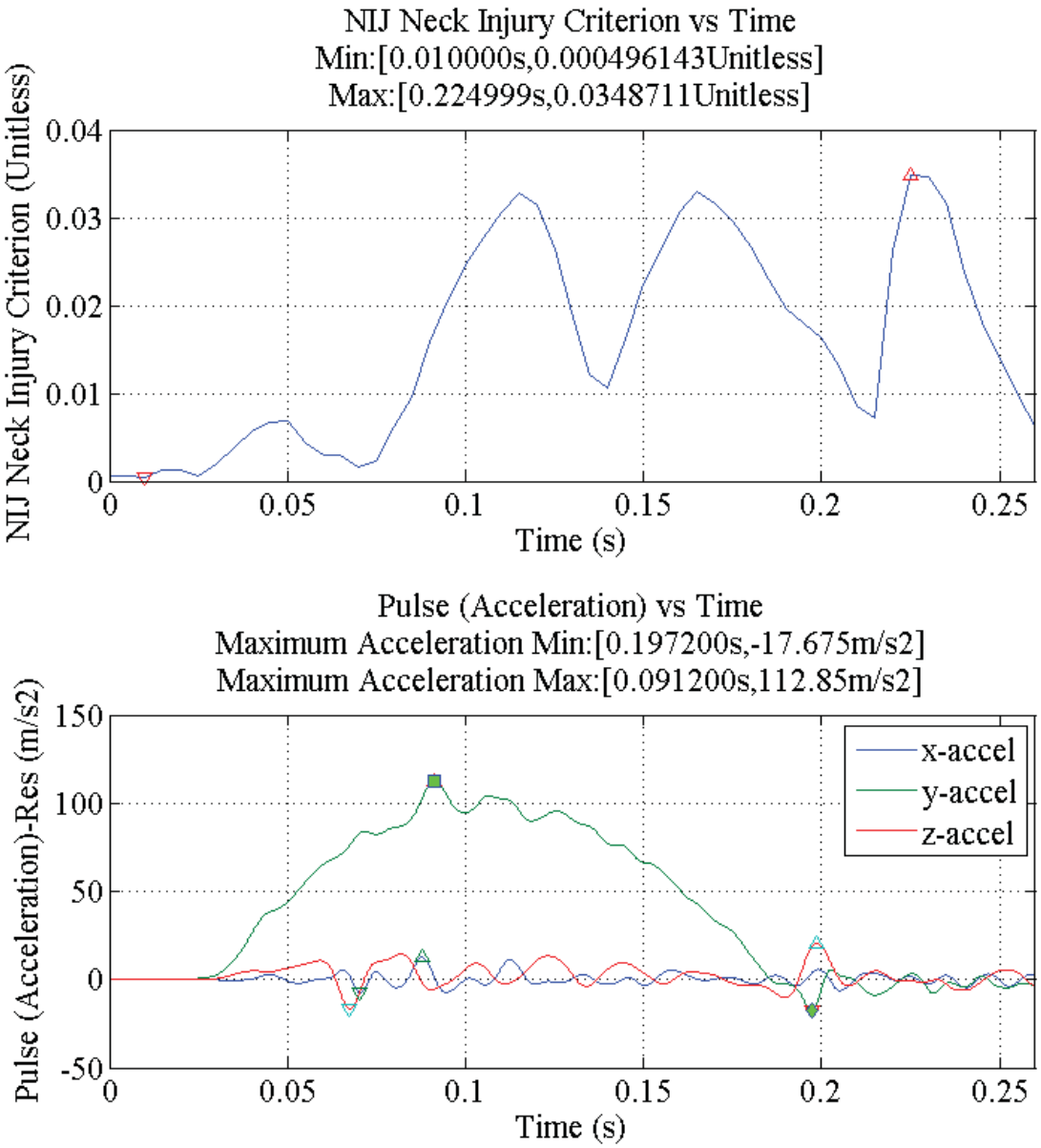

Figure 110: N_{ij} for simulation 8245 (Lateral), long pulse.

Appendix 8: Thorax Injury, Sternal Deflection

Table 6: Tabulated Sternal Deflection

Simulation	Sternal Deflection (cm)
8202, Frontal, Short pulse	-0.854
8202, Frontal, Long pulse	-1.300
8208, Spinal, Short pulse, X-axis gravity	1.165
8208, Spinal, Short pulse, Z-axis gravity	1.334
8208, Spinal, Long pulse, X-axis gravity	0.996
8212, Rear, Short pulse	-4.122
8212, Rear, Long pulse	-4.103
8245, Lateral, Short pulse	1.177
8245, Lateral, Long pulse	1.099

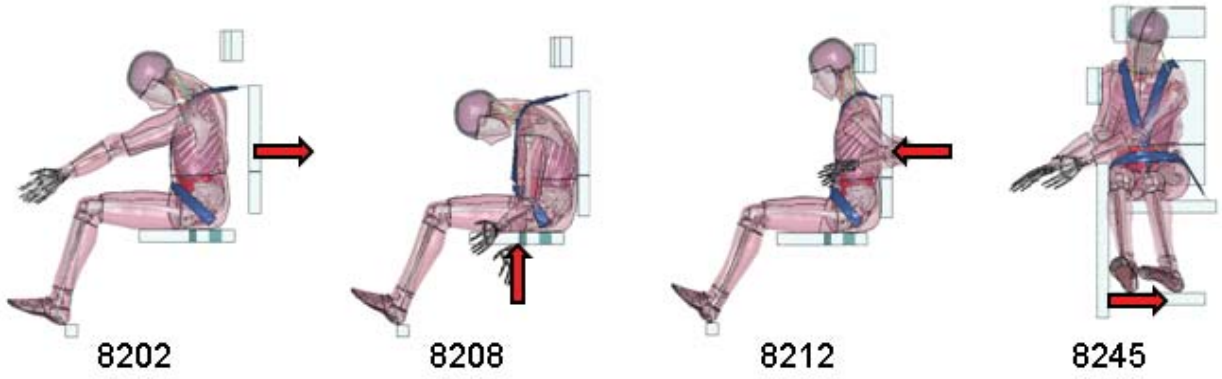

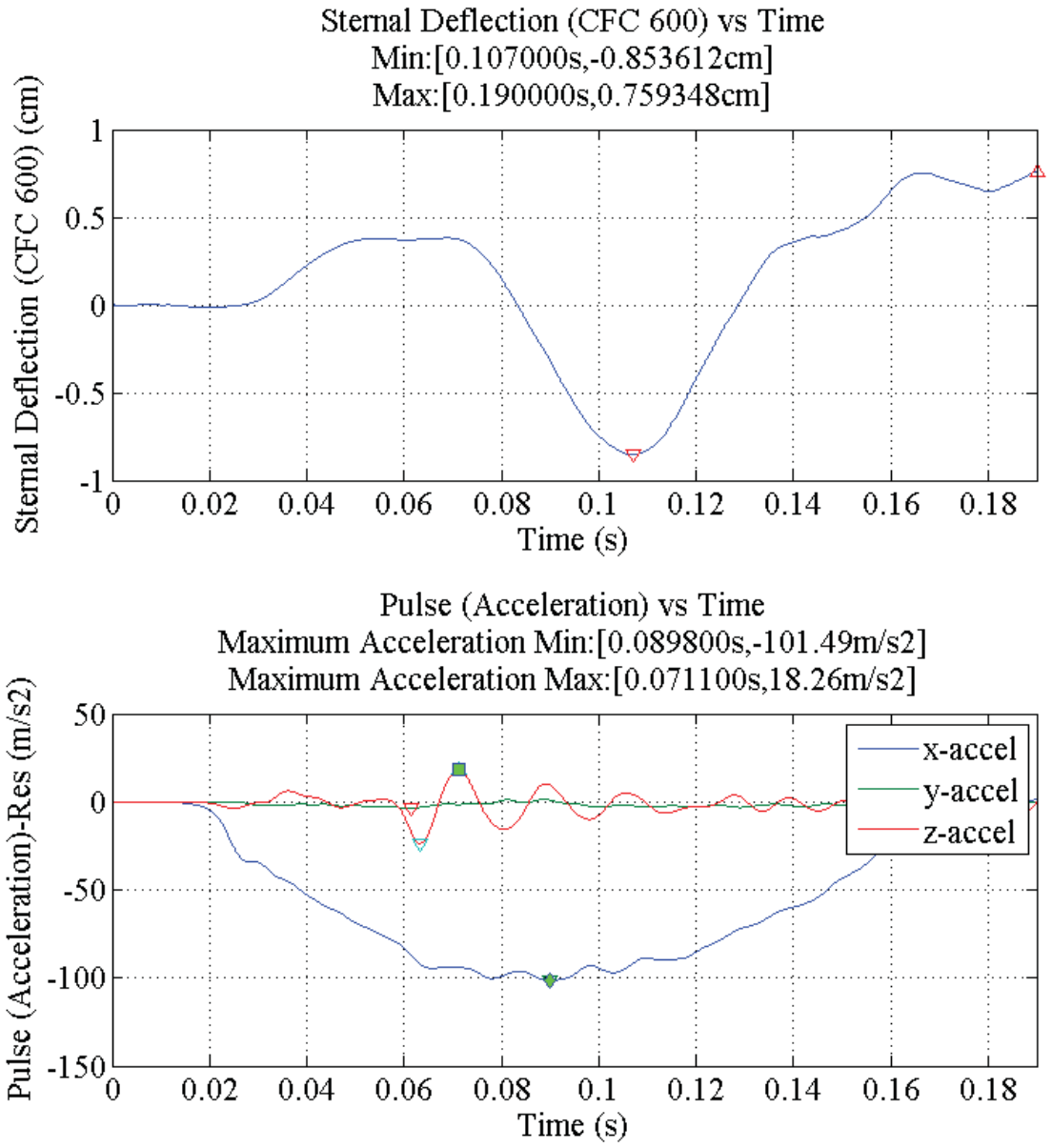

Figure 111: Sternal Deflection for simulation 8202 (Frontal), short pulse.

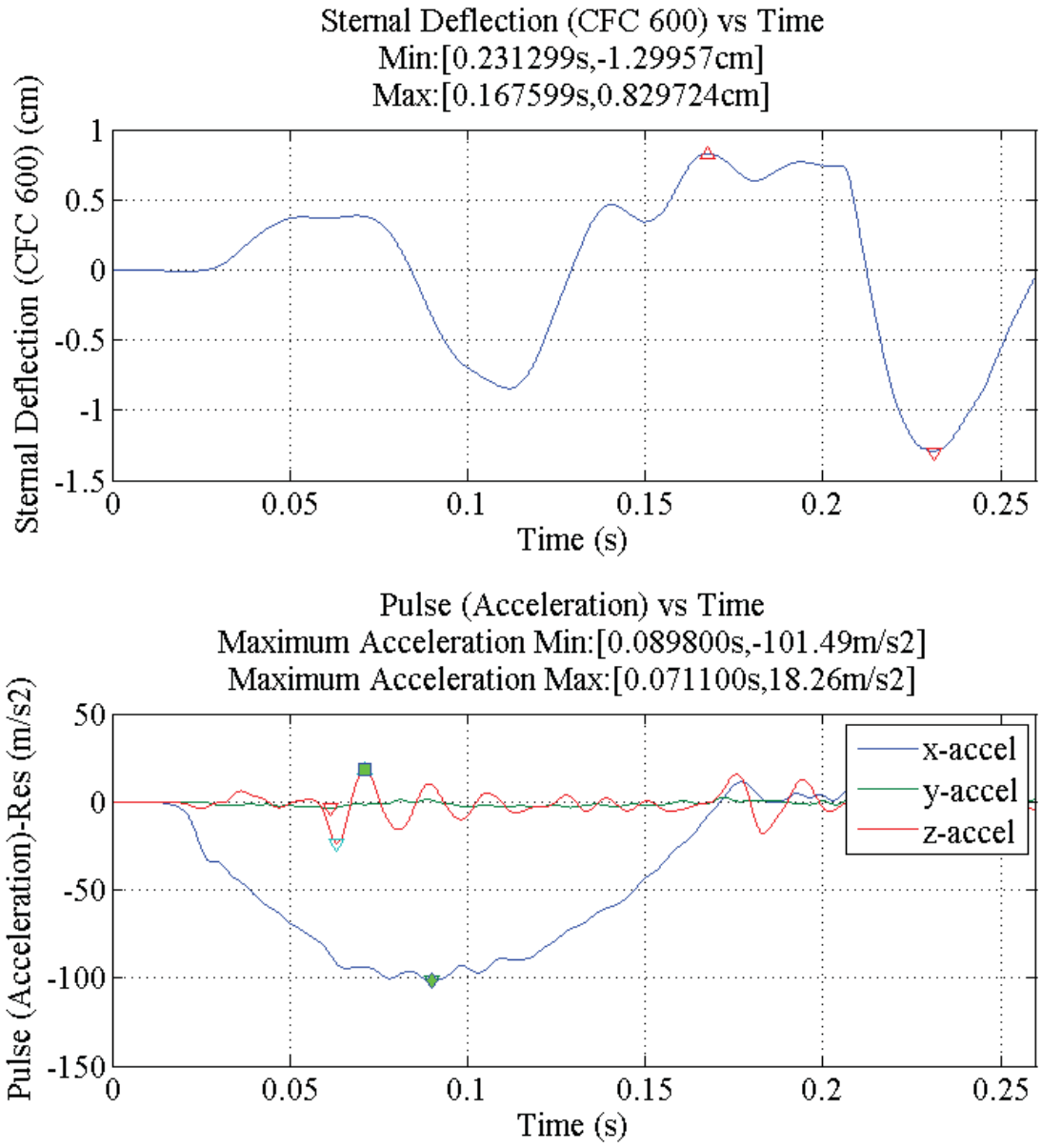

Figure 112: Sternal Deflection for simulation 8202 (Frontal), long pulse.

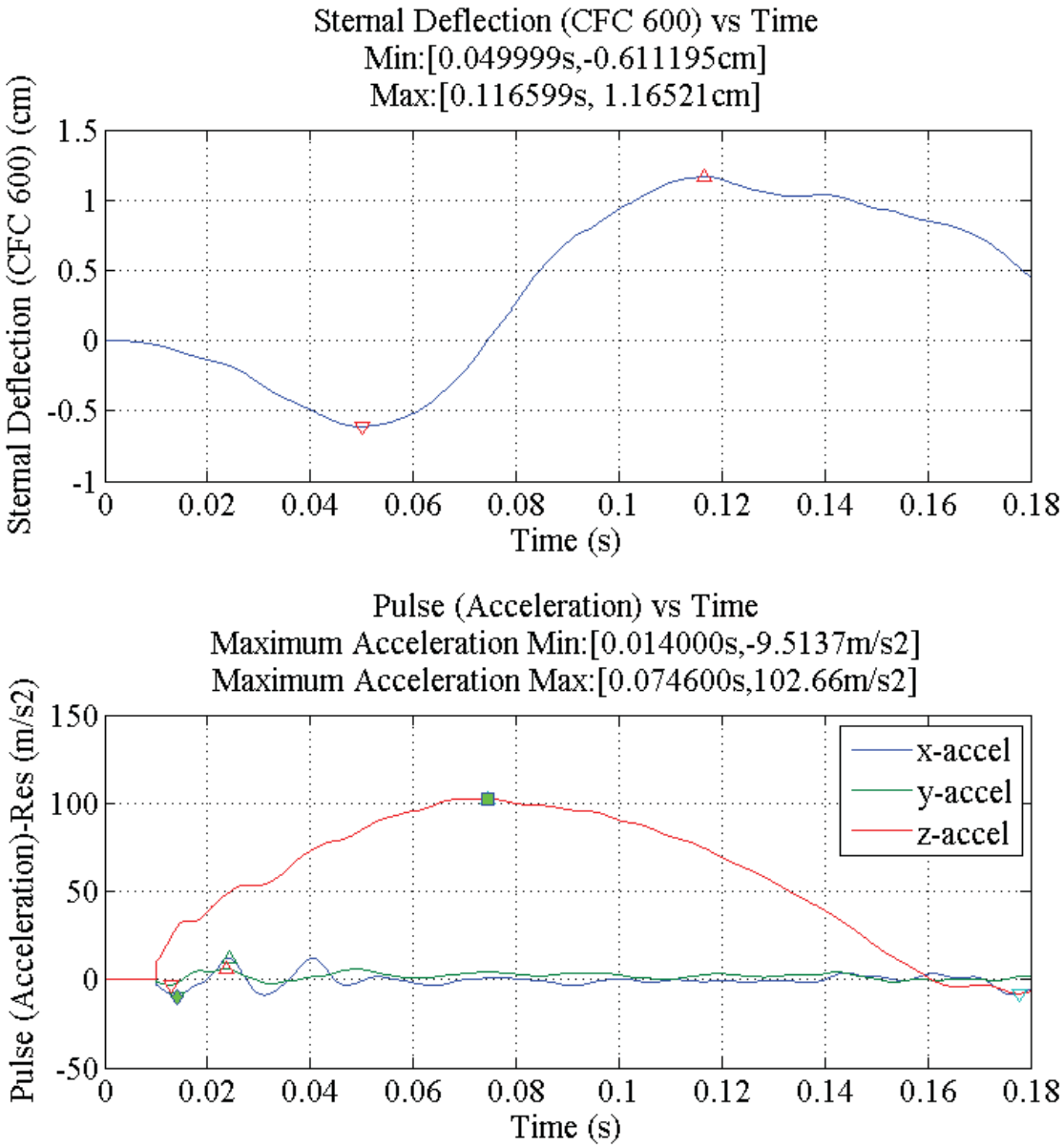

Figure 113: Sternal Deflection for simulation 8208 (Spinal), short pulse, X-axis gravity.

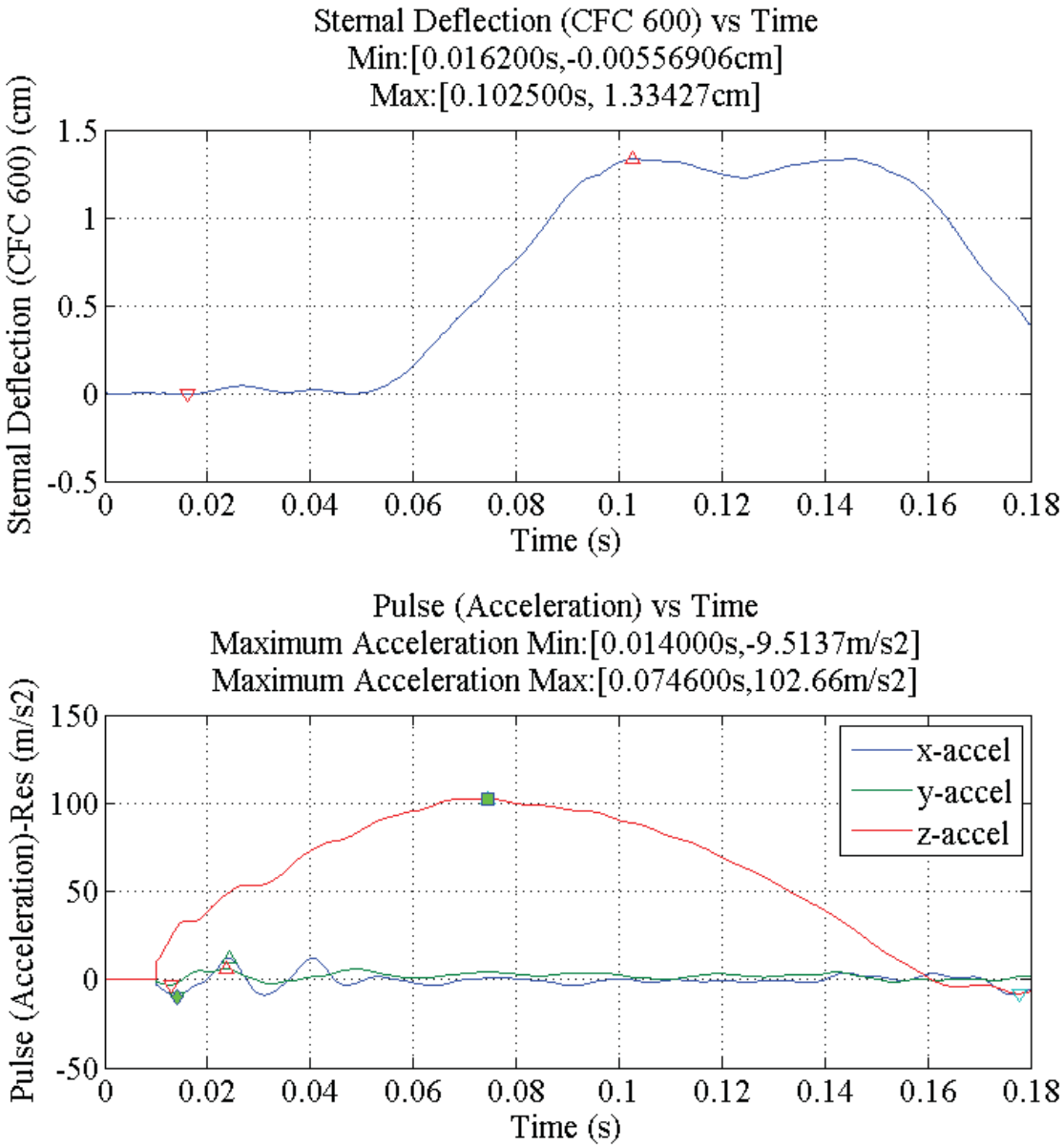

Figure 114: Sternal Deflection for simulation 8208 (Spinal), short pulse, Z-axis gravity.

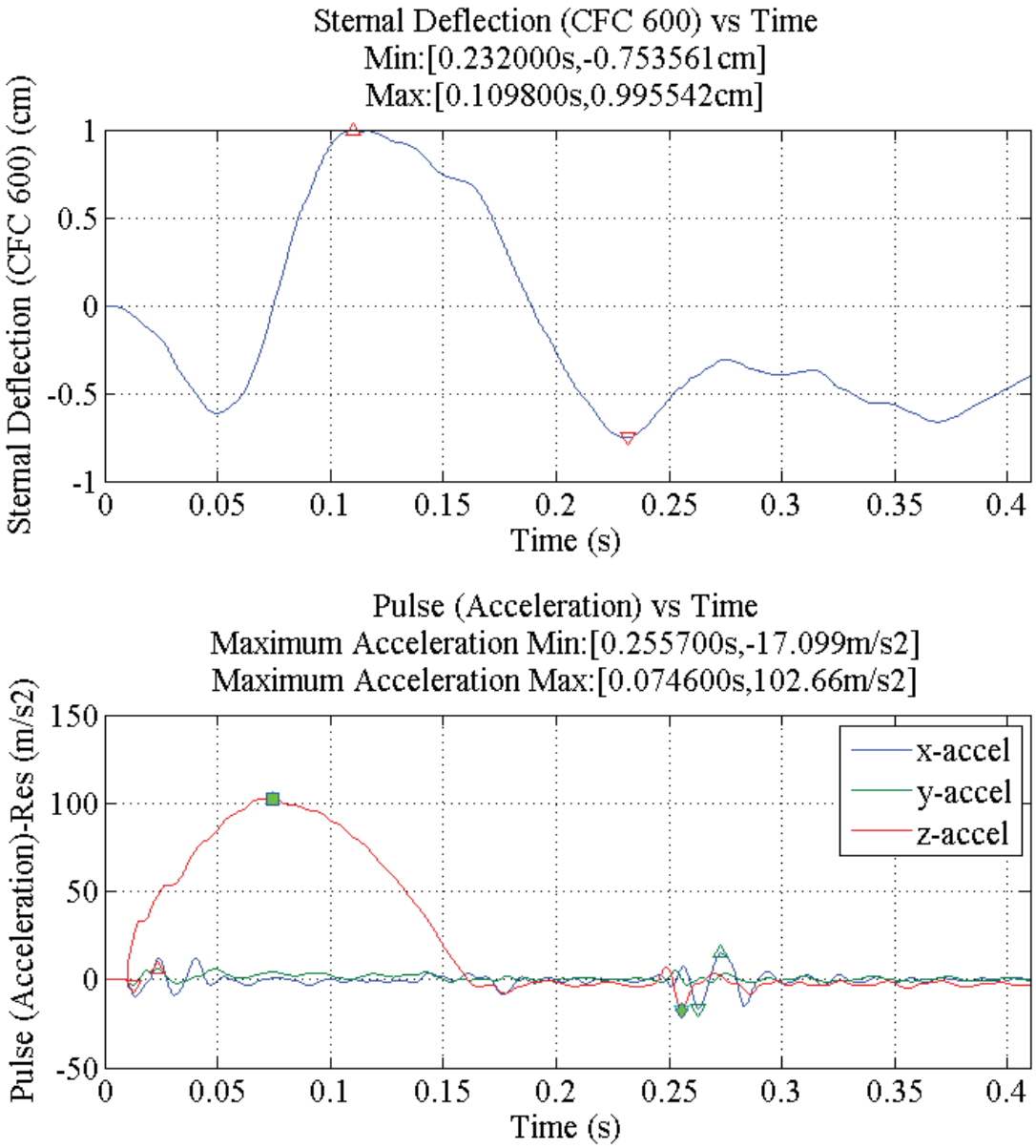

Figure 115: Sternal Deflection for simulation 8208 (Spinal), long pulse, X-axis gravity.

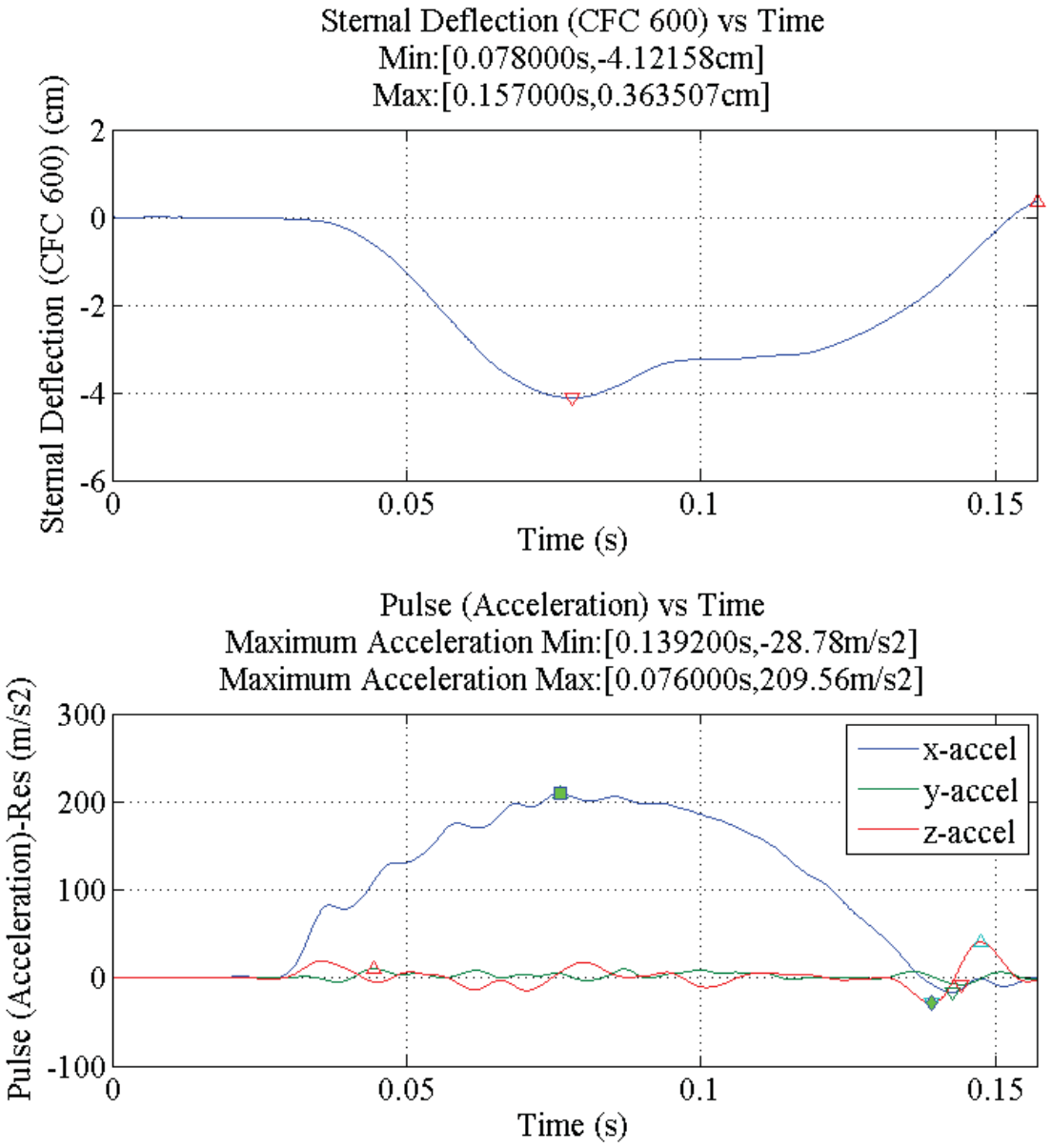

Figure 116: Sternal Deflection for simulation 8212 (Rear), short pulse.

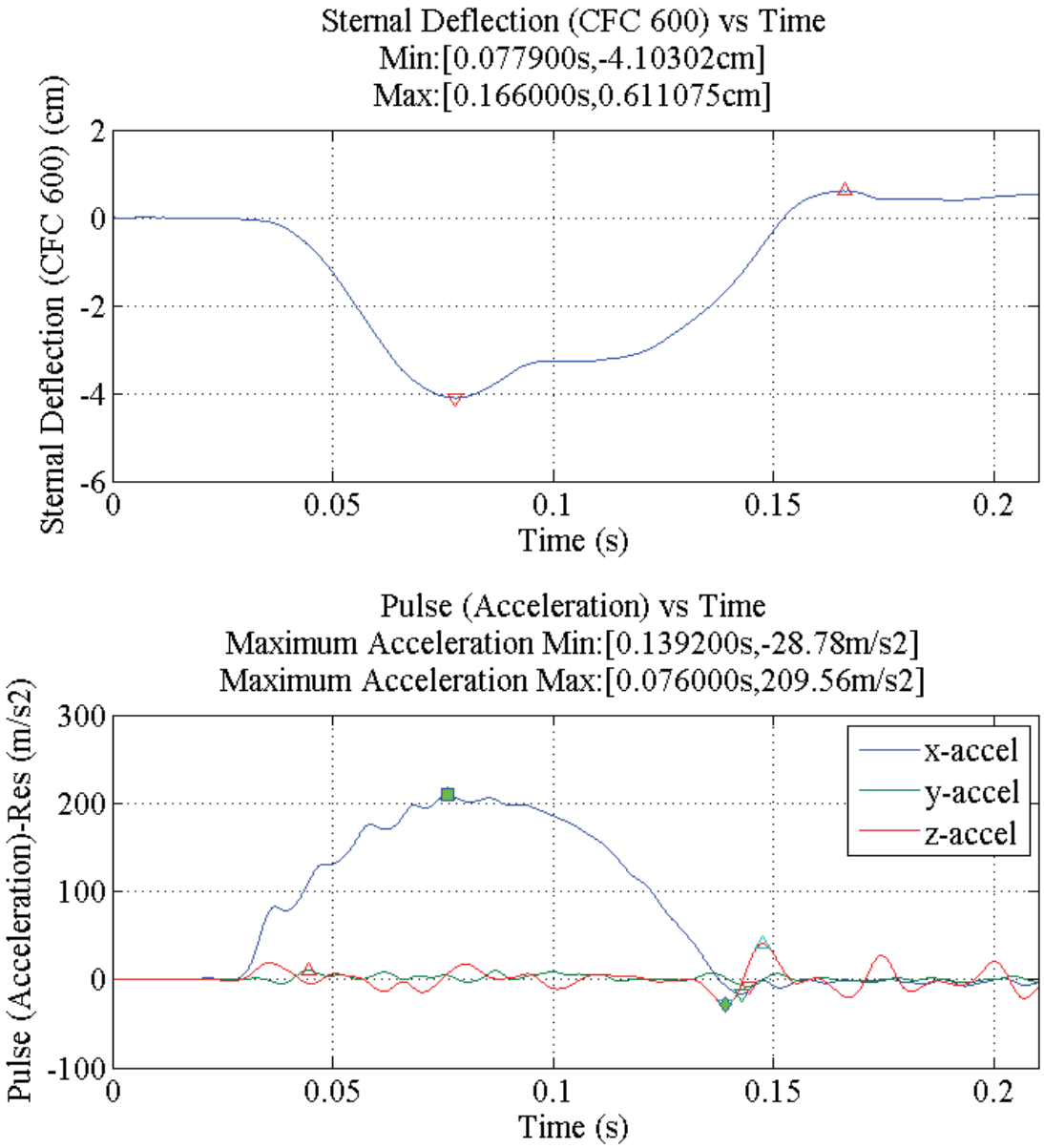

Figure 117: Sternal Deflection for simulation 8212 (Rear), long pulse.

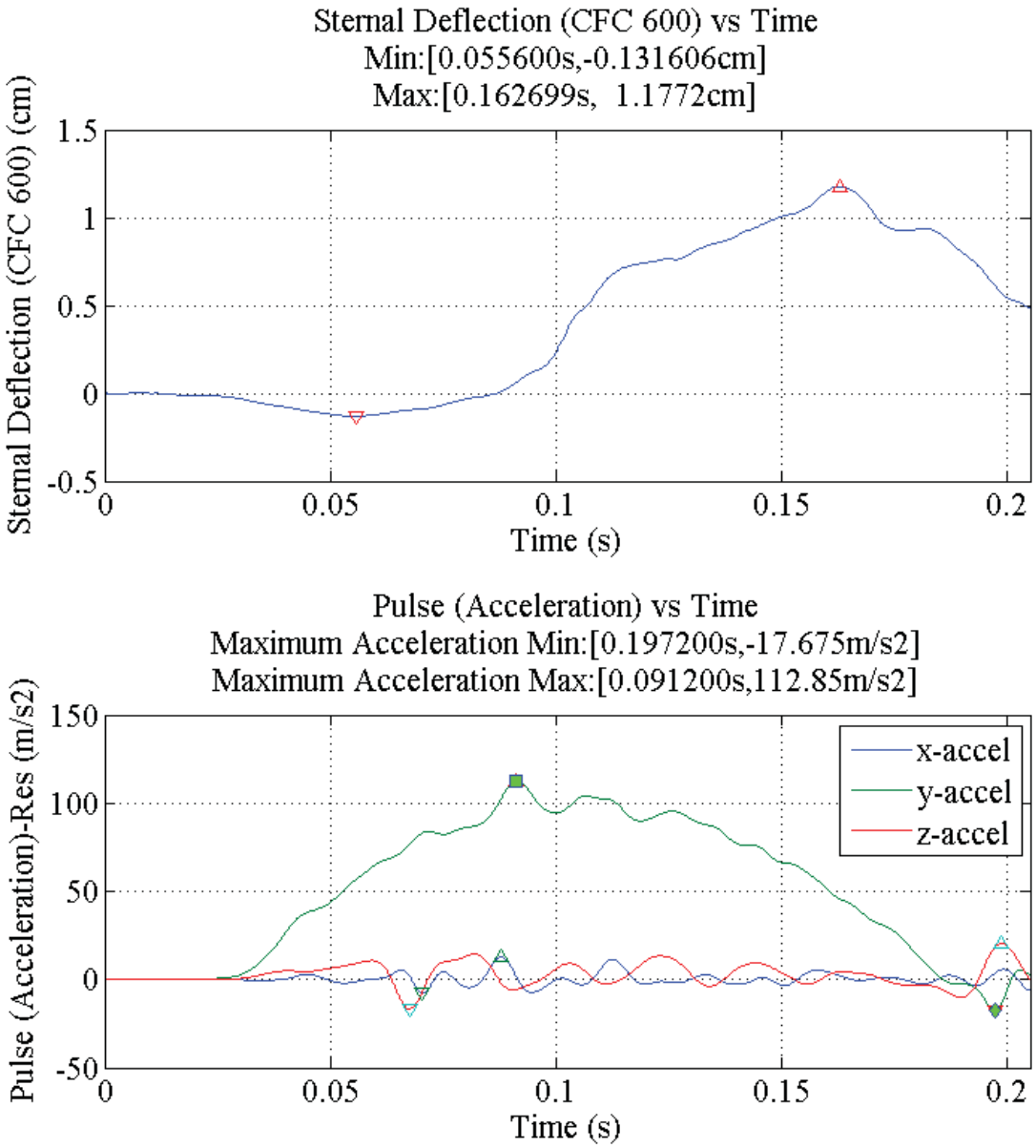

Figure 118: Sternal Deflection for simulation 8245 (Lateral), short pulse.

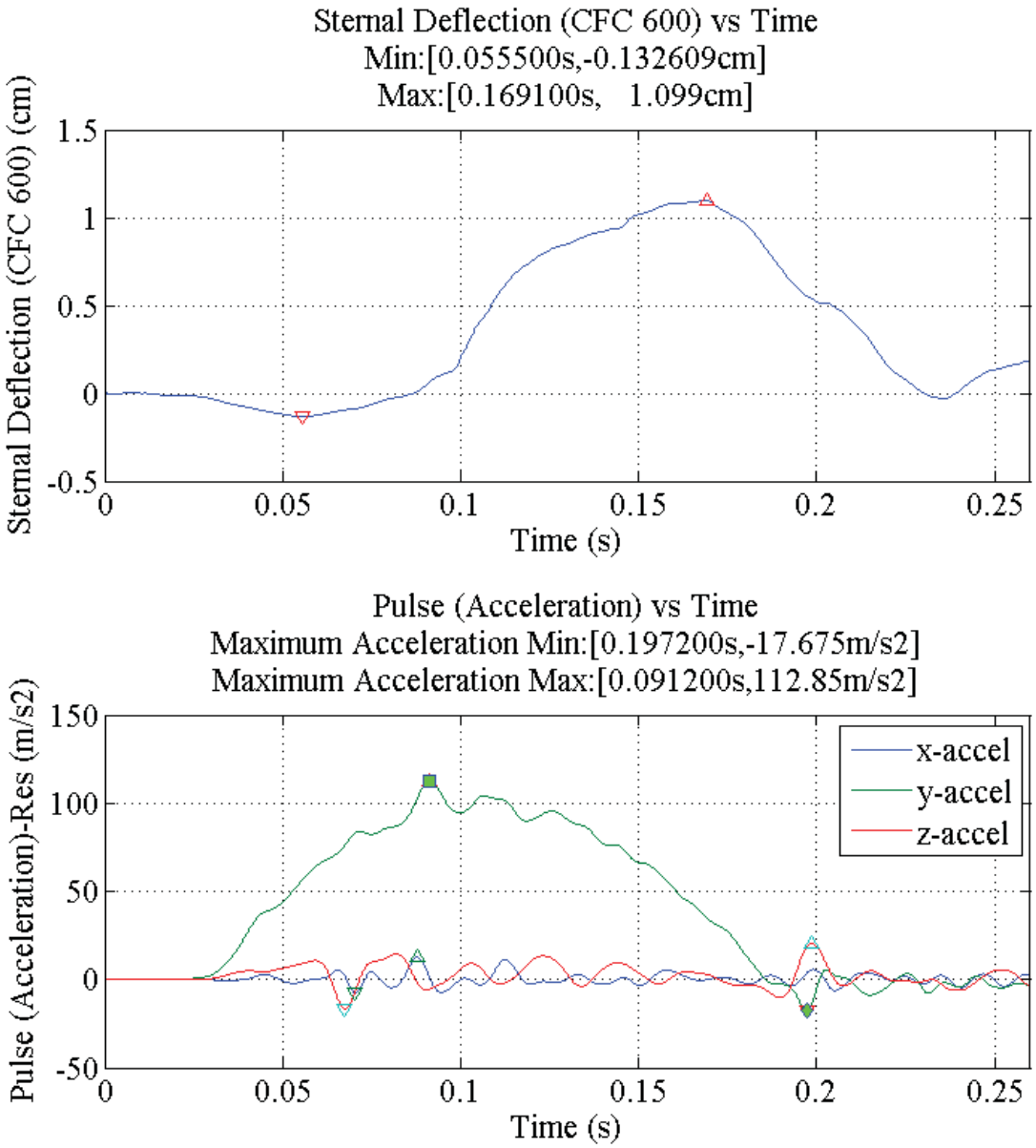

Figure 119: Sternal Deflection for simulation 8245 (Lateral), long pulse.

Appendix 9: Thorax Injury, Right Side Chest Deflection

Table 7: Tabulated Right Side Chest Deflection

Simulation	Right Side Chest Deflection (cm)
8202, Frontal, Short pulse	1.652
8202, Frontal, Long pulse	1.674
8208, Spinal, Short pulse, X-axis gravity	1.700
8208, Spinal, Short pulse, Z-axis gravity	1.988
8208, Spinal, Long pulse, X-axis gravity	1.580
8212, Rear, Short pulse	-4.057
8212, Rear, Long pulse	-4.047
8245, Lateral, Short pulse	1.852
8245, Lateral, Long pulse	1.811

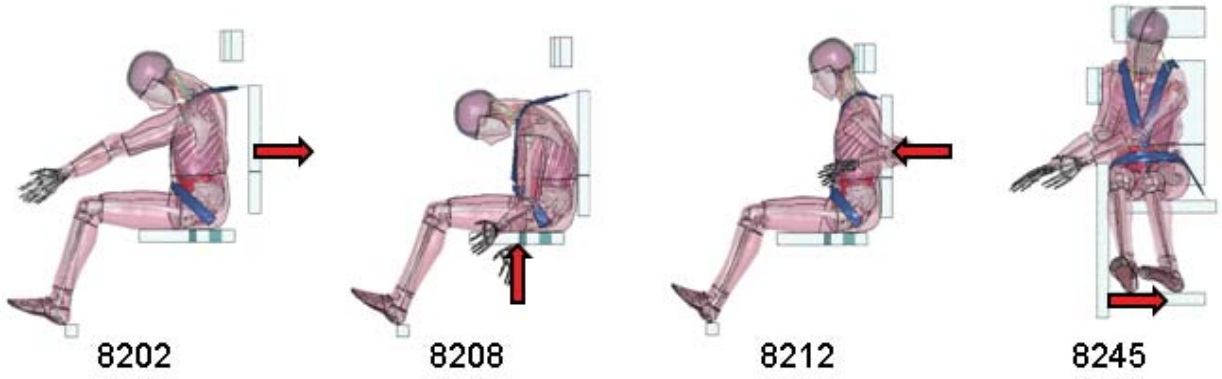

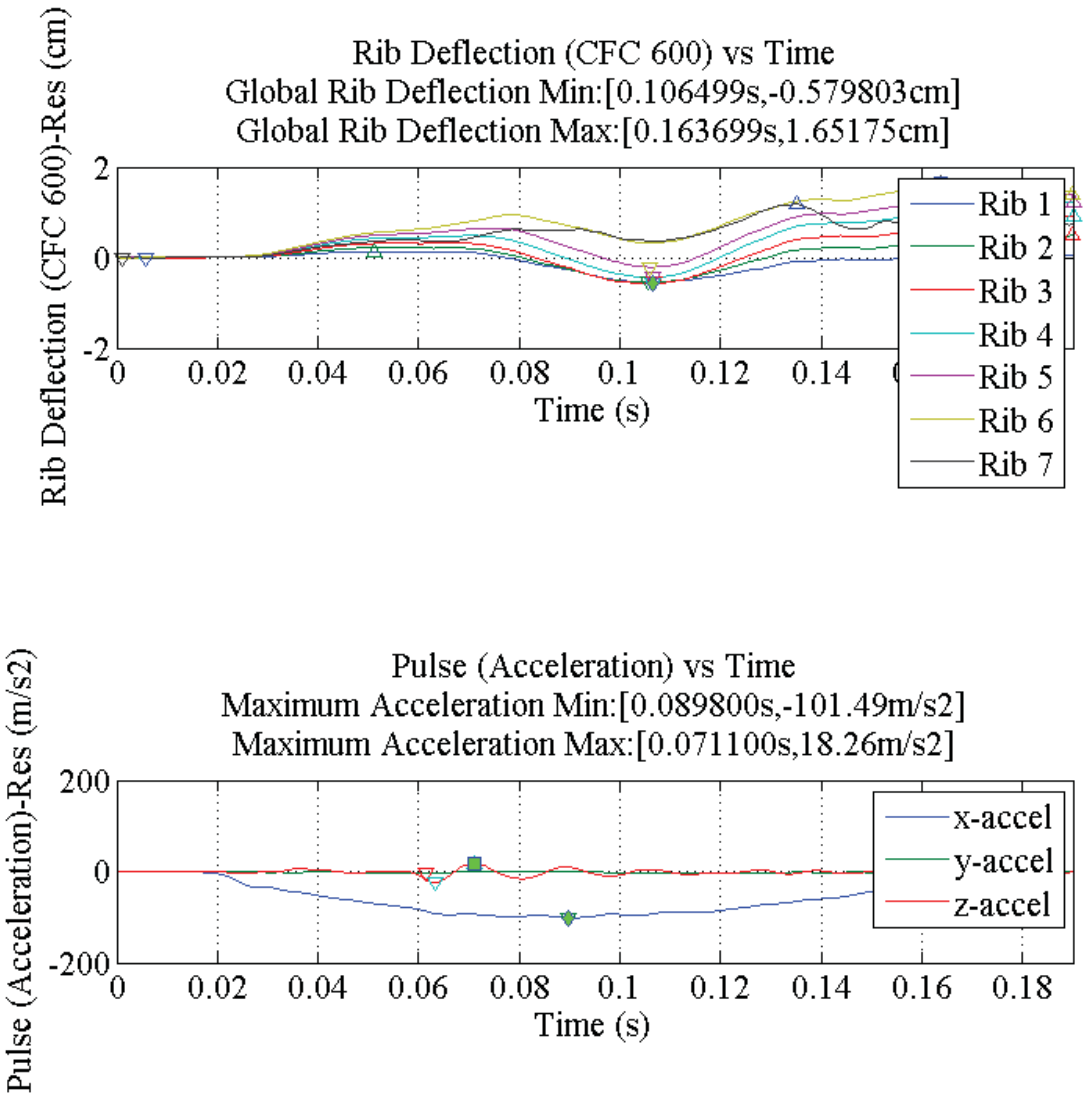

Figure 120: Right Side Chest Deflection for simulation 8202 (Frontal), short pulse.

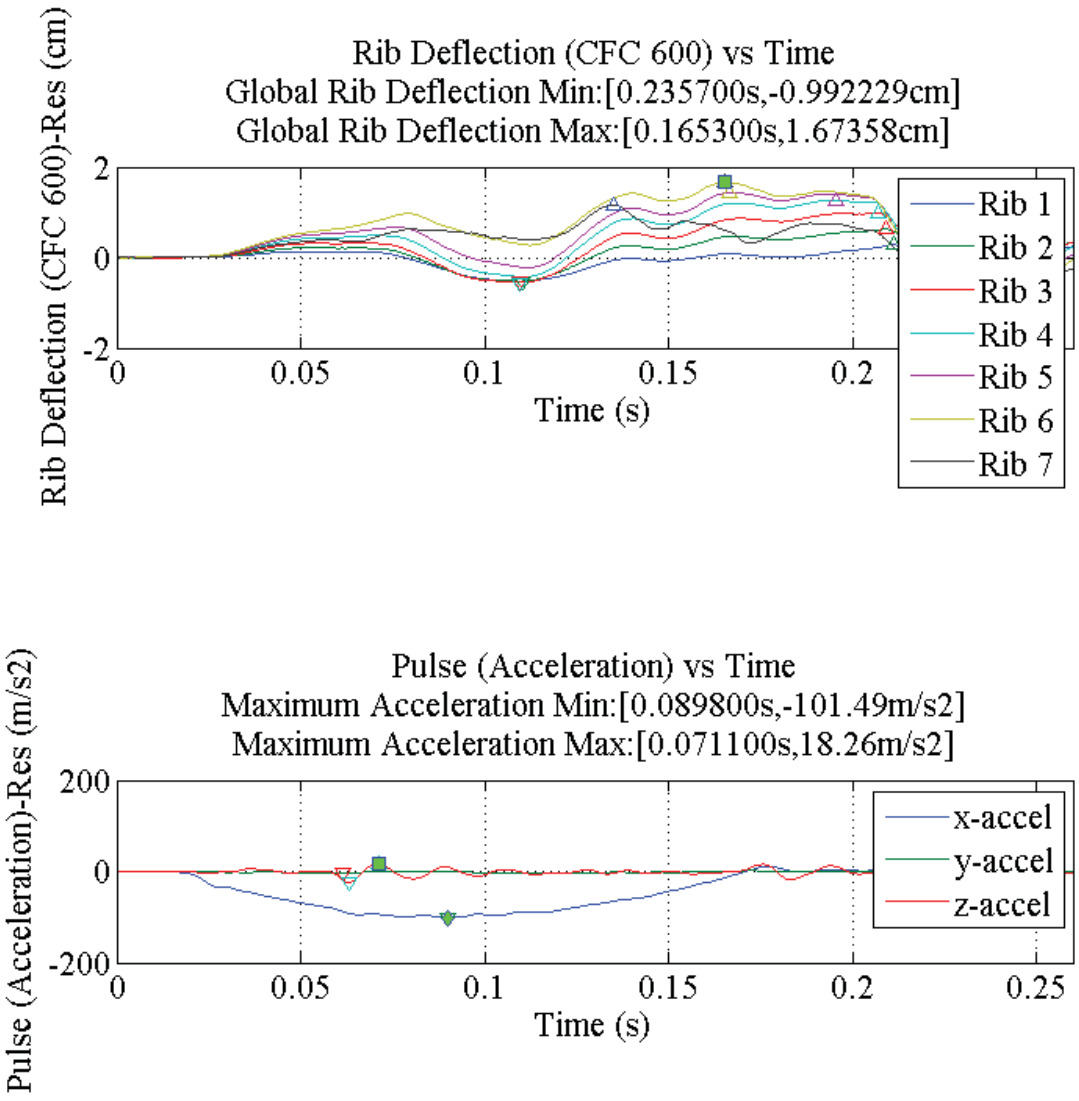

Figure 121: Right Side Chest Deflection for simulation 8202 (Frontal), long pulse.

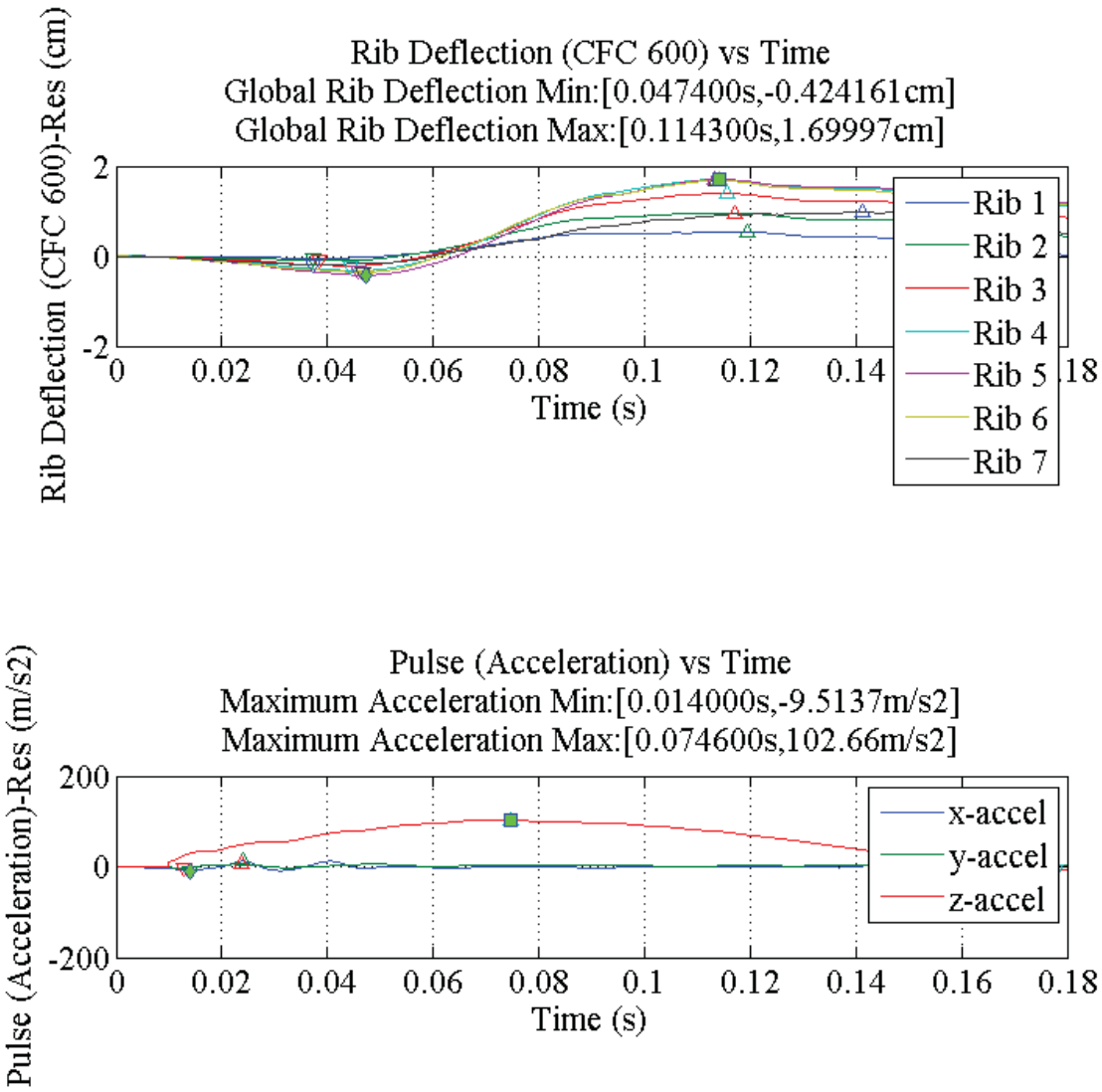

Figure 122: Right Side Chest Deflection for simulation 8208 (Spinal), short pulse, X-axis gravity.

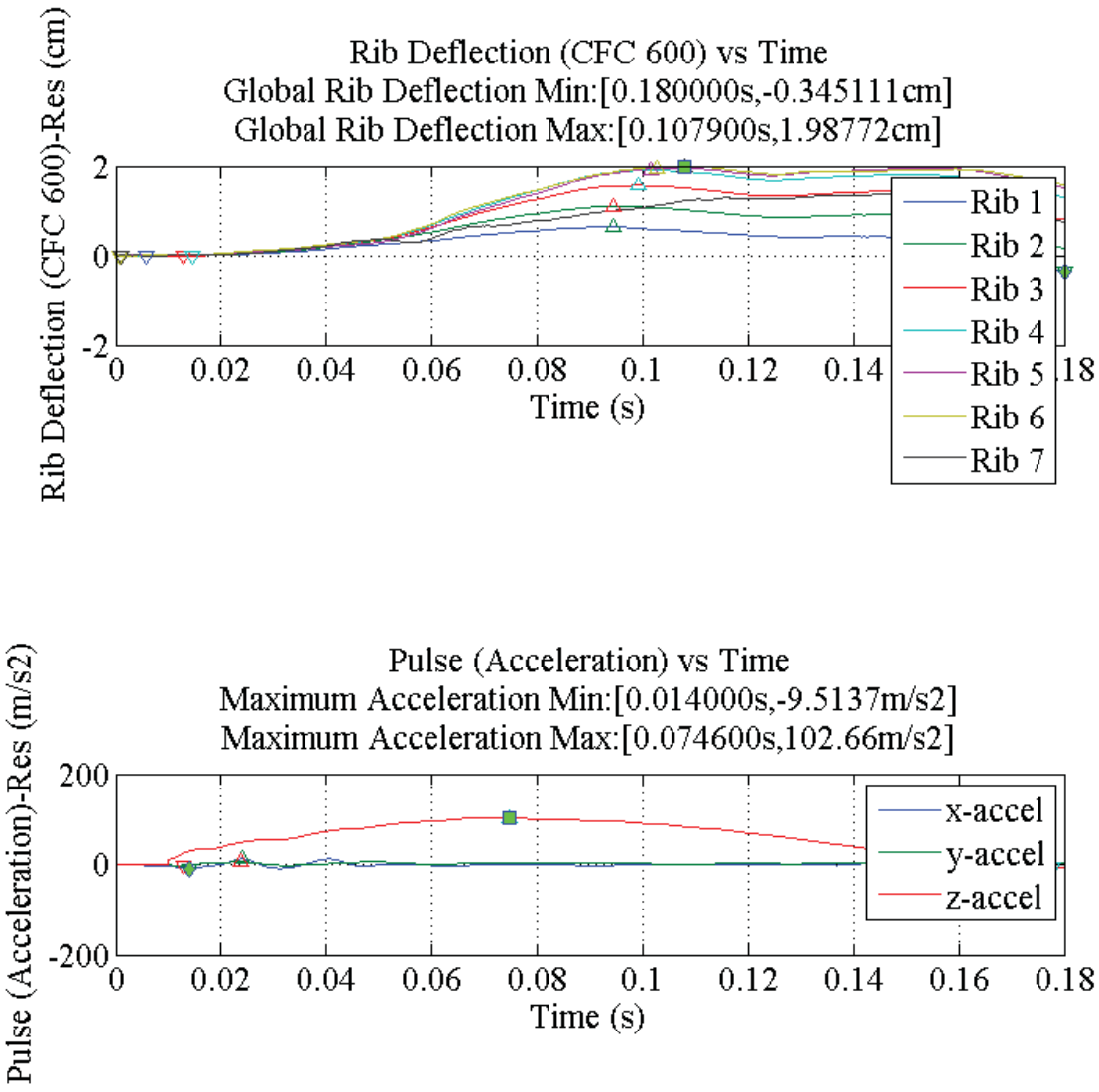

Figure 123: Right Side Chest Deflection for simulation 8208 (Spinal), short pulse, Z-axis gravity.

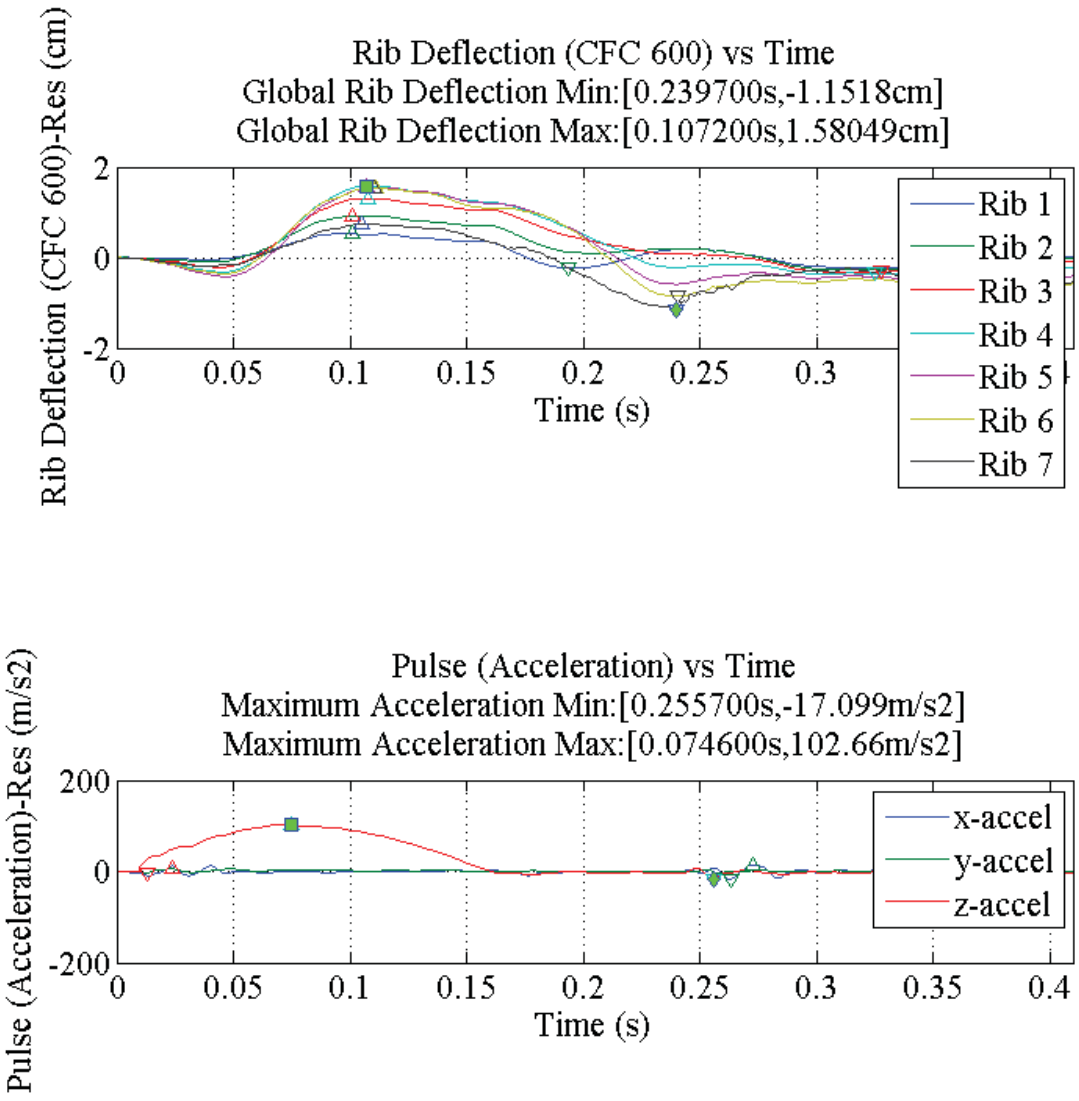

Figure 124: Right Side Chest Deflection for simulation 8208 (Spinal), long pulse, X-axis gravity.

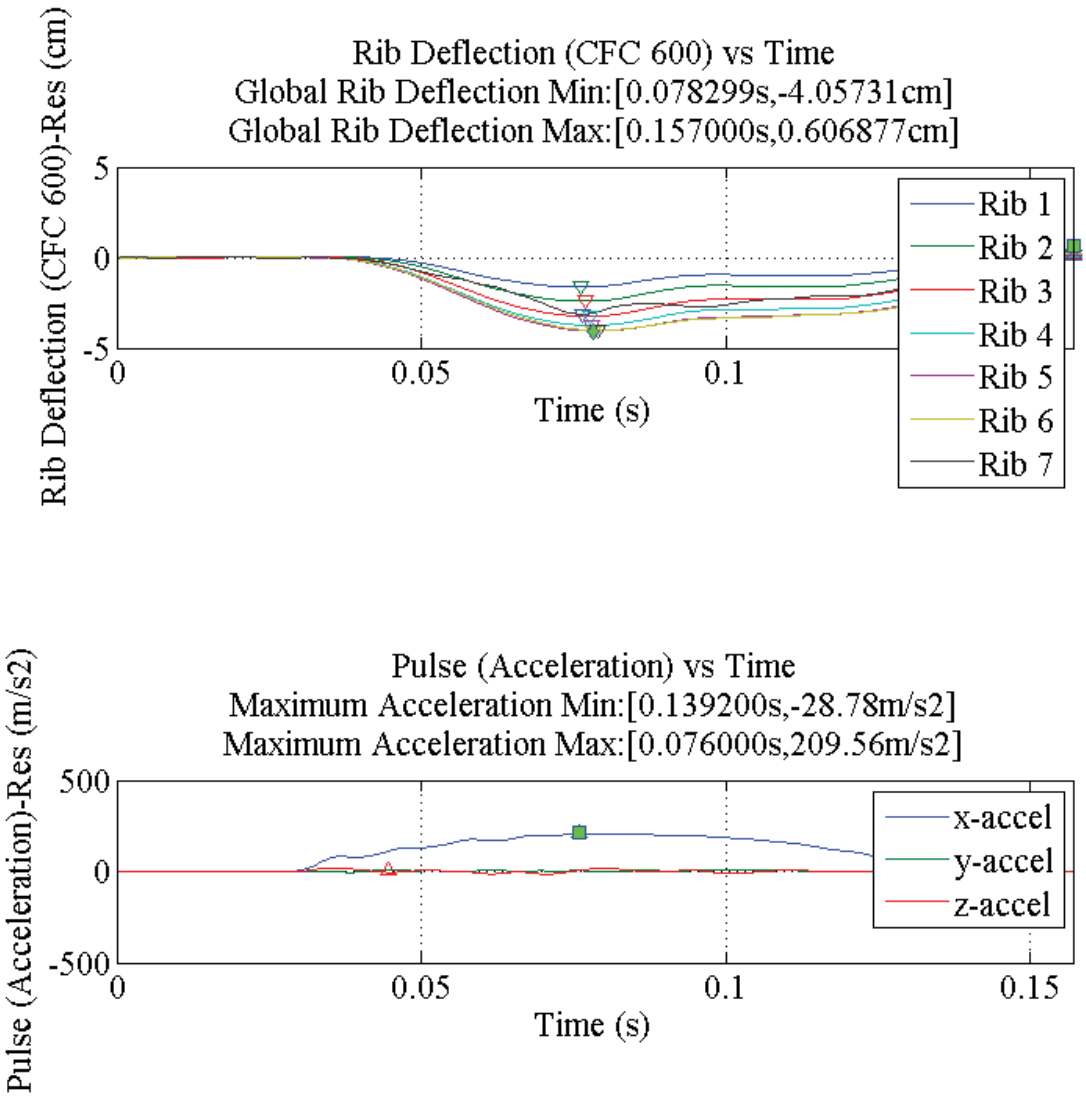

Figure 125: Right Side Chest Deflection for simulation 8212 (Rear), short pulse.

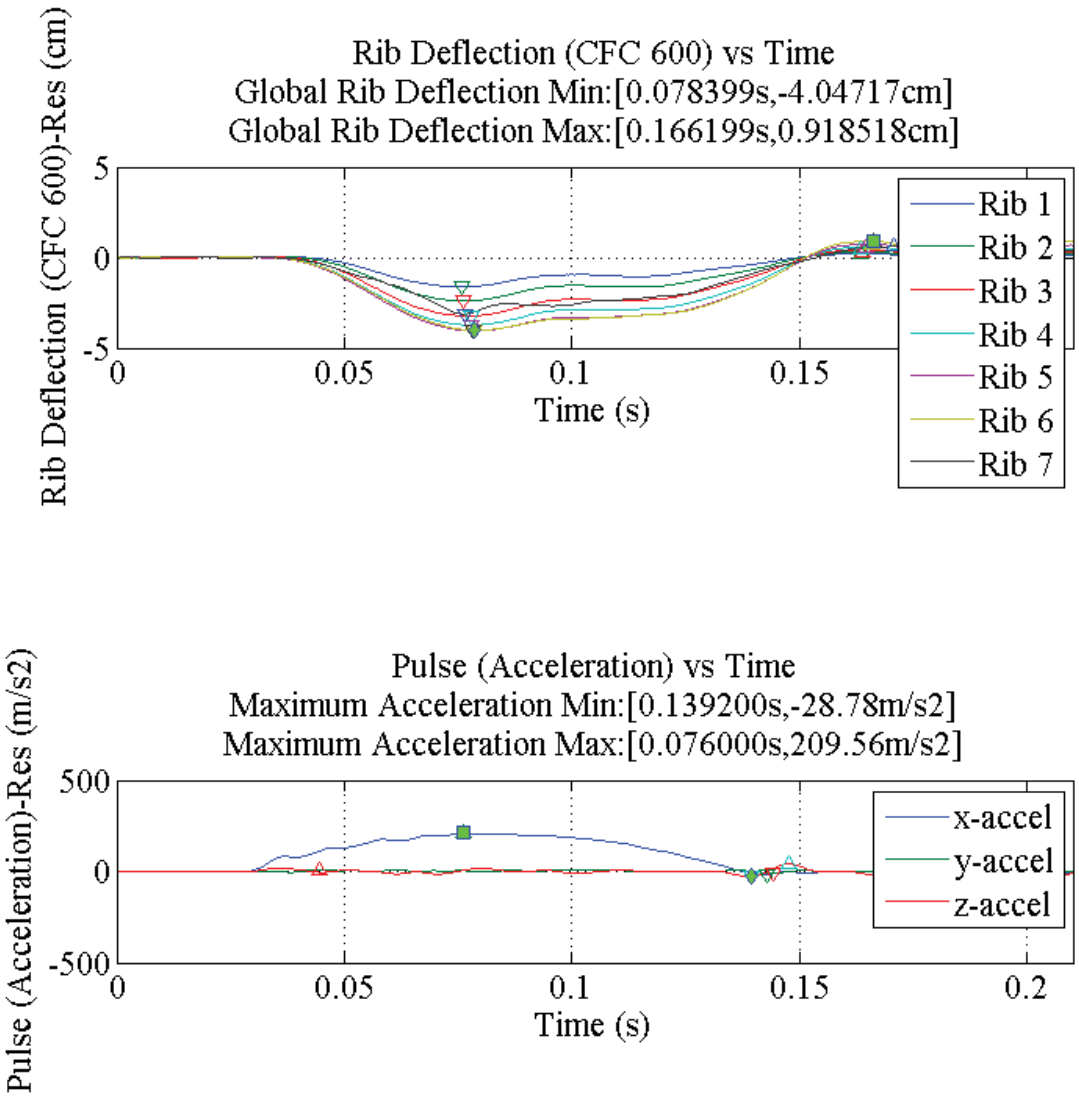

Figure 126: Right Side Chest Deflection for simulation 8212 (Rear), long pulse.

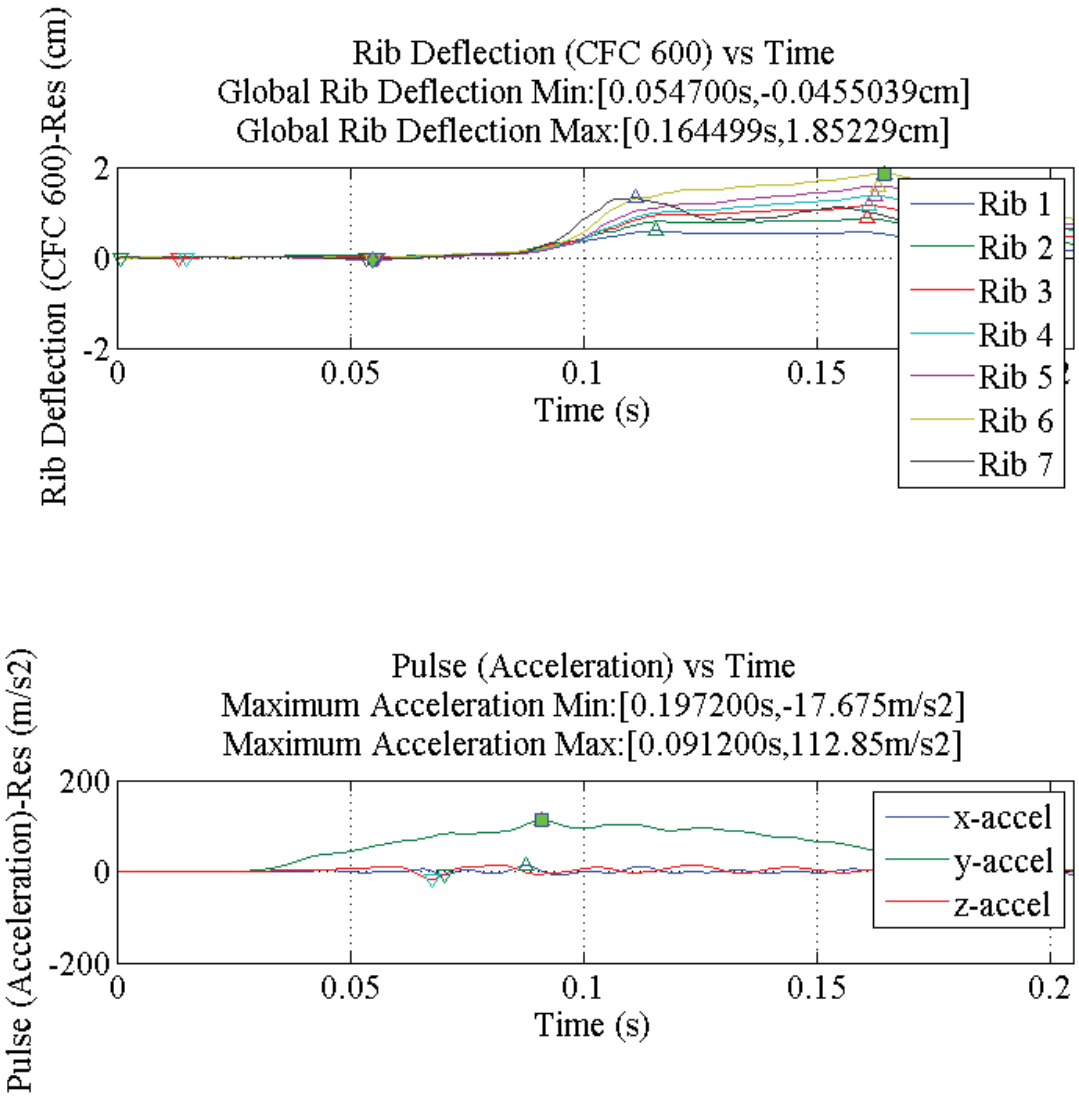

Figure 127: Right Side Chest Deflection for simulation 8245 (Lateral), short pulse.

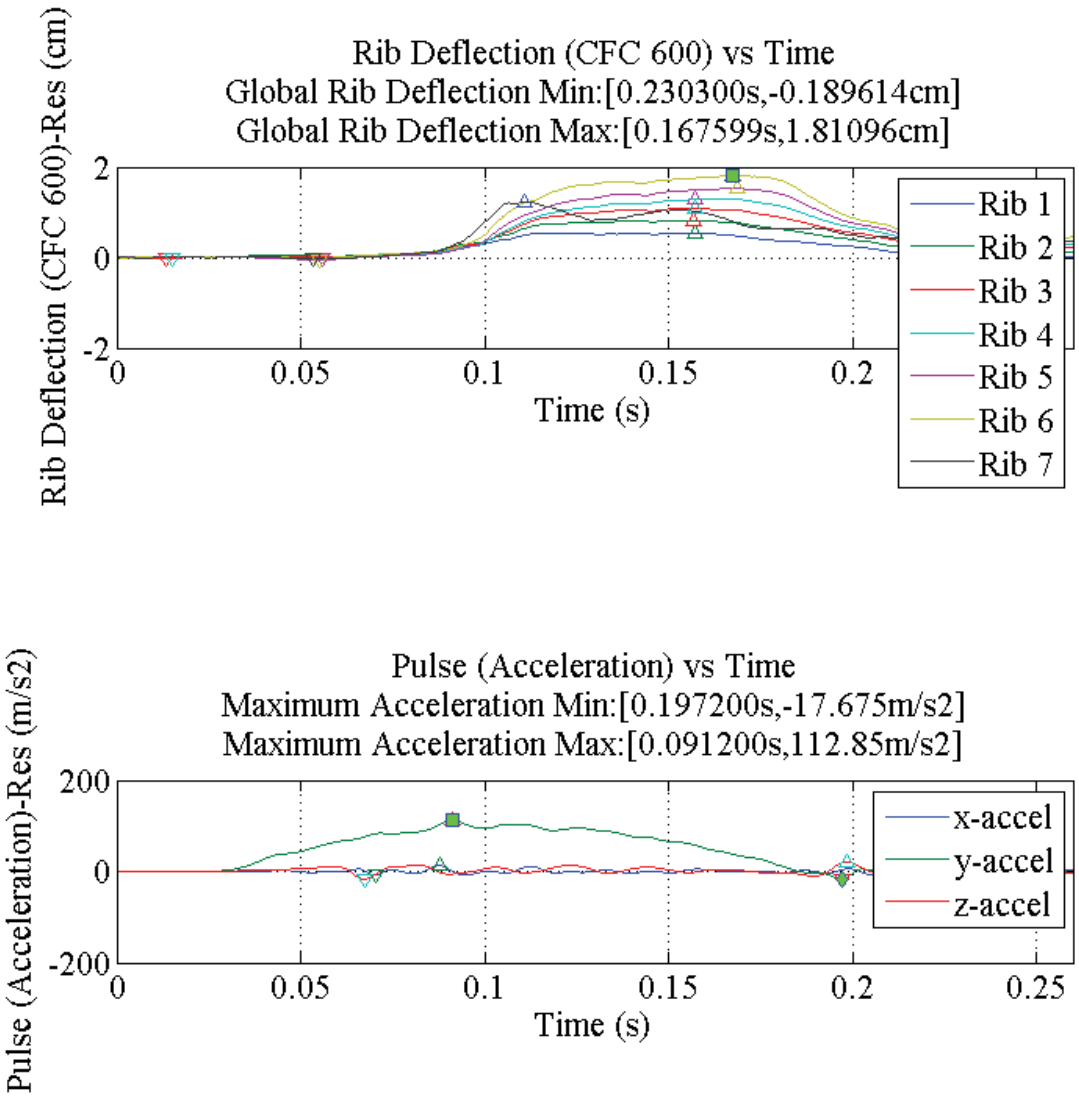

Figure 128: Right Side Chest Deflection for simulation 8245 (Lateral), long pulse.

Appendix 10: Thorax Injury, Left Side Chest Deflection

Table 8: Tabulated Left Side Chest Deflection

Simulation	Left Side Chest Deflection (cm)
8202, Frontal, Short pulse	1.652
8202, Frontal, Long pulse	1.674
8208, Spinal, Short pulse, X-axis gravity	1.700
8208, Spinal, Short pulse, Z-axis gravity	1.700
8208, Spinal, Long pulse, X-axis gravity	1.580
8212, Rear, Short pulse	-4.057
8212, Rear, Long pulse	-4.047
8245, Lateral, Short pulse	1.852
8245, Lateral, Long pulse	1.811

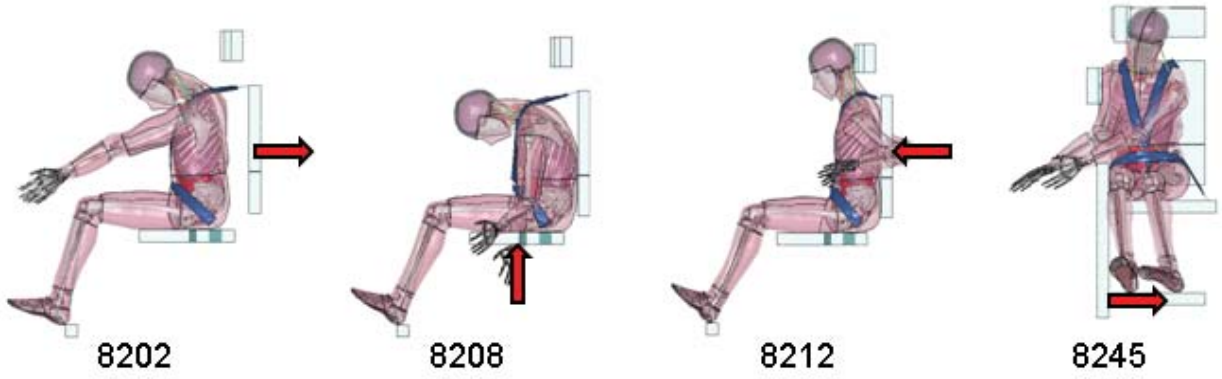

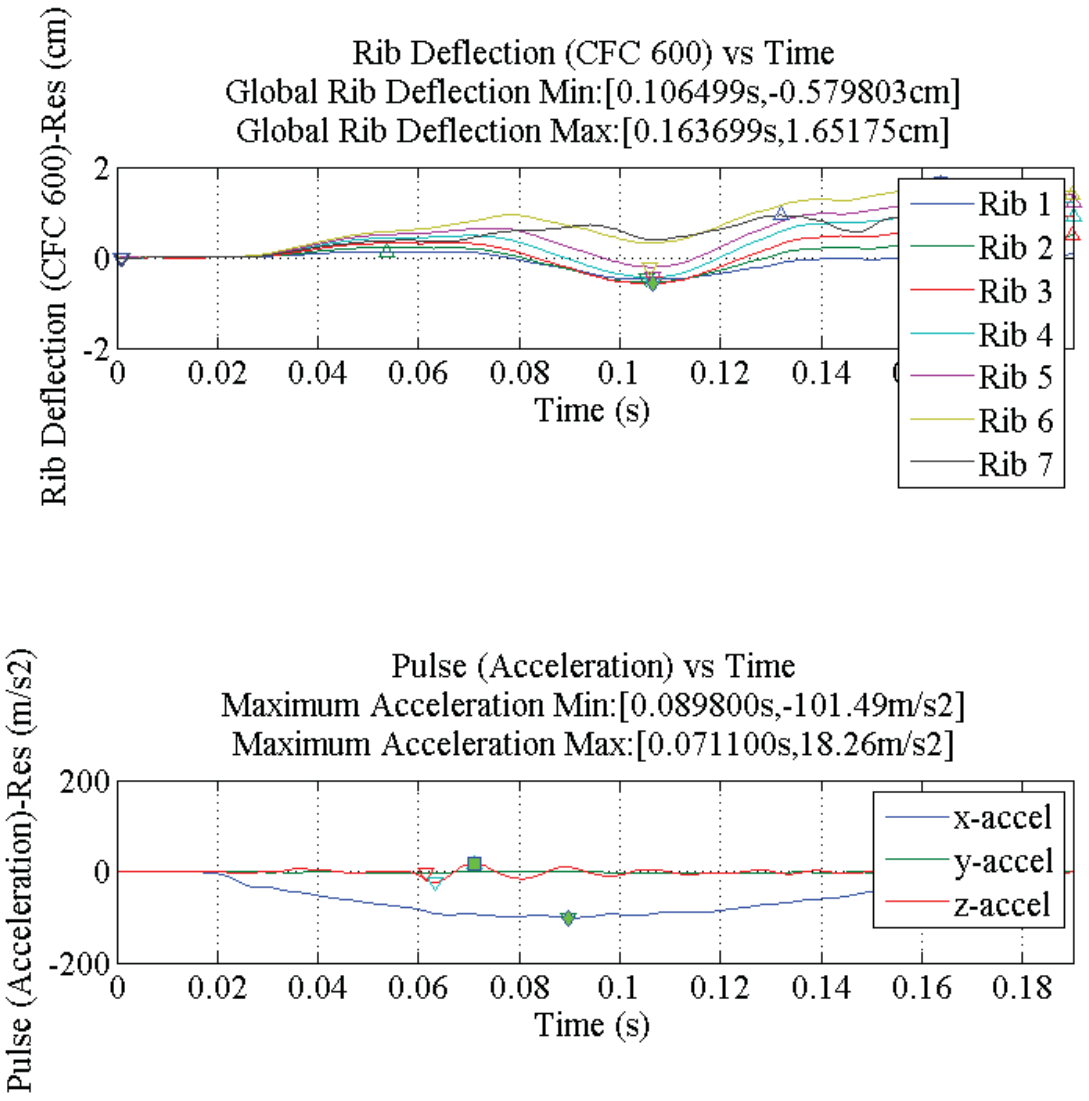

Figure 129: Left Side Chest Deflection for simulation 8202 (Frontal), short pulse.

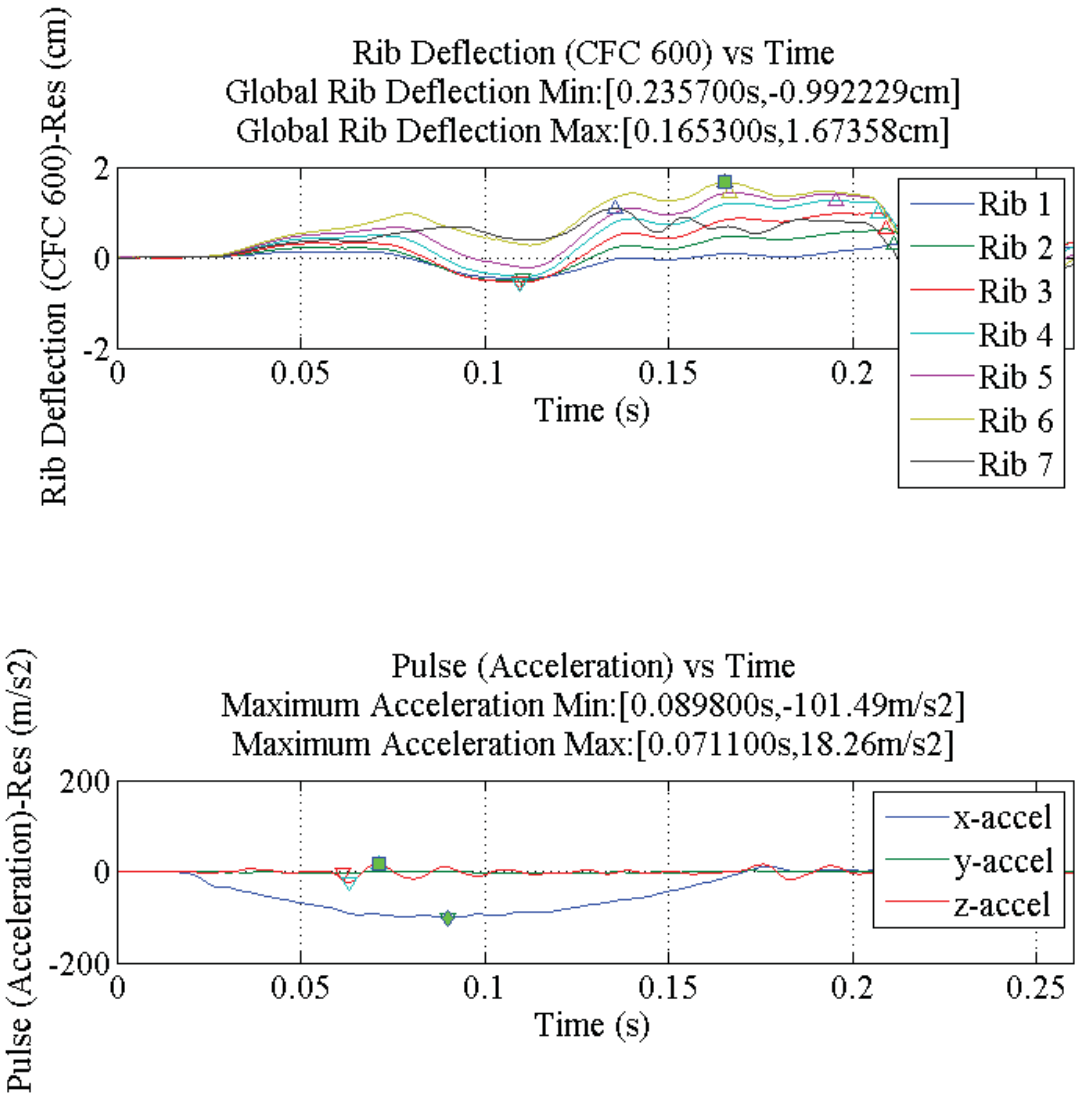

Figure 130: Left Side Chest Deflection for simulation 8202 (Frontal), short pulse.

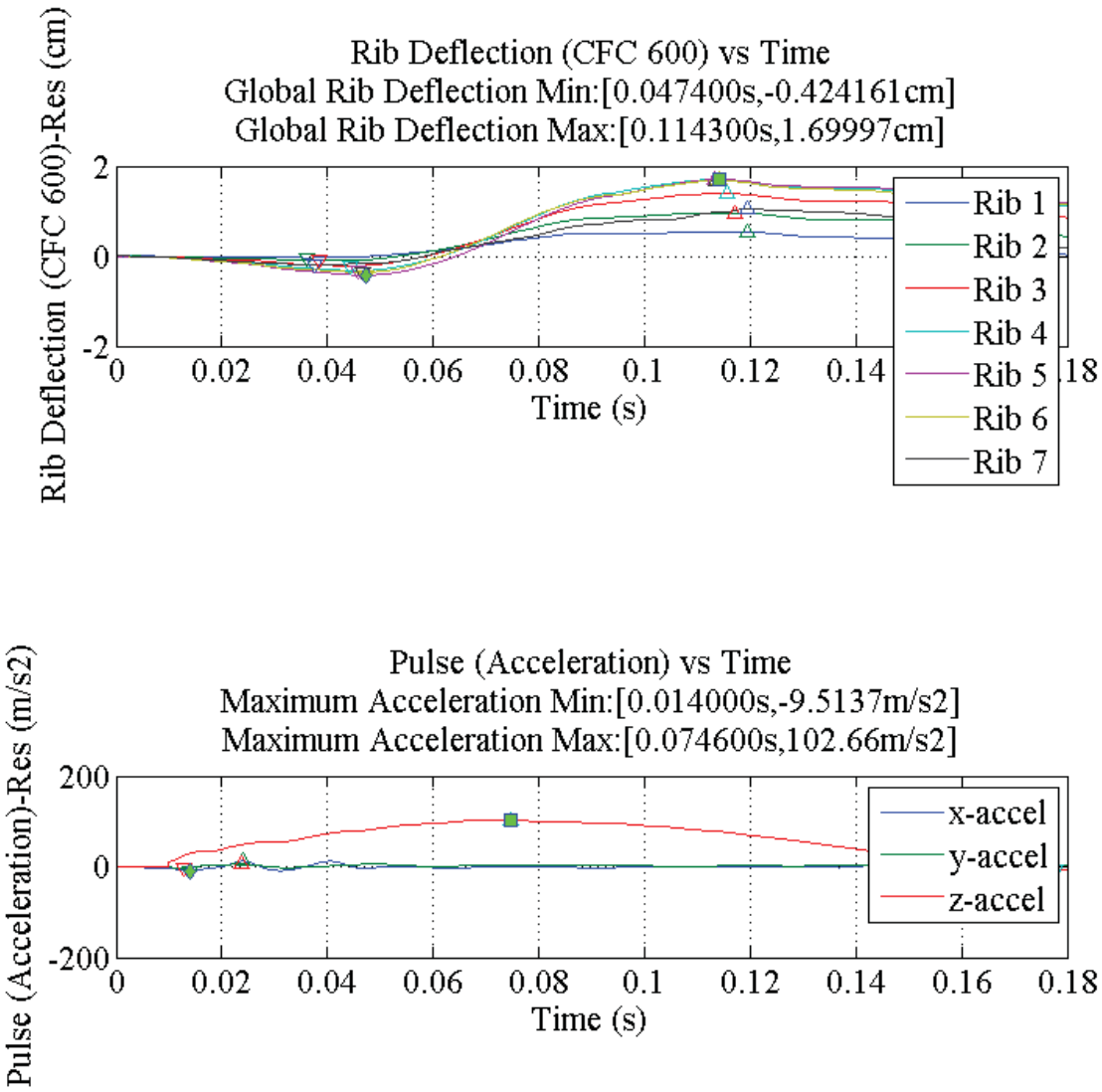

Figure 131: Left Side Chest Deflection for simulation 8208 (Spinal), short pulse, X-axis gravity.

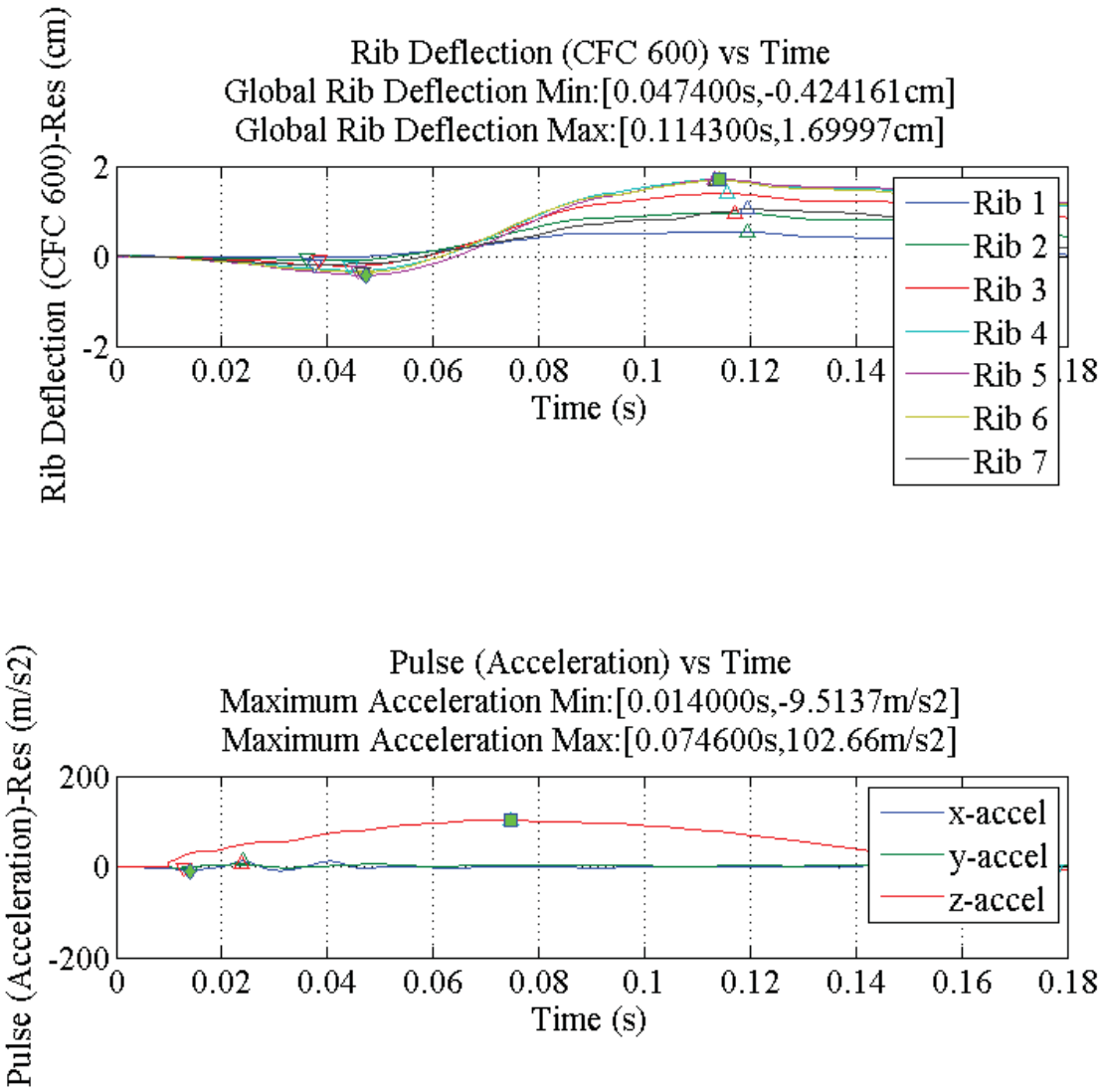

Figure 132: Left Side Chest Deflection for simulation 8208 (Spinal), short pulse, Z-axis gravity.

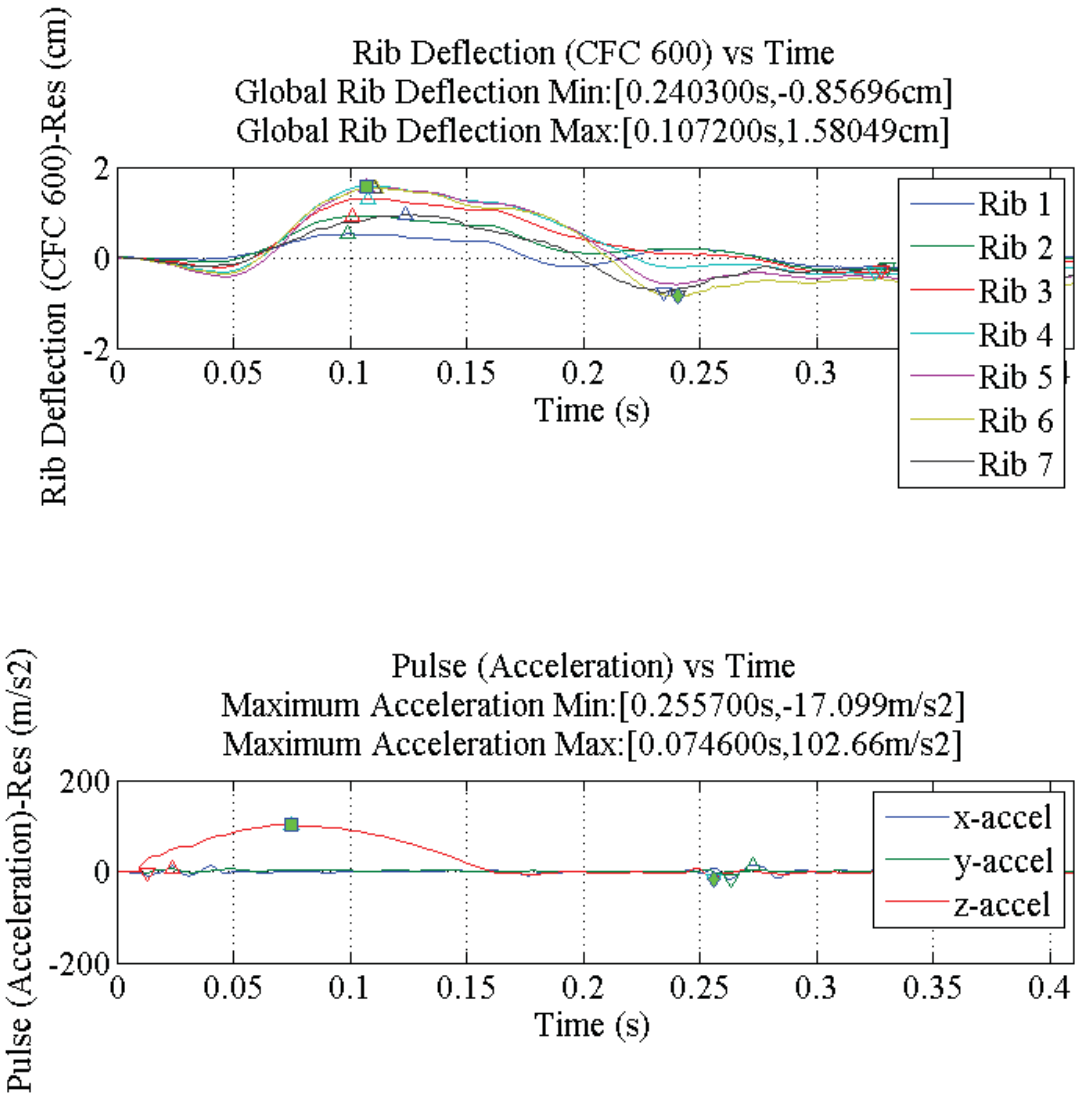

Figure 133: Left Side Chest Deflection for simulation 8208 (Spinal), long pulse, X-axis gravity.

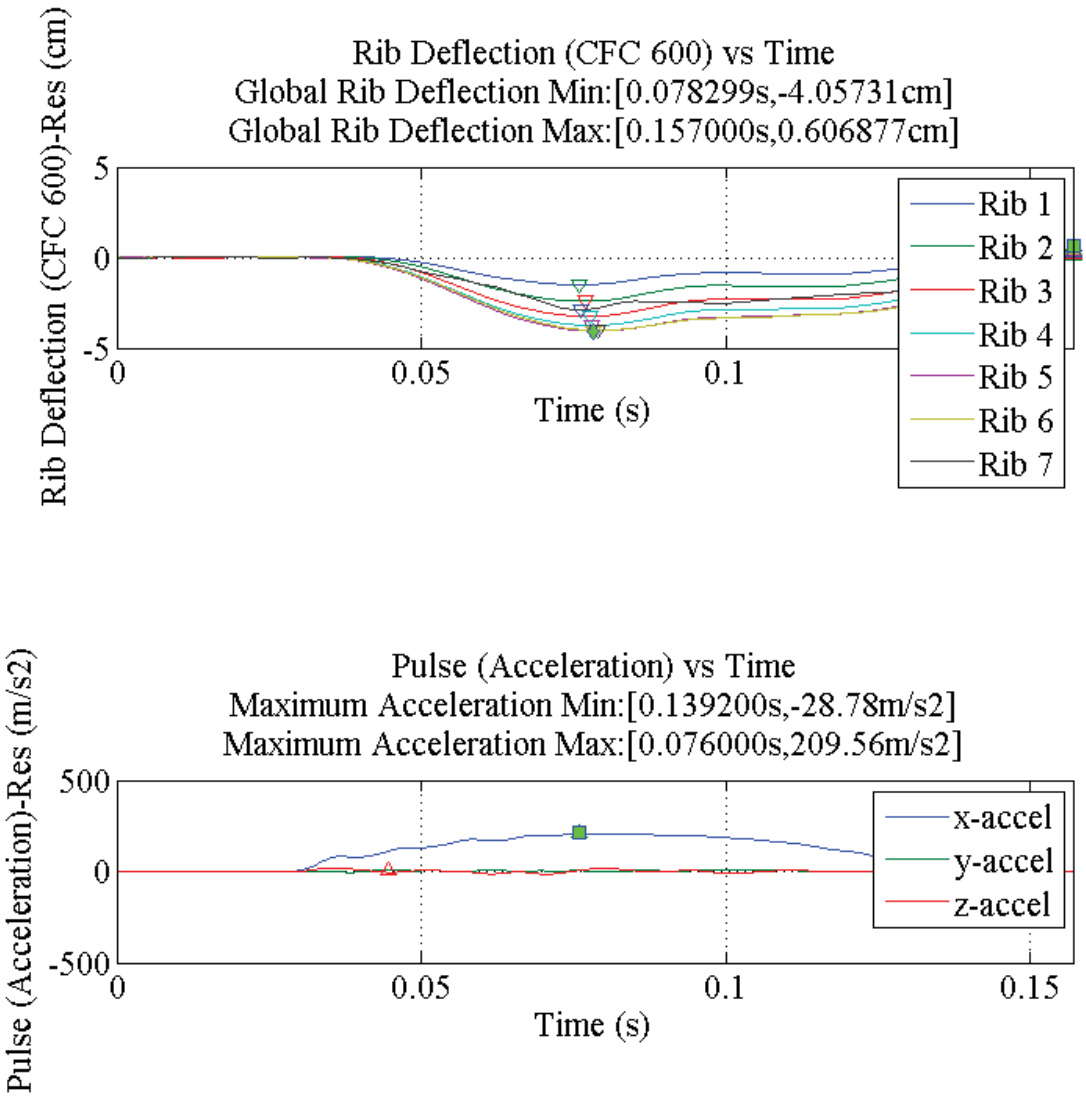

Figure 134: Left Side Chest Deflection for simulation 8212 (Rear), short pulse.

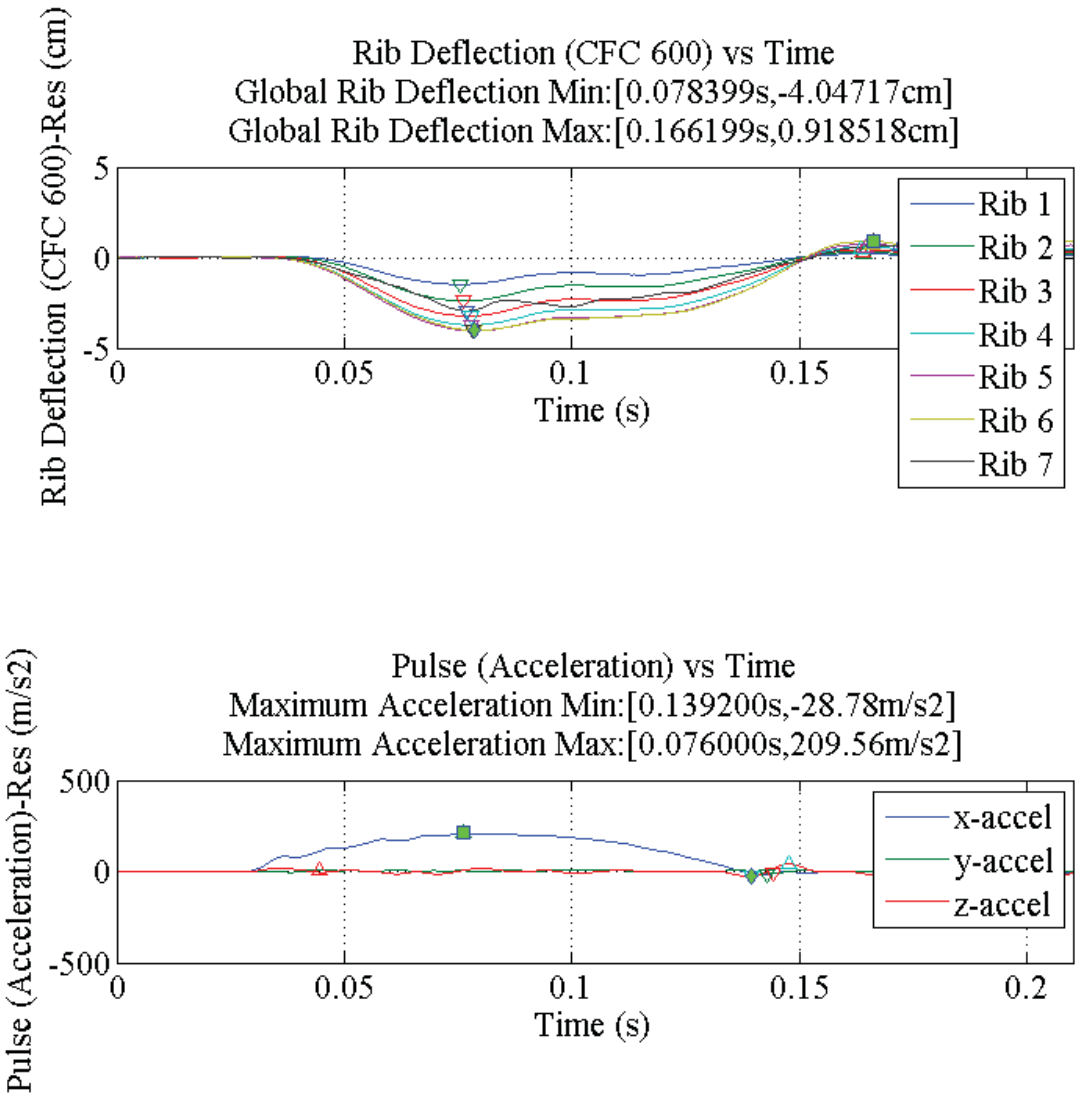

Figure 135: Left Side Chest Deflection for simulation 8212 (Rear), long pulse.

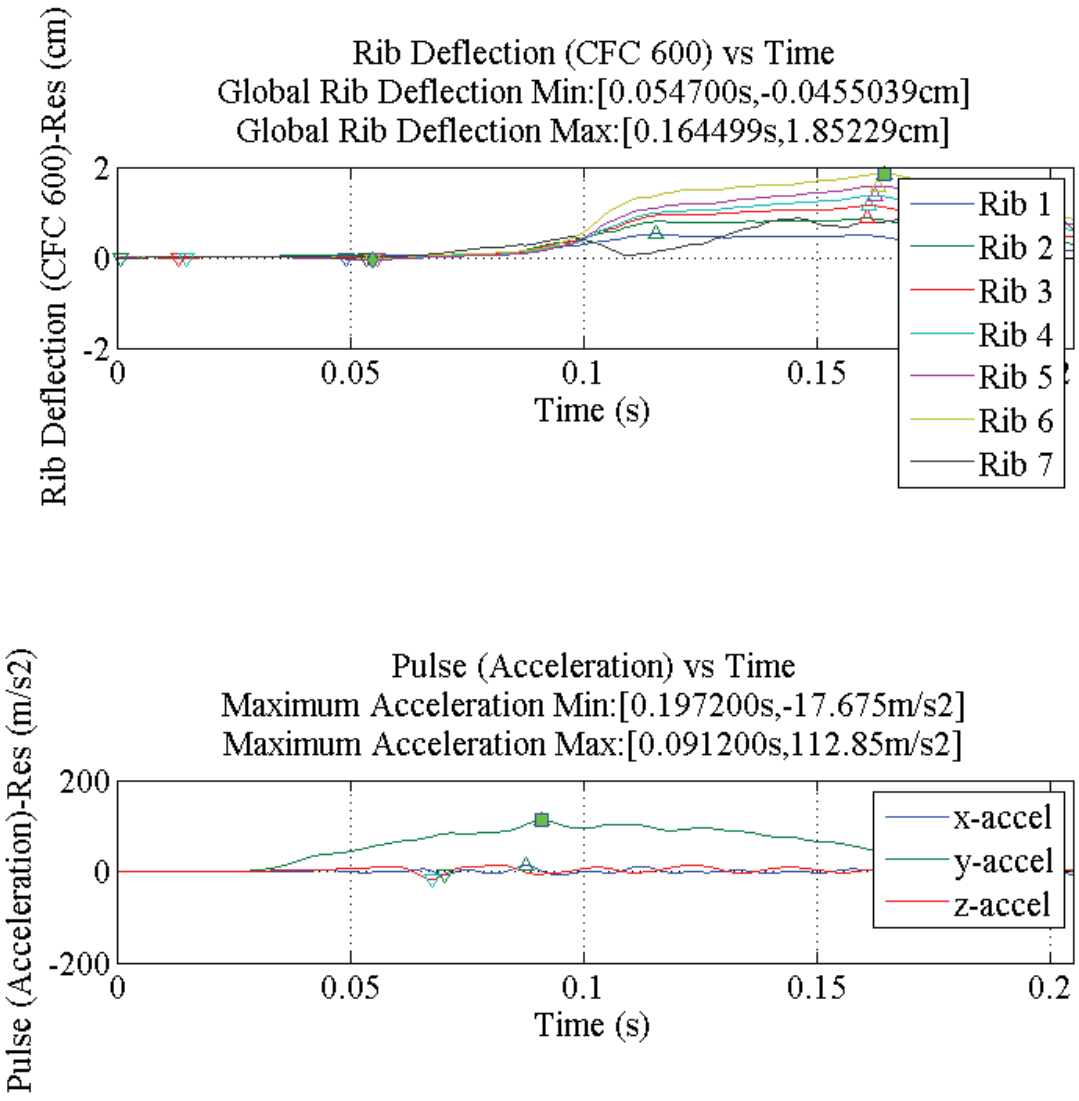

Figure 136: Left Side Chest Deflection for simulation 8245 (Lateral), short pulse.

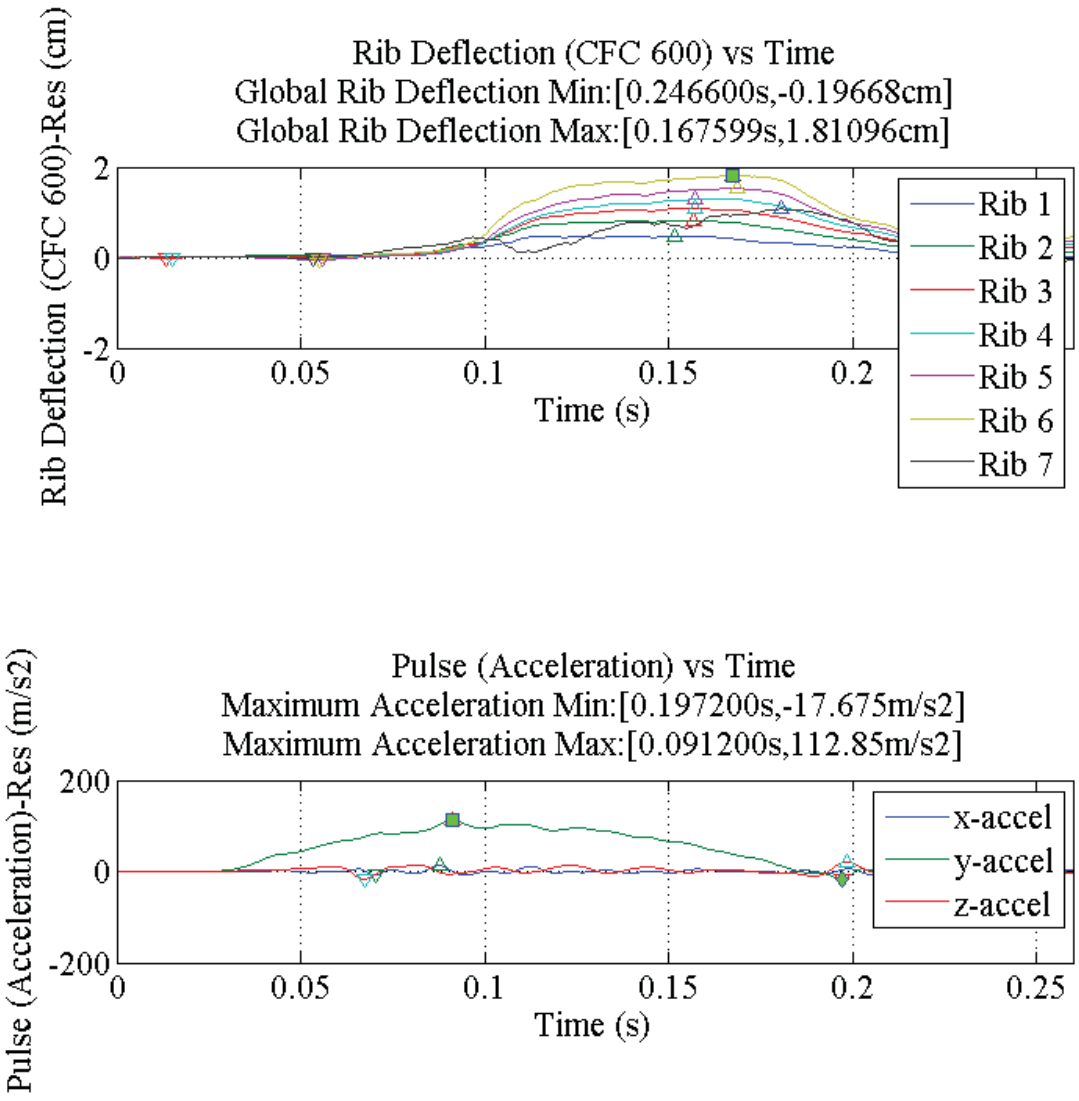

Figure 137: Left Side Chest Deflection for simulation 8245 (Lateral), long pulse.

Appendix 11: Thorax Injury, Chest Acceleration

Table 9: Tabulated Chest Acceleration

Simulation	Chest Acceleration (g's)
8202, Frontal, Short pulse	19.435
8202, Frontal, Long pulse	26.553
8208, Spinal, Short pulse, X-axis gravity	13.869
8208, Spinal, Short pulse, Z-axis gravity	15.578
8208, Spinal, Long pulse, X-axis gravity	13.458
8212, Rear, Short pulse	29.141
8212, Rear, Long pulse	29.214
8245, Lateral, Short pulse	29.869
8245, Lateral, Long pulse	31.030

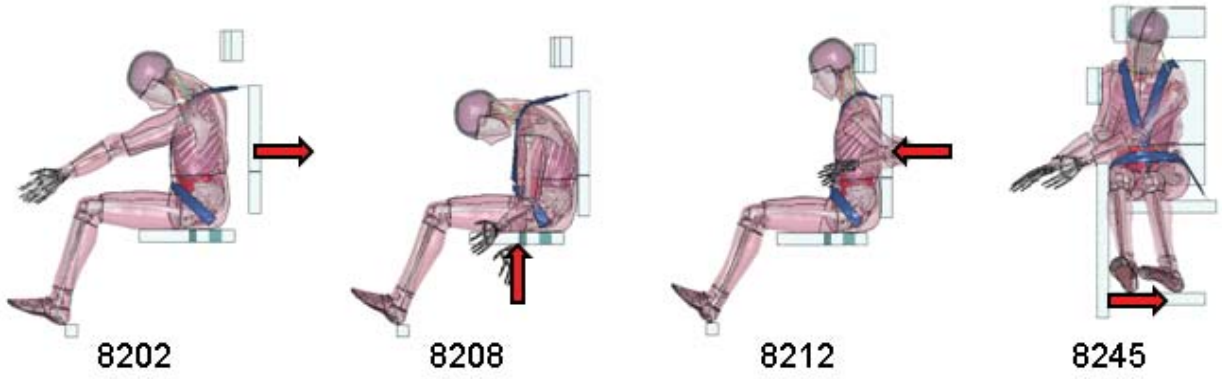

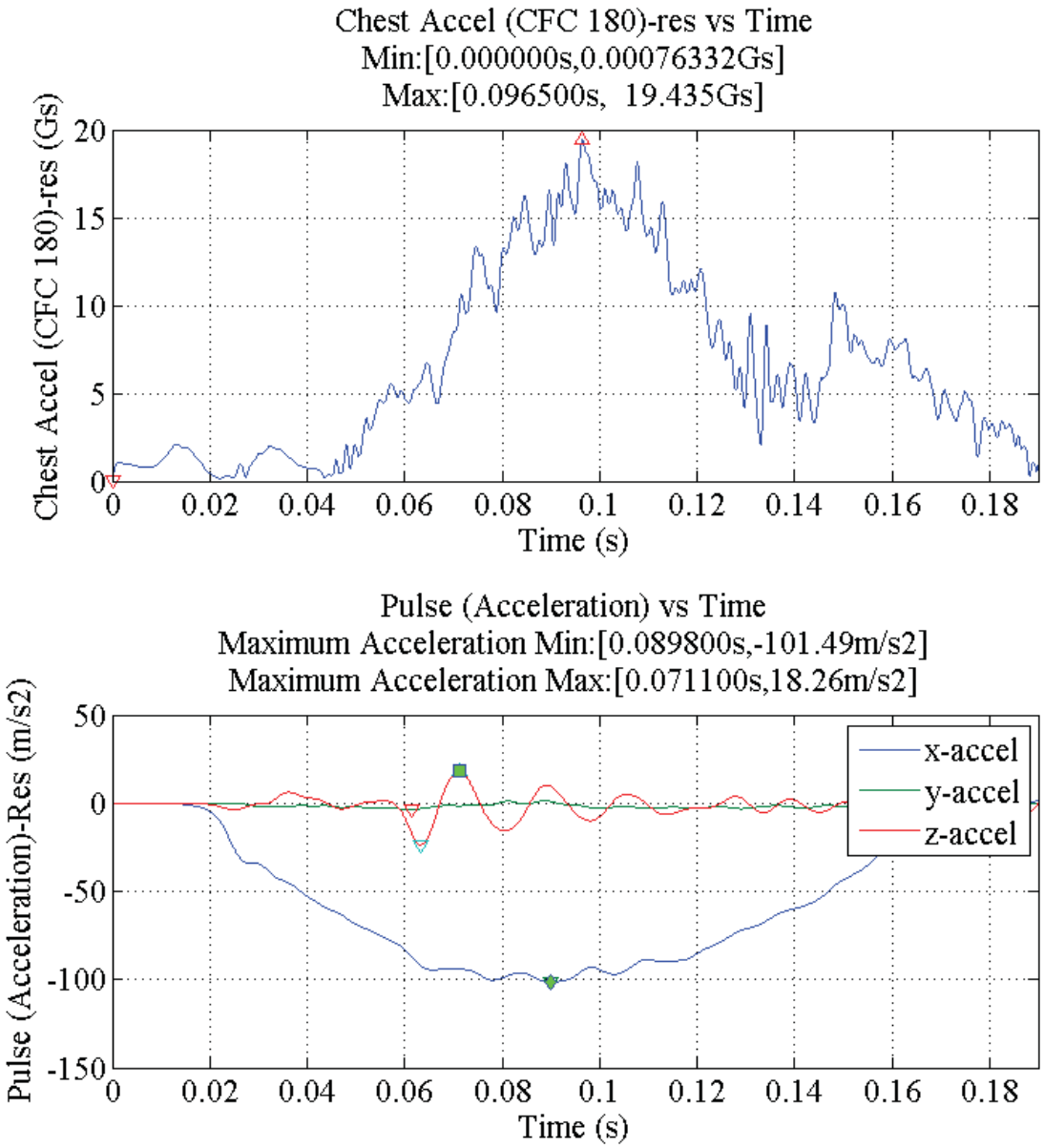

Figure 138: Chest Acceleration for simulation 8202 (Frontal), short pulse.

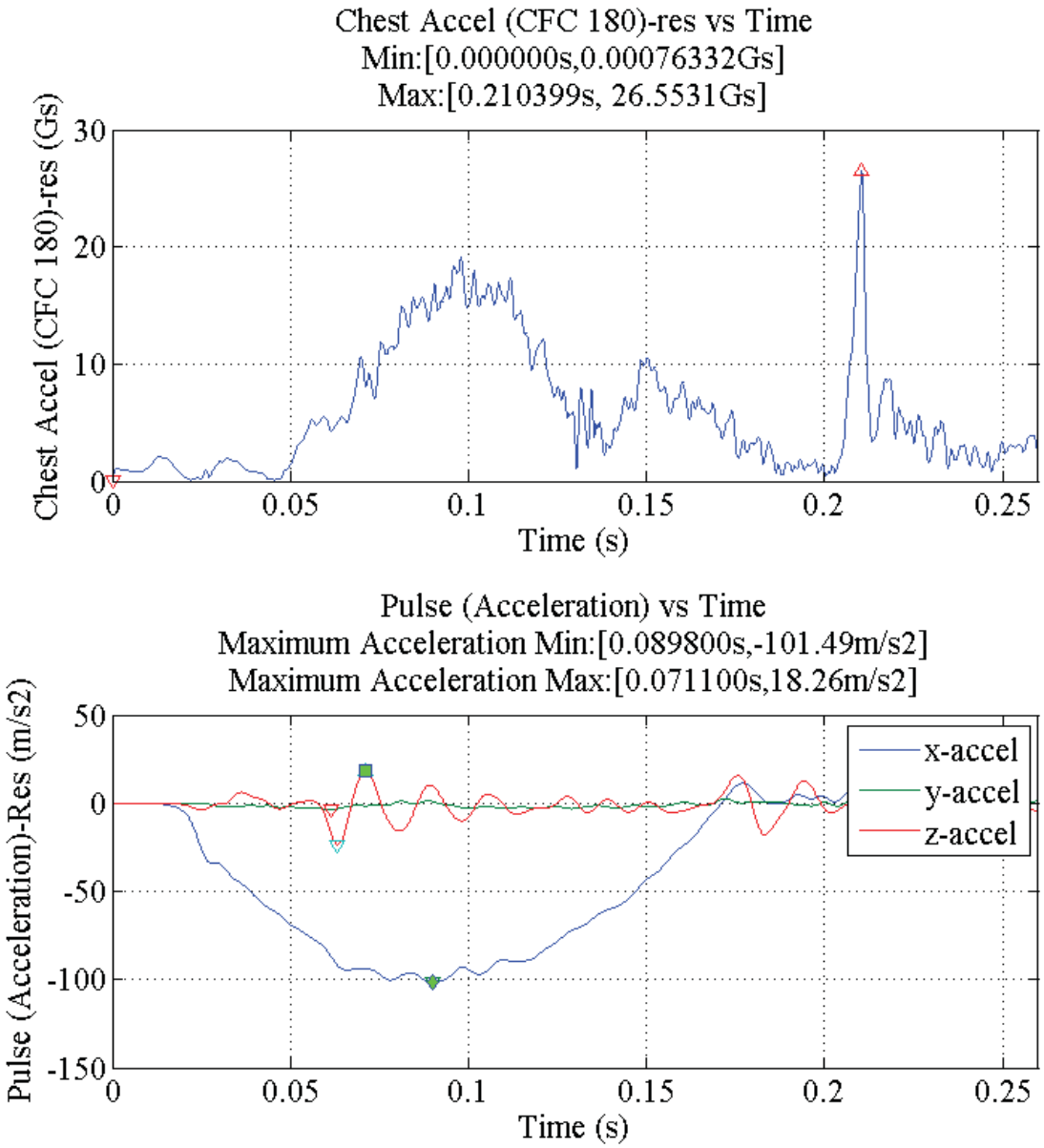

Figure 139: Chest Acceleration for simulation 8202 (Frontal), long pulse.

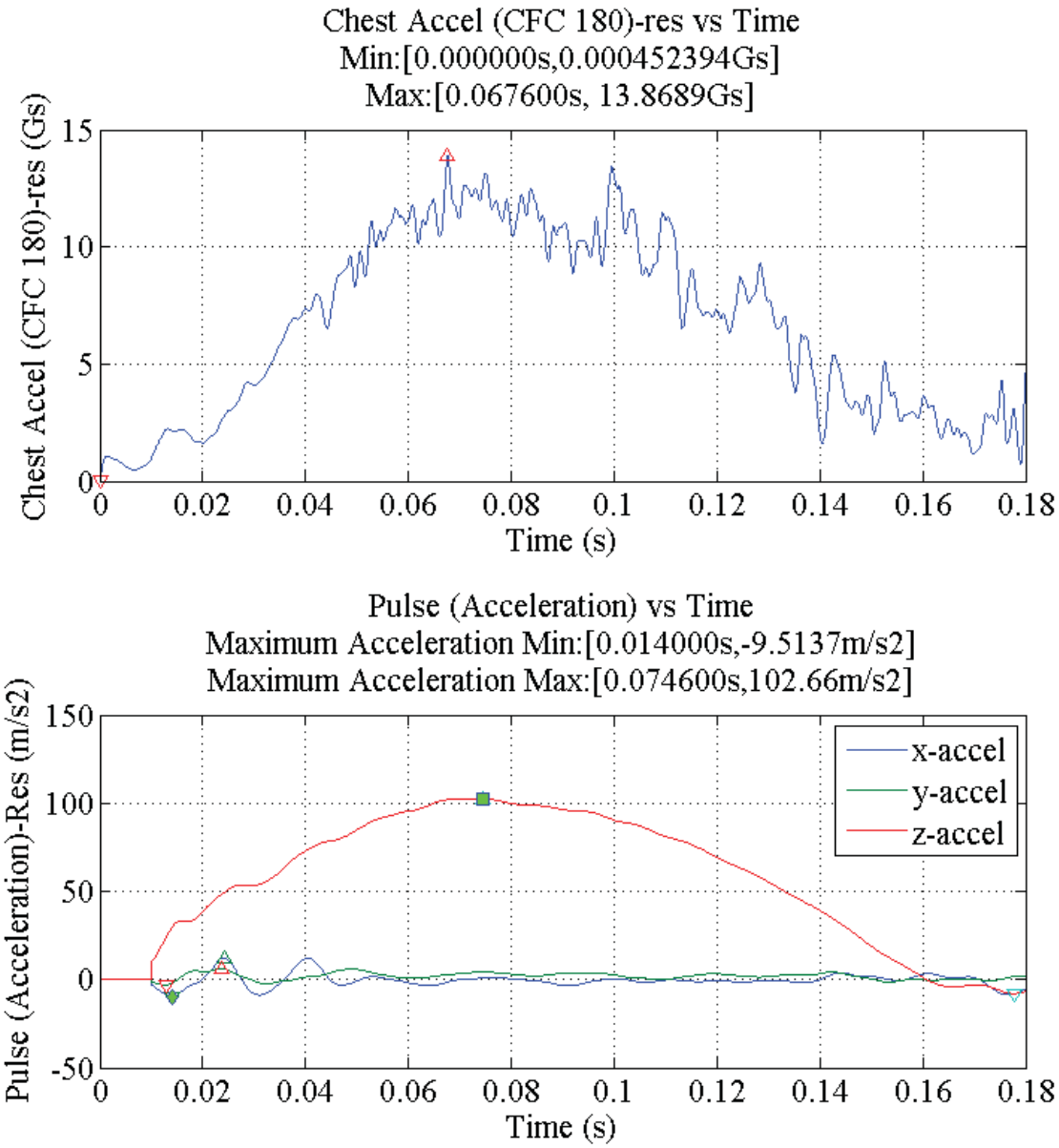

Figure 140: Chest Acceleration for simulation 8208 (Spinal), short pulse, X-axis gravity.

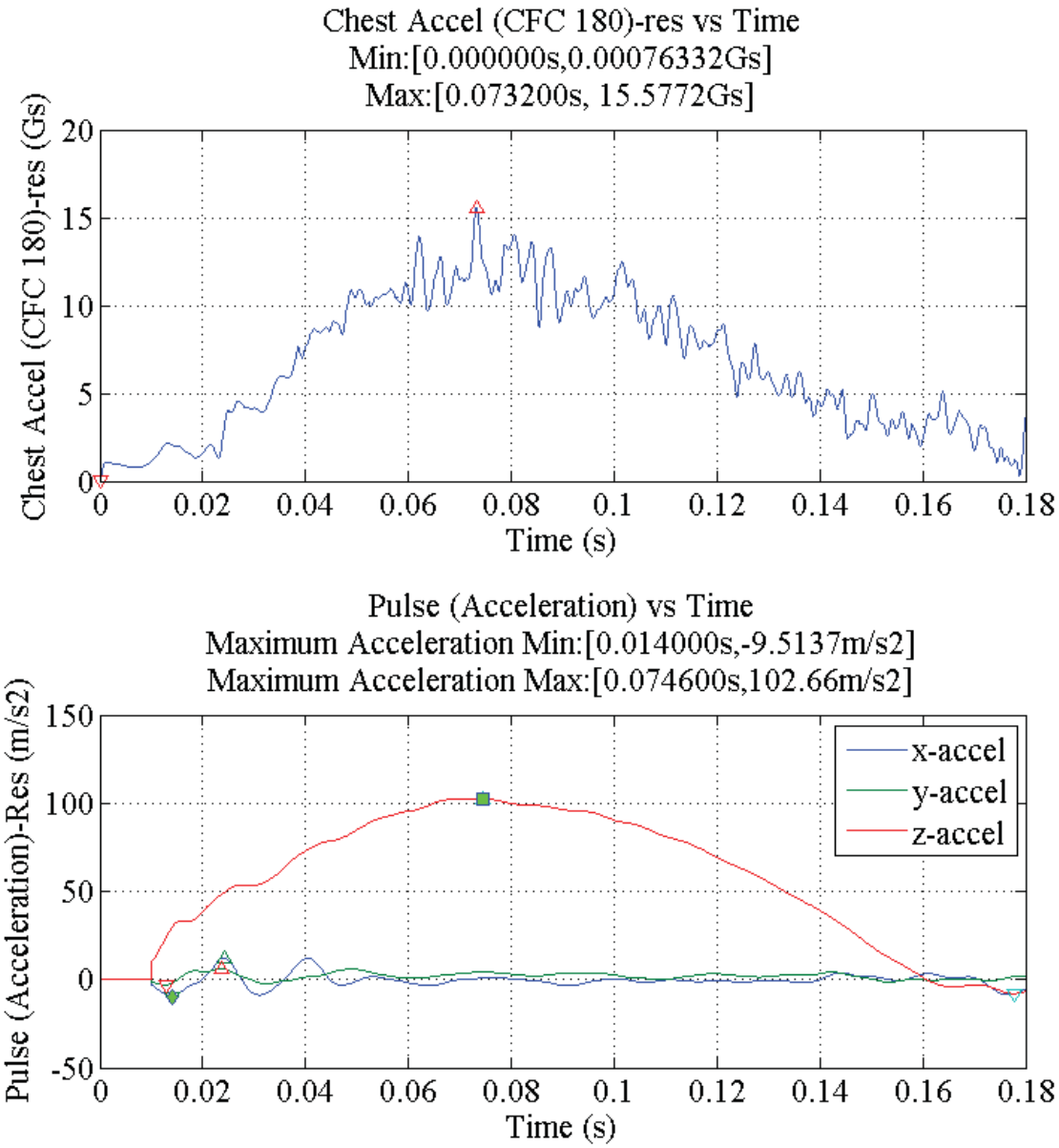

Figure 141: Chest Acceleration for simulation 8208 (Spinal), short pulse, Z-axis gravity.

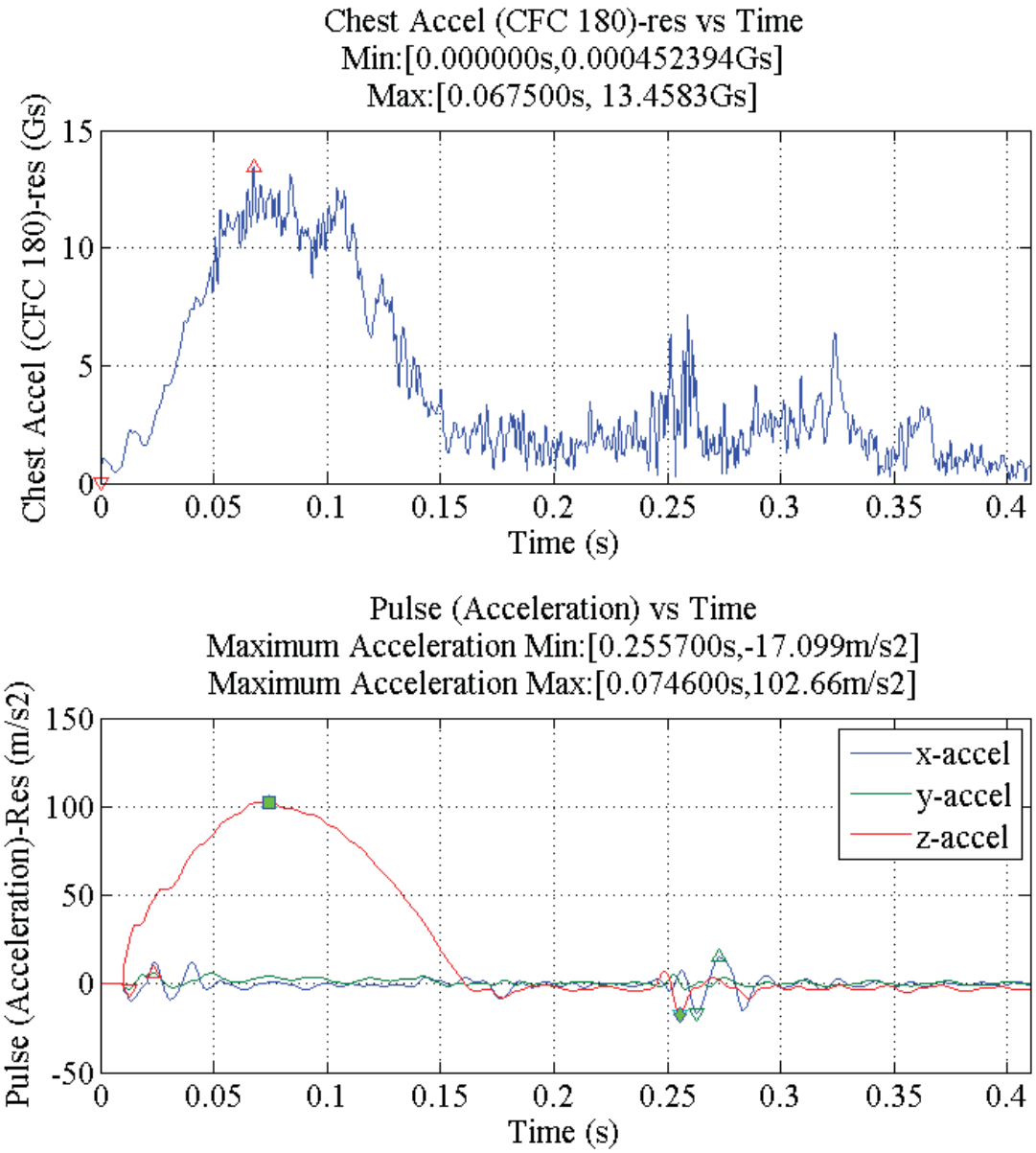

Figure 142: Chest Acceleration for simulation 8208 (Spinal), long pulse, X-axis gravity.

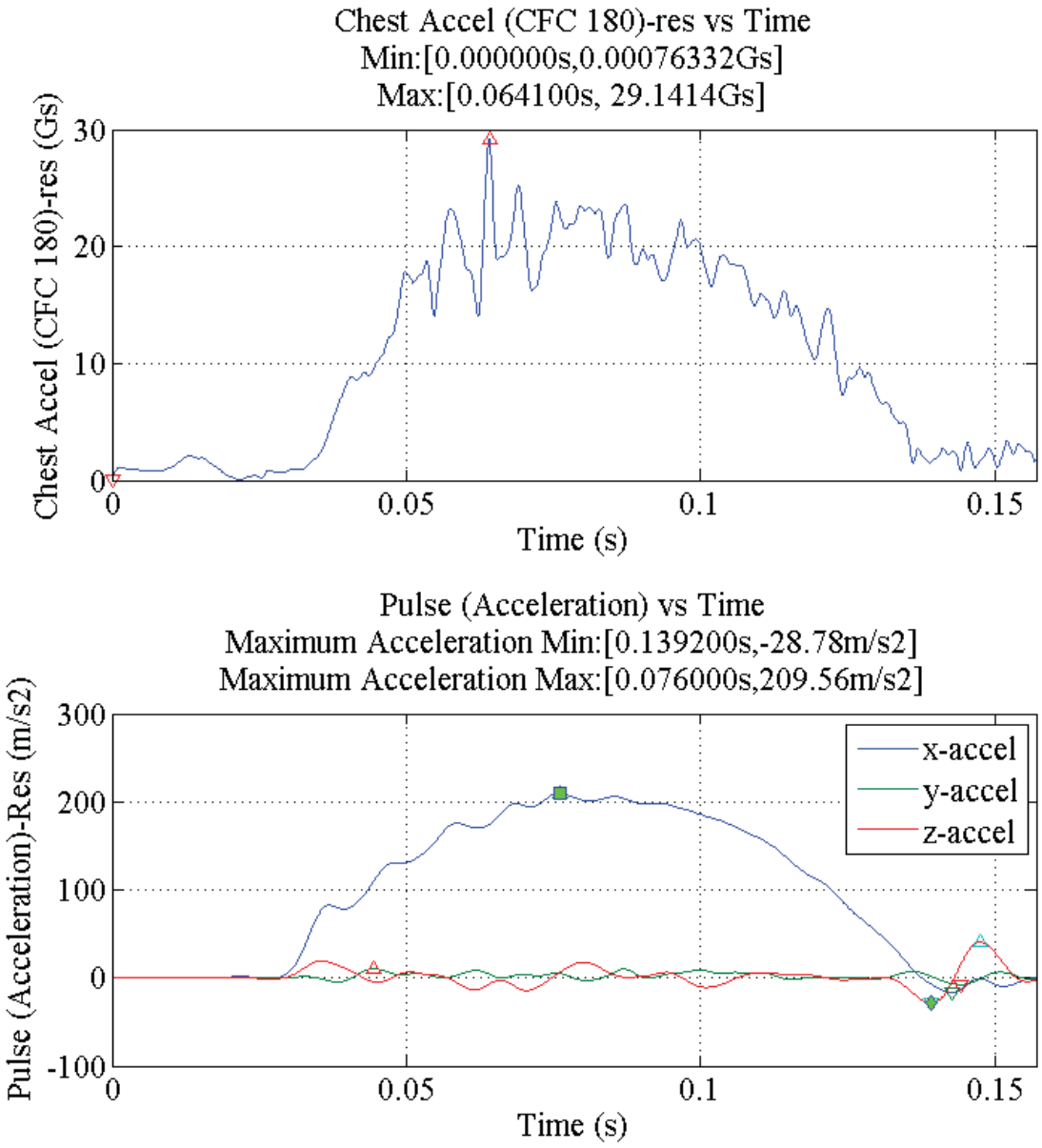

Figure 143: Chest Acceleration for simulation 8212 (Rear), short pulse.

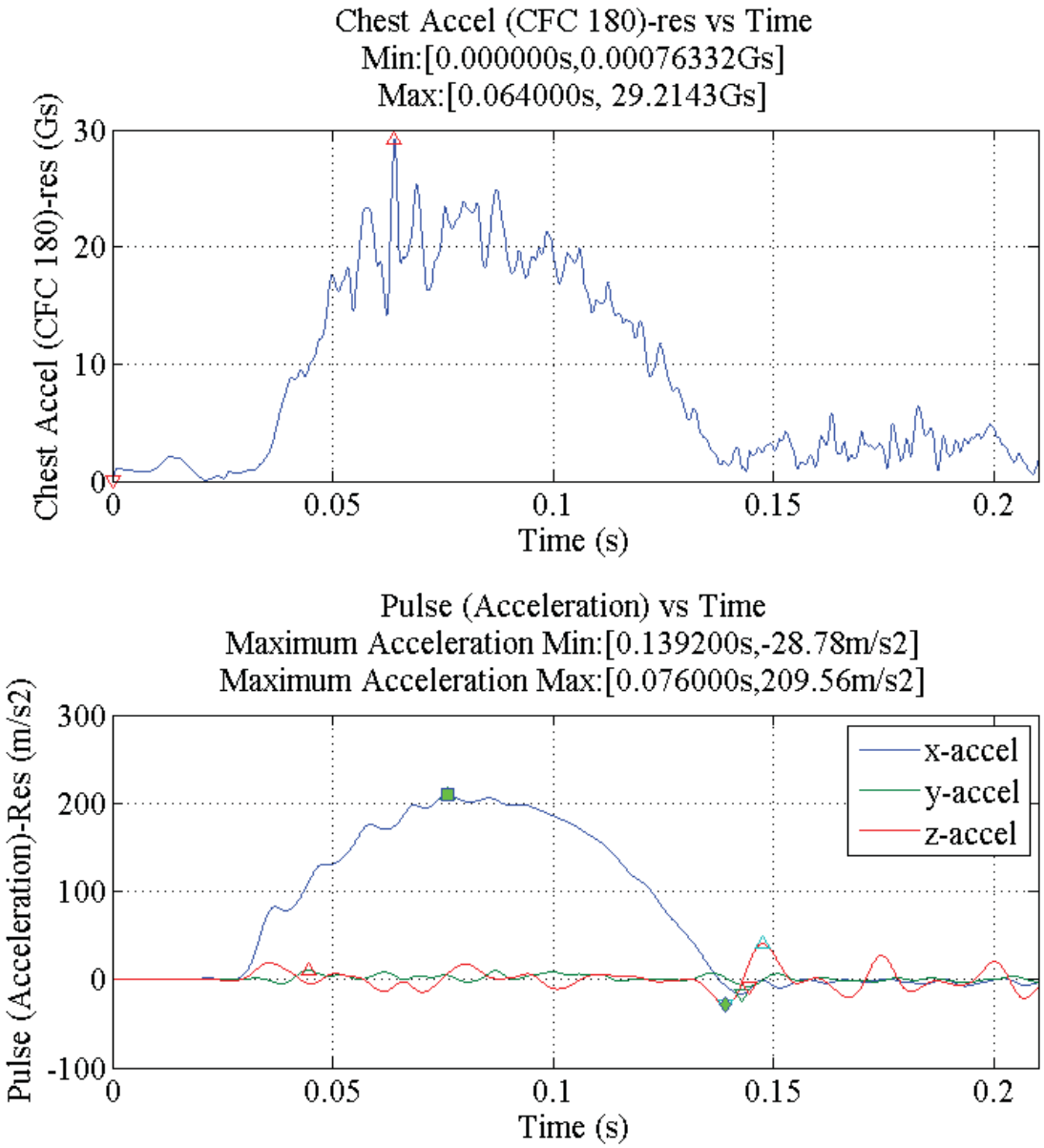

Figure 144: Chest Acceleration for simulation 8212 (Rear), long pulse.

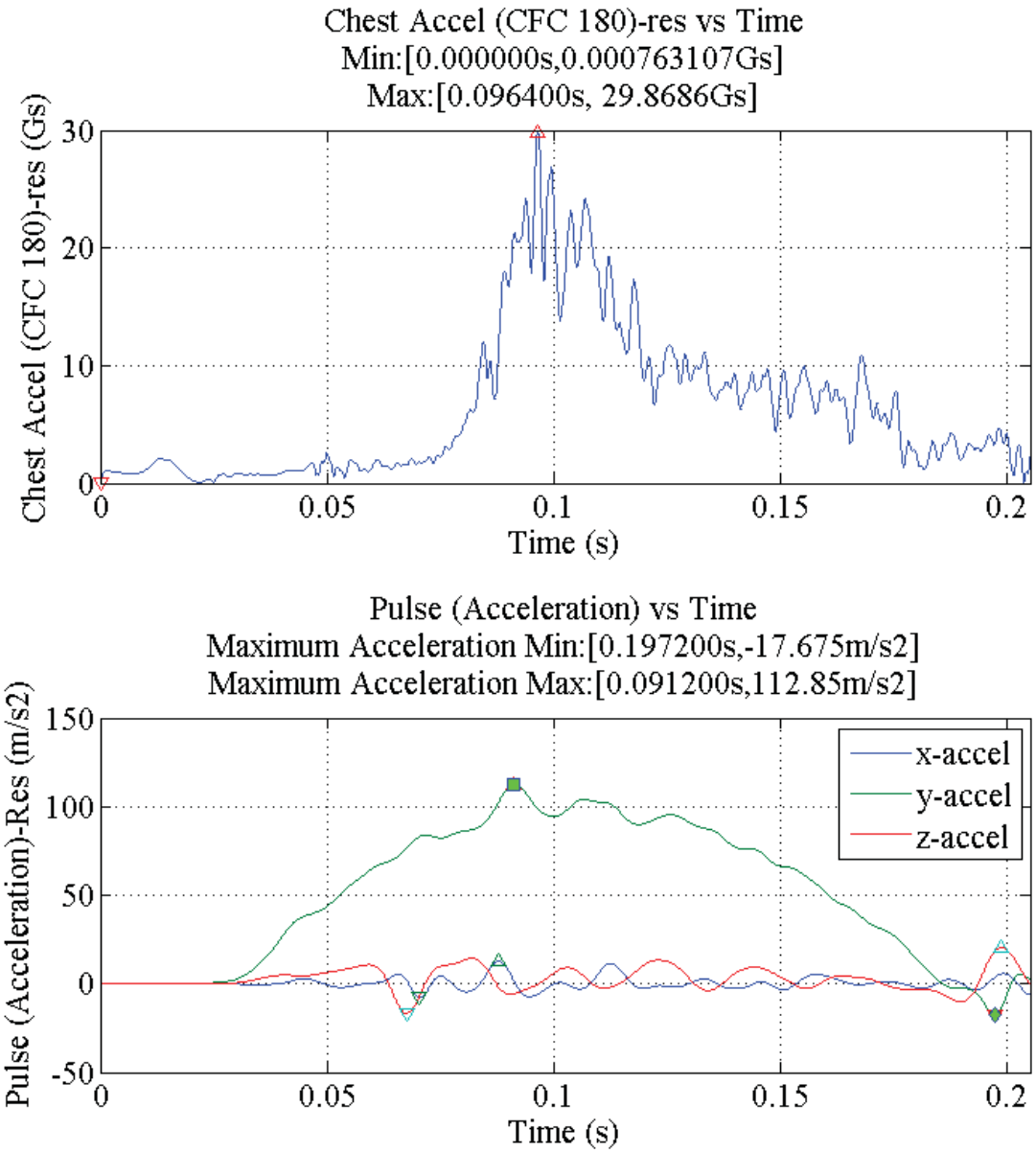

Figure 145: Chest Acceleration for simulation 8245 (Lateral), short pulse.

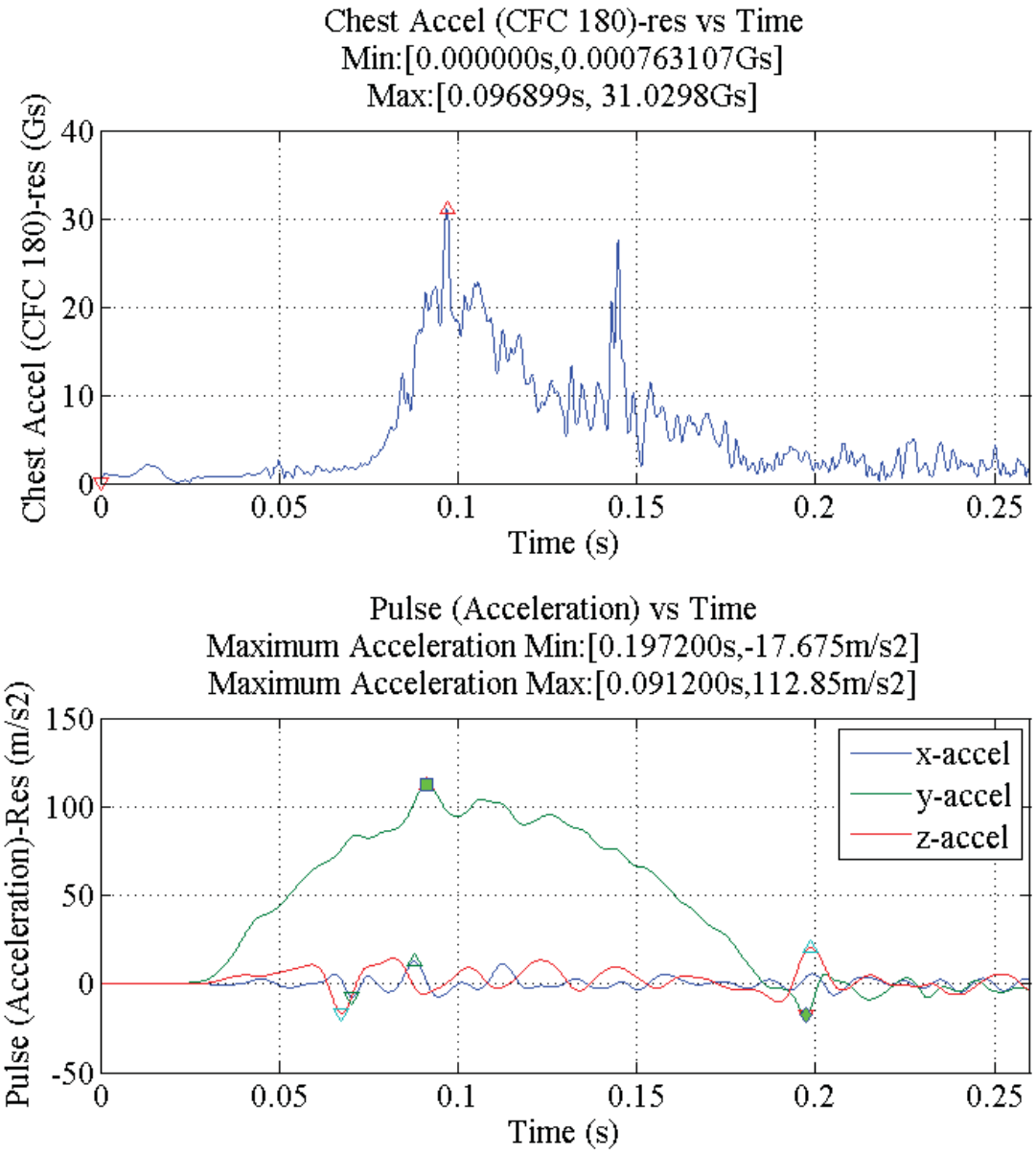

Figure 146: Chest Acceleration for simulation 8245 (Lateral), long pulse.

Appendix 12: Lumbar Spin Injury, Lumbar Spine Force

Table 10: Tabulated Lumbar Spine Force

Simulation	Lumbar Force (N)
8202, Frontal, Short pulse	1005.45
8202, Frontal, Long pulse	992.09
8208, Spinal, Short pulse, X-axis gravity	1784.99
8208, Spinal, Short pulse, Z-axis gravity	2097.77
8208, Spinal, Long pulse, X-axis gravity	1795.05
8212, Rear, Short pulse	415.48
8212, Rear, Long pulse	388.51
8245, Lateral, Short pulse	816.22
8245, Lateral, Long pulse	945.47

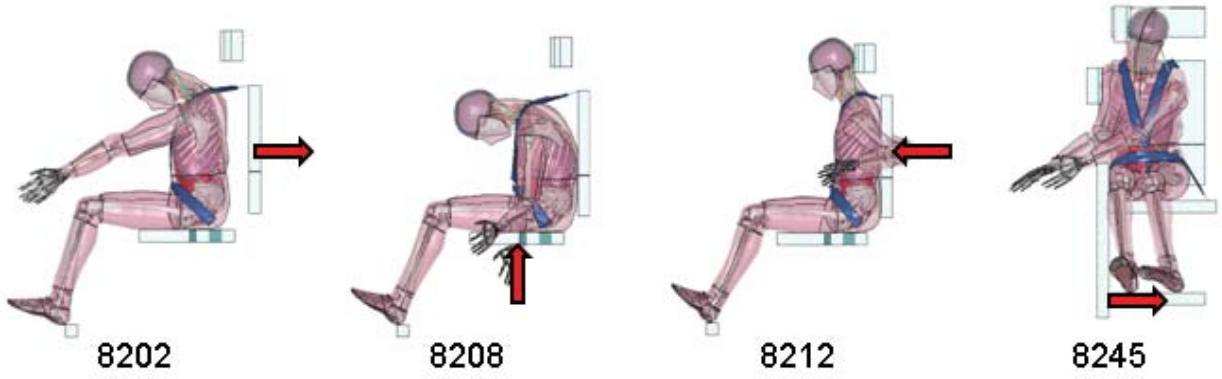

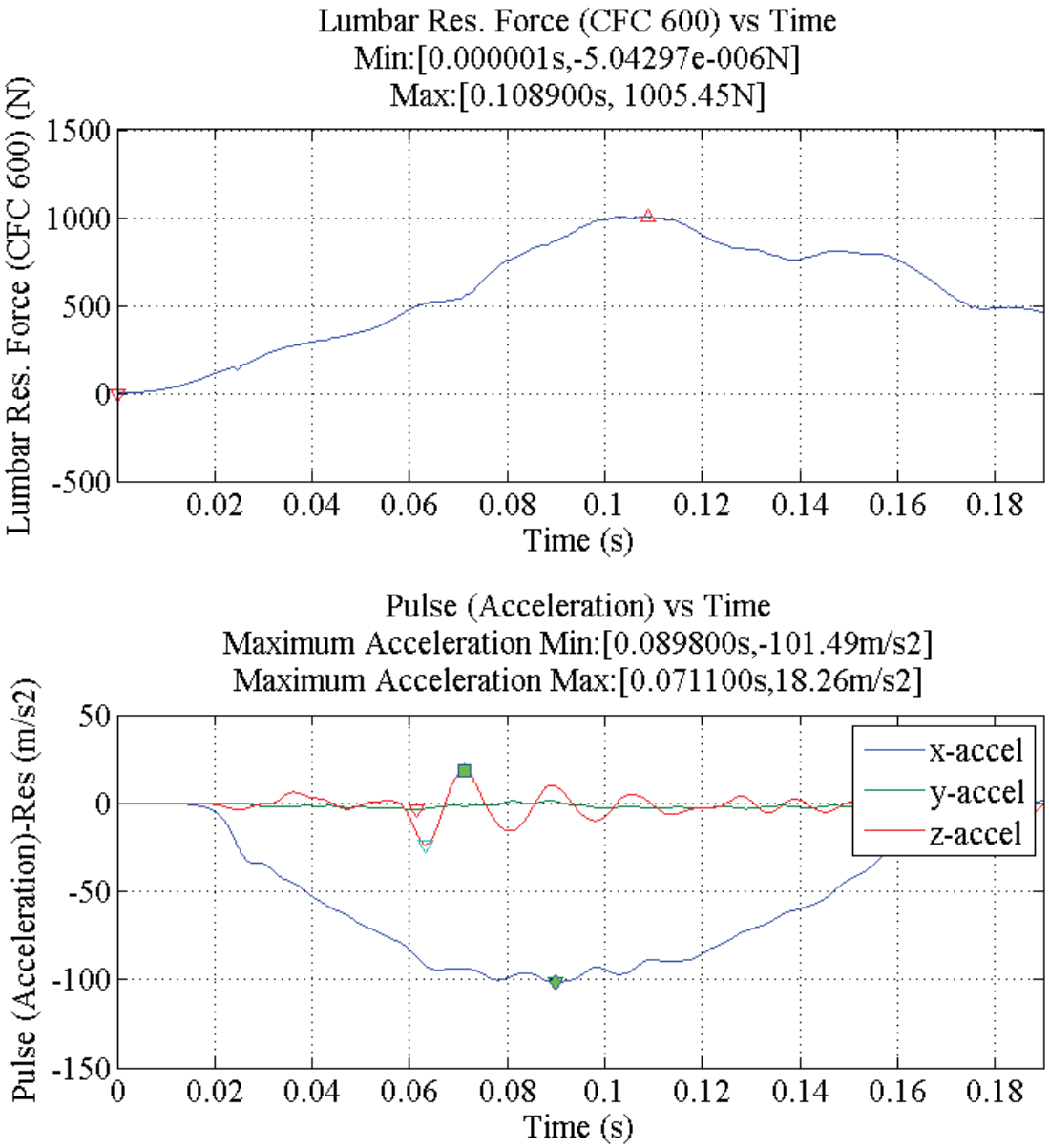

Figure 147: Lumbar Spine Force for simulation 8202 (Frontal), short pulse.

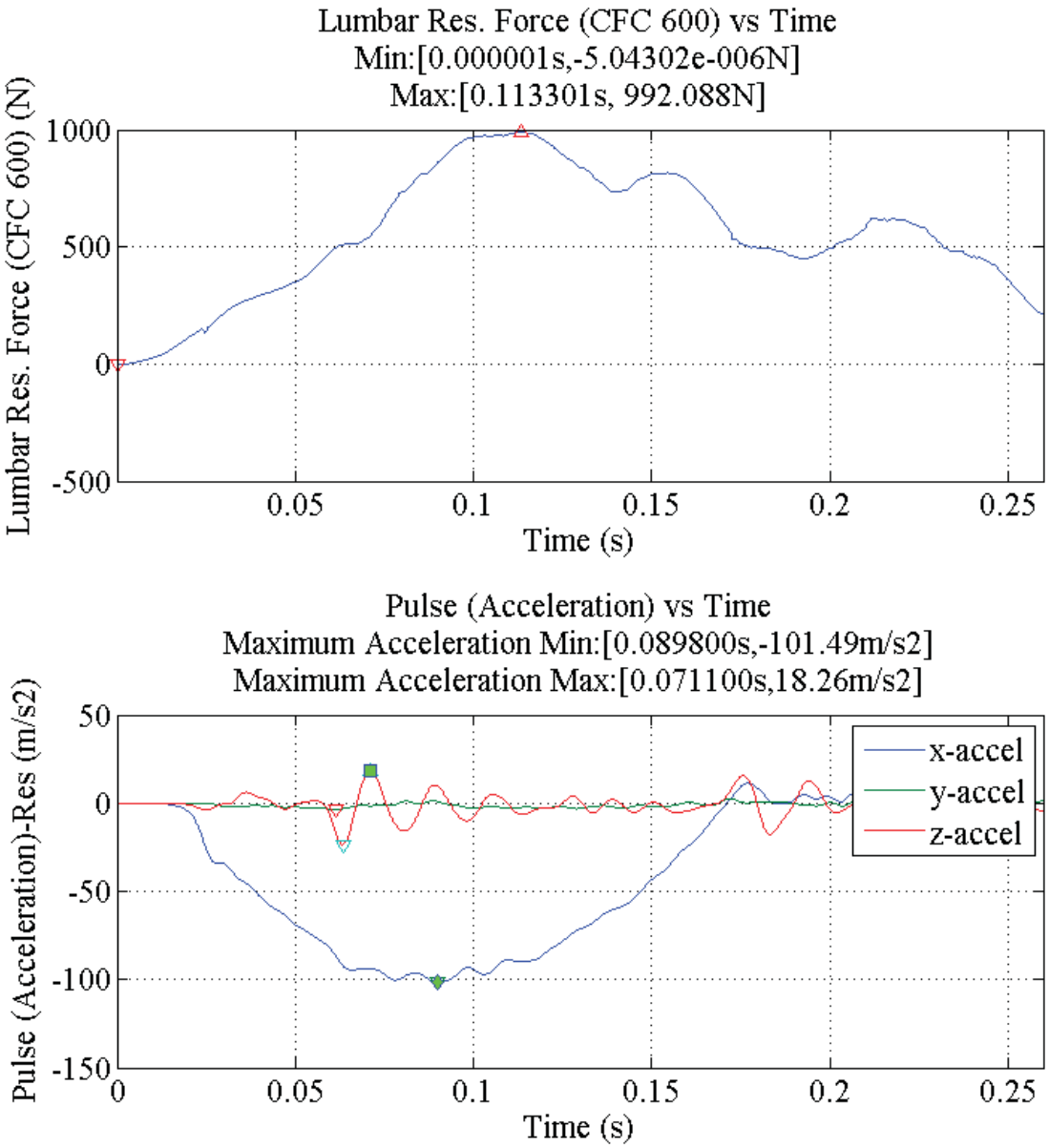

Figure 148: Lumbar Spine Force for simulation 8202 (Frontal), long pulse.

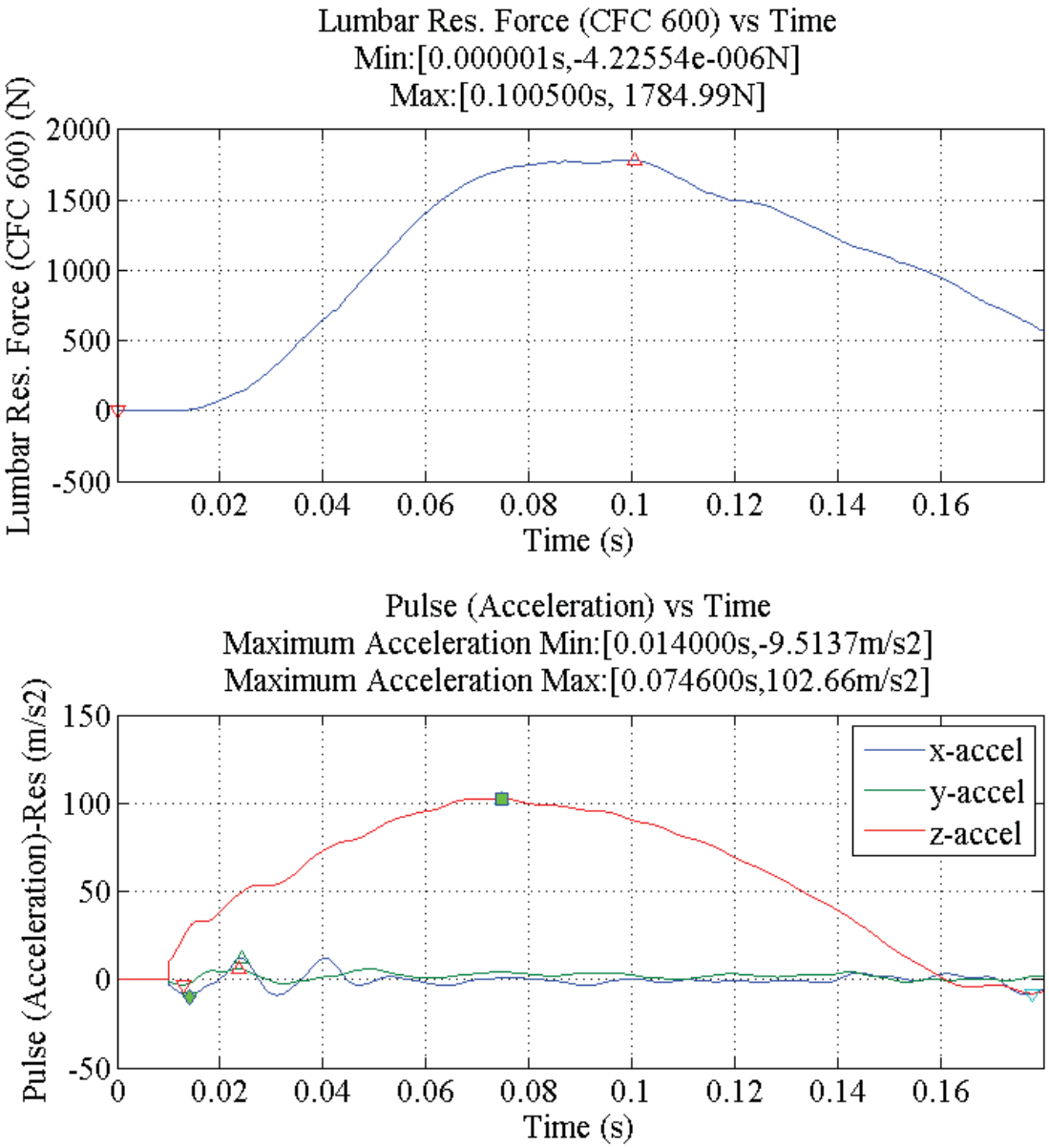

Figure 149: Lumbar Spine Force for simulation 8208 (Spinal), short pulse, X-axis gravity.

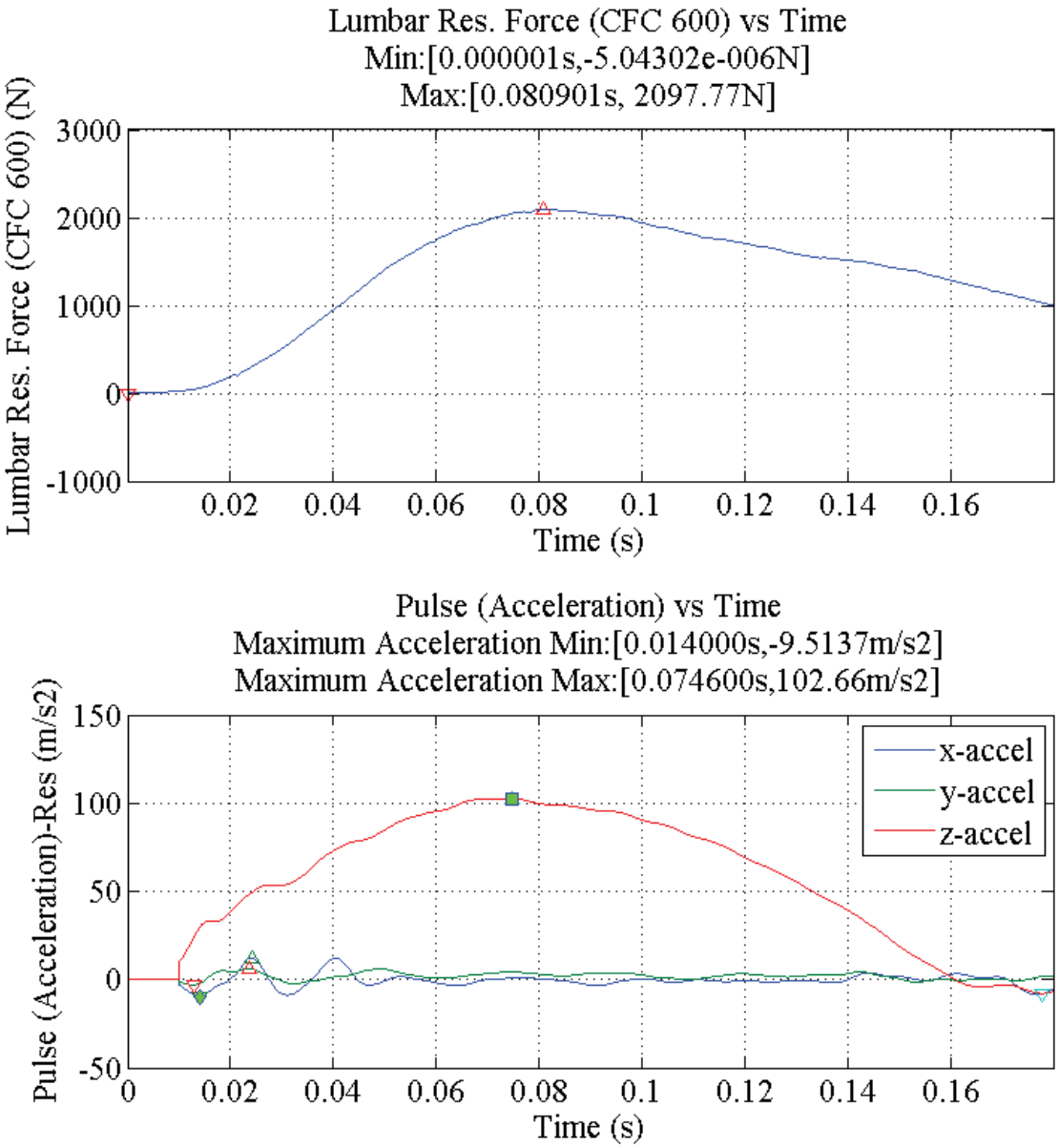

Figure 150: Lumbar Spine Force for simulation 8208 (Spinal), short pulse, Z-axis gravity.

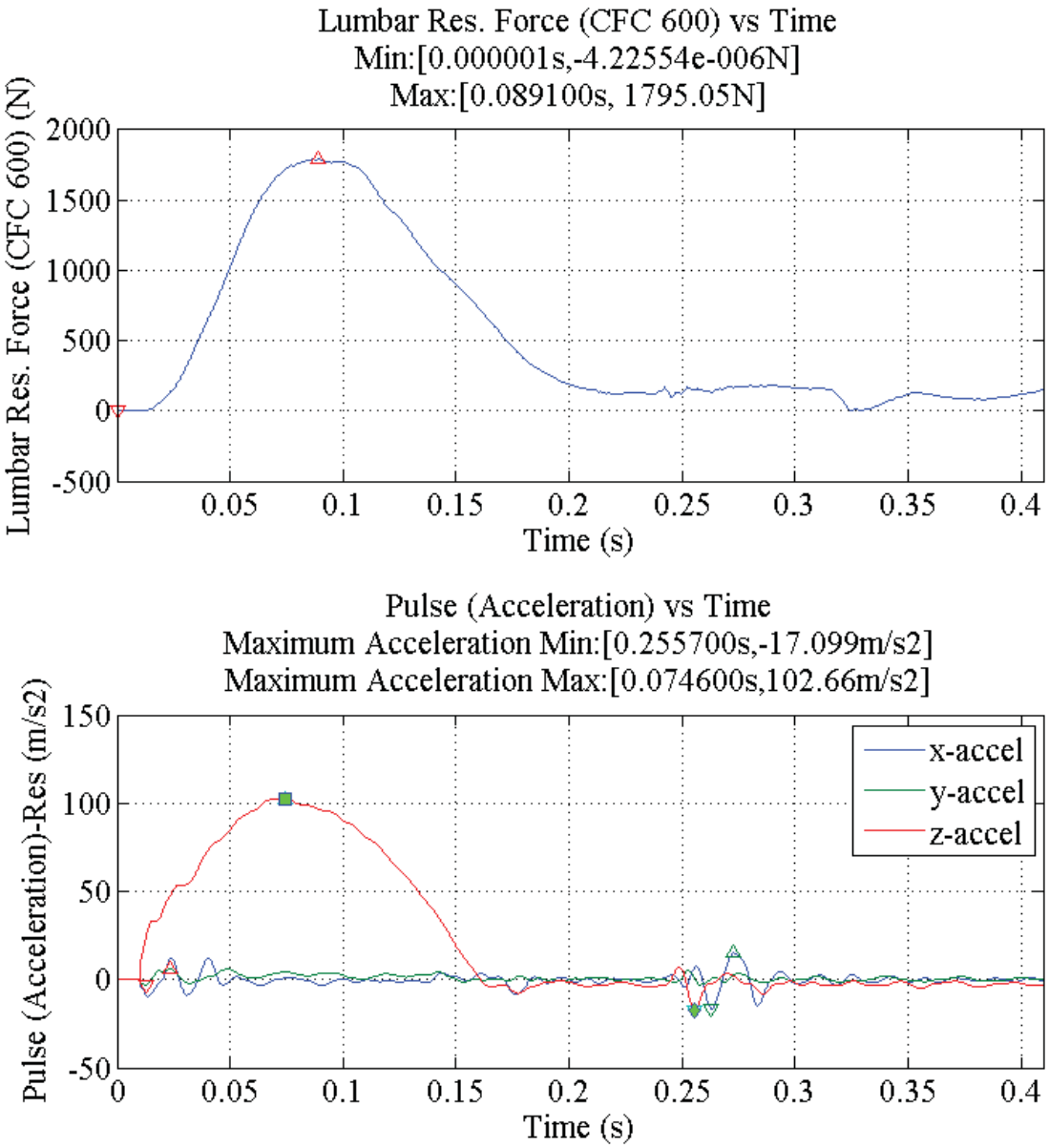

Figure 151: Lumbar Spine Force for simulation 8208 (Spinal), long pulse, X-axis gravity.

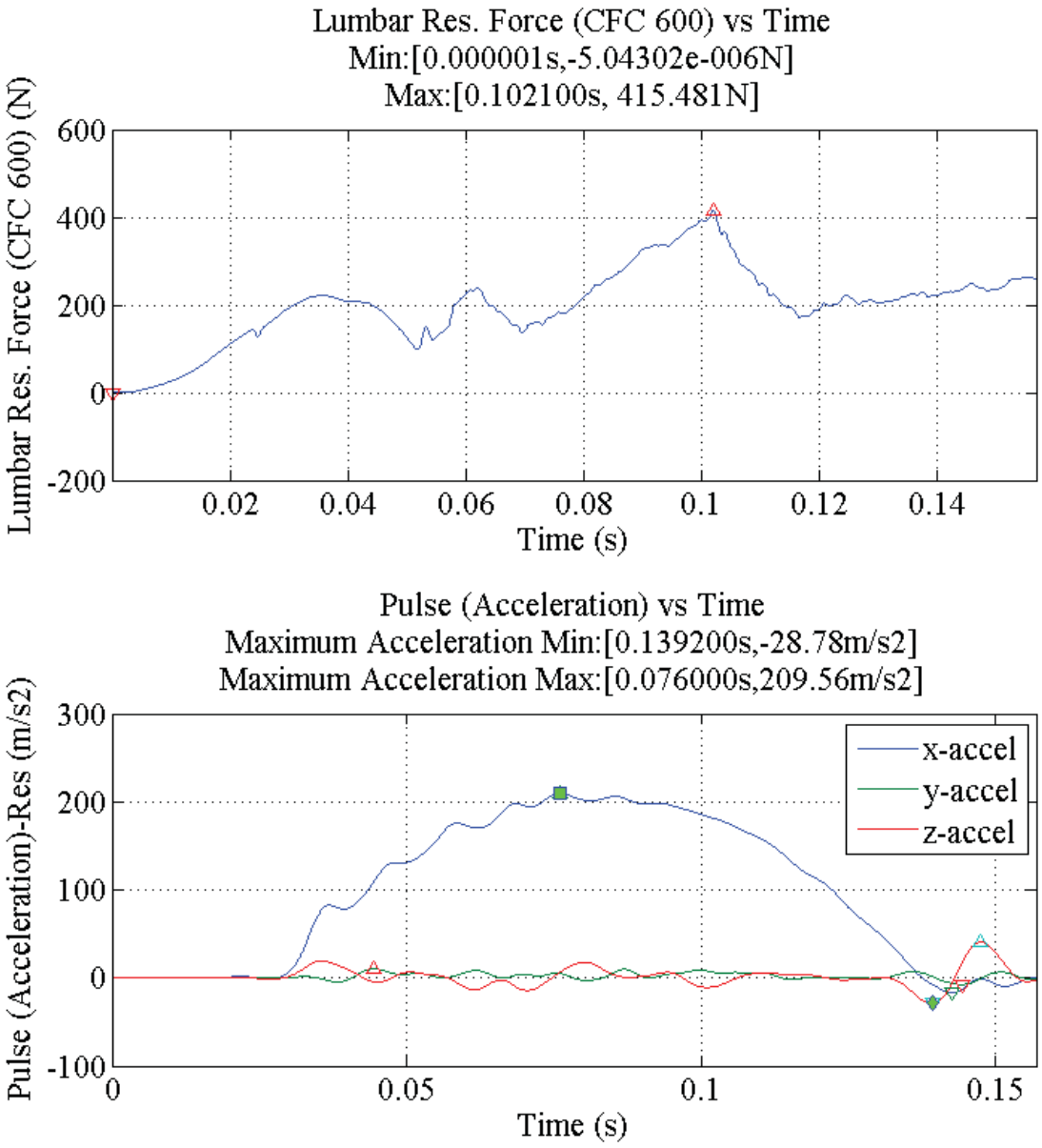

Figure 152: Lumbar Spine Force for simulation 8212 (Rear), short pulse.

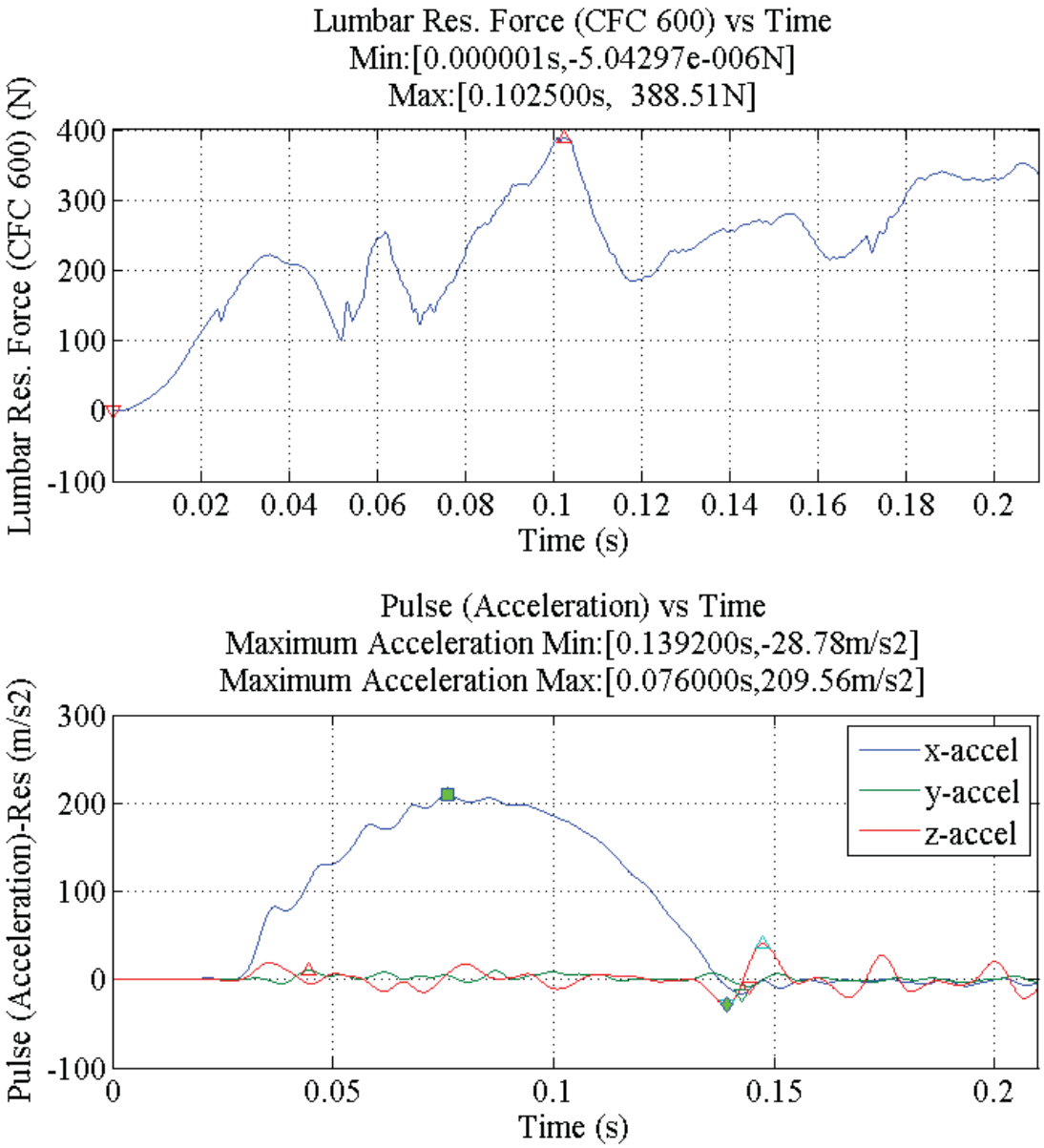

Figure 153: Lumbar Spine Force for simulation 8212 (Rear), long pulse.

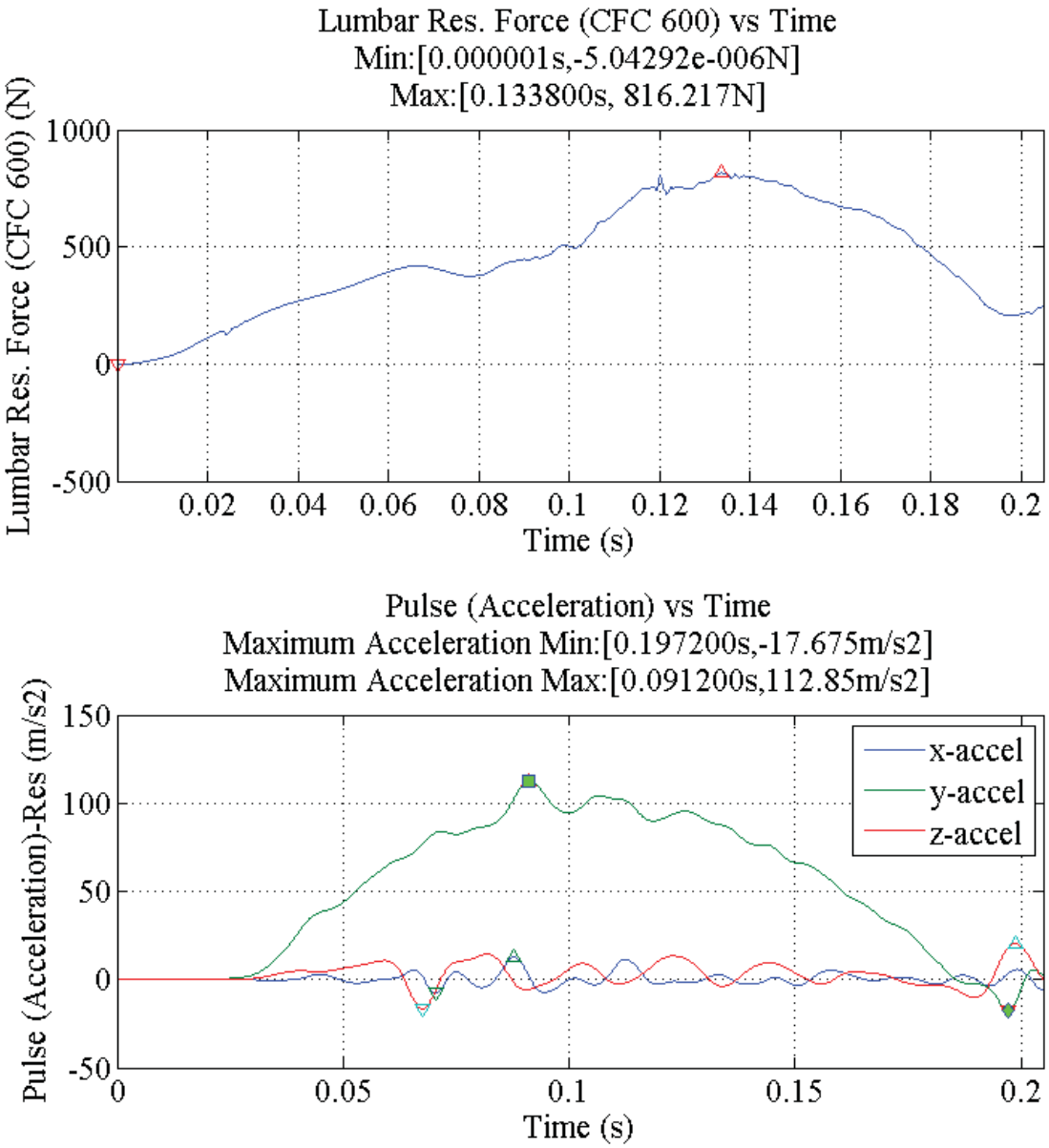

Figure 154: Lumbar Spine Force for simulation 8245 (Lateral), short pulse.

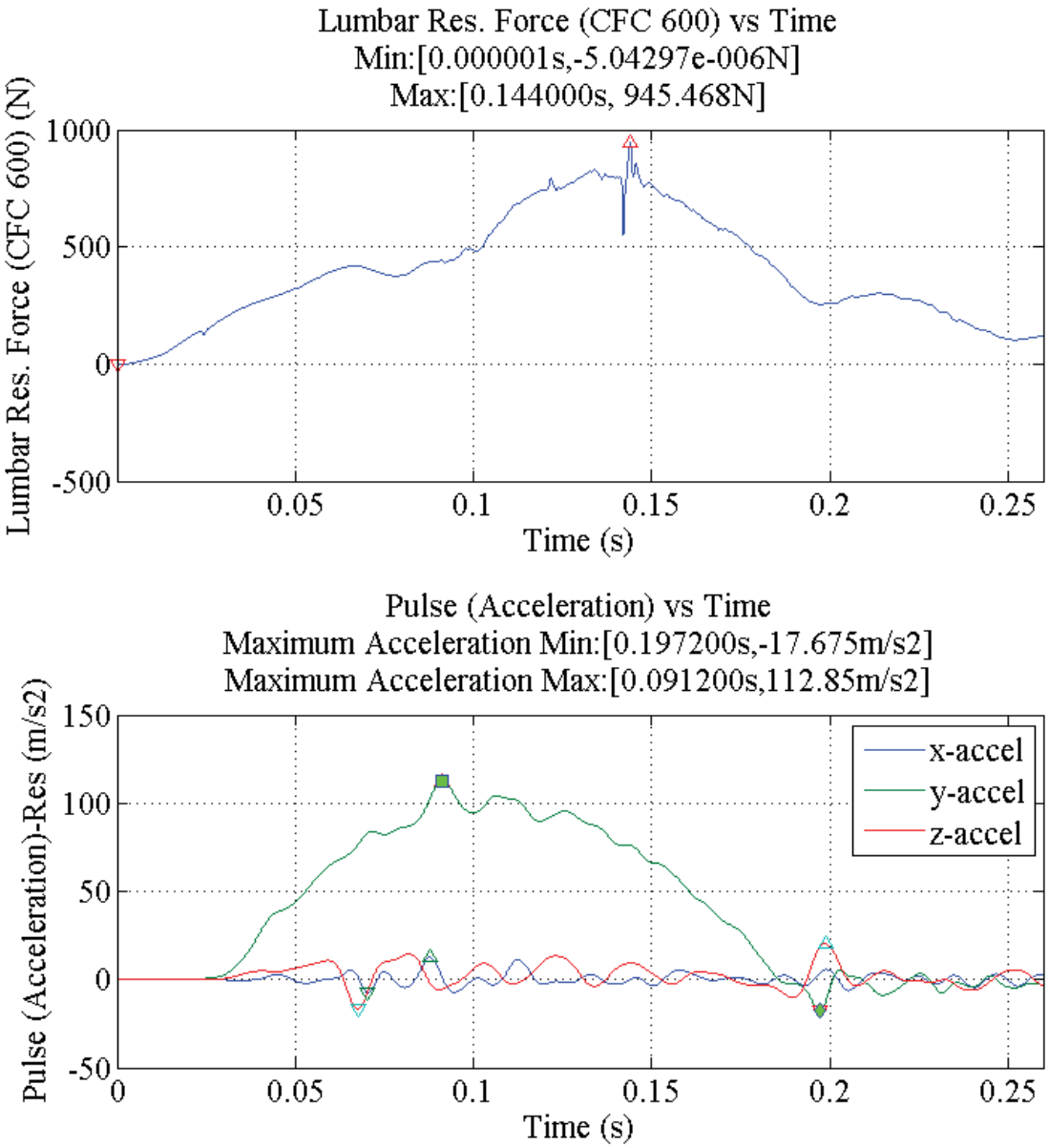

Figure 155: Lumbar Spine Force for simulation 8245 (Lateral), long pulse.

Appendix 13: Lower Extremity Injury, Right Femur Force

Table 11: Tabulated Right Femur Force

Simulation	Right Femur Force (N)
8202, Frontal, Short pulse	582.68
8202, Frontal, Long pulse	583.86
8208, Spinal, Short pulse, X-axis gravity	151.93
8208, Spinal, Short pulse, Z-axis gravity	149.60
8208, Spinal, Long pulse, X-axis gravity	170.87
8212, Rear, Short pulse	2410.20
8212, Rear, Long pulse	2481.40
8245, Lateral, Short pulse	467.04
8245, Lateral, Long pulse	482.87

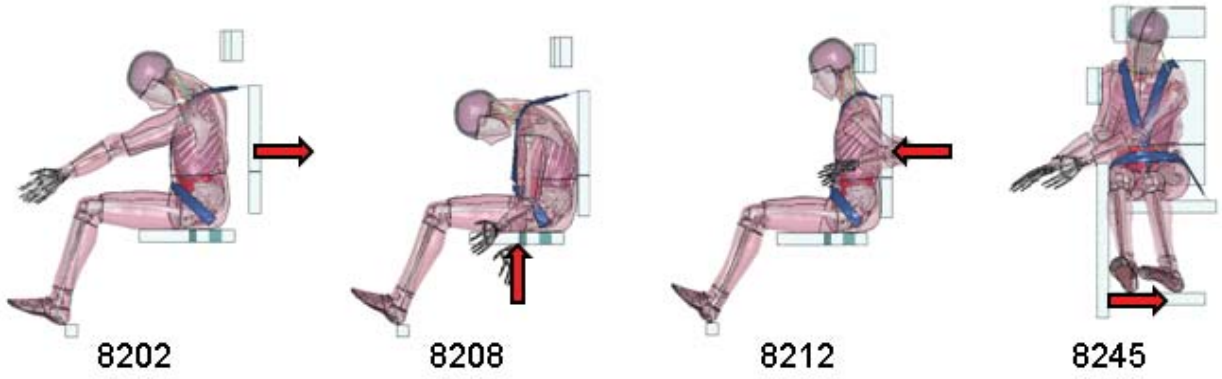

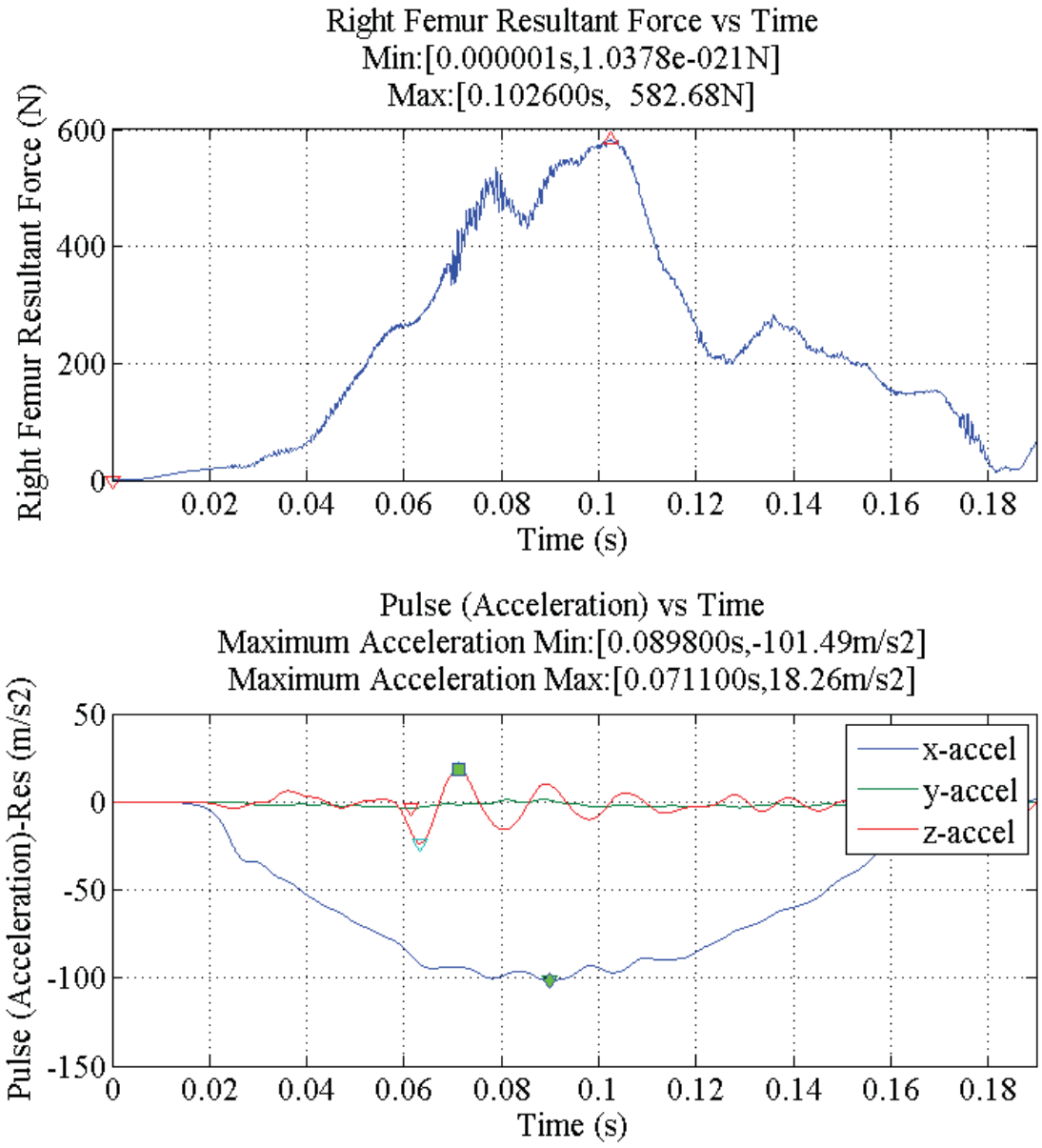

Figure 156: Right Femur Force for simulation 8202 (Frontal), short pulse.

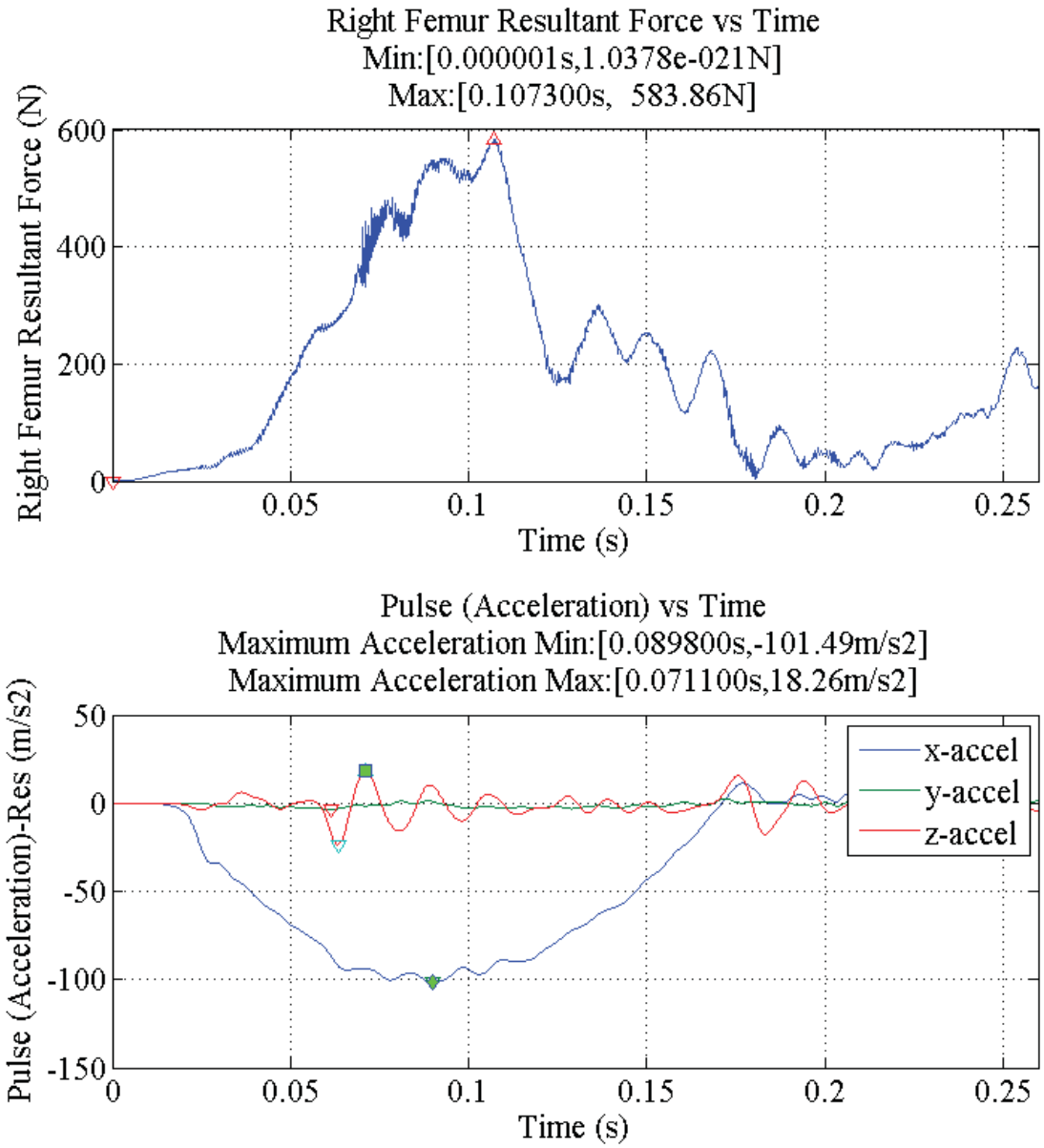

Figure 157: Right Femur Force for simulation 8202 (Frontal), long pulse.

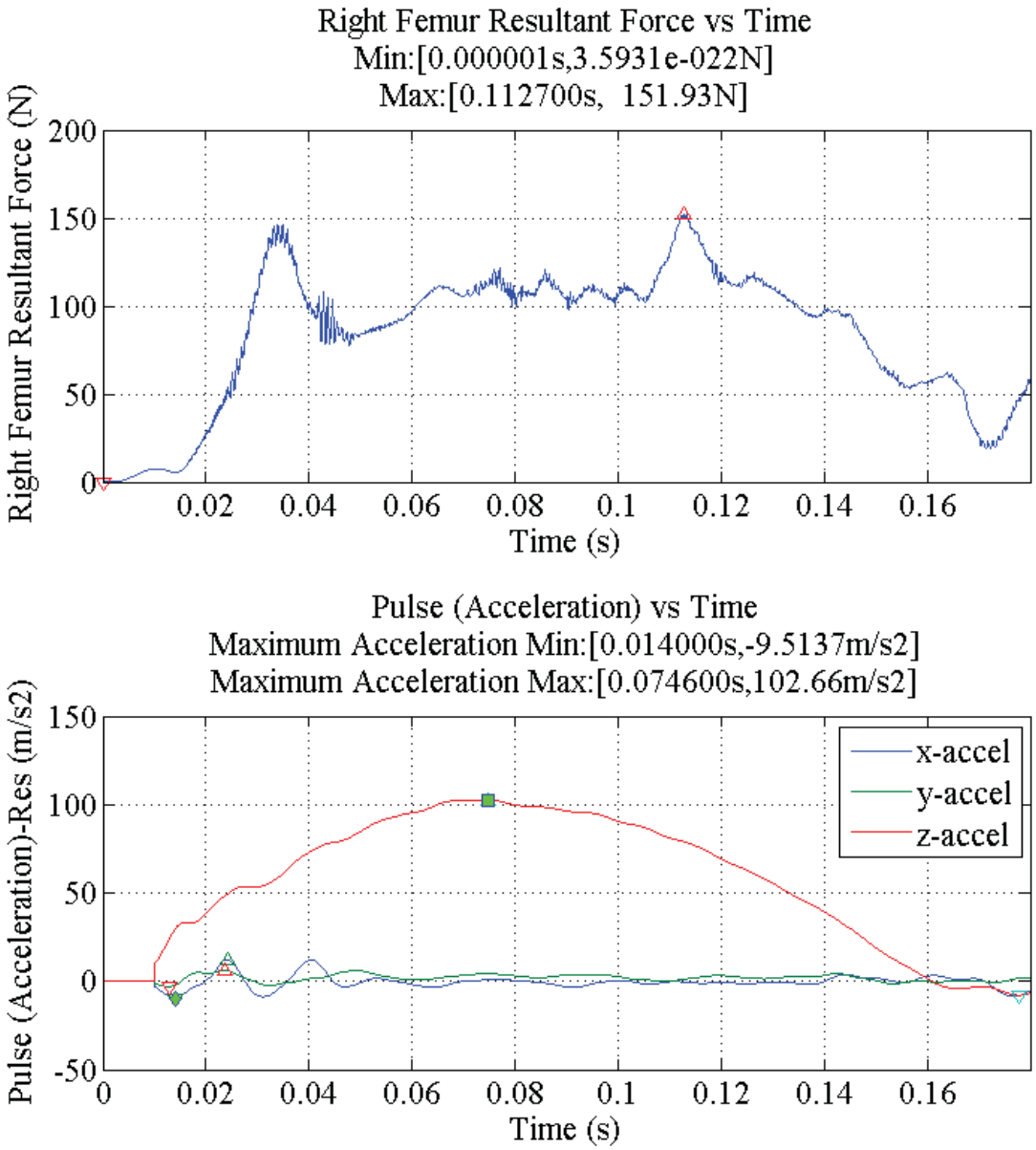

Figure 158: Right Femur Force for simulation 8208 (Spinal), short pulse, X-axis gravity.

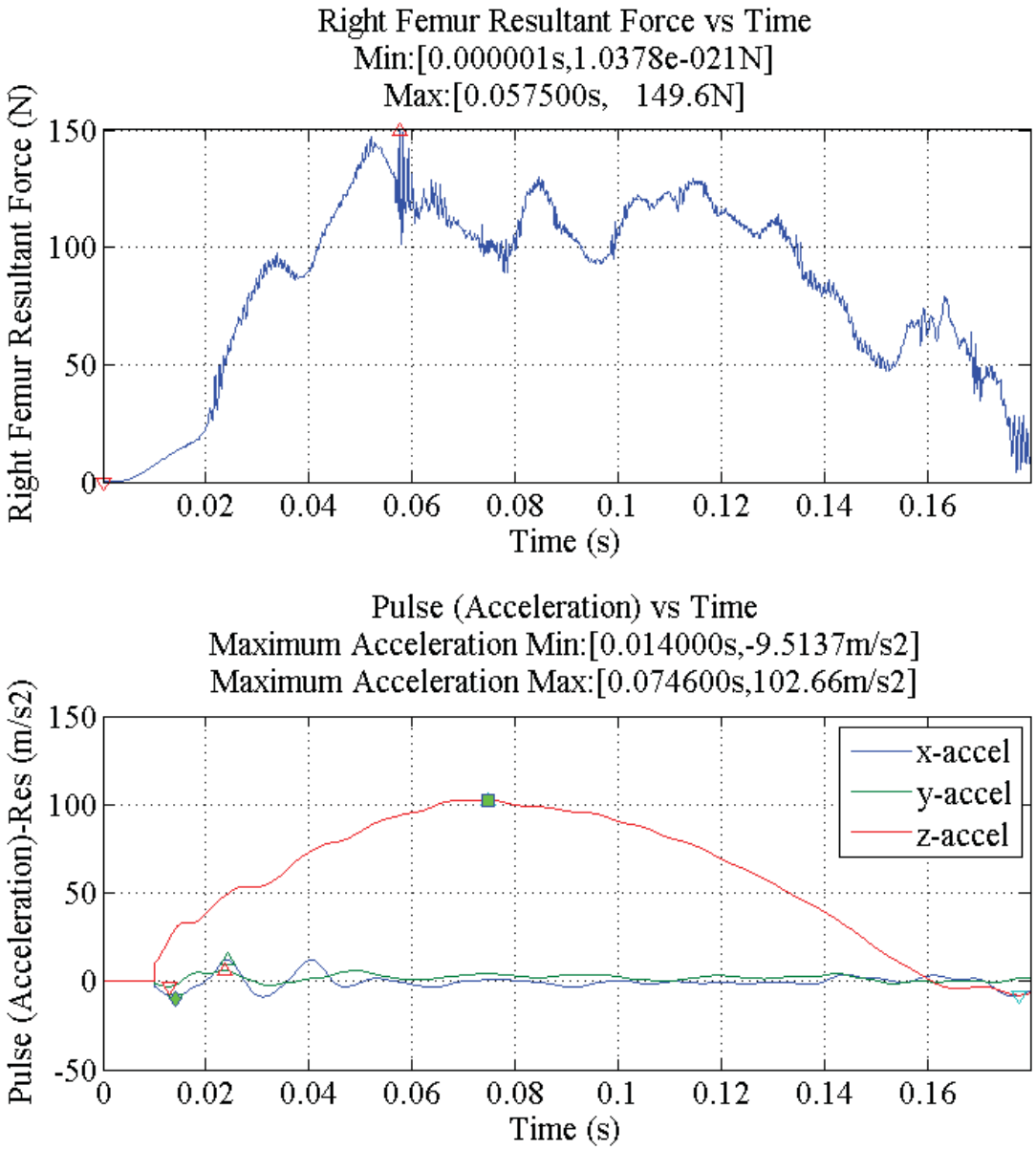

Figure 159: Right Femur Force for simulation 8208 (Spinal), short pulse, Z-axis gravity.

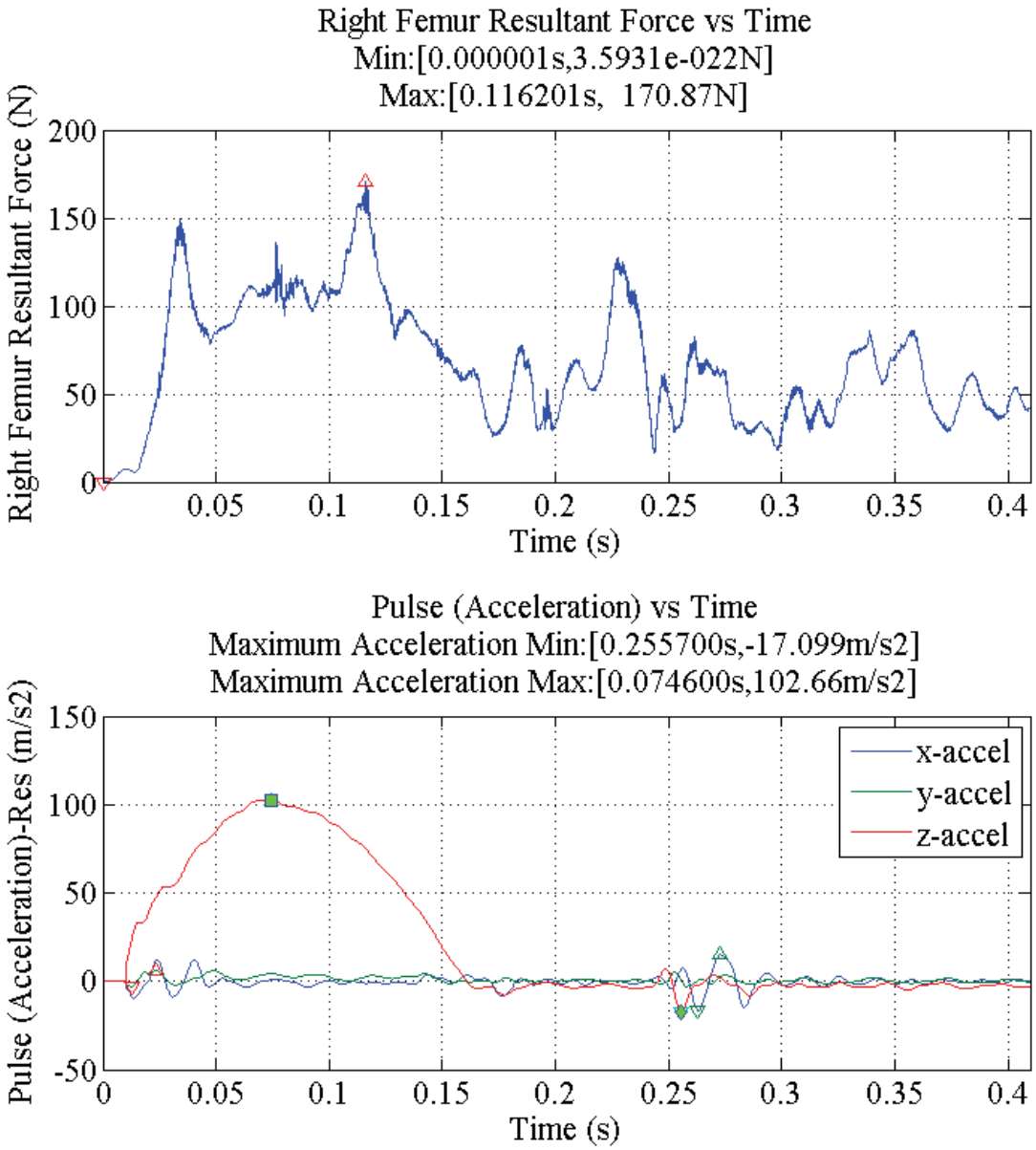

Figure 160: Right Femur Force for simulation 8208 (Spinal), long pulse, X-axis gravity.

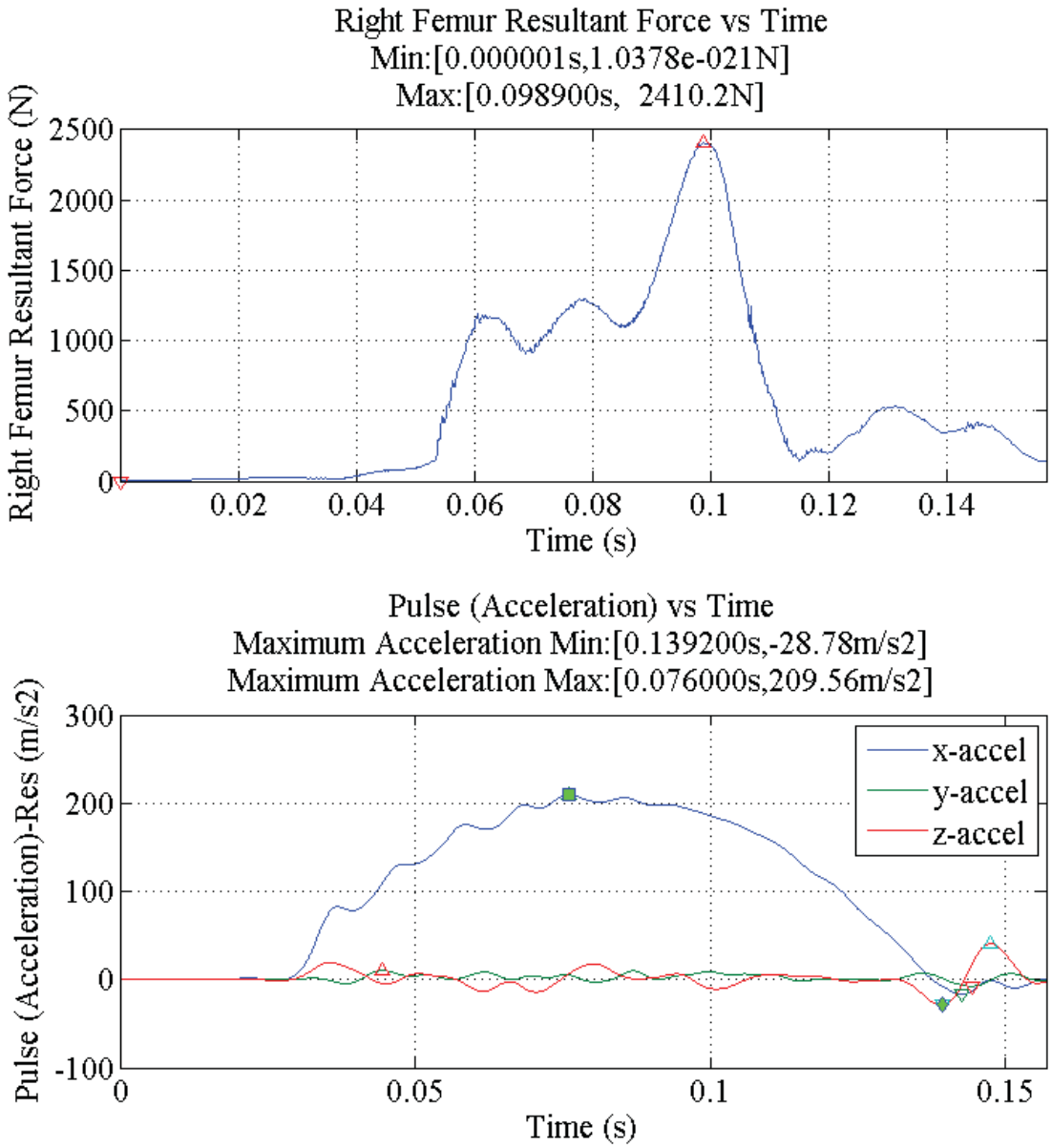

Figure 161: Right Femur Force for simulation 8212 (Rear), short pulse.

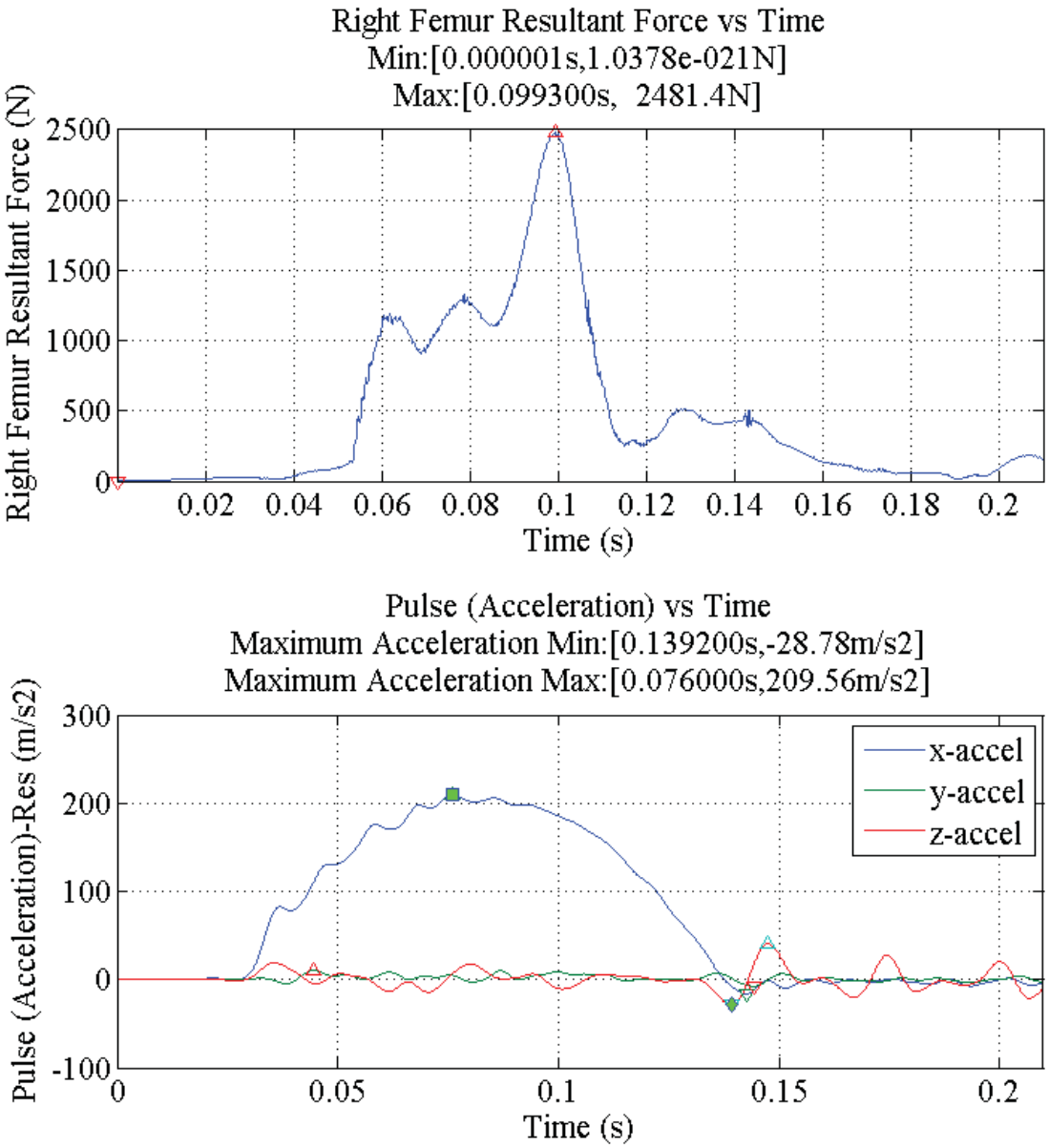

Figure 162: Right Femur Force for simulation 8212 (Rear), long pulse.

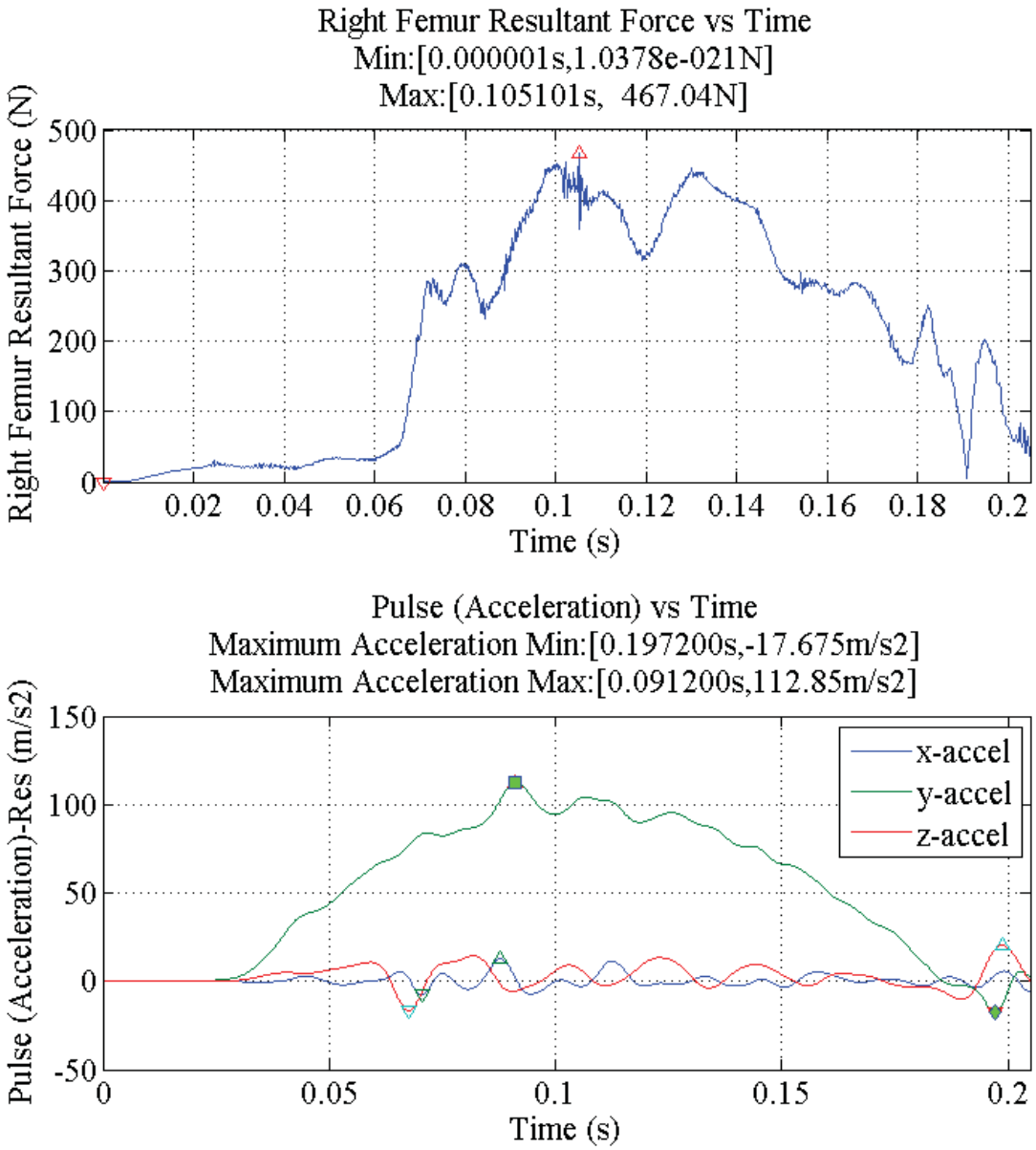

Figure 163: Right Femur Force for simulation 8245 (Lateral), short pulse.

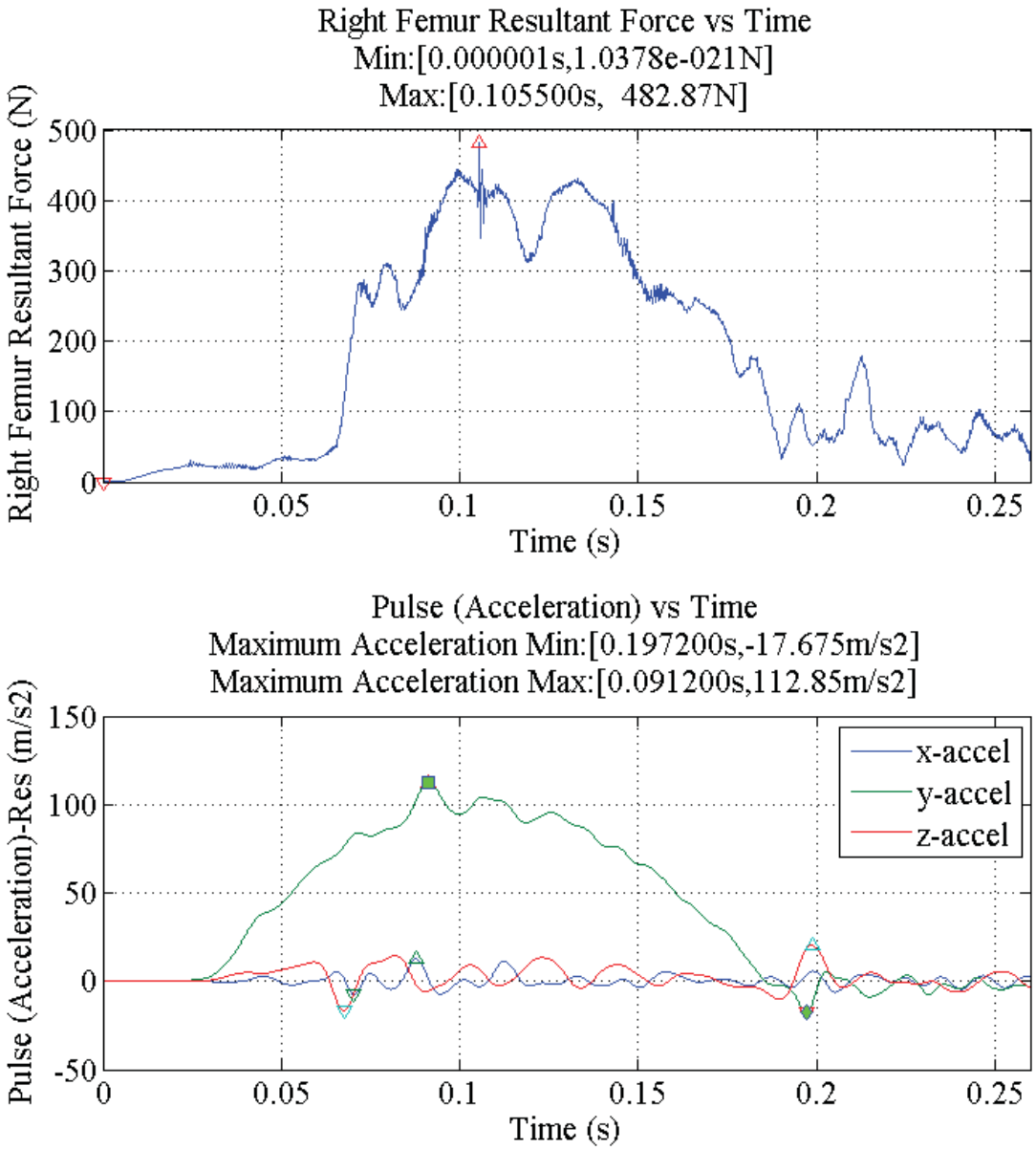

Figure 164: Right Femur Force for simulation 8245 (Lateral), long pulse.

Appendix 14: Lower Extremity Injury, Left Femur Force

Table 12: Tabulated Left Femur Force

Simulation	Left Femur Force (N)
8202, Frontal, Short pulse	595.39
8202, Frontal, Long pulse	576.70
8208, Spinal, Short pulse, X-axis gravity	150.49
8208, Spinal, Short pulse, Z-axis gravity	144.42
8208, Spinal, Long pulse, X-axis gravity	150.74
8212, Rear, Short pulse	2585.00
8212, Rear, Long pulse	2388.50
8245, Lateral, Short pulse	855.02
8245, Lateral, Long pulse	874.53

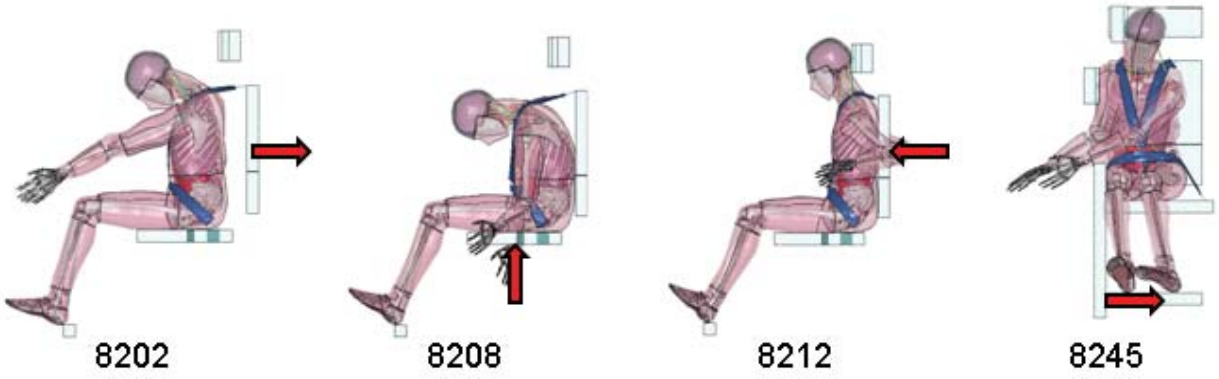

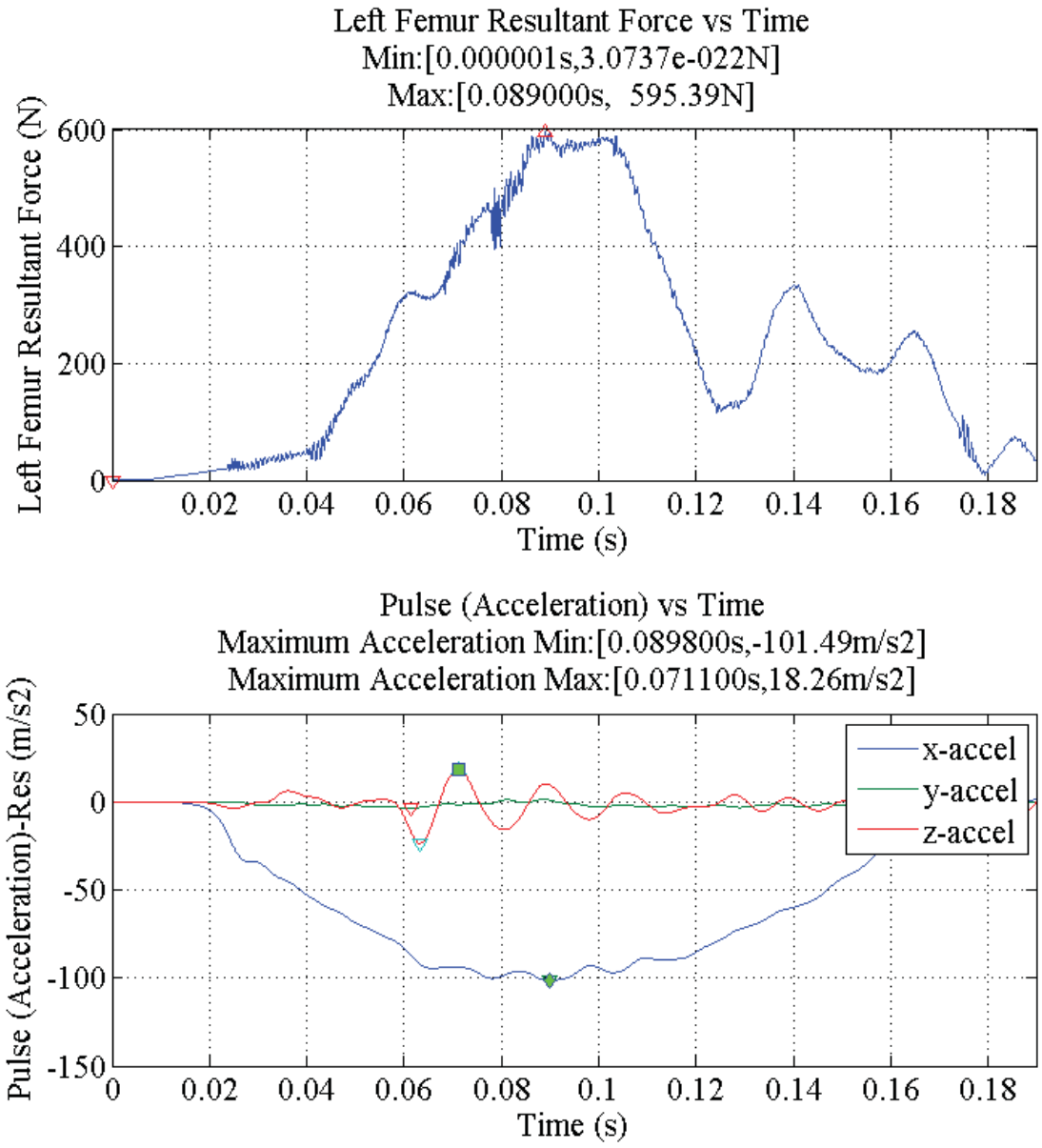

Figure 165: Left Femur Force for simulation 8202 (Frontal), short pulse.

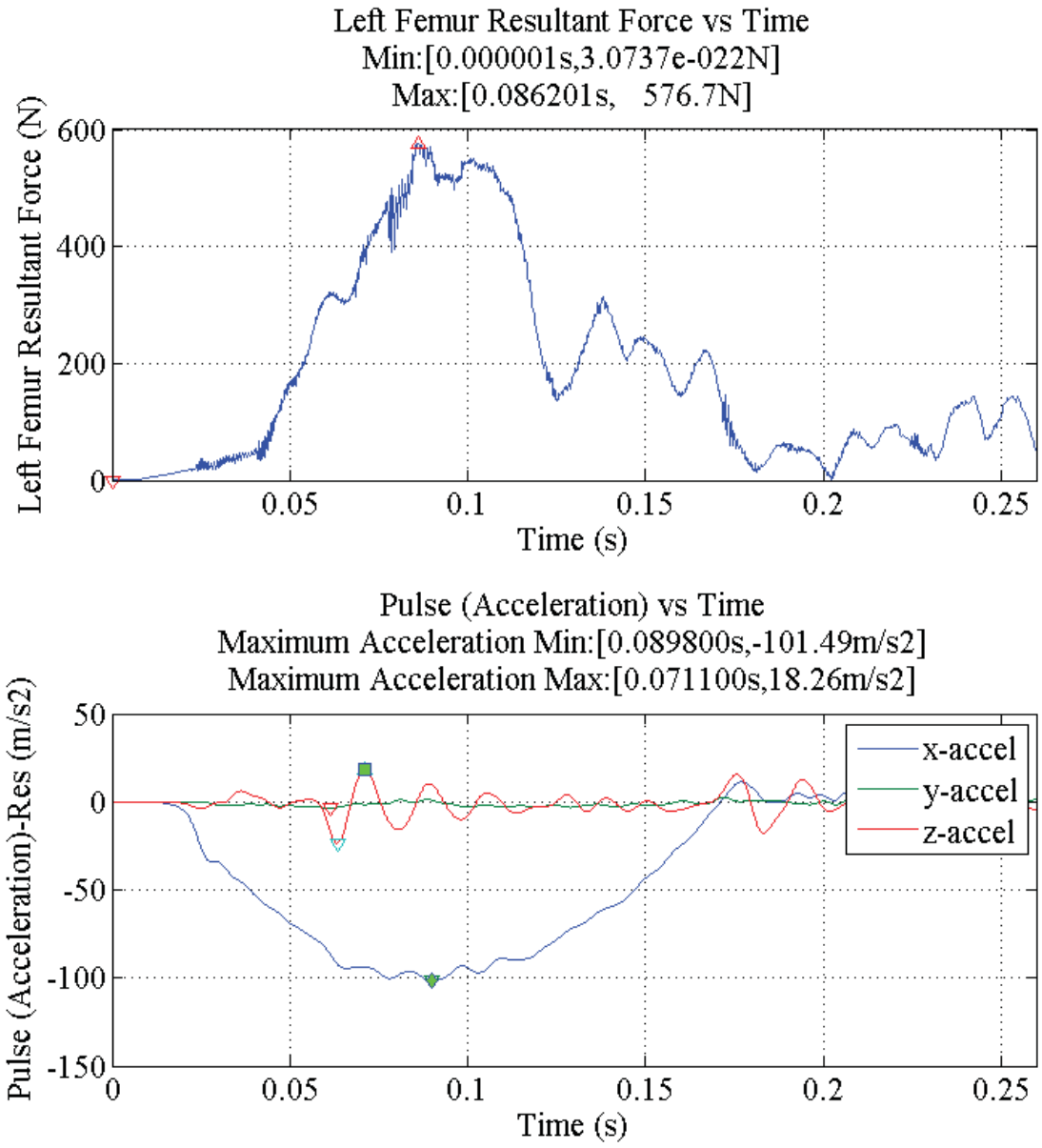

Figure 166: Left Femur Force for simulation 8202 (Frontal), long pulse.

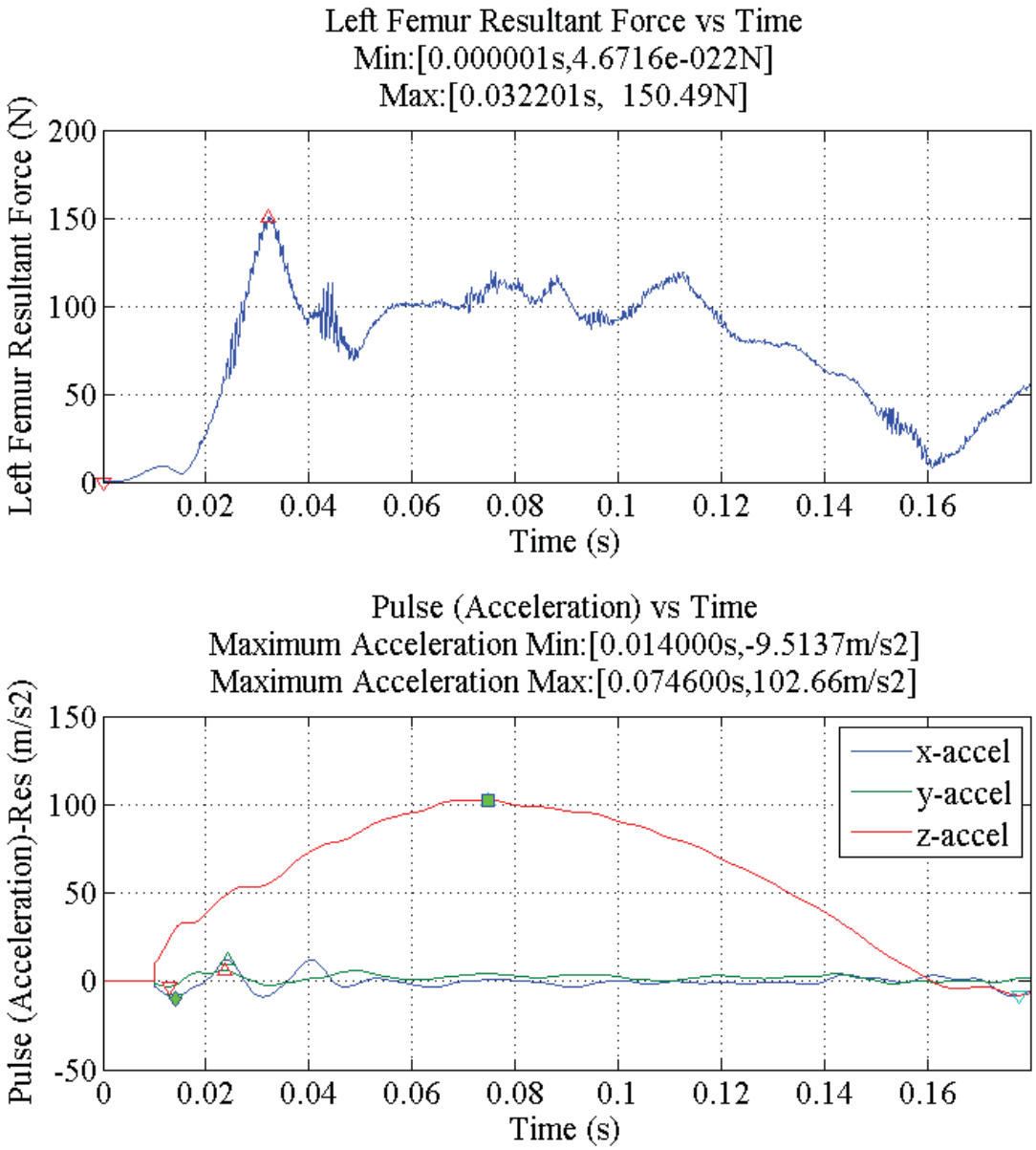

Figure 167: Left Femur Force for simulation 8208 (Spinal), short pulse, X-axis gravity.

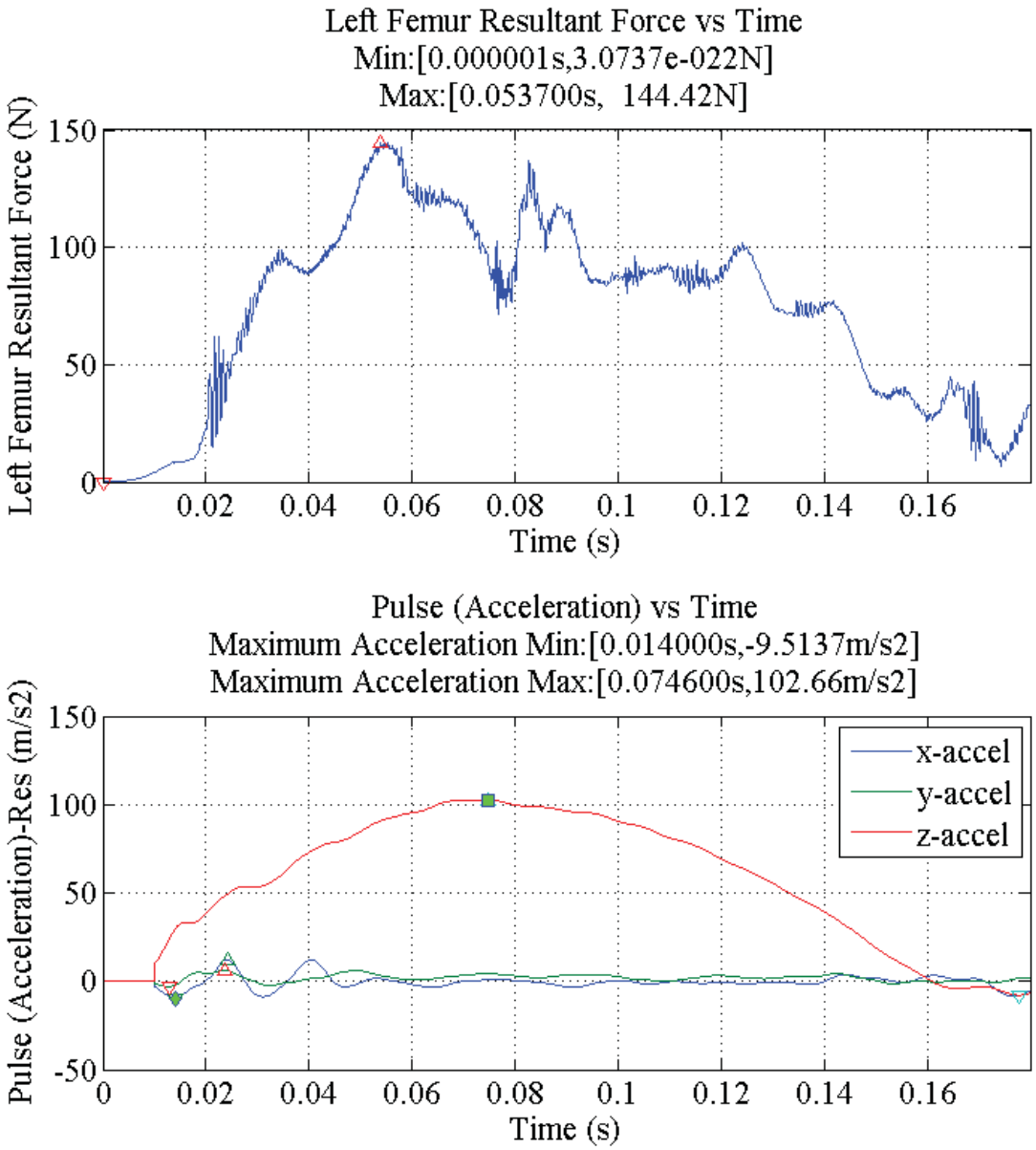

Figure 168: Left Femur Force for simulation 8208 (Spinal), short pulse, Z-axis gravity.

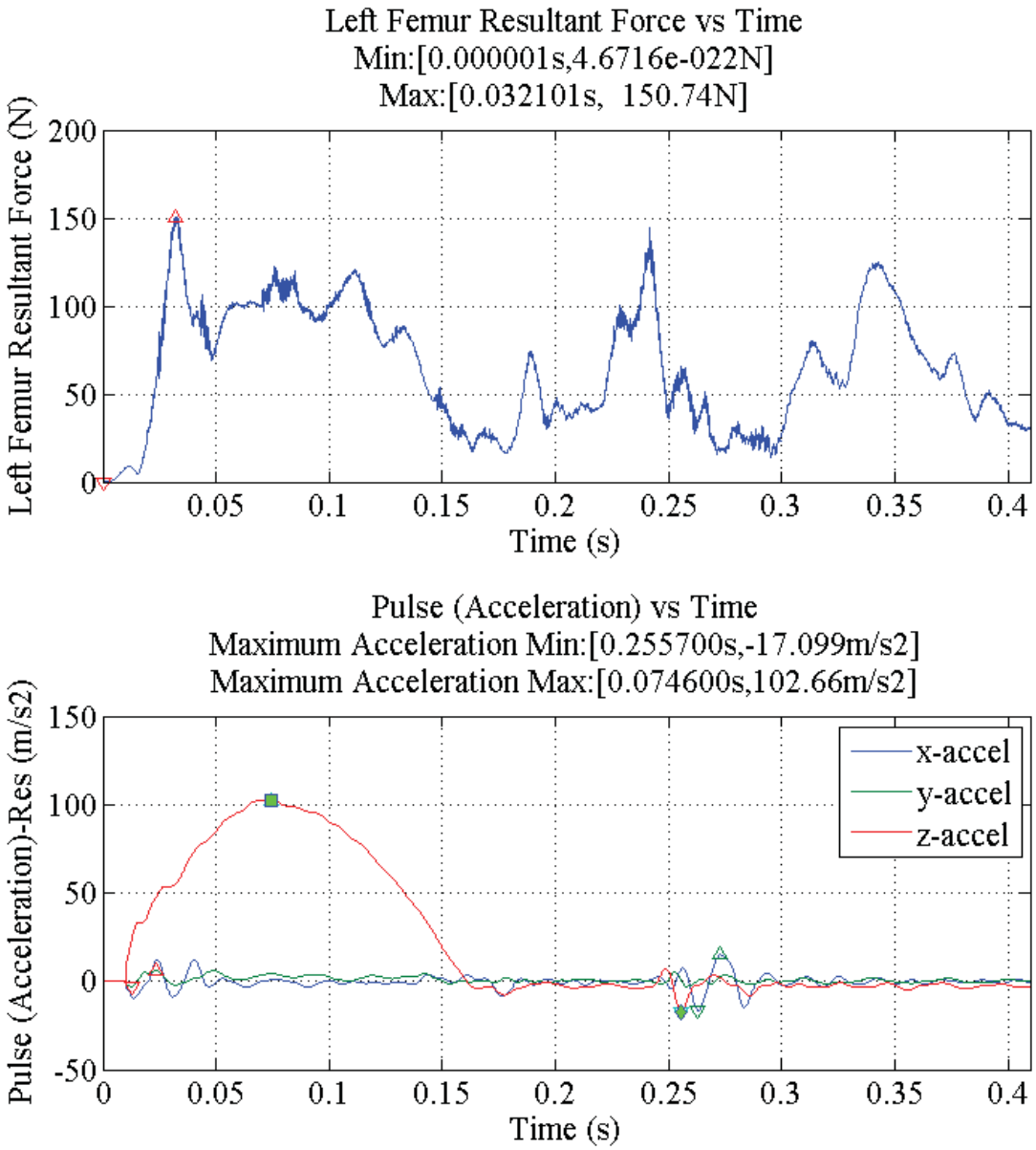

Figure 169: Left Femur Force for simulation 8208 (Spinal), long pulse, X-axis gravity.

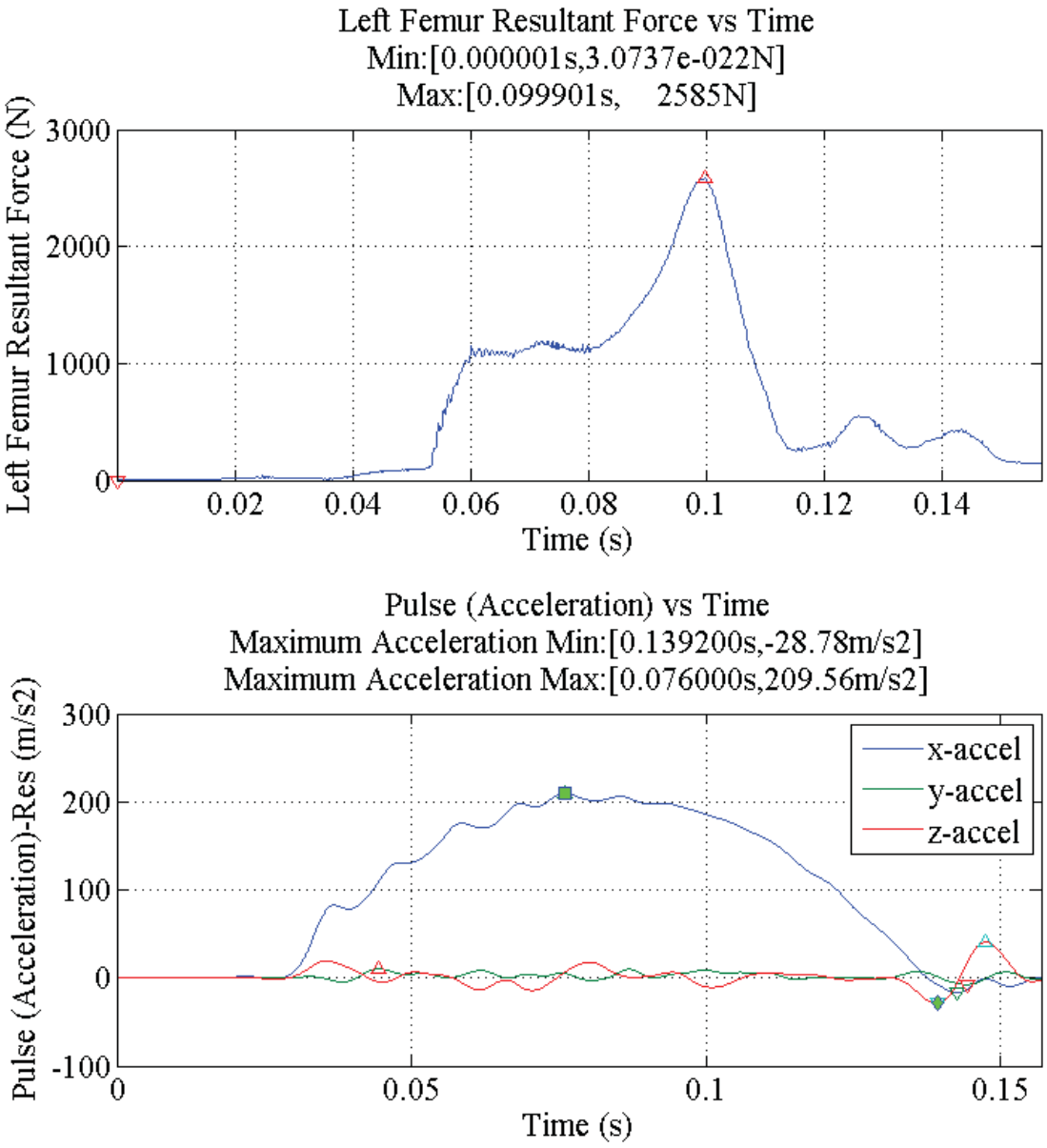

Figure 170: Left Femur Force for simulation 8212 (Rear), short pulse.

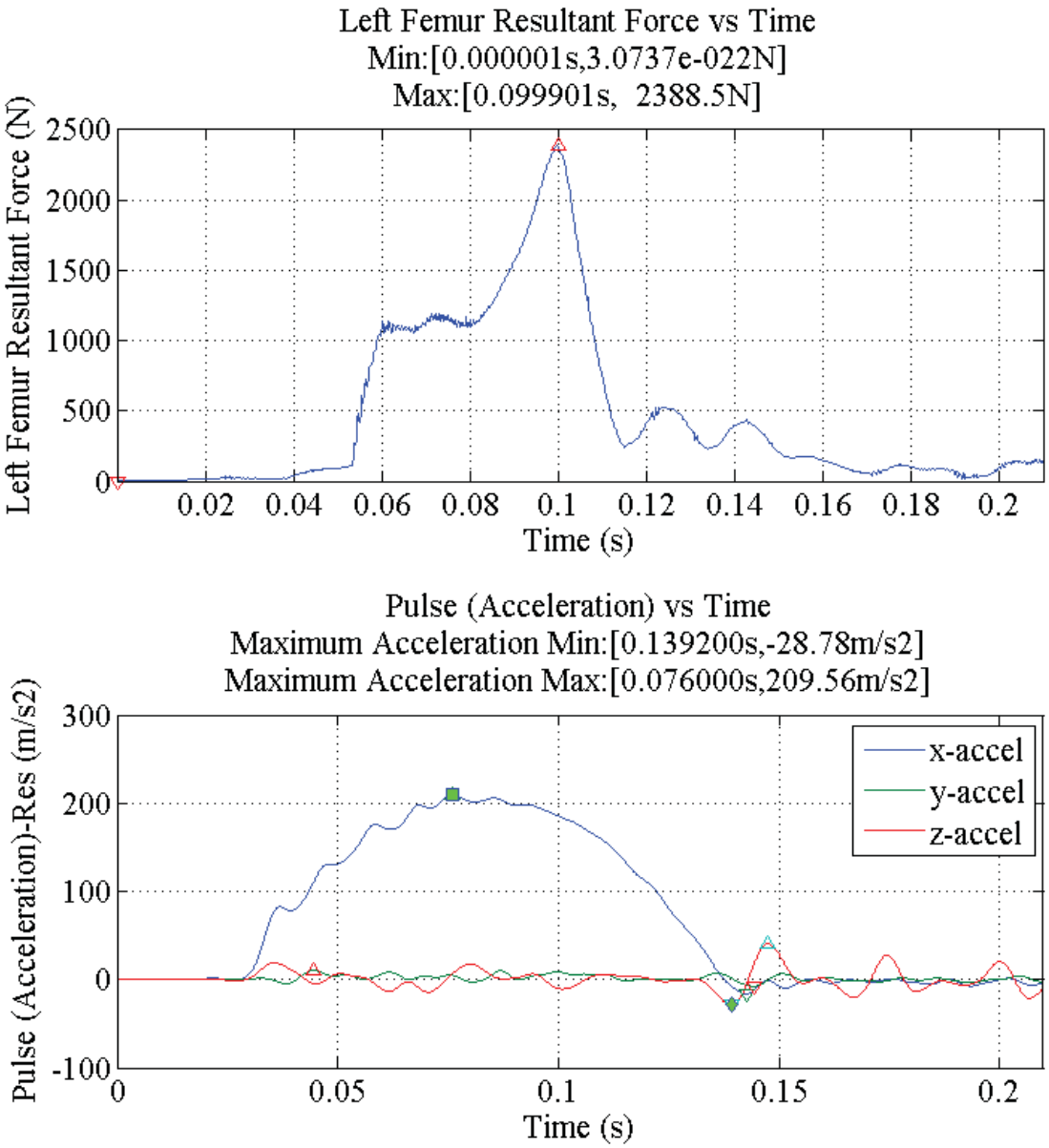

Figure 171: Left Femur Force for simulation 8212 (Rear), long pulse.

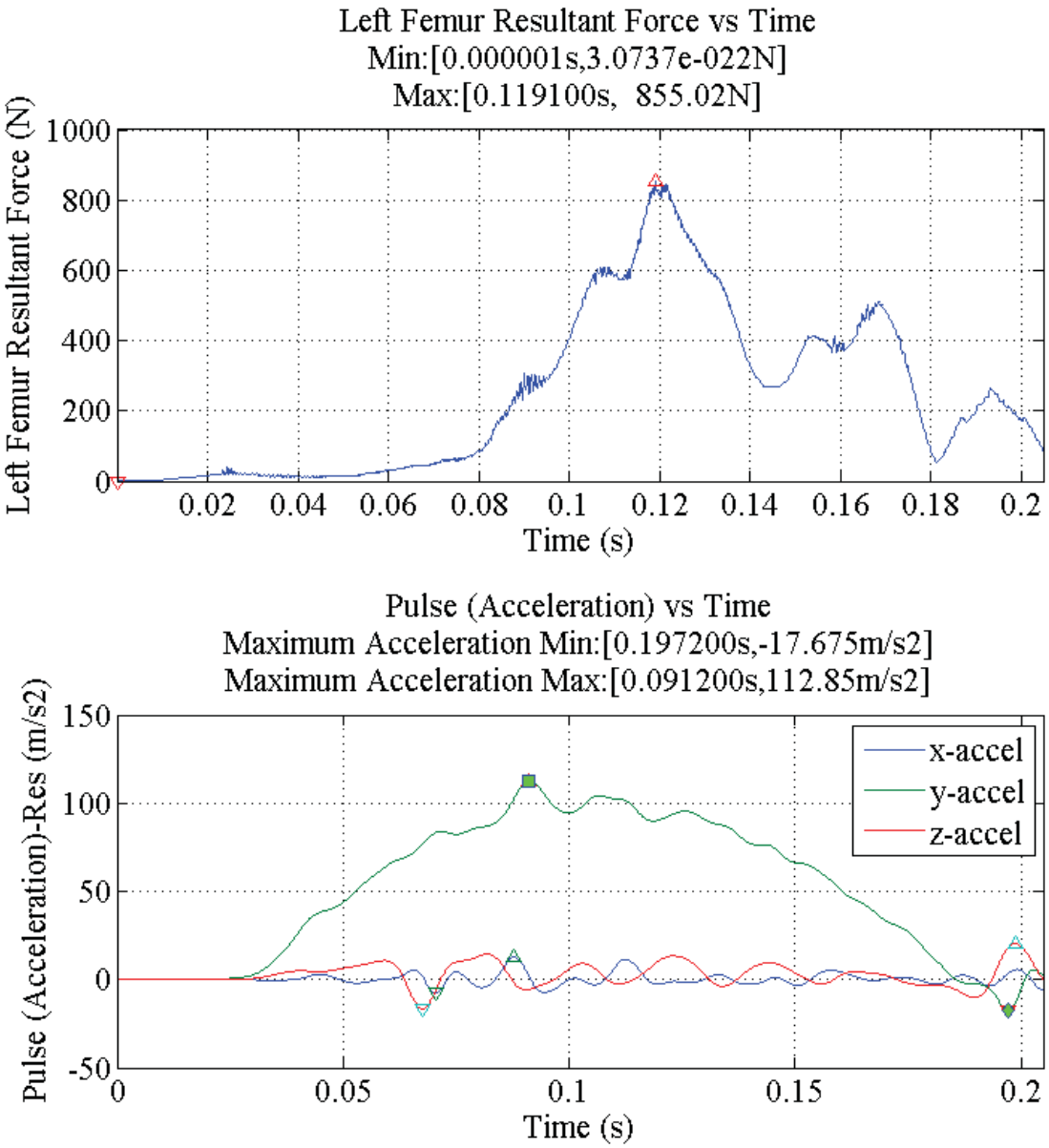

Figure 172: Left Femur Force for simulation 8245 (Lateral), short pulse.

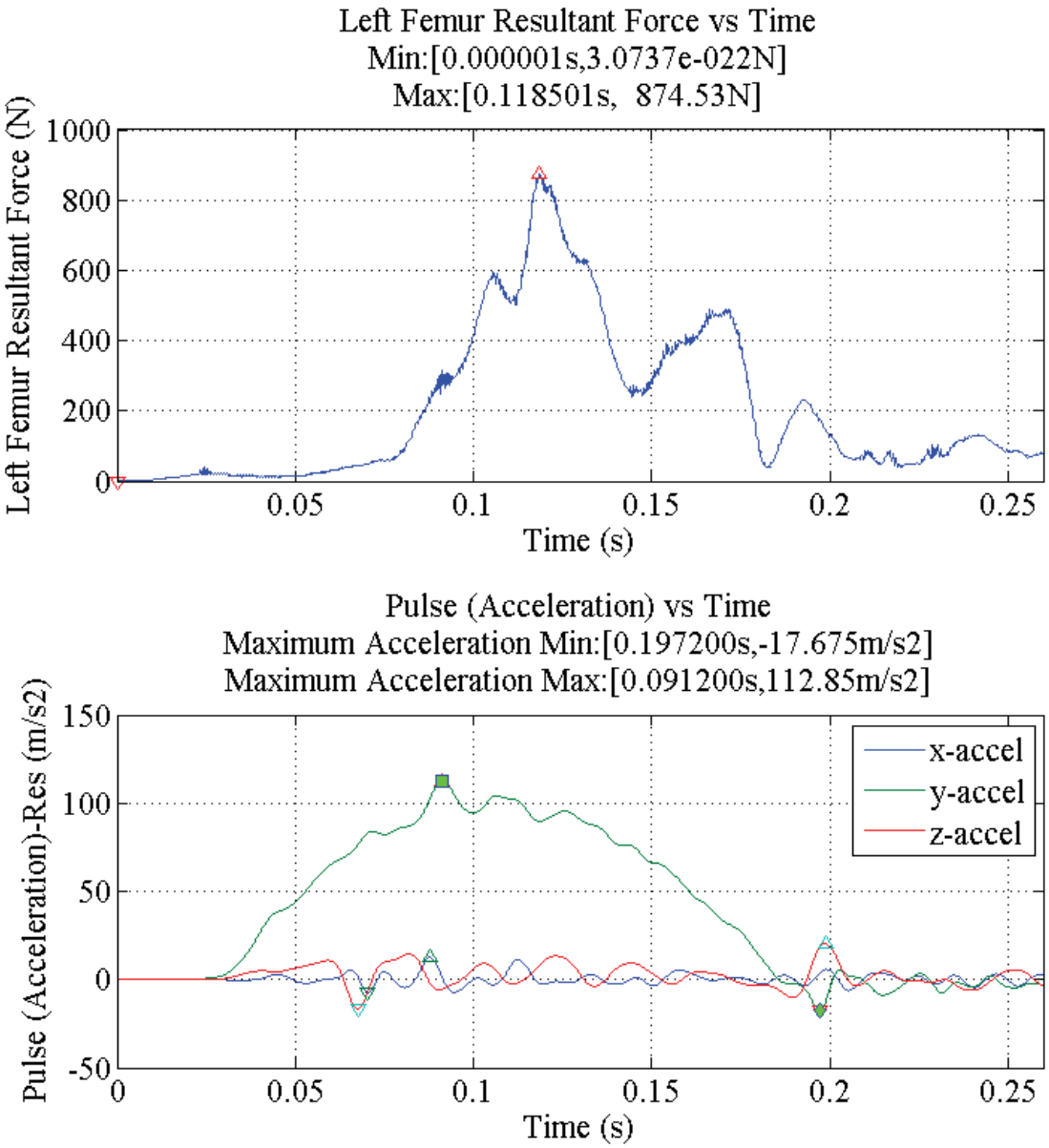

Figure 173: Left Femur Force for simulation 8245 (Lateral), long pulse.

Appendix 15: Lower Extremity Injury, Right Tibia Force

Table 13: Tabulated Right Tibia Force

Simulation	Right Tibia Force (N)
8202, Frontal, Short pulse	415.71
8202, Frontal, Long pulse	402.87
8208, Spinal, Short pulse, X-axis gravity	321.23
8208, Spinal, Short pulse, Z-axis gravity	285.22
8208, Spinal, Long pulse, X-axis gravity	366.29
8212, Rear, Short pulse	1608.50
8212, Rear, Long pulse	1638.70
8245, Lateral, Short pulse	610.81
8245, Lateral, Long pulse	612.42

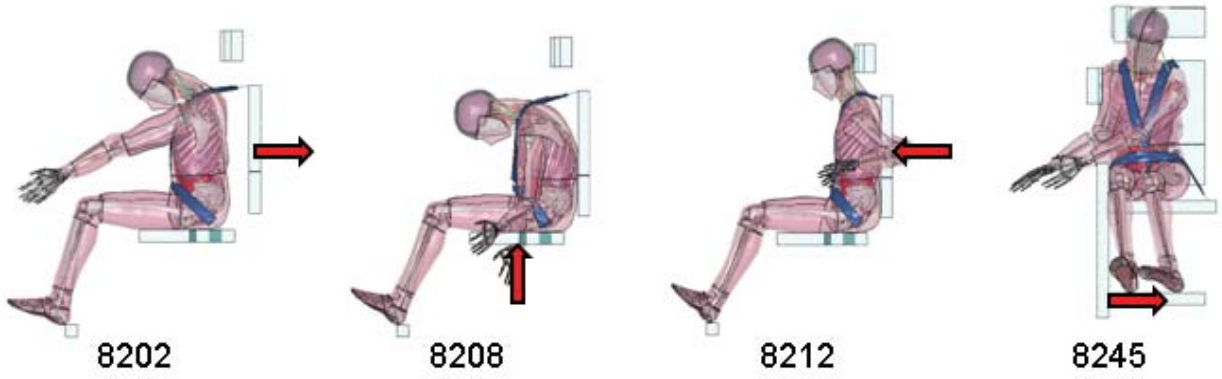

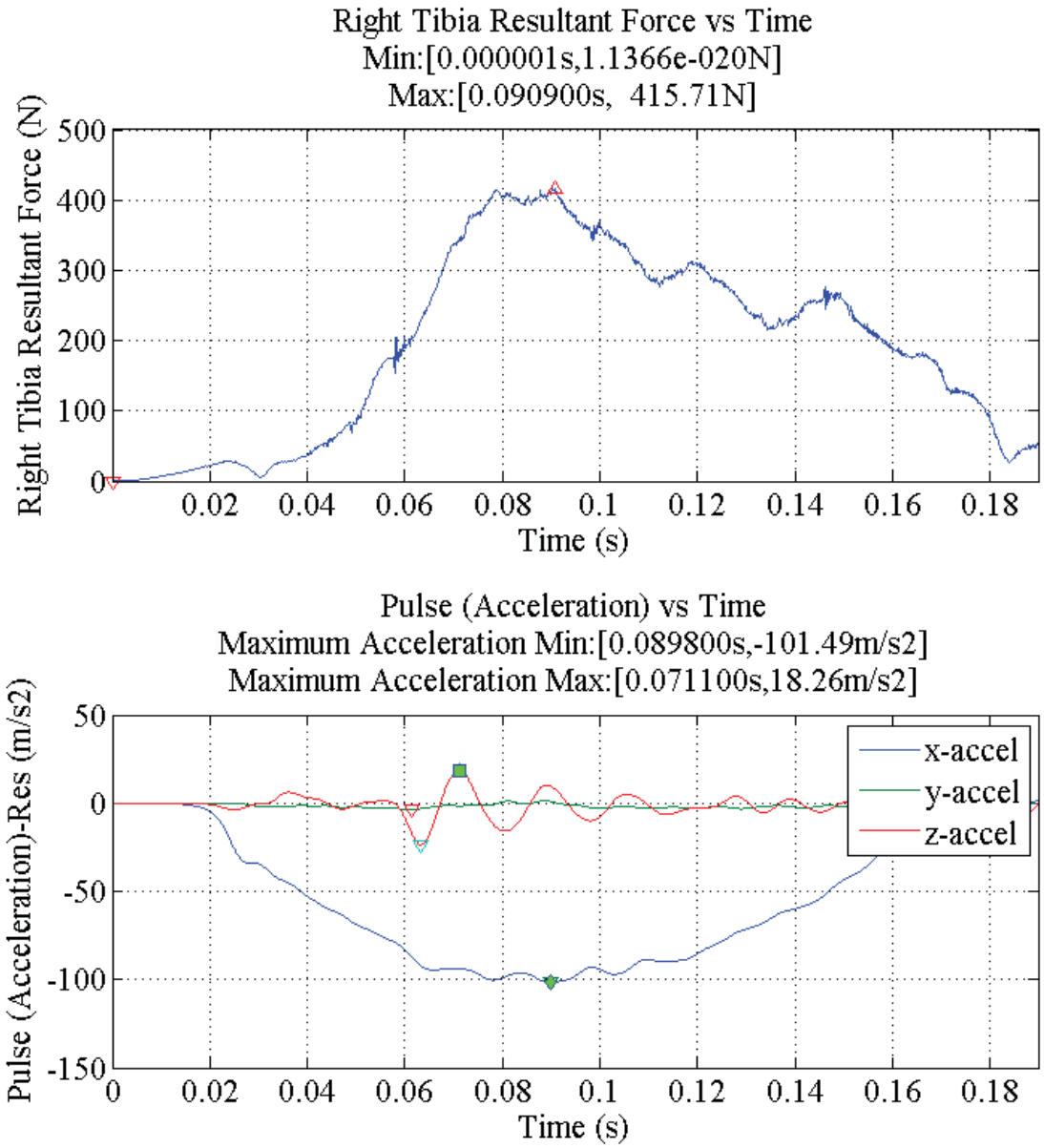

Figure 174: Right Tibia Force for simulation 8202 (Frontal), short pulse.

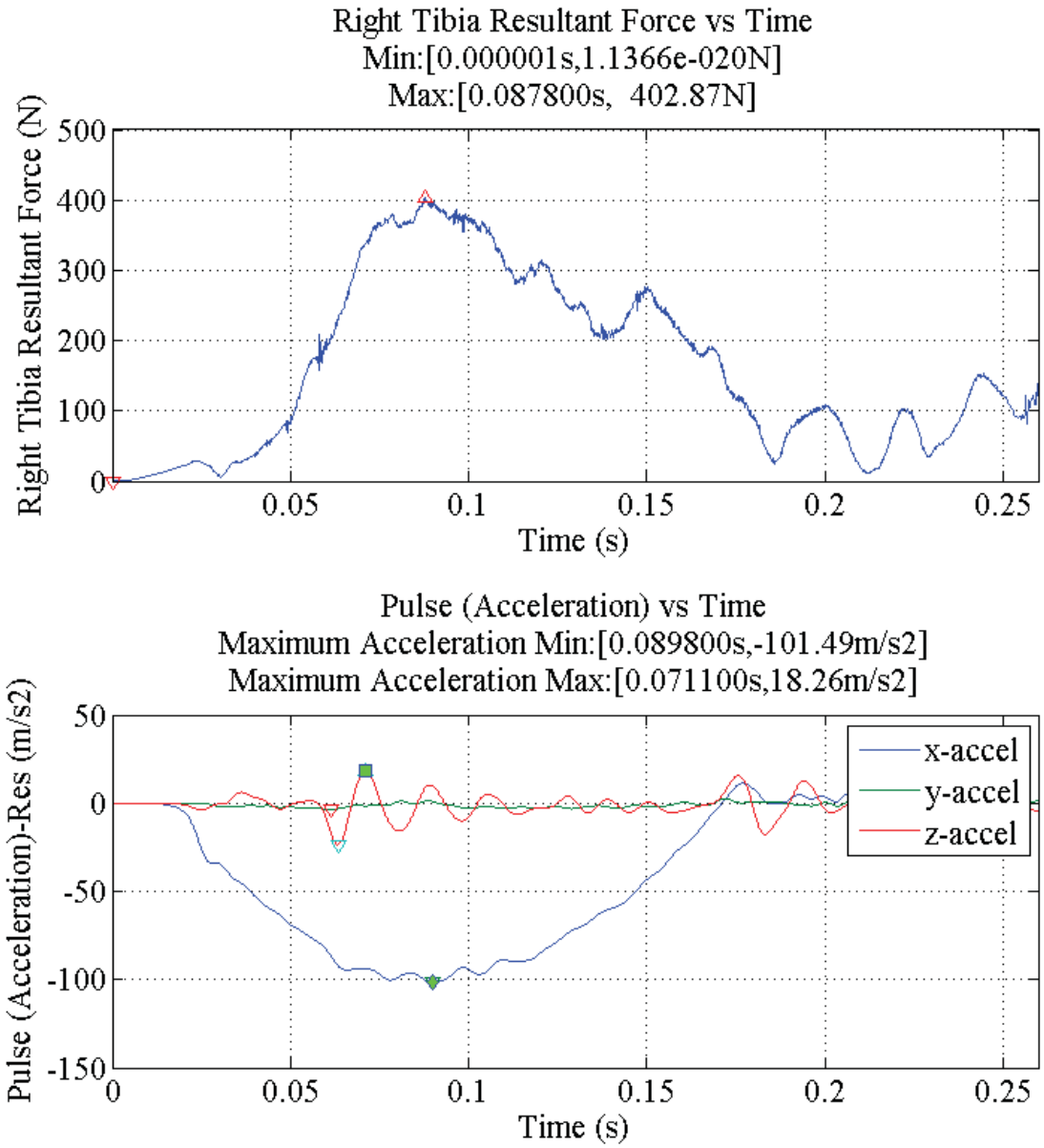

Figure 175: Right Tibia Force for simulation 8202 (Frontal), long pulse.

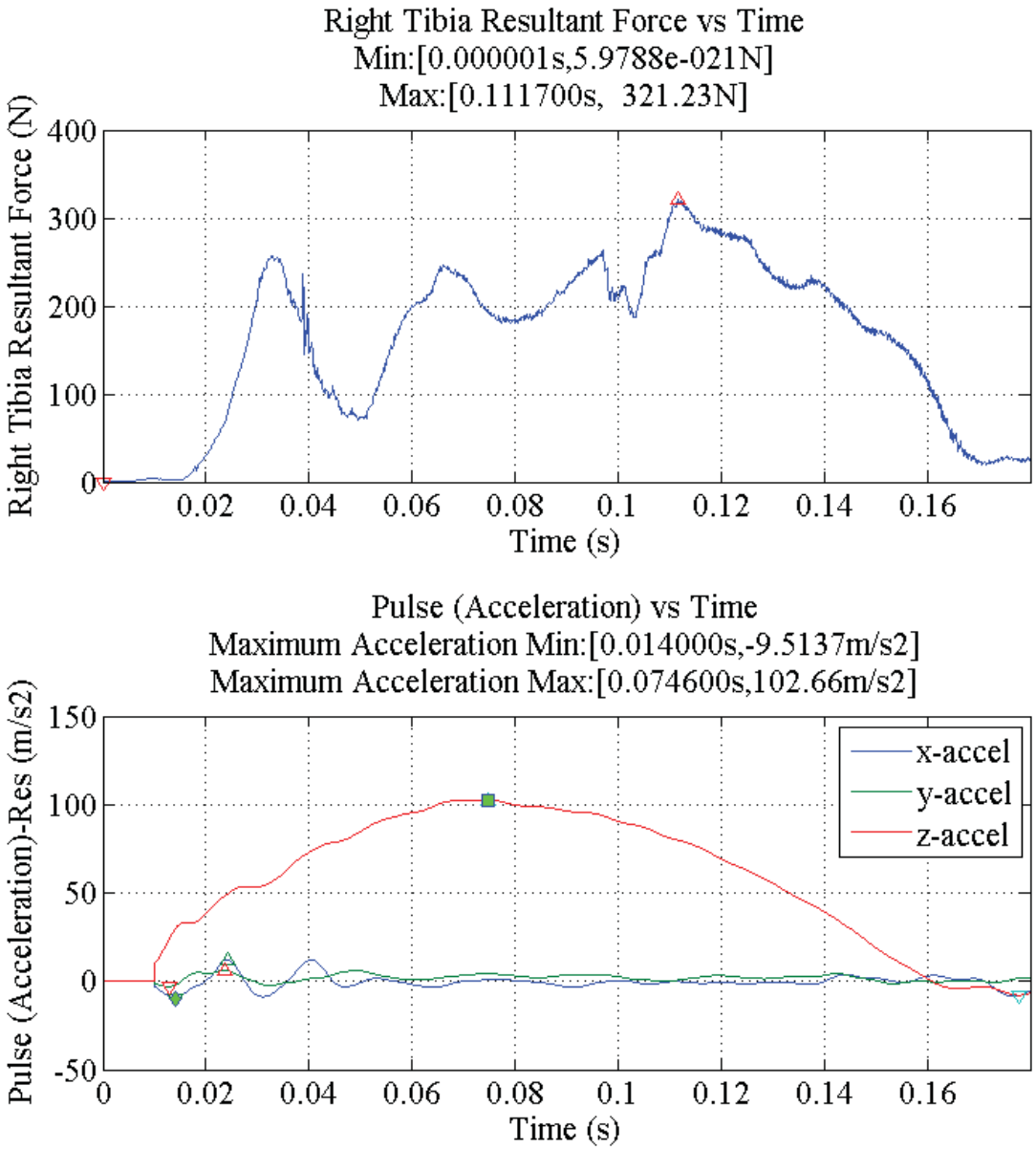

Figure 176: Right Tibia Force for simulation 8208 (Spinal), short pulse, X-axis loading.

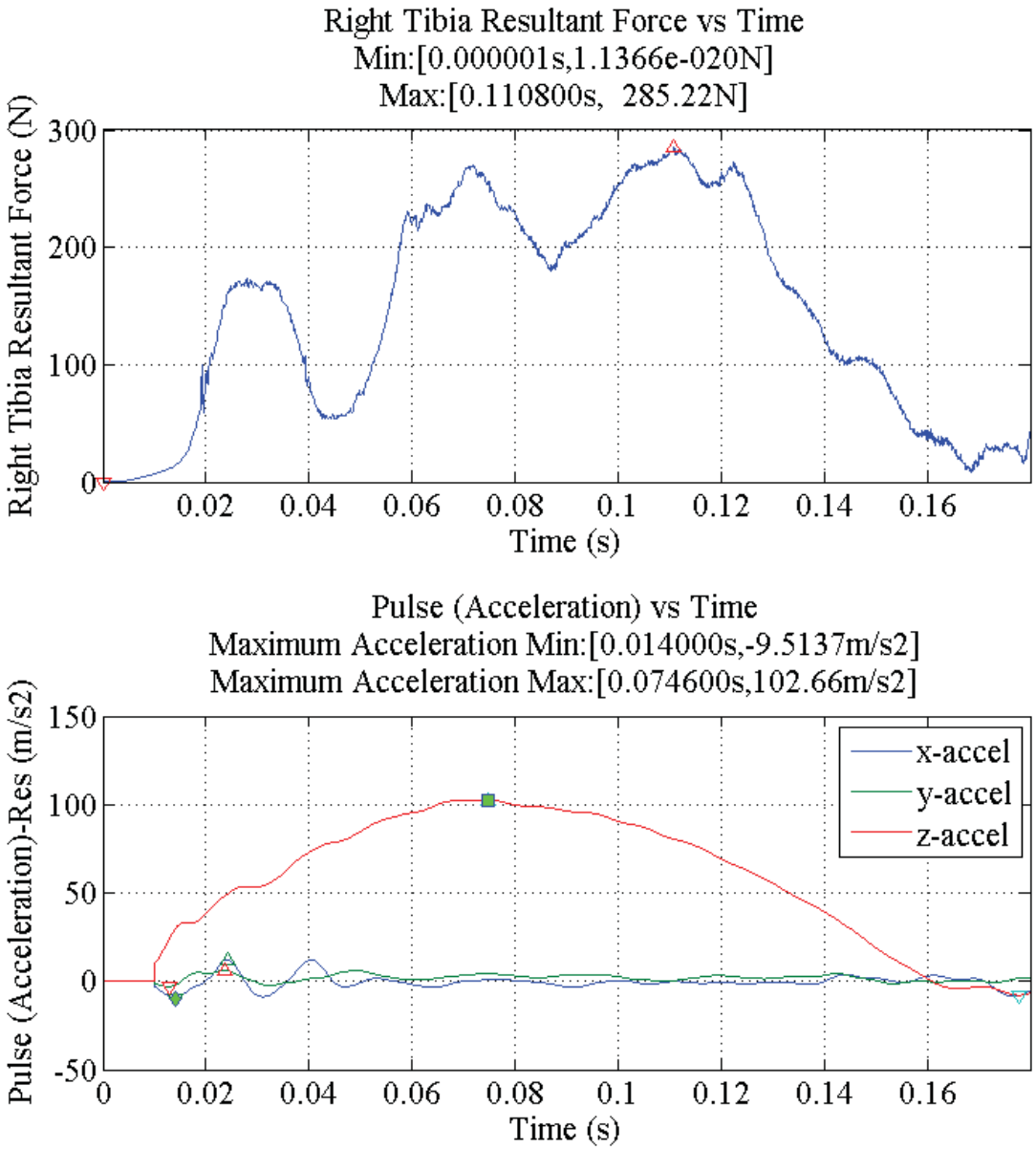

Figure 177: Right Tibia Force for simulation 8208 (Spinal), short pulse, Z-axis loading.

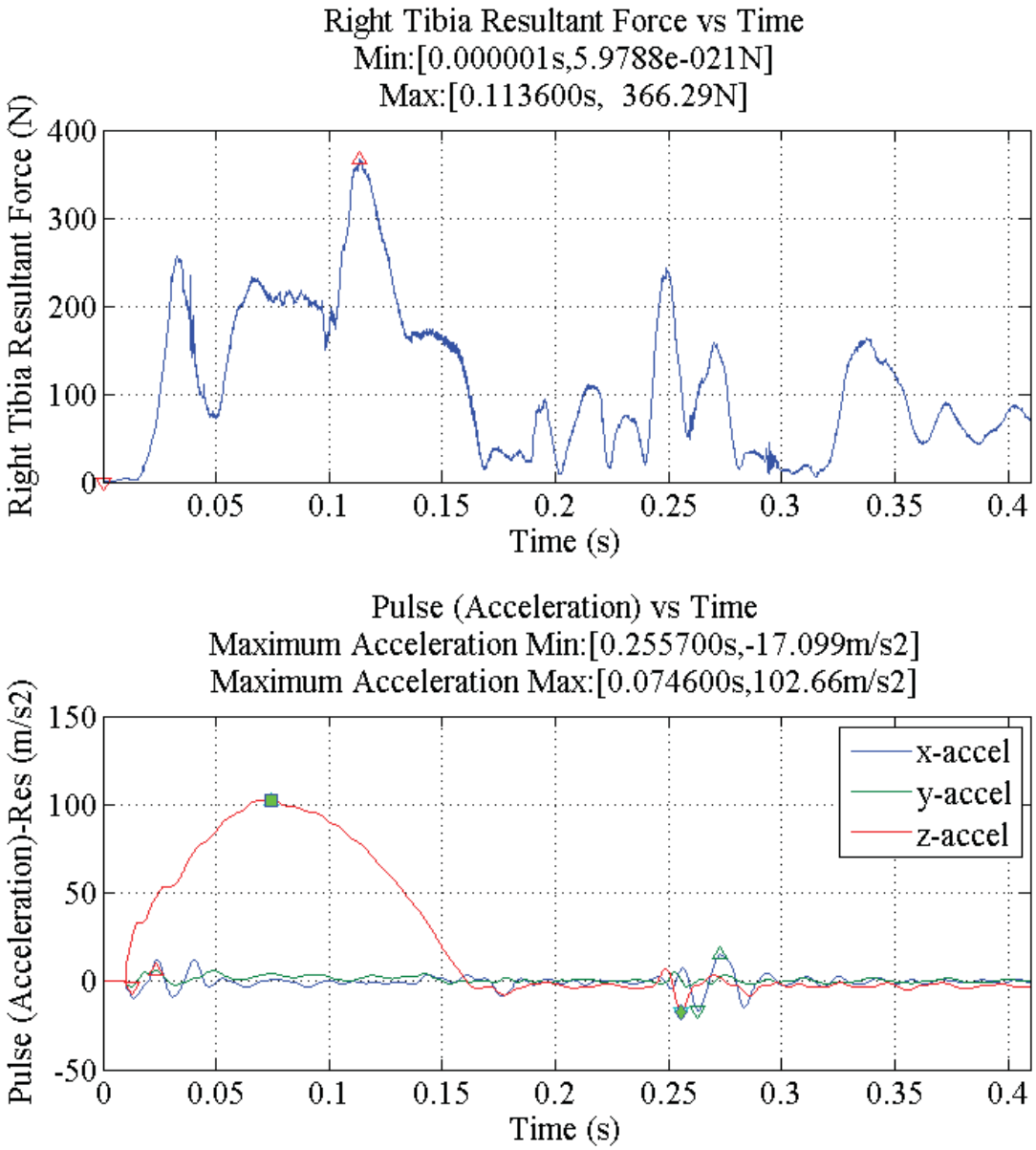

Figure 178: Right Tibia Force for simulation 8208 (Spinal), long pulse, X-axis loading.

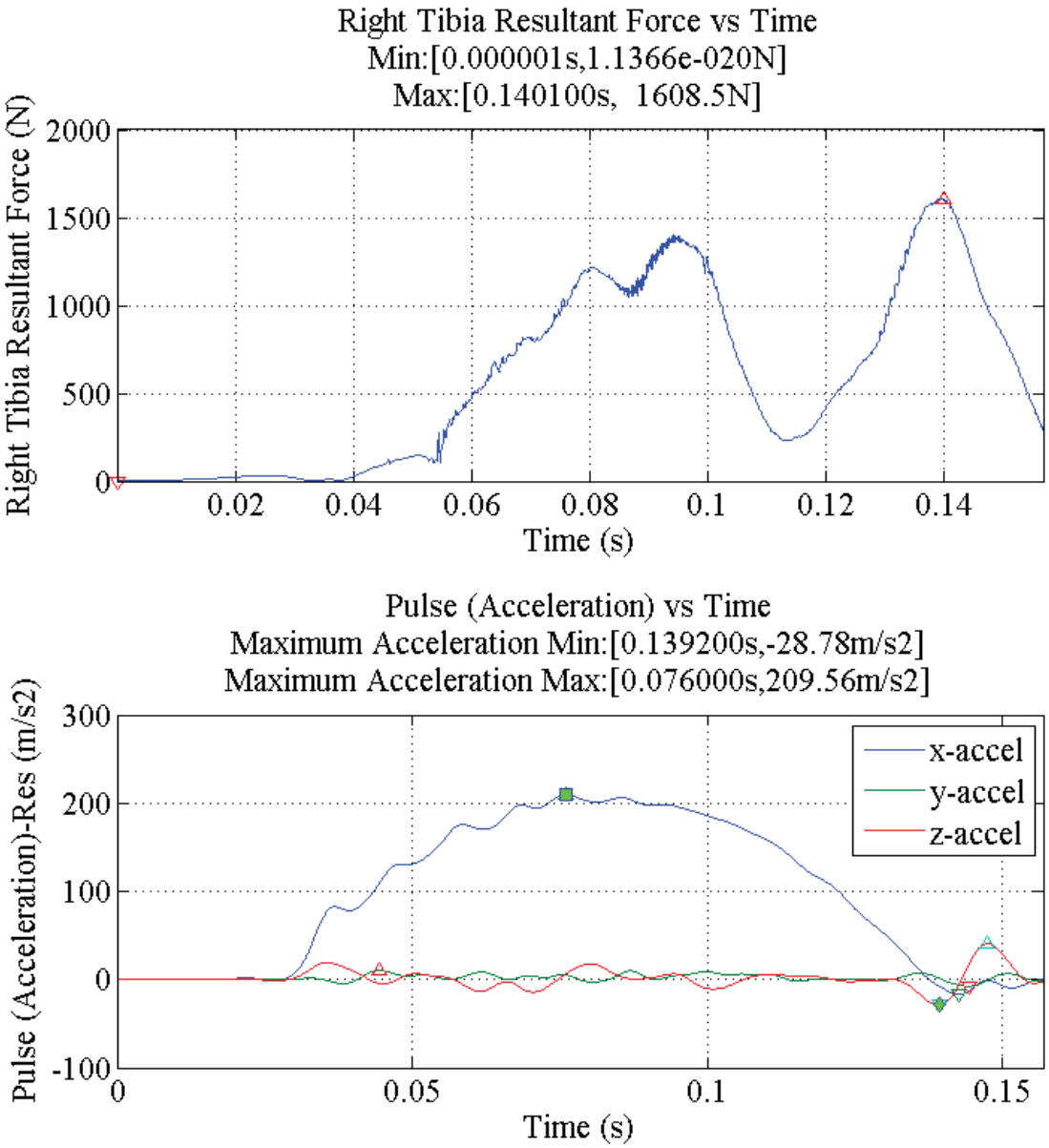

Figure 179: Right Tibia Force for simulation 8212 (Rear), short pulse.

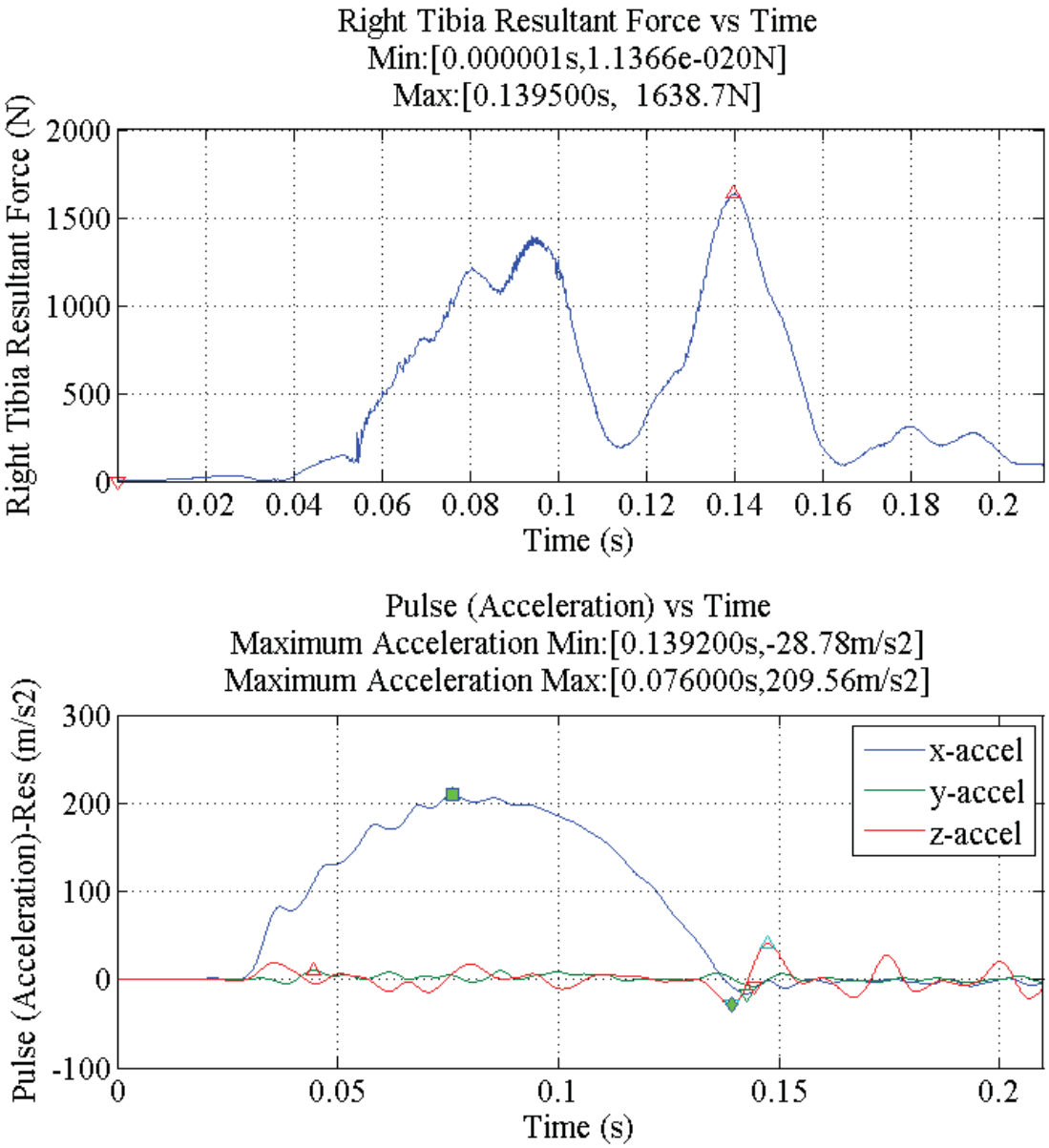

Figure 180: Right Tibia Force for simulation 8212 (Rear), long pulse.

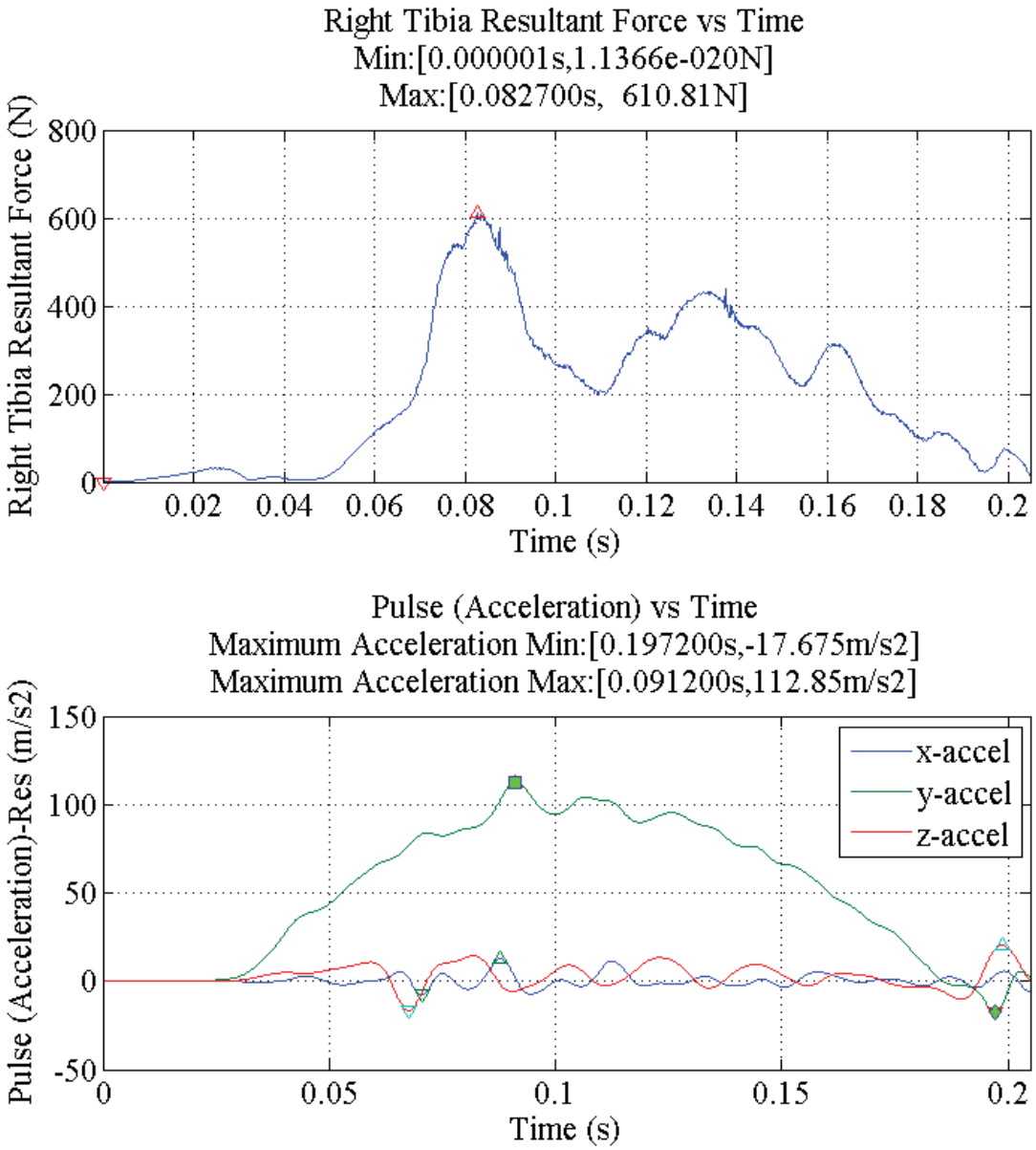

Figure 181: Right Tibia Force for simulation 8245 (Lateral), short pulse.

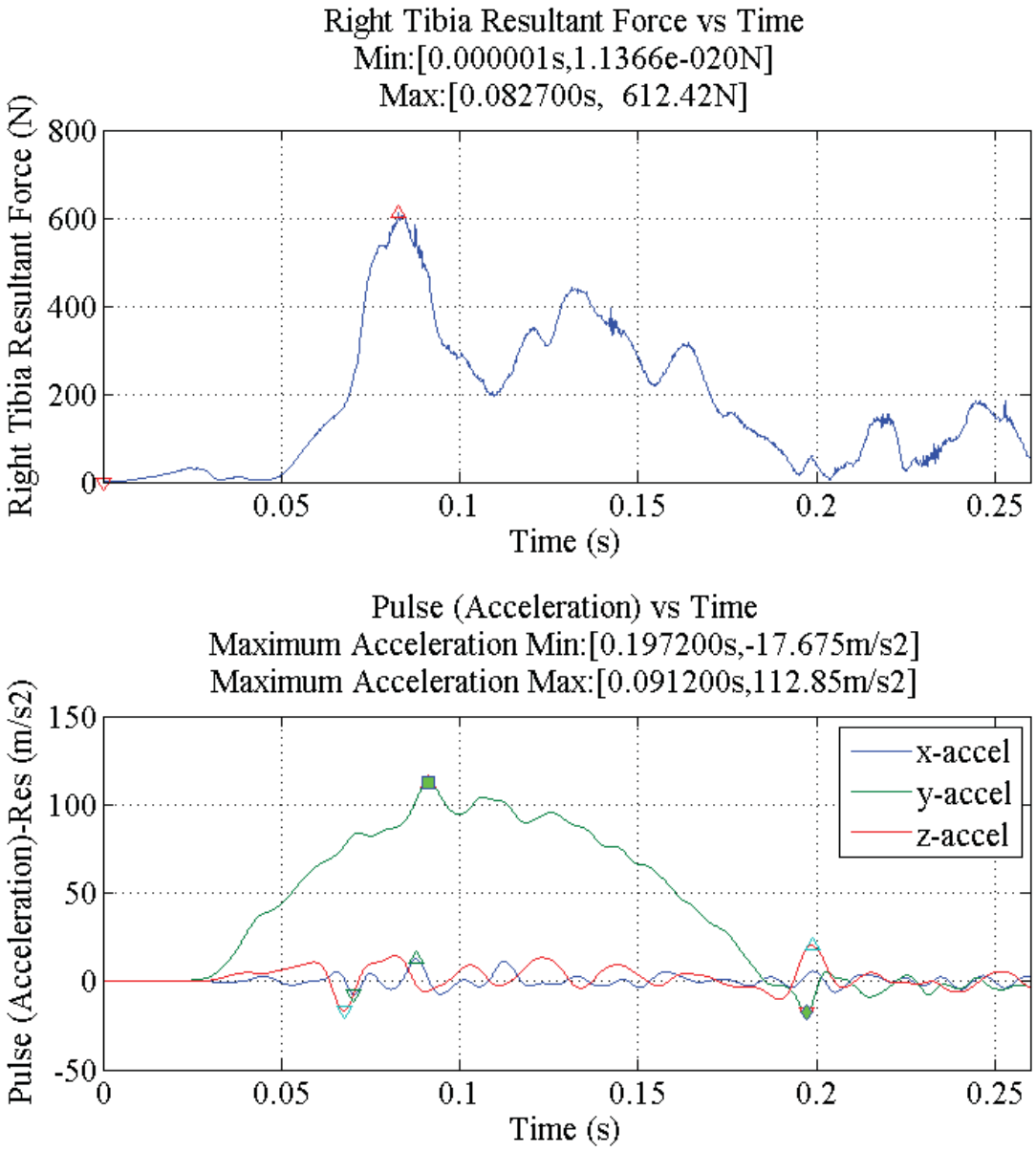

Figure 182: Right Tibia Force for simulation 8245 (Lateral), long pulse.

Appendix 16: Lower Extremity Injury, Left Tibia Force

Table 14: Tabulated Left Tibia Force

Simulation	Left Tibia Force (N)
8202, Frontal, Short pulse	440.58
8202, Frontal, Long pulse	423.77
8208, Spinal, Short pulse, X-axis gravity	286.27
8208, Spinal, Short pulse, Z-axis gravity	281.36
8208, Spinal, Long pulse, X-axis gravity	317.19
8212, Rear, Short pulse	1469.30
8212, Rear, Long pulse	1421.10
8245, Lateral, Short pulse	2275.20
8245, Lateral, Long pulse	2305.10

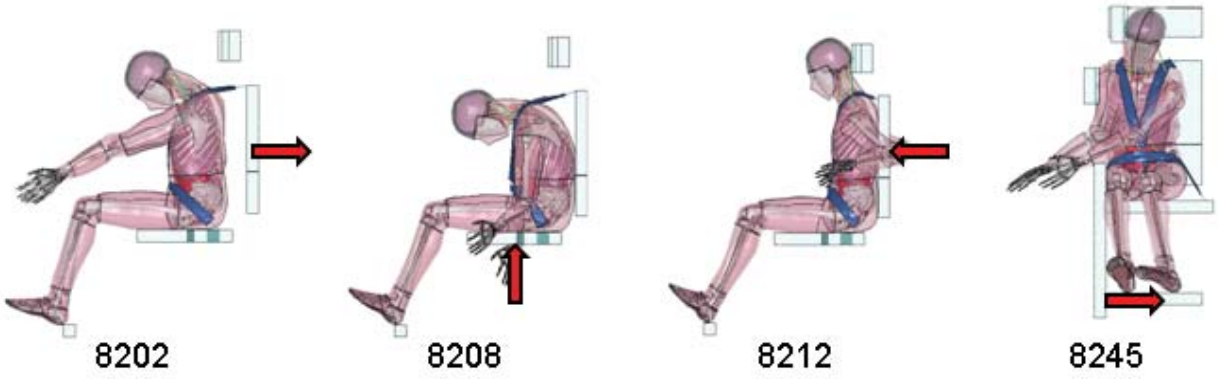

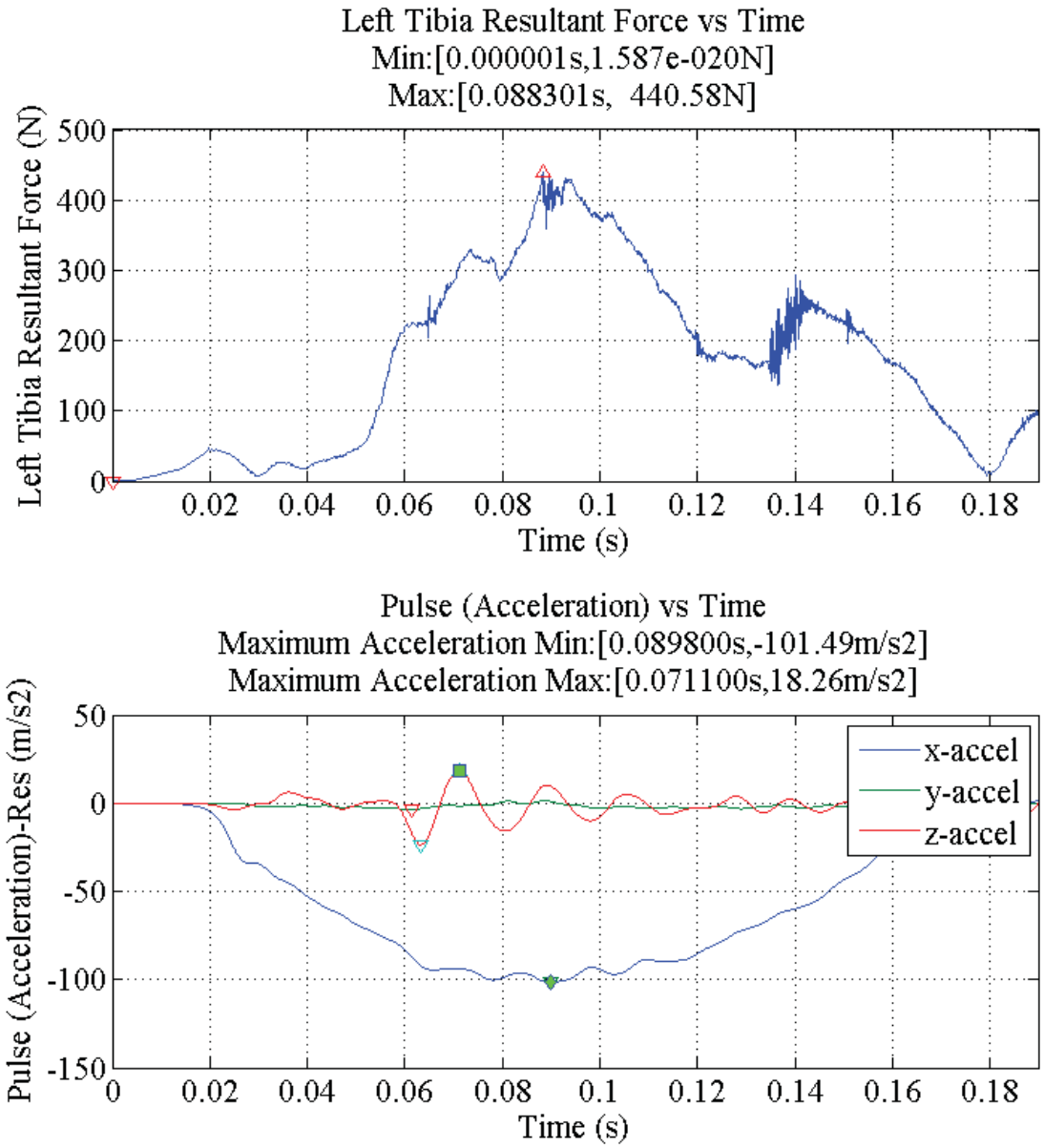

Figure 183: Left Tibia Force for simulation 8202 (Frontal), short pulse.

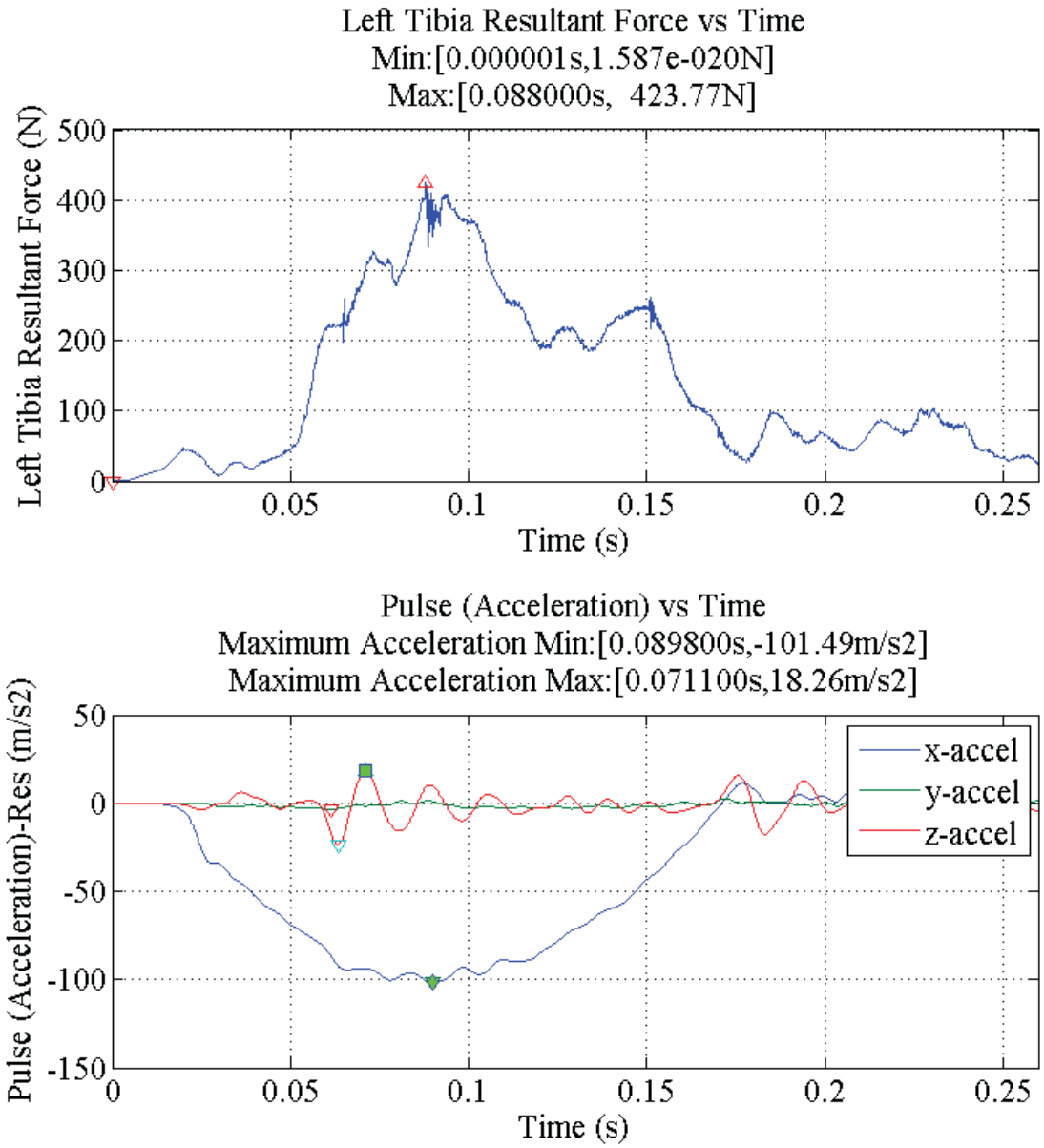

Figure 184: Left Tibia Force for simulation 8202 (Frontal), long pulse.

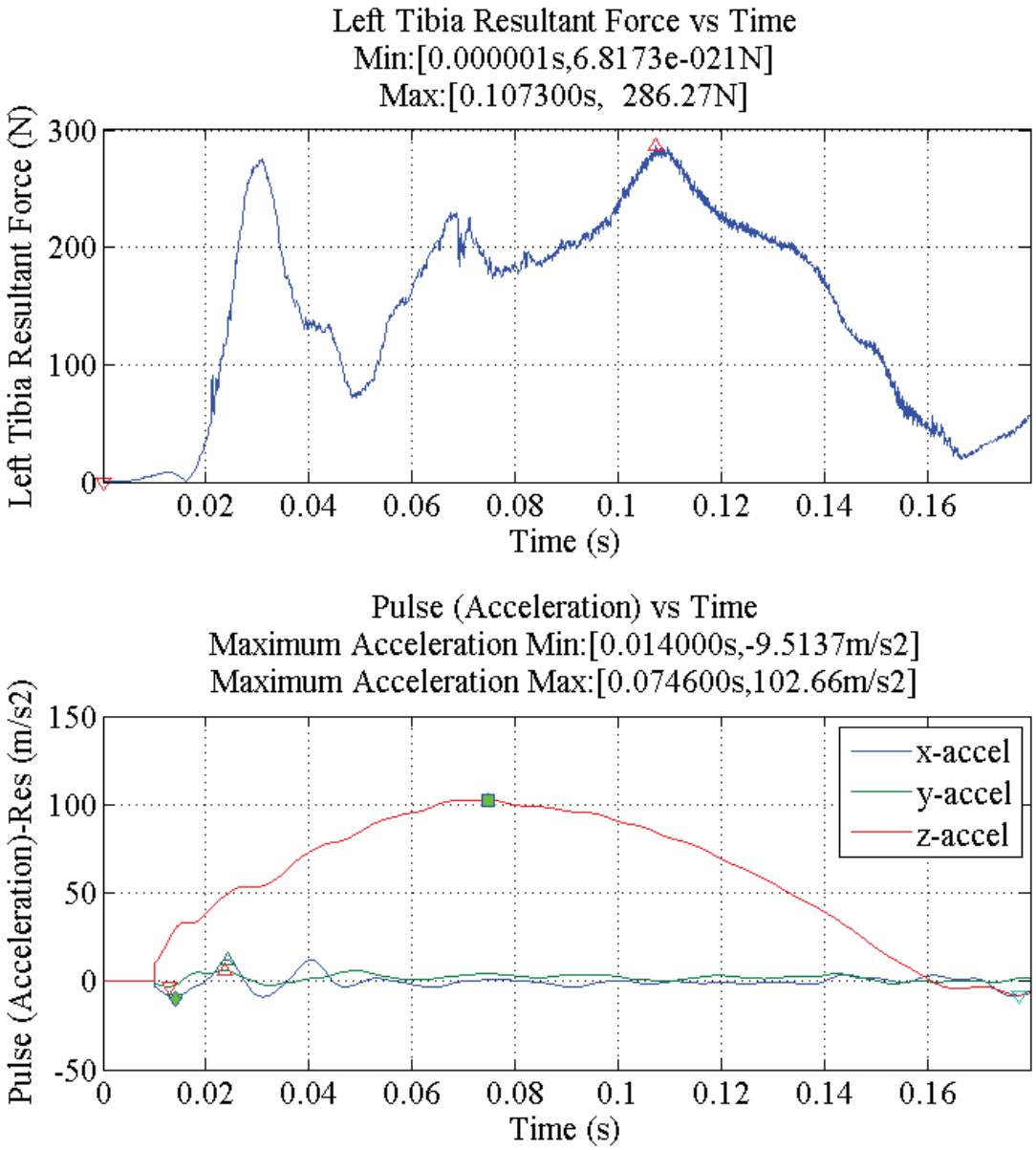

Figure 185: Left Tibia Force for simulation 8208 (Spinal), short pulse, X-axis gravity.

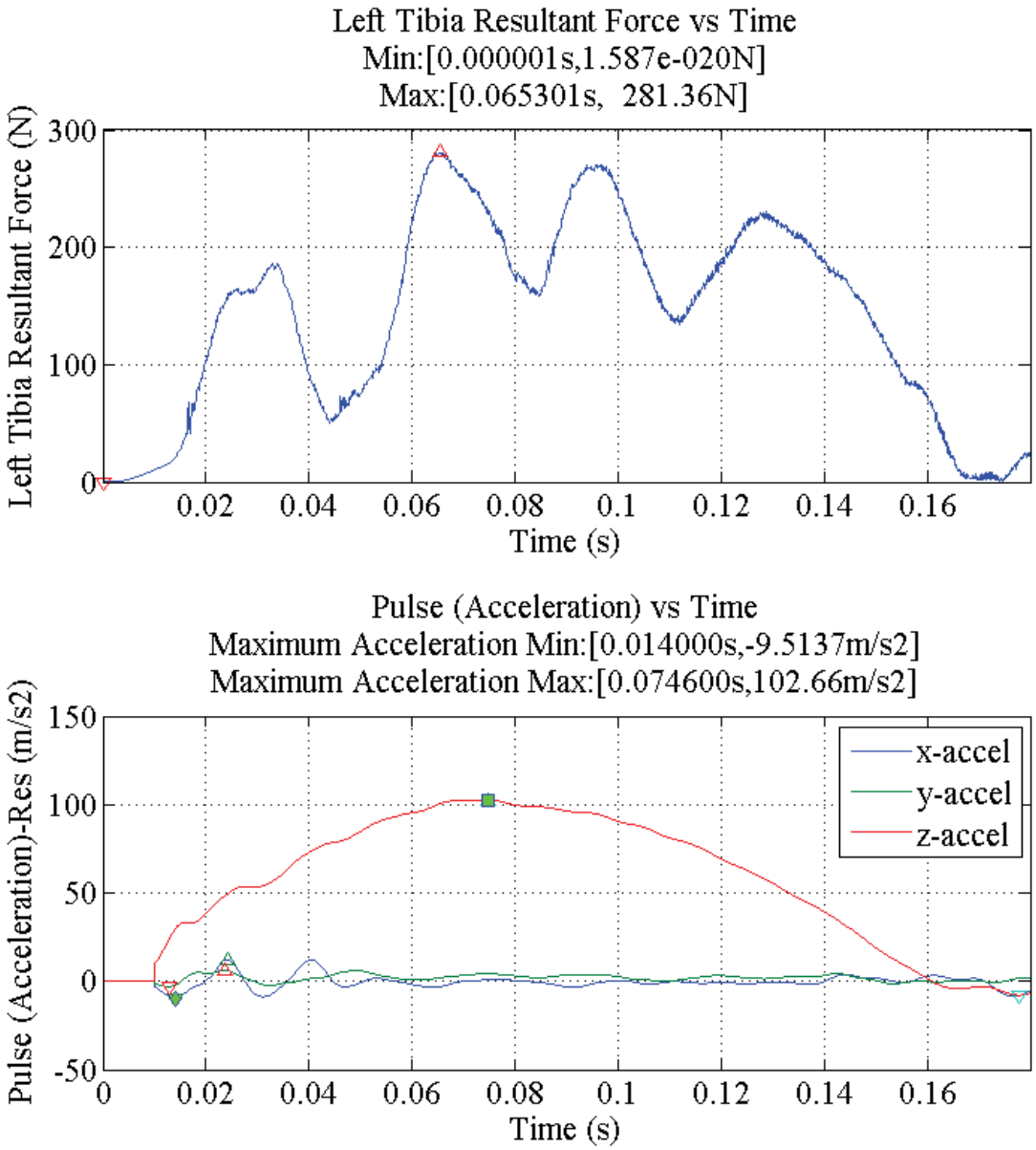

Figure 186: Left Tibia Force for simulation 8208 (Spinal), short pulse, Z-axis gravity.

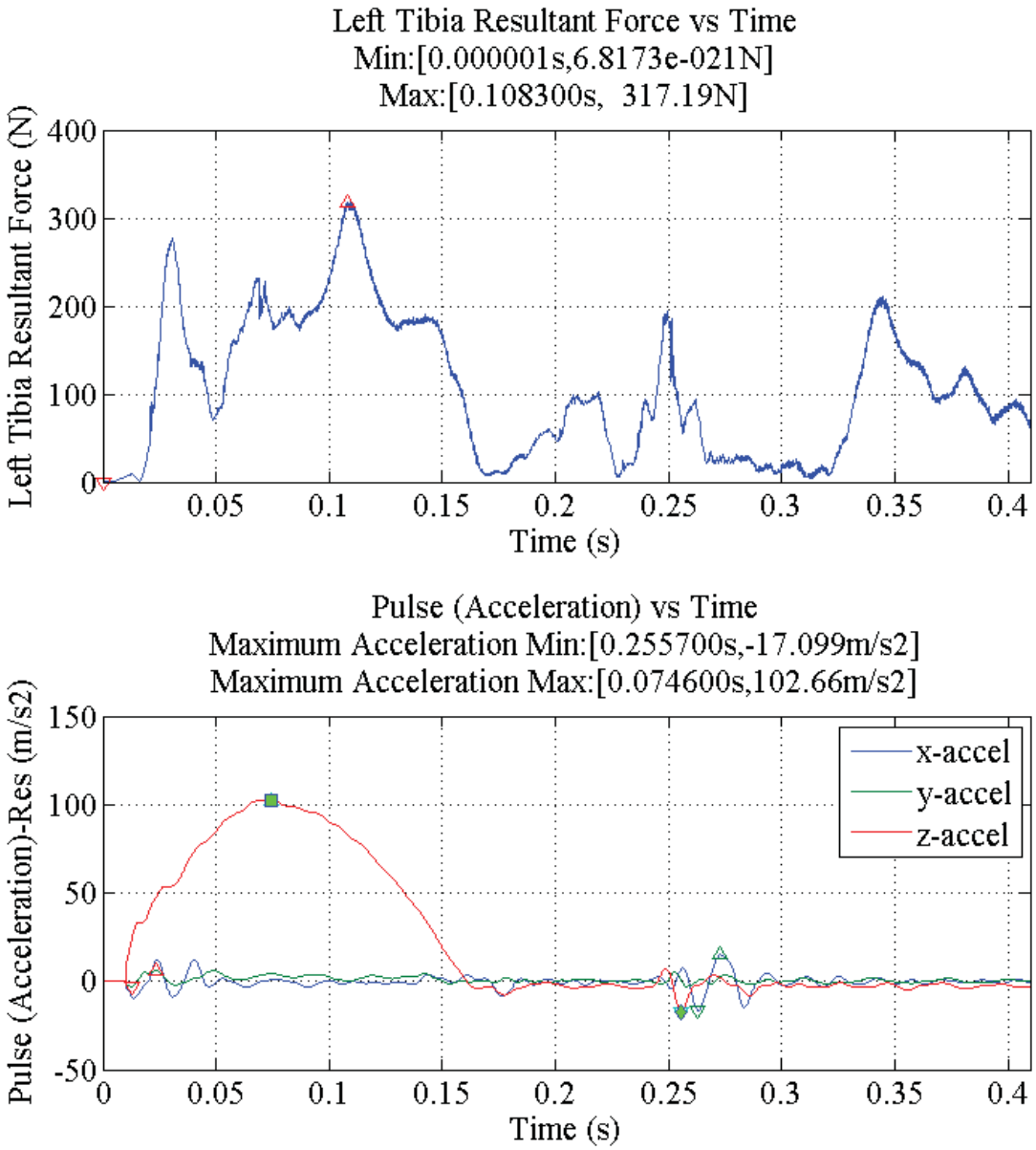

Figure 187: Left Tibia Force for simulation 8208 (Spinal), long pulse, X-axis gravity.

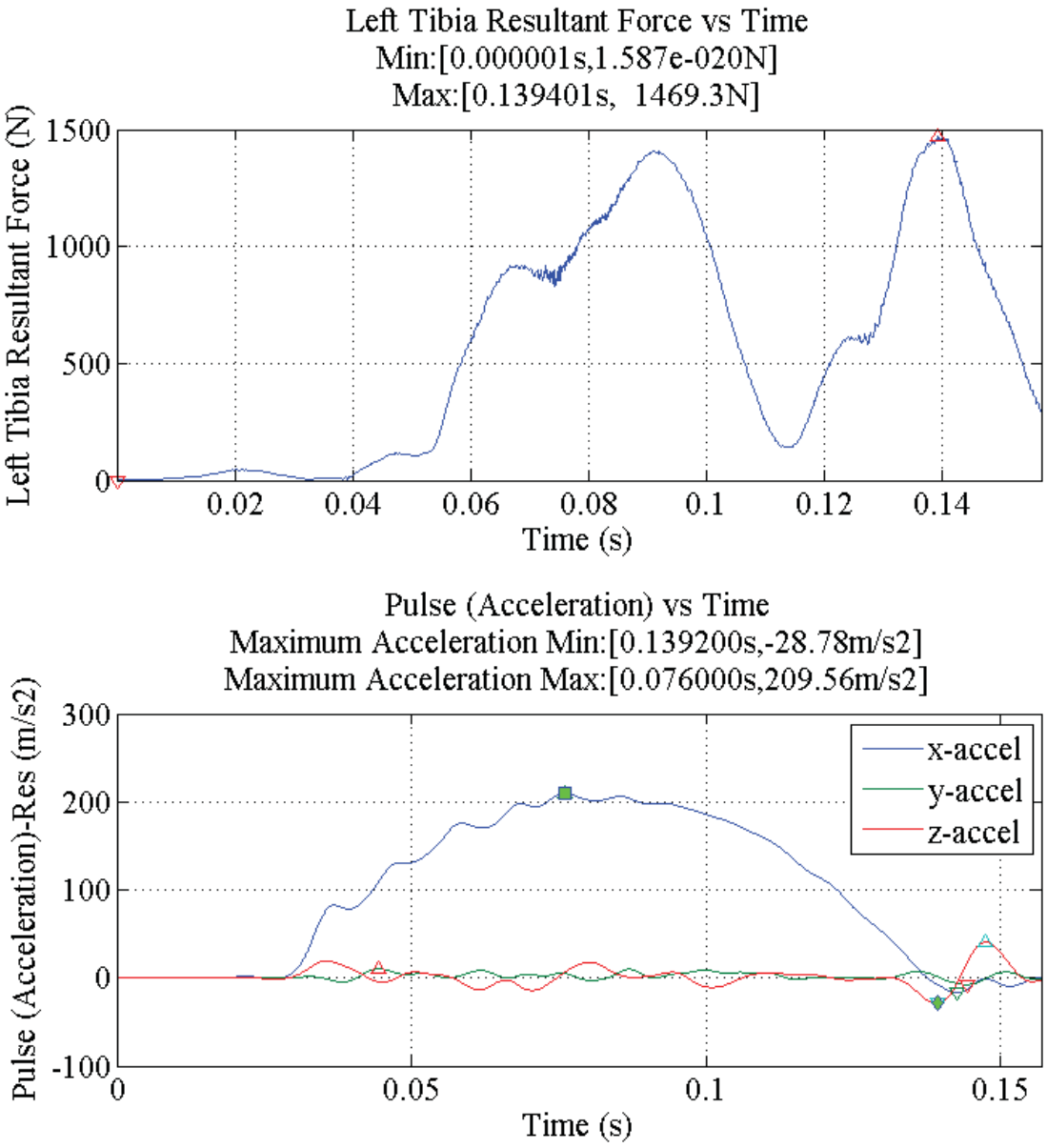

Figure 188: Left Tibia Force for simulation 8212 (Rear), short pulse.

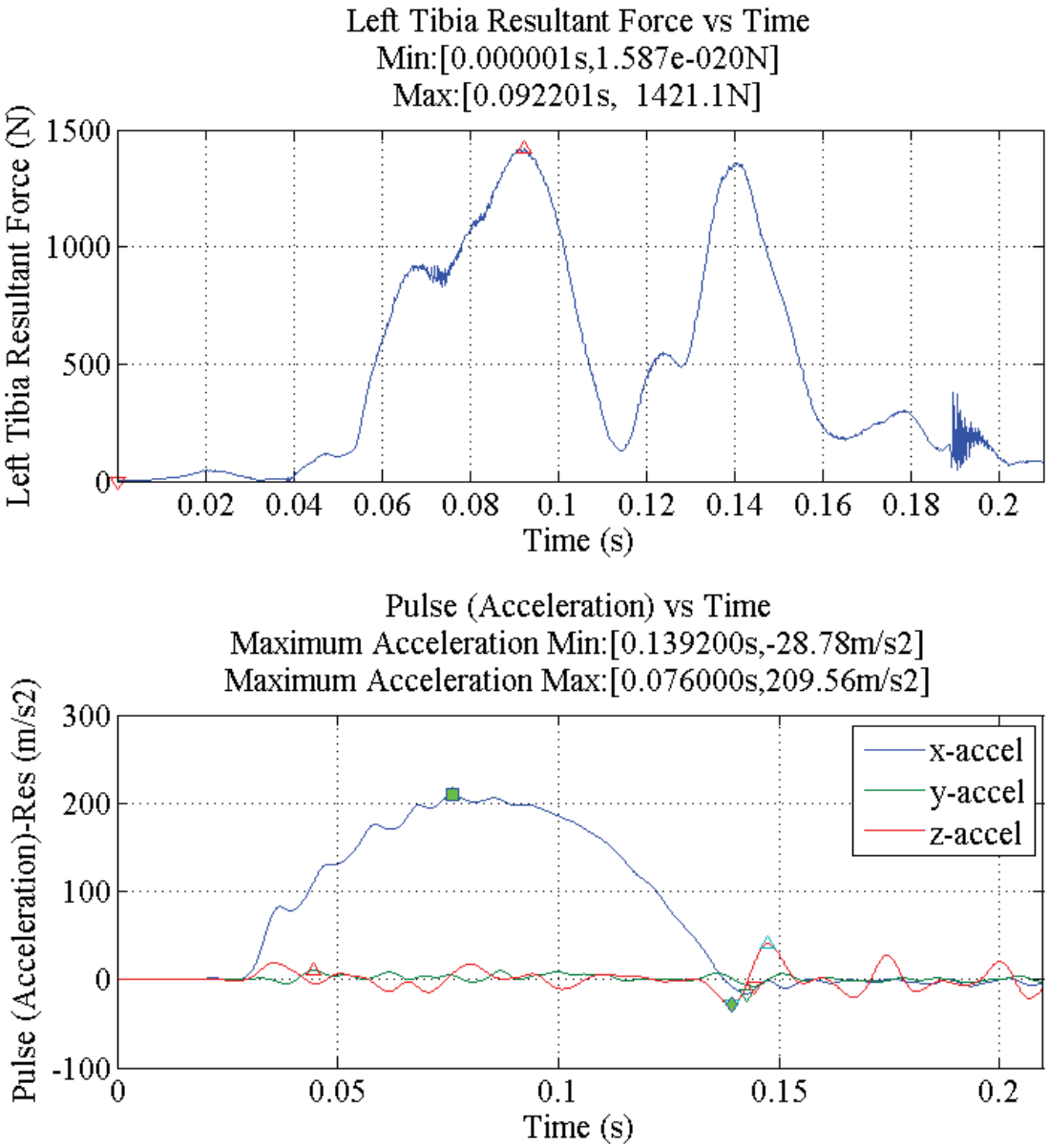

Figure 189: Left Tibia Force for simulation 8212 (Rear), long pulse.

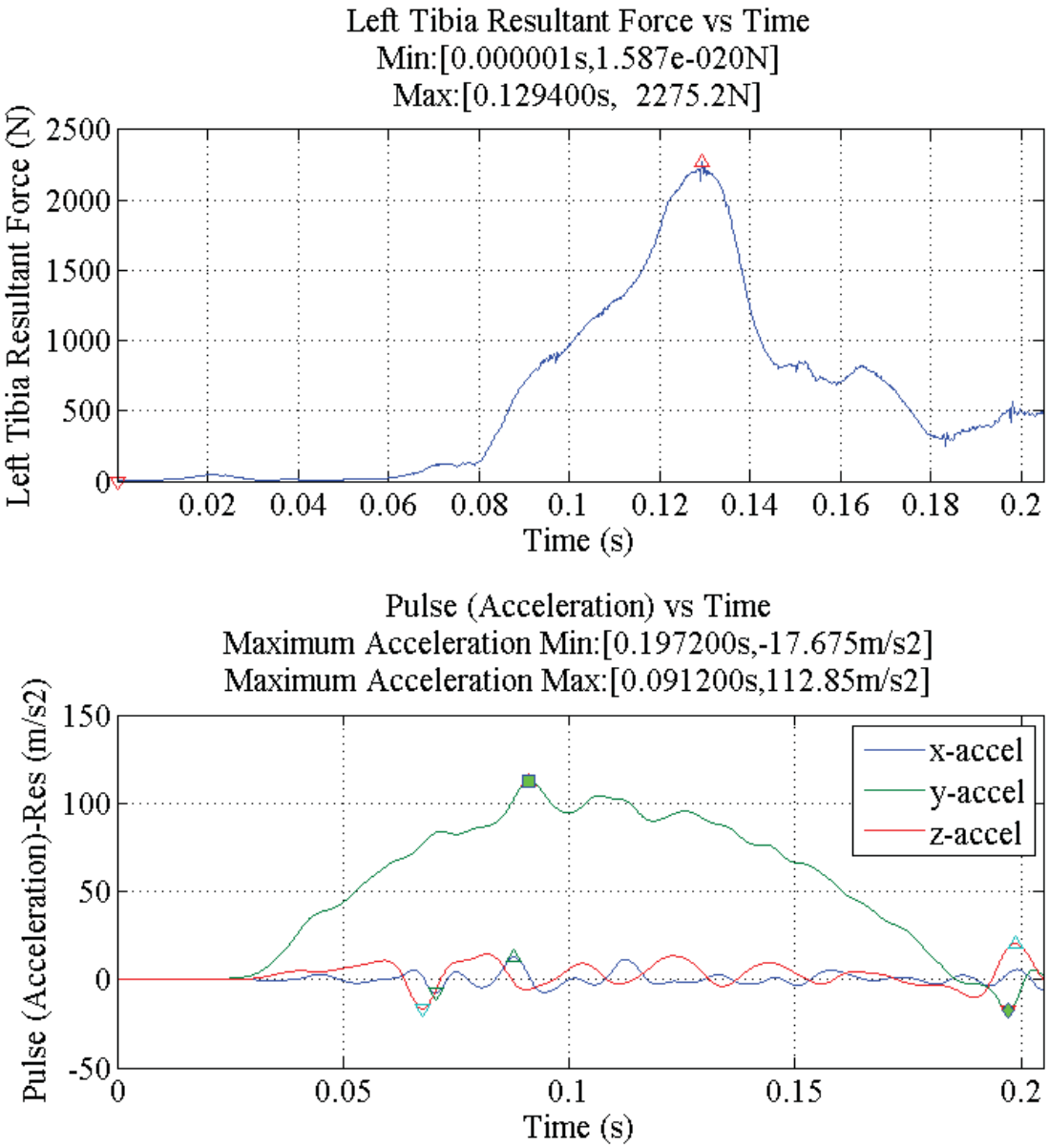

Figure 190: Left Tibia Force for simulation 8245 (Lateral), short pulse.

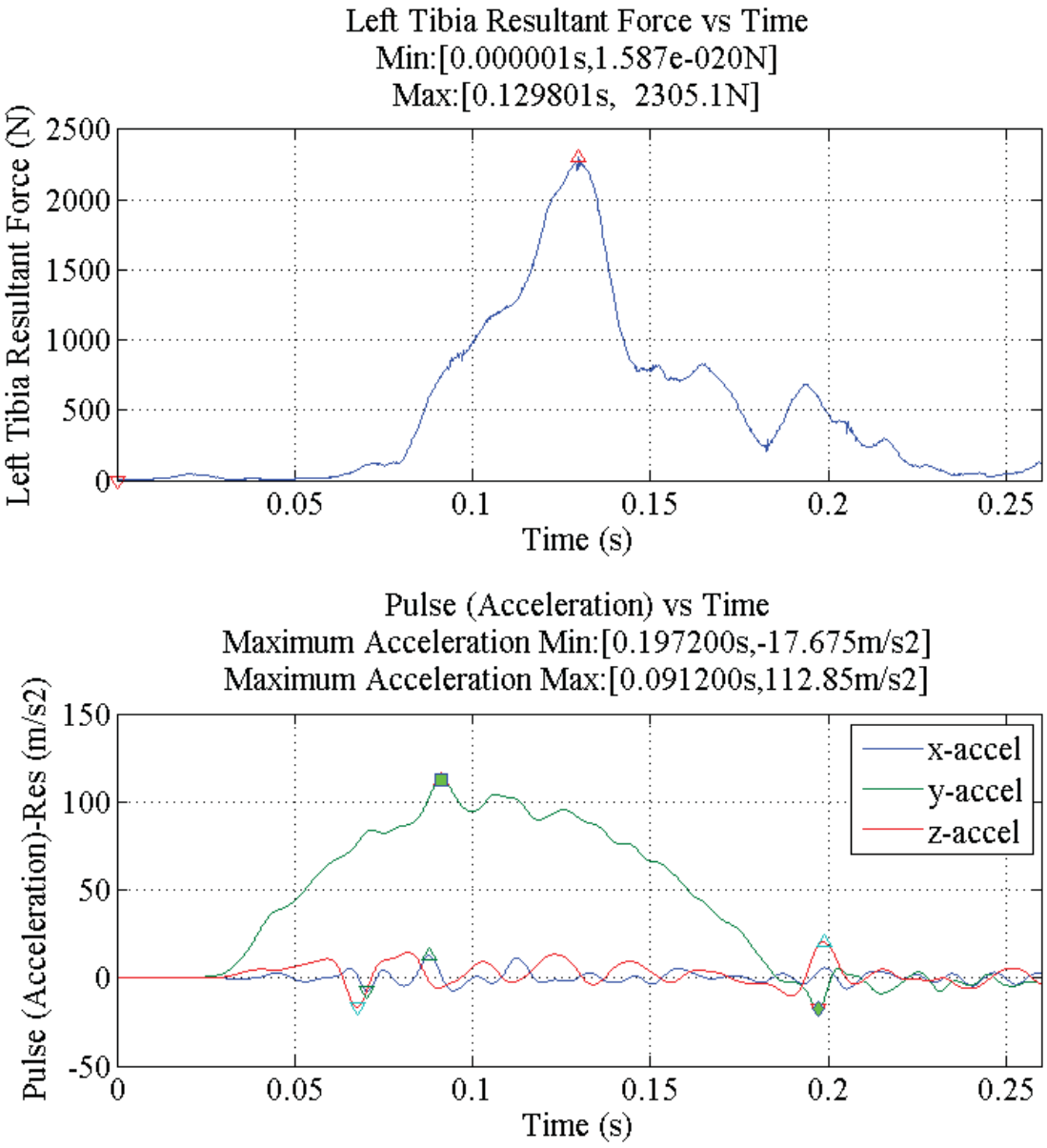

Figure 191: Left Tibia Force for simulation 8245 (Lateral), long pulse.

Appendix 17: Images from each simulation result.

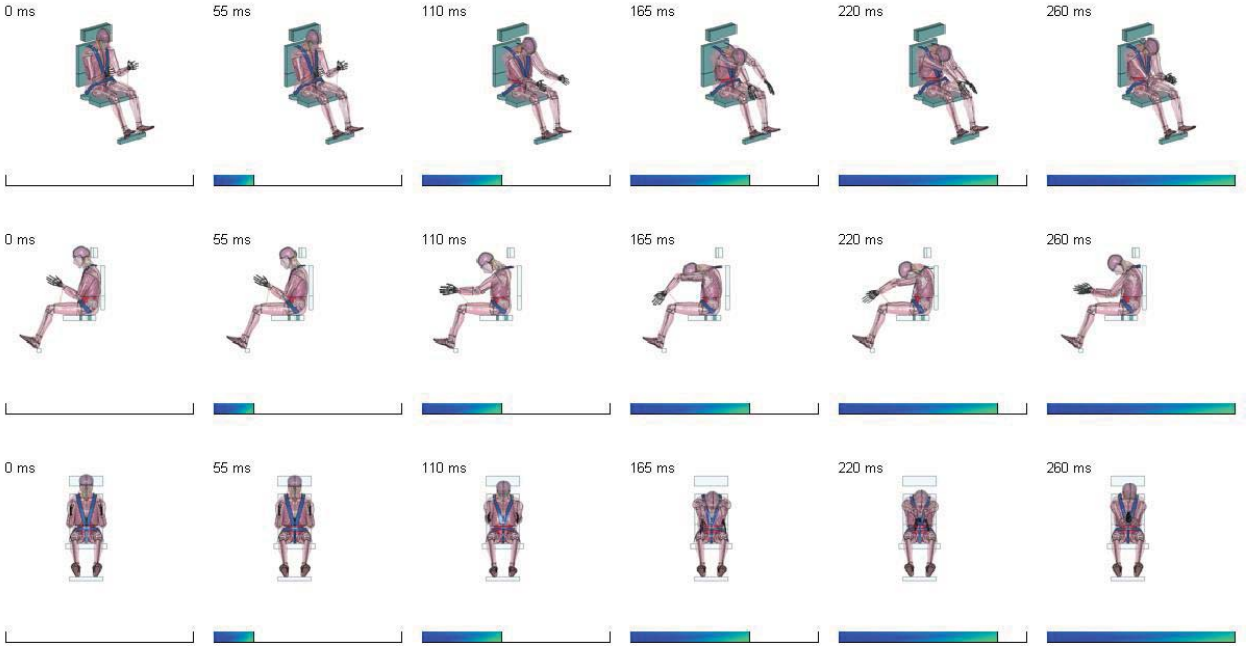

Figure 192: Resultant images from simulation 8202, frontal impact.

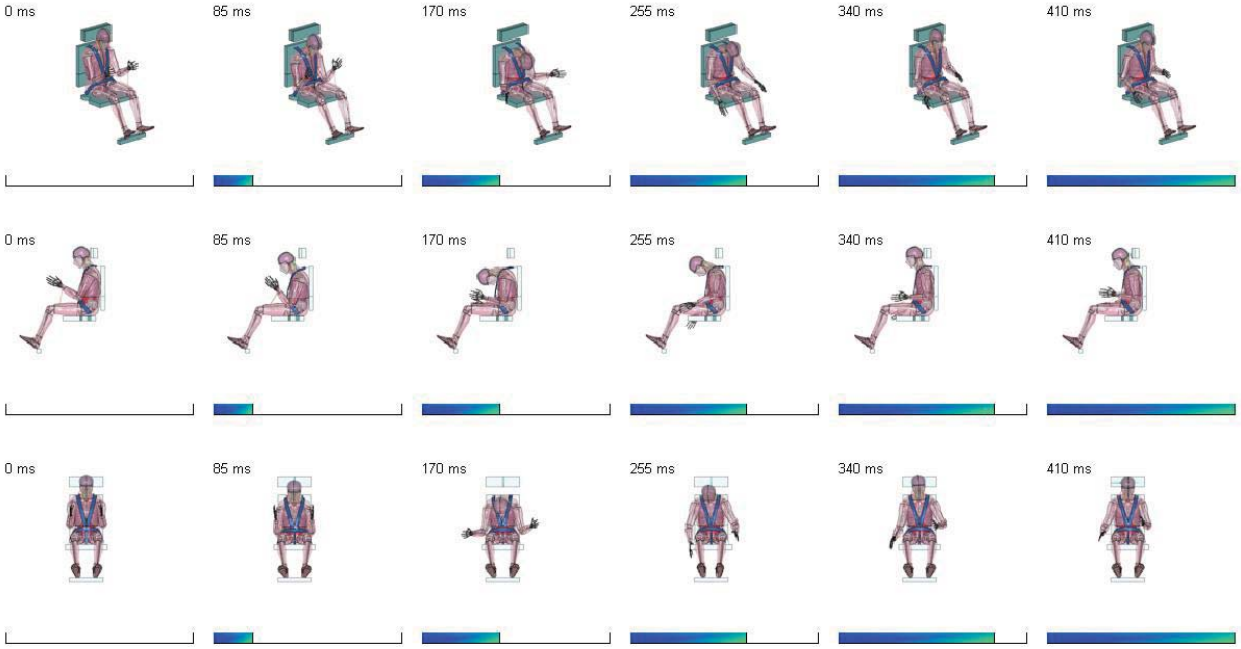

Figure 193: Resultant images from simulation 8208, spinal impact.

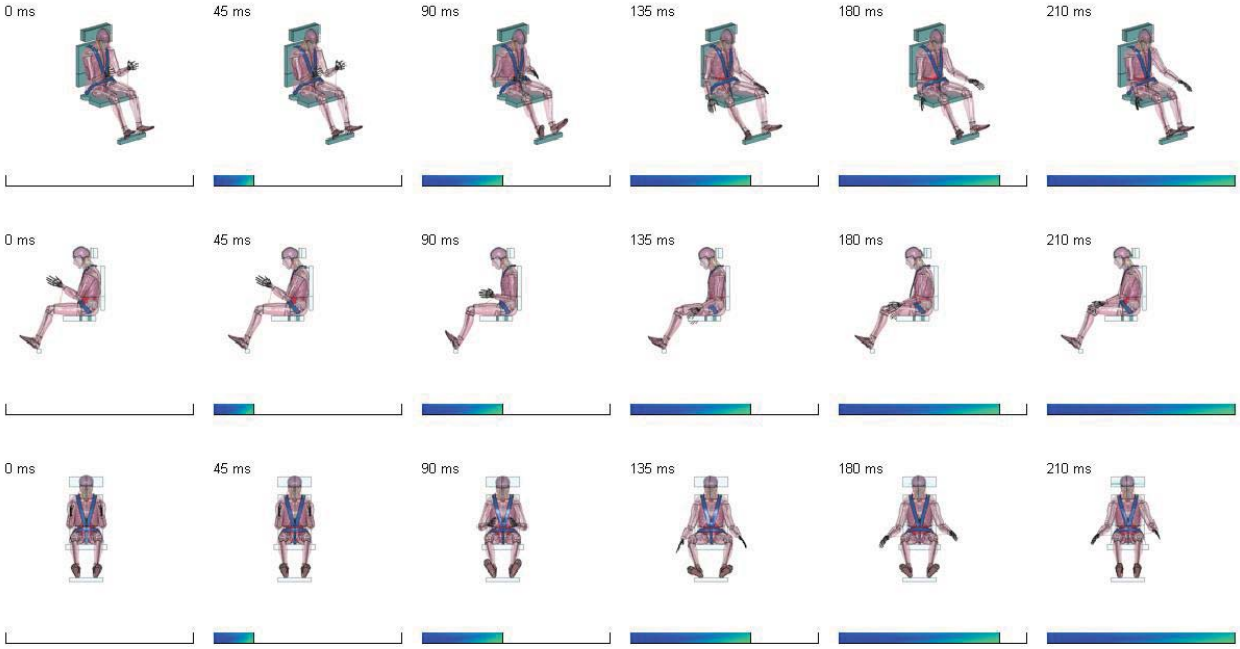

Figure 194: Resultant images from simulation 8212, rear impact.

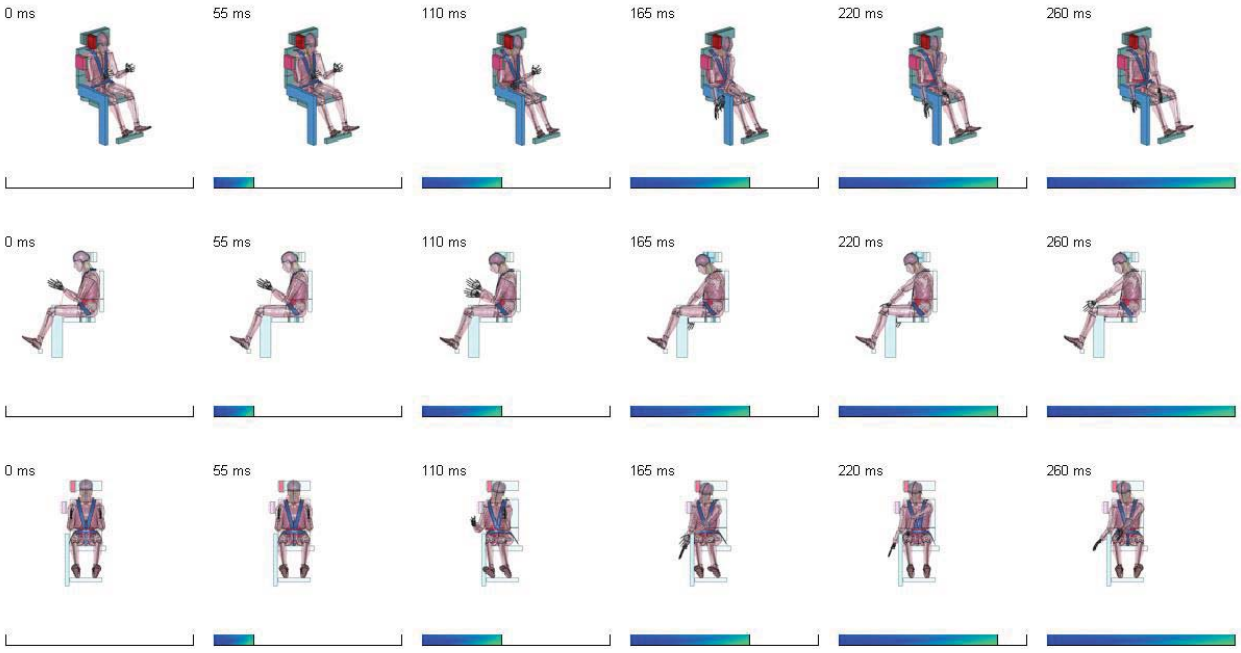

Figure 195: Resultant images from simulation 8245, lateral impact.

REPORT DOCUMENTATION PAGE

Form Approved
OMB No. 0704-0188

1. REPORT DATE *(DD-MM-YYYY)*	2. REPORT TYPE	3. DATES COVERED *(From - To)*
01- 09 - 2016	Technical Memorandum	

4. TITLE AND SUBTITLE
Crew Exploration Vehicle (CEV) (Orion) Occupant Protection
Appendices Part 2

5a. CONTRACT NUMBER

5b. GRANT NUMBER

5c. PROGRAM ELEMENT NUMBER

6. AUTHOR(S)
Currie-Gregg, Nancy J.; Gernhardt, Michael L.; Lawrence, Charles; Somers, Jeffrey T.

5d. PROJECT NUMBER

5e. TASK NUMBER

5f. WORK UNIT NUMBER
869021.01.05.01.03

7. PERFORMING ORGANIZATION NAME(S) AND ADDRESS(ES)
NASA Langley Research Center
Hampton, VA 23681-2199

8. PERFORMING ORGANIZATION REPORT NUMBER
L-20753

9. SPONSORING/MONITORING AGENCY NAME(S) AND ADDRESS(ES)
National Aeronautics and Space Administration
Washington, DC 20546-0001

10. SPONSOR/MONITOR'S ACRONYM(S)
NASA

11. SPONSOR/MONITOR'S REPORT NUMBER(S)
NASA/TM-2016-219337/Volume II/Part 2

12. DISTRIBUTION/AVAILABILITY STATEMENT
Unclassified - Unlimited
Subject Category 16-Space Transportation and Safety
Availability: NASA STI Program (757) 864-9658

13. SUPPLEMENTARY NOTES

14. ABSTRACT

Dr. Nancy J. Currie, of the NASA Engineering and Safety Center (NESC), Chief Engineer at Johnson Space Center (JSC), requested an assessment of the Crew Exploration Vehicle (CEV) occupant protection as a result of issues identified by the Constellation Program and Orion Project. The NESC, in collaboration with the Human Research Program (HRP), investigated new methods associated with occupant protection for the Crew Exploration Vehicle (CEV), known as Orion. The primary objective of this assessment was to investigate new methods associated with occupant protection for the CEV, known as Orion, that would ensure the design provided minimal risk to the crew during nominal and contingency landings in an acceptable set of environmental and spacecraft failure conditions. This documents contains the Appendices to the main NESC assessment report. NASA/TM-2013-217380, "Application of the Brinkley Dynamic Response Criterion to Spacecraft Transient Dynamic Events." supercedes this document.

15. SUBJECT TERMS
NASA Engineering and Safety Center; Crew Exploration Vehicle; Human Research Program; Crew Module; Brinkley Dynamic Response; Anthropomorphic Test Devices

16. SECURITY CLASSIFICATION OF:			17. LIMITATION OF ABSTRACT	18. NUMBER OF PAGES	19a. NAME OF RESPONSIBLE PERSON
a. REPORT	b. ABSTRACT	c. THIS PAGE			STI Help Desk (email: help@sti.nasa.gov)
					19b. TELEPHONE NUMBER *(Include area code)*
U	U	U	UU	219	(443) 757-5802